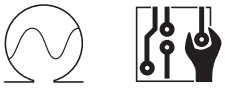

Technische Universität München
Fakultät für Elektrotechnik und Informationstechnik
Lehrstuhl für Entwurfsautomatisierung

Non-Gaussian Correlated Multivariate Modeling for Variability Abstraction in Integrated Circuit Analysis

André Lange

Vollständiger Abdruck der von der Fakultät für Elektrotechnik und Informationstechnik der Technischen Universität München zur Erlangung des akademischen Grades eines

Doktor-Ingenieurs (Dr.-Ing.)

genehmigten Dissertation.

Vorsitzender: Prof. Dr.-Ing. Georg Sigl

Prüfer der Dissertation:

1. Prof. Dr.-Ing. Ulf Schlichtmann
2. Prof. Dr.-Ing. Erich Barke, Leibniz Universität Hannover

Die Dissertation wurde am 17. Mai 2016 bei der Technischen Universität München eingereicht und durch die Fakultät für Elektrotechnik und Informationstechnik am 12. September 2016 angenommen.

Acknowledgments

I would like to express my gratitude to Professor Dr. Ulf Schlichtmann for supporting the independent research that is documented in this thesis. His advice helped to disseminate the obtained results in various conference papers and one journal paper. Additionally, I would like to thank Professor Dr. Erich Barke for his willingness to survey this thesis.

Furthermore, I would like to acknowledge the support and opportunities which have been offered by my colleagues at the Fraunhofer Institute for Integrated Circuits IIS, Division Engineering of Adaptive Systems EAS in Dresden, Germany. In particular, I would like to thank Dr. Manfred Dietrich and Roland Jancke for supporting my work and providing the organizational background. Additionally, I would like to thank Dr. Joachim Haase and Dr. Christoph Sohrmann for their ideas and the fruitful discussions on various research topics.

Major results documented in this thesis were obtained in the research projects CoolE-Design (German Federal Ministry of Education and Research [BMBF], ID 16N10183) and SUPERTHEME (European Union Seventh Framework Programme, FP7/2007-2013, grant agreement number 318458). I would like to acknowledge the cooperation with the partners in these projects and beyond, especially Dr. Joachim Müller and his team, Dr. Hendrik T. Mau, Dr. Sabine Kolodinski, and Ingolf Lorenz (GLOBALFOUNDRIES, Dresden, Germany); Professor Asen Asenov (University of Glasgow and Gold Standard Simulations, Glasgow, Scotland); as well as Dr. Frédéric Roger (ams, Premstaetten, Austria).

I would like to acknowledge the typesetting support from Dr. Robert Fischbach and Dr. Martin Barke. Furthermore, I would like to thank Dr. Joachim Haase, Dr. Uwe Hatnik, Katja Polotzek, Dr. Torsten Reich, Dr. Peter Schwarz, and Dr. rer. nat. Sascha Trostorff for proofreading and their recommendations.

Finally, I appreciate the love and support of my family. I would like to express my gratitude especially to my parents as well as to Tabea and Cedric.

Abstract

Process variations and atomic-level fluctuations cause variations in the performance parameters of integrated circuits. To accurately predict the circuit behavior before manufacturing, these effects have to be addressed in the design phase already. For this purpose, a variety of methods have evolved. However, they appear tailored to particular problems and often make simplifying, potentially inaccurate assumptions, such as corners or Gaussian distributions. This thesis presents a multivariate modeling approach that can be equally applied at multiple levels of abstraction. It treats selected parameters of arbitrary underlying models as multivariate random variables, which are described by combinations of generalized lambda distributions and Spearman's rank correlation coefficients. Inherently, this approach supports correlated and non-Gaussian parameters so that it enhances the state of the art. Application scenarios in device compact modeling, standard cell modeling and corresponding gate level analyses, and analog behavioral modeling demonstrate the universality and accuracy of this modeling approach.

Kurzfassung

Durch Variationen im Herstellungsprozess und auf der atomaren Ebene schwanken die Kenngrößen integrierter Schaltungen. Um aussagekräftige Informationen über das Schaltungsverhalten vor der Fertigung zu erhalten, müssen diese Variationen bereits im Entwurfsprozess berücksichtigt werden. Zu diesem Zweck sind verschiedenste Verfahren verfügbar. Häufig sind sie aber auf einzelne, spezielle Problemstellungen zugeschnitten und treffen vereinfachende Annahmen, z.B. Corners oder normalverteilte Größen. Diese Arbeit stellt einen multivariaten Ansatz zur Modellierung von Variationen vor, der auf unterschiedlichen Abstraktionsebenen gleichermaßen angewendet werden kann. Er fasst ausgewählte Parameter eines beliebigen zugrundeliegenden Modells als mehrdimensionale Zufallsvariable zusammen. Durch deren Beschreibungen mit verallgemeinerten Lambda-Verteilungen und Spearman'schen Rangkorrelationskoeffizienten werden korrelierte sowie nichtnormalverteilte Größen unterstützt und dadurch der Stand der Technik erweitert. In den Anwendungsbeispielen auf unterschiedlichen Abstraktionsebenen, Transistormodelle, Standardzellmodelle und ihrer Anwendung in Analysen auf der Gatterebene sowie analoge Verhaltensmodelle, werden die Allgemeingültigkeit und Genauigkeit des Ansatzes aufgezeigt.

Table of Contents

List of Figures

List of Tables

List of Symbols

$\mathbf{A}$	matrix
$\mathbf{A}^{\mathrm{T}}$	transpose of matrix $\mathbf{A}$
$\mathbf{A}^{-1}$	inverse of matrix $\mathbf{A}$
$\lvert\mathbf{A}\rvert$	determinant of matrix $\mathbf{A}$
$\mathbf{a}$	vector
$\widetilde{a}$	estimator or empirical value of quantity a
$\alpha_{\mathrm{X},3}$	skew of univariate *random variable* (RV) X
$\alpha_{\mathrm{X},4}$	kurtosis of univariate RV X
$(1-\alpha_c)$	confidence level
β_j^{wc}	worst-case distance
$\mathrm{E}\left[.\right]$	expectation operator
FR	failure rate
G	univariate standard Gaussian RV, $G\sim\mathrm{N}(0,1)$
$\boldsymbol{G}$	multivariate RV with correlated standard Gaussian components
$\boldsymbol{G_{std}}$	multivariate standard Gaussian RV
$\mathbf{I}$	identity matrix
LSB	lower specification boundary
$\mu_{\mathrm{X}},\ \boldsymbol{\mu}_{\mathbf{X}}$	mean value of univariate RV X, mean vector of multivariate RV $\boldsymbol{X}$
N	sample size
$\mathrm{N}(\mu,\sigma^2)$	univariate Gaussian distribution with parameters μ and σ
$\mathbf{N}(\boldsymbol{\mu},\boldsymbol{\Sigma})$	multivariate Gaussian distribution with mean vector $\boldsymbol{\mu}$ and covariance matrix $\boldsymbol{\Sigma}$
$\mathbf{R}_{\mathbf{X}}$	Spearman's rank correlation matrix of RV $\boldsymbol{X}$; intra-instance Spearman's rank correlation matrix of circuit element X
$\mathbf{R}_{\mathbf{X},\mathbf{X}}$	inter-instance Spearman's rank correlation matrix for circuit element X
$\mathbf{R}_{\mathbf{X},\mathbf{Y}}$	inter-element Spearman's rank correlation matrix for elements X and Y
$\mathbb{R}_{\mathbf{A}}$	region of acceptability
$\mathbb{R}_{\mathbf{T}}$	tolerance region
$\mathbb{R}_{\mathbf{X}}$	input parameter space
$\mathbb{R}_{\mathbf{Z}}$	performance space
$\rho^{(\mathrm{pe})}$	Pearson's correlation coefficient

$\rho^{(\mathrm{sp})}$	Spearman's correlation coefficient
$\mathrm{rk}\left(x^{(\mathrm{k})}\right)$	rank of k-th observation in sample $\tilde{X}$
$\mathbf{S}$	sensitivity matrix
$\boldsymbol{\Sigma}_{\mathbf{X}}$	covariance matrix of RV $\boldsymbol{X}$
$\boldsymbol{\Sigma}_{\mathbf{X},\mathbf{X}}$	inter-instance covariance matrix for circuit element X
$\boldsymbol{\Sigma}_{\mathbf{X},\mathbf{Y}}$	covariance matrix between RVs $\boldsymbol{X}$ and $\boldsymbol{Y}$; inter-element covariance matrix for elements X and Y
σ_{X}	standard deviation of univariate RV X
$\boldsymbol{U}$	multivariate uniform RV
U	univariate uniform RV
$\mathrm{U}(a,b)$	univariate uniform distribution with parameters a and b
USB	upper specification boundary
$\mathrm{Var}\left[X\right]$	variance of univariate RV X
$\Phi\left(.\right)$	*cumulative distribution function* (CDF) of standard Gaussian distribution
$\Phi^{-1}(.)$	quantile function of standard Gaussian distribution
$\phi_{\mathrm{X}}(.)$	CDF of RV X
$\phi_{\mathrm{X}}^{-1}(.)$	quantile function of RV X
$\varphi_{\mathrm{X}}(.)$	*probability density function* (PDF) of RV X
X, Y, Z	univariate RV
$\boldsymbol{X}, \boldsymbol{Y}, \boldsymbol{Z}$	multivariate RV
$\tilde{X},\ \tilde{\boldsymbol{X}}$	sample from univariate RV X or multivariate RV $\boldsymbol{X}$
X_i	i-th component of multivariate RV $\boldsymbol{X}$
$x^{(\mathrm{k})},\ \boldsymbol{x}^{(\mathrm{k})}$	k-th observation in sample $\tilde{X}$ or $\tilde{\boldsymbol{X}}$
$x^{<\mathrm{k}>}$	k-th component of order statistics of sample $\tilde{X}$
$\boldsymbol{x}_{\mathbf{det}}^{(\mathrm{corner})}$	deterministic corner
$\boldsymbol{x}_{\mathbf{stat}}^{(\mathrm{corner})}$	statistical corner
$\boldsymbol{x}_{\mathbf{stat,wc}}^{(\mathrm{corner})}$	worst-case statistical corner
$\boldsymbol{x}_{\mathbf{j}}^{(\mathrm{WCP})}$	worst-case point for performance parameter y_j
Ψ	parametric yield

List of Abbreviations

AOCV	*advanced on-chip variations*
BPV	*backward propagation of variance*
BSIM	*Berkeley short-channel insulated gate field effect transistor model*
CDF	*cumulative distribution function*
DRAM	*dynamic random access memory*
EM	*electro migration*
FET	*field effect transistor*
GLD	*Generalized Lambda Distribution*
GLD-FKML	*Generalized Lambda Distribution in parametrization after Freimer, Kollia, Mudholkar, and Lin [FKML88]*
GLD-RS	*Generalized Lambda Distribution in parametrization after Ramberg and Schmeiser [RS74]*
HDL	*hardware description language*
HSMC	*High-Sigma Monte Carlo*
IC	*integrated circuit*
KS	*Kolmogorov-Smirnov*
LER	*line edge roughness*
MC	*Monte Carlo*
MCSSTA	*Monte Carlo-based statistical static timing analysis*
NFET	*n-channel field effect transistor*
NPM	*non-linear power method*
OCV	*on-chip variations*
POCV	*parametric on-chip variations*
PCA	*principal component analysis*

PDF	*probability density function*
PDK	*process design kit*
PFET	*p-channel field effect transistor*
QBPV	*quadratic backward propagation of variance*
Q-Q	*quantile-quantile*
RDF	*random dopant fluctuation*
RO	*ring oscillator*
RV	*random variable*
SB	*statistical blockade*
SOI	*silicon on insulator*
SPICE	*simulation program with integrated circuit emphasis*
SRAM	*static random access memory*
SSTA	*statistical static timing analysis*
STA	*static timing analysis*
SW	*Shapiro-Wilk*
VHDL	*Very High Speed Integrated Circuit Hardware Description Language*
WCD	*worst-case distance*
WCP	*worst-case point*
WCV	*worst-case vector*

1 Introduction

1.1 Overview

Modern everyday life is dominated by *integrated circuits* (ICs). These products of the semiconductor industry enable cost-effective high-performance computation capabilities and are essential in intelligent extremely low-power applications. Some well-known application examples are multifunctional consumer devices, high-speed wired and mobile communication, intelligent driver assistance systems in cars, industrial or home automation systems, and health technology [ITR11c].

Due to their widespread usage, ICs have an enormous impact on the world-wide economy. The annual sales of the semiconductor industry are depicted in Fig. 1.1. While a cyclical time behavior with partially dramatic variations can be observed, the overall trend is rising. For example, global semiconductor sales reached $US\$\ 300\ billion$ in 2011 [Cha12] and nearly $US\$\ 336\ billion$ in 2014 [Ros15].

One key driver of the success of ICs has been *technology scaling*. In 1965, Gordon Moore analyzed the circuit complexity economically. He found that approximately

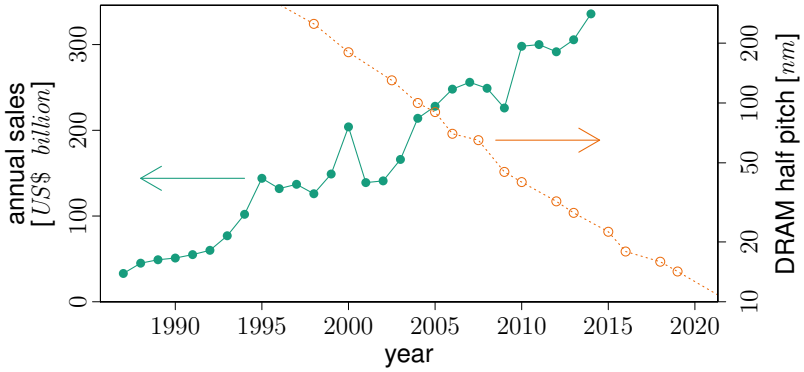

Fig. 1.1: Semiconductor sales (data from [Cha12, Ros13, Ros15]) and DRAM half pitch evolutions ([ITR11b], Tab. D)

doubling the circuit complexity every year had led to minimum component costs. As a pure economic consideration, he predicted that this trend would remain approximately constant for a further $5-10\,years$ [Moo65]. To achieve this goal, the structure sizes, that is device and interconnect geometries, needed to be reduced. In consequence, voltages and doping concentrations had to be adapted [DGR+74]. Assuming subsequent technology generations have been separated by a constant scaling factor $\kappa=\sqrt{2}$, scaling trends for selected technology characteristics are illustrated in Fig. 1.2. They demonstrate that both circuit delay and power dissipation could be dramatically improved by technology scaling.

Until today, these scaling principles have served as a road map for the semiconductor industry and been known as *Moore's law* [ITR11b]. With a scaling factor $\kappa\approx\sqrt{2}$, the transistor density approximately doubled from one technology generation to the next [Boh07]. While new technology generations were introduced every $3\,years$ until about 1990, this duration has shortened to about $2\,years$ since then. However, scaling to reach semiconductor feature sizes in the regime of $100\,nm$ and below posed various technological challenges. To solve them, enhanced process steps have been developed and new materials have been introduced. These improvements, some of which are listed in Tab. 1.1, have come at the cost of an increasingly complex manufacturing process.

As an example for technology scaling, achieved and expected feature sizes in *dynamic random access memory* (DRAM) products over time are depicted in Fig. 1.1. With structure sizes of $20\,nm$ to $30\,nm$ in mass production today, semiconductors are approaching physical limits and atomic scales.

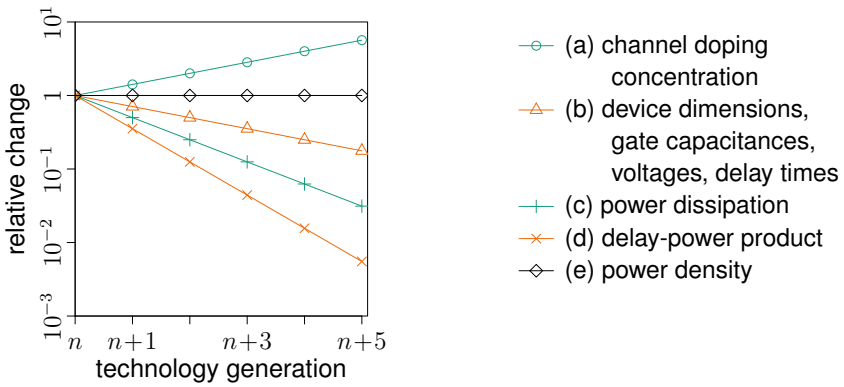

Fig. 1.2: Principles of semiconductor scaling trends [DGR+74] with a scaling factor of $\kappa=\sqrt{2}$

Tab. 1.1: Selected recent major improvements in semiconductor manufacturing

Technological achievement	References
Copper wiring reduced interconnect resistivity and limited *electro migration* (EM).	[Adv00], [Cat00], [Hil04]
Strain engineering boosted transistor performance at the $90\,nm$ technology node.	[TAA$^+$04]
High-k metal gate transistors lowered transistor gate leakage in a $45\,nm$ technology.	[MAA$^+$07]
Fully-depleted tri-gate transistors combine low leakage and high performance at the $22\,nm$ technology node and below.	[AAB$^+$12]

To further increase the performance of ICs, different trends have evolved. On the one hand, especially in digital circuits for logic operations and signal processing, a further miniaturization is expected to continue Moore's law and referred to as *More Moore*. On the other hand, *More than Moore*, the diversification by adding non-digital functionality, such as high-frequency analog components or micro-mechanical elements, to ICs offers application specific integrated system solutions [ITR11b].

Irrespective of their concrete application, most recent ICs face similar criteria in performance, such as high speed and low power consumption; quality, such as functionality, variability, and reliability; as well as economy, such as low requirements in die area and considerably low costs [ITR11b], which can only be achieved with well-organized fabrication and design processes.

1.2 Motivation

In a simplified manner, the organization of semiconductor processing is illustrated in Fig. 1.3: it may take place in different fabrication plants, so-called fabs; in these fabs, lots of typically 25 wafers are handled; and on each wafer, multiple ICs are manufactured side by side [DH12, MI93]. The details of the particular processing steps, such as implantation, oxidation, or deposition, and their integration are beyond the scope of this thesis and, for instance, discussed in [Hil04, WT86, Wol90].

Obviously, variations can occur within all these hierarchical levels in the manufacturing process, that is between fabs, lots, wafers, and ICs. These process variations affect each individual IC as a whole. They shift certain parameters of all circuit elements, for instance *n-channel field effect transistors* (NFETs) and *p-channel field effect tran-*

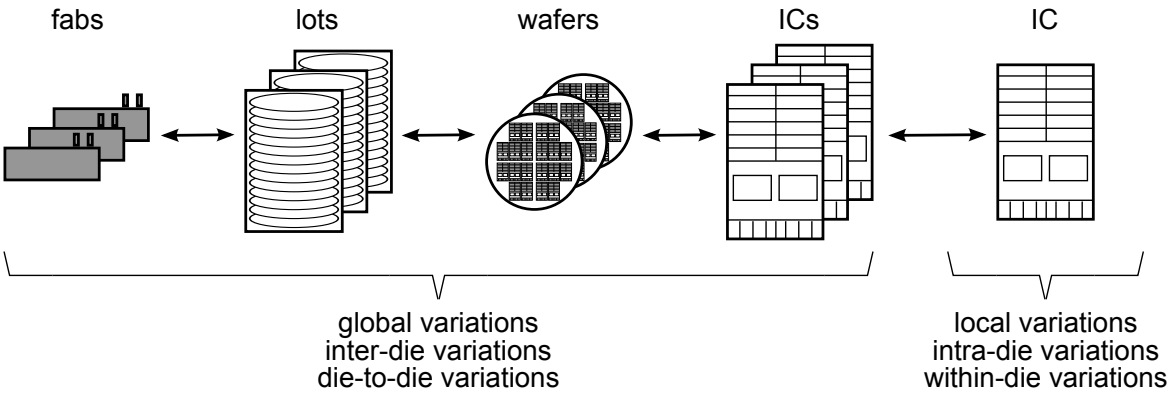

Fig. 1.3: Simplified organization of *integrated circuit* (IC) manufacturing

sistors (PFETs), equally so that they are referred to as *global variations* (inter-die, die-to-die variations) [BC09, DH12]. Examples for global variations are

- lot-to-lot variations due to differences in the temperature and the supply of chemicals in batch processes, such as conventional material deposition, etching, oxidation, and chemical mechanical polishing [Hil04, WT86];
- wafer-to-wafer and across-wafer substrate resistivity variations of up to $\pm 8\,\%$ for p-type and $\pm 20\,\%$ for n-type silicon wafers due to uneven doping concentrations from temperature instabilities and segregation during wafer fabrication [WT86];
- wafer-to-wafer variations from single-wafer processing steps, for instance due to dose variations in ion implantation or temperature fluctuations in rapid thermal processing [Hil04, WT86];
- or die-to-die line width and overlay variations due to misalignments of photo masks, focus variations, and variations in other sub-steps of lithography [Hil04, LLP06, ONB08].

In addition, process variations can introduce *local variability* (intra-die, within-die variability), for instance during lithography, etching, or chemical-mechanical polishing [ONB08]. Local variability shifts certain parameters of each circuit component individually and gains importance with shrinking feature sizes. Its most important example is *mismatch*, causing identically designed devices within an IC to differ in their properties and behaviors [PDW89].

Technology scaling has brought semiconductors close to atomic-scale dimensions so that atomic material structures, energy quantization, and quantum mechanics have gained importance. Atomic-level fluctuations due to the discreteness of charge and the granularity of matter have introduced additional local variability that has to be taken

into consideration in the description of semiconductor devices [Ase07, ONB08]. These effects include

- *random dopant fluctuation* (RDF): the number (by $5\,\%$ to $10\,\%$ in small transistors [BFG+06, ONB08]) and location of channel dopants varies from one transistor to another [ONB08, KKK+08, KGB+11, Sah10];
- *line edge roughness* (LER): shapes transferred to the IC during lithography are not straight but differ from their base lines, affecting both transistors and interconnects [Ase07, KKK+08, ONB08, Sah10, TCR+09];
- interface roughness: interface roughness on a nanometer-length scale may be 1 to 2 atomic layers [BFG+06, Sah10], potentially accounting for a $50\,\%$ variation in gate dielectric thickness in the $65\,nm$ node and below [BFG+06, ONB08, Sah10];
- and random grains: in the polycrystalline structure of the gate dielectric or in metal gates, grains of random size and orientation can be observed with their boundaries influencing the electrical behavior of transistors [BFG+06, BRA07, Sah10].

For a long time, global variations dominated IC variability [MI93]. However, local variability has rapidly been gaining importance at shrinking geometries and emerging atomic-level fluctuations. In a $65\,nm$ technology, random local variations were even reported to dominate the overall variability [Hir10]. Increasing relative variations have worsened the variability issues and made the variability handling in IC design more complicated [Mir12, Sah10].

From a designer's perspective, global and local effects contribute to IC performance variability. Circuits with $30\,\%$ maximum frequency variations and up to $10-20\,X$ leakage power variations were reported [Mir12, ONB08], and the impact of variability on circuit performance is expected to grow further with ongoing technology scaling [Dec05, Mir12]. To achieve a reasonable quality of future ICs, global and local variations have to be taken into consideration appropriately already during design to predict the impact of variability on the circuit behavior.

1.3 Contributions and Goals of this Thesis

Variability has been and will remain a key challenge in IC design [ITR11a, Mir12]. In this thesis, the term *variability* denotes time-independent global and local variations from process variations and atomic-level fluctuations. Further effects, such as time-dependent parameter evolutions due to degradation, are not considered.

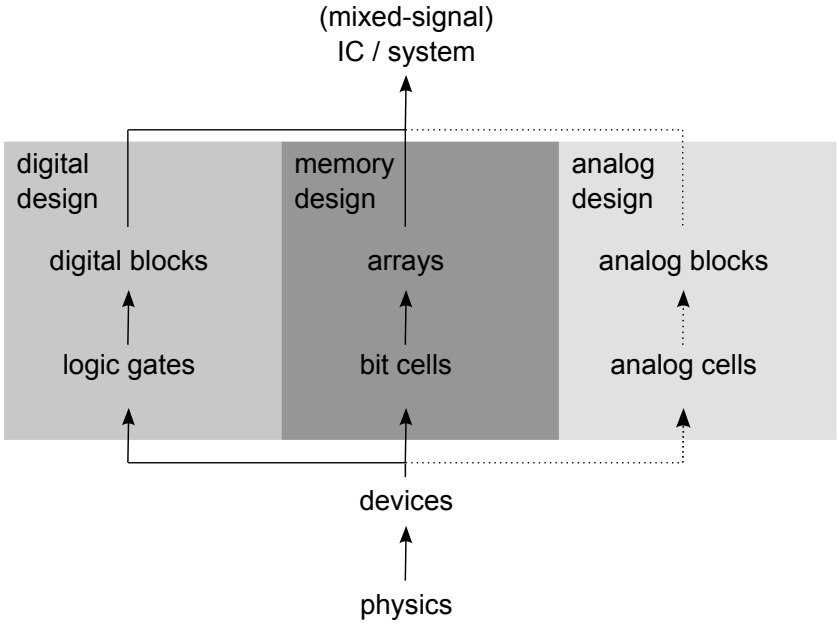

Fig. 1.4: Abstraction levels in IC design to handle variability; digital and memory design from [ITR11a] and possible future extension for analog circuit design

Many ICs are mixed-signal systems that can consist of digital and analog parts as well as memories with dedicated design and analysis methods. To handle the complexity in IC design, abstraction levels for variability have been proposed for digital circuits and memories [ITR11a]. Their illustration in Fig. 1.4 is supplemented by a possible extension to analog circuits, which is considered in this thesis. Clearly, variability arises in the physical layer where many effects are understood. However, variability information has to be transferred to the device level and further abstracted to logic gates and digital blocks, to bit cells and memory arrays, or to analog cells and blocks.

The review of existing approaches in this thesis reveals that a variety of solutions for variability handling are already available. However, they

- appear tailored to particular tasks and are, therefore, not general;
- often only consider particular performance parameters, such as circuit timing;
- and make simplifying assumptions, for instance linear approximations of parameter dependencies or Gaussian distributions.

Therefore, although a lot of research has been carried out already, how to tackle variability in future IC design has not yet been solved. Furthermore, existing solutions do not seem to be widely used [Mir12].

This thesis is intended to contribute to an adequate variability handling IC design and analysis. In particular, it addresses the topic of how to *consistently transfer variability information between different abstraction levels*. For this purpose, a fully statistical modeling approach is established in this thesis. It combines parameter correlations and *generalized lambda distributions* (GLDs) to capture

- global and local variations,
- arbitrary statistical correlations,
- and nearly arbitrary distribution shapes.

Thus, the approach is flexible and applicable on multiple abstractions levels, and it offers a solution to correlated non-Gaussian modeling, which was considered impractical, for instance in [LLP06].

This thesis demonstrates the capabilities and benefits of the developed variability modeling approach at different application scenarios: device compact models, standard cell models for digital design, and analog behavioral models.

1.4 Organization

This thesis is organized as follows. Chap. 2 provides the theoretical background for this thesis with an introduction into statistics and variability abstraction. In Chap. 3, the state of the art in variability handling is reviewed for the device level, digital design, *static random access memory* (SRAM) design, and analog design with its limitations being outlined. Based on research results that were published in [LSJ+11], [LH12], [LJH+13], [LSJ+14], [LHDK14], [LHE+15], as well as [LSJ+16], a fully statistical multivariate variability modeling approach for IC design and analysis is established in Chap. 4. In Chap. 5, multivariate models are determined from characterization data for different application scenarios: device compact models, standard cell models, and analog behavioral models. Furthermore, it is demonstrated how these models can be applied in statistical circuit analyses on different levels of abstraction. Chap. 6 concludes this thesis by summarizing its content and contributions as well as outlining directions for future research.

2 Selected Principles of Statistics

This chapter introduces some basics of statistics. While it focuses on aspects that are required and applied throughout this thesis, for example, [Dwa70, Eve06, FEHP11, HE07, HEK09] present more profound and detailed information.

2.1 Univariate Random Variables

2.1.1 Definitions, Descriptions, and Characteristic Values

A *univariate random variable* (RV) X is a variable that can obtain different values x according to a probability distribution [Eve06]. The possible values are referred to as realizations or observations [Eve06, HEK09].

Different functions, for instance the *cumulative distribution function* (CDF) $\phi_{\mathrm{x}}(.)$, the *quantile function* $\phi_{\mathrm{x}}^{-1}(.)$, and the *probability density function* (PDF) $\varphi_{\mathrm{x}}(.)$, interchangeably describe a RV X whereas one of them is sufficient [Eve06, HEK09]. The CDF

$$x_t \;\longmapsto\; \phi_{\mathrm{x}}(x_t) = \mathrm{Prob}\left[X \leq x_t\right] = p_t, \tag{2.1}$$

defines the probability that a realization of the RV X is smaller than or equal to a threshold x_t [Dwa70, HEK09]. The inverse of the CDF, the quantile function [HF96]

$$x_t = \phi_{\mathrm{x}}^{-1}(p_t) = \inf\left\{x :\ \phi_{\mathrm{x}}(x) \geq p_t\right\} \qquad \text{with} \qquad 0 \leq p_t \leq 1, \tag{2.2}$$

assigns the threshold x_t to a probability p_t. The PDF of a continuous RV [HEK09],

$$\varphi_{\mathrm{x}}(x_t) = \left.\frac{\mathrm{d}\phi_{\mathrm{x}}(x)}{\mathrm{dx}}\right|_{x_t} \qquad \Longleftrightarrow \qquad \phi_{\mathrm{x}}(x_t) = \int_{-\infty}^{x_t} \varphi_{\mathrm{x}}(x)\mathrm{dx}. \tag{2.3}$$

is the first-order derivative of a differentiable CDF. It has to fulfill the conditions $\varphi_{\mathrm{X}}(x) \geq 0 \ \forall \ x$ and $\int_{-\infty}^{\infty} \varphi_{\mathrm{X}}(x) \, \mathrm{dx} = 1$ to be valid [HEK09].

In addition to these functions, the distribution moments and derived quantities are characteristic values, which define a RV X to a large extent. The most important of these characteristic values are the *mean value* μ_{X} as the measure of location, the *variance* $\mathrm{Var}\,[X]$ or the *standard deviation* σ_{X} as the measures of scale, and the *skew* $\alpha_{\mathrm{X},3}$ as well as the *kurtosis* $\alpha_{\mathrm{X},4}$ as the measures of shape [Fle78, KD00, VM83]. With the expected value [HEK09]

$$\mathrm{E}\,[X] = \int_{-\infty}^{\infty} x \cdot \varphi_{\mathrm{X}}(x) \mathrm{dx}, \tag{2.4}$$

these quantities are defined as [Eve06, HE07, KD00]

$$\mu_{\mathrm{X}} = \mathrm{E}\,[X]\,, \tag{2.5}$$

$$\mathrm{Var}\,[X] = \sigma_{\mathrm{X}}^2 = \mathrm{E}\left[(X - \mu_{\mathrm{X}})^2\right], \tag{2.6}$$

$$\alpha_{\mathrm{X},3} = \frac{\mathrm{E}\left[(X - \mu_{\mathrm{X}})^3\right]}{\sigma_{\mathrm{X}}^3}, \text{ and} \tag{2.7}$$

$$\alpha_{\mathrm{X},4} = \frac{\mathrm{E}\left[(X - \mu_{\mathrm{X}})^4\right]}{\sigma_{\mathrm{X}}^4}. \tag{2.8}$$

For the measures of shape, two basic properties exist. First, the skew $\alpha_{\mathrm{X},3} = 0$ represents a RV with a symmetric distribution, and a skew $\alpha_{\mathrm{X},3} \neq 0$ represents a RV with an asymmetric distribution. Second, large values for the kurtosis indicate RVs with at least one pronounced distribution tail [Eve06].

2.1.2 Examples of Probability Distributions and Visualization

Important examples for univariate probability distributions are the *Gaussian distribution*, also referred to as *normal distribution*; the *uniform distribution*; and the *lognormal distribution*. Examples of these distributions are depicted in Fig. 2.1.

First, a Gaussian RV X_{G}, denoted $X_{\mathrm{G}} \sim \mathrm{N}(\mu, \sigma^2)$, is defined by the PDF [FEHP11, HEK09, KD00]

$$\varphi_{\mathrm{X_G}}(x) = \frac{1}{\sigma\sqrt{2\pi}} \cdot \exp\left(-\frac{1}{2}\left(\frac{x-\mu}{\sigma}\right)^2\right) \tag{2.9}$$

with the parameters μ and σ, which measure the location and the scale of the distribution. A closed form CDF and a closed-form quantile function do not exist. The most important special case $\mathrm{N}(0,1)$ is referred to as *standard Gaussian distribution*. Its CDF is denoted $\Phi(.)$; available in tabular form [HEK09]; and implemented in mathematical software, for instance in *R* [R C14]. In this thesis, standard Gaussian RVs will be denoted G.

Second, a uniform RV X_U, denoted $X_\mathrm{U} \sim \mathrm{U}(a,b)$, is defined by the PDF and CDF [Eve06, FEHP11, HEK09, KD00]

$$\varphi_{X_\mathrm{U}}(x) = \begin{cases} \frac{1}{b-a} & : a \le x \le b \\ 0 & : \text{else} \end{cases} \quad \Longleftrightarrow \quad \phi_{X_\mathrm{U}}(x) = \begin{cases} 0 & : x < a \\ \frac{x-a}{b-a} & : a \le x \le b \\ 1 & : x > b \end{cases}. \tag{2.10}$$

Its parameters a and $b > a$ define the boundaries of the rectangular PDF, see Fig. 2.1(a). The most important special case $\mathrm{U}(0,1)$ has the boundaries $a = 0$ and $b = 1$.

Third, a lognormal RV X_L, denoted $X_\mathrm{L} \sim \mathrm{L}(m, \sigma_l)$, is defined by the PDF [FEHP11]

$$\varphi_{X_\mathrm{L}}(x) = \frac{1}{x\sigma_l\sqrt{2\pi}} \cdot \exp\left(-\frac{[\log(x/m)]^2}{2\sigma_l^2}\right), \quad x > 0 \tag{2.11}$$

with the parameters $m, \sigma_l > 0$. In (2.11), $\log(.)$ denotes the natural logarithm. If X_G is Gaussian, then $X_\mathrm{L} = \exp(X_\mathrm{G})$ is lognormal.

For Gaussian, uniform, and lognormal distributions, Tab. 2.1 summarizes the characteristic values defined in Sec. 2.1.1. The table includes general definitions, special

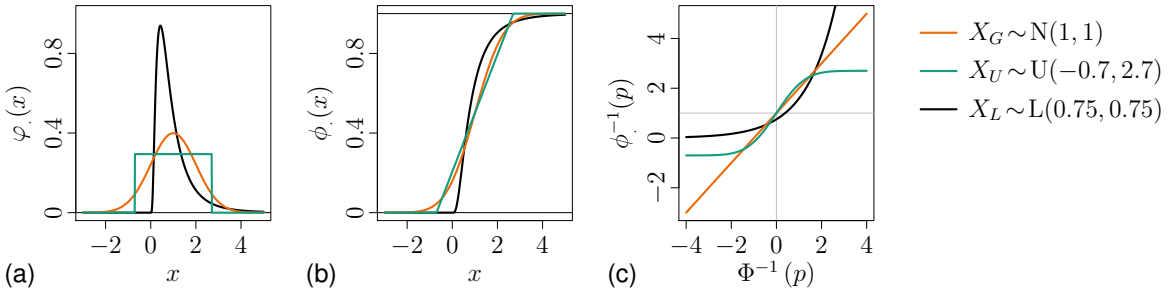

Fig. 2.1: Visualization of example probability distributions; (a) *probability density functions* (PDFs), (b) *cumulative distribution functions* (CDFs), (c) *quantile-quantile* (Q-Q) plots [Eve06]

Tab. 2.1: Characteristic values of Gaussian, uniform, and lognormal distributions [FEHP11, HEK09, KD00]; for lognormal distributions: $\omega = \exp(\sigma_l^2) > 1$ [FEHP11]

Distribution	Denotation	Mean value	Standard deviation	Skew	Kurtosis
Gaussian	$X_{\mathrm{G}} \sim \mathrm{N}(\mu, \sigma^2)$	$\mu_{x_{\mathrm{G}}} = \mu$	$\sigma_{x_{\mathrm{G}}} = \sigma$	$\alpha_{x_{\mathrm{G}},3} = 0$	$\alpha_{x_{\mathrm{G}},4} = 3$
	$G \sim \mathrm{N}(0,1)$	$\mu_{\mathrm{G}} = 0$	$\sigma_{\mathrm{G}} = 1$	$\alpha_{\mathrm{G},3} = 0$	$\alpha_{\mathrm{G},4} = 3$
	$X_{\mathrm{G}} \sim \mathrm{N}(1,1)$	$\mu_{x_{\mathrm{G}}} = 1$	$\sigma_{x_{\mathrm{G}}} = 1$	$\alpha_{x_{\mathrm{G}},3} = 0$	$\alpha_{x_{\mathrm{G}},4} = 3$
Uniform	$X_{\mathrm{U}} \sim \mathrm{U}(a,b)$	$\mu_{x_{\mathrm{U}}} = \frac{a+b}{2}$	$\sigma_{x_{\mathrm{U}}} = \frac{b-a}{2 \cdot \sqrt{3}}$	$\alpha_{x_{\mathrm{U}},3} = 0$	$\alpha_{x_{\mathrm{U}},4} = 1.8$
	$X_{\mathrm{U}} \sim \mathrm{U}(0,1)$	$\mu_{x_{\mathrm{U}}} = 0.5$	$\sigma_{x_{\mathrm{U}}} \approx 0.289$	$\alpha_{x_{\mathrm{U}},3} = 0$	$\alpha_{x_{\mathrm{U}},4} = 1.8$
	$X_{\mathrm{U}} \sim \mathrm{U}(-0.7, 2.7)$	$\mu_{x_{\mathrm{U}}} = 1$	$\sigma_{x_{\mathrm{U}}} \approx 0.981$	$\alpha_{x_{\mathrm{U}},3} = 0$	$\alpha_{x_{\mathrm{U}},4} = 1.8$
Lognormal	$X_{\mathrm{L}} \sim \mathrm{L}(m, \sigma_l)$	$\mu_{x_{\mathrm{L}}} = m \exp\left(\frac{1}{2}\sigma_l^2\right)$	$\sigma_{x_{\mathrm{L}}} = m\sqrt{\omega(\omega-1)}$	$\alpha_{x_{\mathrm{L}},3} = (\omega+2)\sqrt{\omega-1} > 0$	$\alpha_{x_{\mathrm{L}},4} = \omega^4 + 2\omega^3 + 3\omega^2 - 3 > 3$
	$X_{\mathrm{L}} \sim \mathrm{L}(\frac{3}{4}, \frac{3}{4})$	$\mu_{x_{\mathrm{L}}} = 0.994$	$\sigma_{x_{\mathrm{L}}} = 0.863$	$\alpha_{x_{\mathrm{L}},3} = 3.263$	$\alpha_{x_{\mathrm{L}},4} = 26.54$

cases, and particular cases chosen to have approximately the same mean values and comparable standard deviations: $\mathrm{N}(1,1)$, $\mathrm{U}(-0.7, 2.7)$, and $\mathrm{L}(\frac{3}{4}, \frac{3}{4})$.

With their skews $\alpha_{x_{\mathrm{G}},3} = \alpha_{x_{\mathrm{U}},3} = 0$, Gaussian and uniform distributions are symmetric. In contrast, lognormal distributions are asymmetric. Uniform distributions are bounded by their parameters $b > a$ so that they do not extend towards extreme values and have a comparably small kurtosis $\alpha_{x_{\mathrm{U}},4} = 1.8$. Compared with Gaussian distributions, lognormal distributions with their positive skews $\alpha_{x_{\mathrm{L}},3} > 0$ and their kurtoses $\alpha_{x_{\mathrm{L}},4} > 3 = \alpha_{x_{\mathrm{G}},4}$ have pronounced upper tails, that is they extend further towards large values than Gaussian distributions.

The particular cases $\mathrm{N}(1,1)$, $\mathrm{U}(-0.7, 2.7)$, and $\mathrm{L}(\frac{3}{4}, \frac{3}{4})$ are depicted in Fig. 2.1 to introduce visualization methods for probability distributions: the PDF plot, the CDF plot, and the *quantile-quantile* (Q-Q). PDF plots and CDF plots are obvious, but *quantile-quantile* (Q-Q) plots require data transformations. They depict quantile functions $\phi^{-1}(p)$ with the abscissa being transformed according to a reference distribution. This thesis follows the usual convention for Q-Q plots to scale the abscissa by the standard Gaussian distribution $\mathrm{N}(0,1)$ with its quantile function $\Phi^{-1}(p)$ [Eve06]. Consequently, Q-Q plots of Gaussian distributions are straight lines while Q-Q plots of non-Gaussian distributions are not straight lines. In this thesis, the axes of Q-Q plots are set such that the graphs for Gaussian distributions correspond with the straight line that bisects the plot axes.

All plots in Fig. 2.1 highlight distribution symmetry and indicate the properties of distribution tails. However, the distribution tails can be best visualized in Q-Q plots. For example, the graph of the $\mathrm{L}(\frac{3}{4}, \frac{3}{4})$ distribution lies above the graph of the $\mathrm{N}(1,1)$ distribution in the first quadrant of the Q-Q plot in Fig. 2.1(c), which demonstrates its pronounced upper distribution tail. The $\mathrm{L}(\frac{3}{4}, \frac{3}{4})$ distribution extends further towards larger values than the $\mathrm{N}(1,1)$ distribution although its standard deviation is smaller. In contrast, the graph of the $\mathrm{U}(-0.7, 2.7)$ distribution lies below the line that bisects the plot axes in the first quadrant, which indicates that it does not have a pronounced upper distribution tail. This principle can be inverted for lower distribution tails. Since, in the third quadrant, the graphs of the $\mathrm{U}(-0.7, 2.7)$ distribution and the $\mathrm{L}(\frac{3}{4}, \frac{3}{4})$ distribution lie above the line that bisects the plot axes, they do not have pronounced lower tails.

In summary, mean value and standard deviation, which are similar for the $\mathrm{N}(1,1)$, $\mathrm{U}(-0.7, 2.7)$, and $\mathrm{L}(\frac{3}{4}, \frac{3}{4})$ distributions depicted in Fig. 2.1, are not necessarily sufficient to describe a univariate RV. Instead, higher-order characteristics, such as the shape parameters skew and kurtosis, should be considered as well.

2.1.3 Selected Transformations and Calculations

To introduce selected transformations and calculations, let X and Y be univariate RVs with mean values μ_{X} and μ_{Y}; variances or standard deviations $\mathrm{Var}\,[X] = \sigma_{\mathrm{X}}^2$ and $\mathrm{Var}\,[Y] = \sigma_{\mathrm{Y}}^2$; skews $\alpha_{\mathrm{X},3}$ and $\alpha_{\mathrm{Y},3}$; as well as kurtoses $\alpha_{\mathrm{X},4}$ and $\alpha_{\mathrm{Y},4}$.

First, linear transformations

$$X \;\rightarrow\; aX + b \tag{2.12}$$

with arbitrary real coefficients a and b can be used to scale an arbitrary RV X. They do not effect the distribution shape, that is skew and kurtosis remain constant: $\alpha_{\mathrm{aX+b},3} = \alpha_{\mathrm{X},3}$ and $\alpha_{\mathrm{aX+b},4} = \alpha_{\mathrm{X},4}$. However, mean value as well as standard deviation or variance are transformed according to

$$\mu_{\mathrm{aX+b}} = a \cdot \mu_{\mathrm{X}} + b \qquad \text{and} \tag{2.13}$$

$$\sigma_{\mathrm{aX+b}} = a \cdot \sigma_{\mathrm{X}} \quad \Longleftrightarrow \quad \mathrm{Var}\,[aX + b] = a^2 \cdot \mathrm{Var}\,[X]\,. \tag{2.14}$$

A particular linear transformation is the standardization of a Gaussian RV $X_{\mathrm{G}} \sim \mathrm{N}(\mu, \sigma^2)$, its conversion into a standard Gaussian RV $G \sim \mathrm{N}(0,1)$ [Eve06, HEK09]:

$$X_{\mathrm{G}} \;\longrightarrow\; G = \frac{X_{\mathrm{G}} - \mu}{\sigma}. \tag{2.15}$$

Second, sums of RVs are often required in variation-aware IC analysis. It is important to note that the sum of Gaussian RVs is Gaussian as well. To calculate the mean value, the variance, and the standard deviation of a sum of RVs, the characteristic values of the summands have to be taken into account [HEK09]:

$$\mu_{\mathrm{X+Y}} = \mu_{\mathrm{X}} + \mu_{\mathrm{Y}} \tag{2.16}$$

$$\begin{aligned} \mathrm{Var}\left[X+Y\right] = \sigma^2_{\mathrm{X+Y}} &= \mathrm{Var}\left[X\right] + \mathrm{Var}\left[Y\right] + 2 \cdot \mathrm{Cov}[X,Y] \\ &= \sigma^2_{\mathrm{X}} + \sigma^2_{\mathrm{Y}} + 2 \cdot \rho^{(\mathrm{pe})}_{\mathrm{X,Y}} \cdot \sigma_{\mathrm{X}} \cdot \sigma_{\mathrm{Y}}. \end{aligned} \tag{2.17}$$

In (2.17),

$$\mathrm{Cov}[X,Y] = \mathrm{E}\left[\left(X - \mu_{\mathrm{X}}\right)\left(Y - \mu_{\mathrm{Y}}\right)\right] \qquad \text{and} \tag{2.18}$$

$$\rho^{(\mathrm{pe})}_{\mathrm{X,Y}} = \frac{\mathrm{Cov}[X,Y]}{\sigma_{\mathrm{X}} \cdot \sigma_{\mathrm{Y}}} \qquad \text{with} \qquad -1 \leq \rho^{(\mathrm{pe})}_{\mathrm{X,Y}} \leq 1 \tag{2.19}$$

are the *covariance* and *Pearson's product moment correlation coefficient*, respectively, which measure the inter-dependency of the RVs X and Y [Eve06, HS12, HEK09]. The values $\mathrm{Cov}[X,Y] = \rho^{(\mathrm{pe})}_{\mathrm{X,Y}} = 0$ indicate uncorrelated components. In particular, if X and Y are Gaussian RVs, Pearson's product moment correlation coefficient measures the linearity of their dependence [Eve06]: $\rho^{(\mathrm{pe})}_{\mathrm{X,Y}} = \pm 1$ mean perfect positive and negative linear dependencies; $\rho^{(\mathrm{pe})}_{\mathrm{X,Y}} = 0$ means no linear dependency. In case the RVs X and Y are Gaussian and their Pearson's product moment correlation coefficient is $\rho^{(\mathrm{pe})}_{\mathrm{X,Y}} = 0$, the RVs X and Y are independent. For the three cases above, the variances or standard deviations of sums of RVs can be derived from (2.17):

$$\rho^{(\mathrm{pe})}_{\mathrm{X,Y}} = -1 : \mathrm{Var}\left[X+Y\right] = \left(\sigma_{\mathrm{X}} - \sigma_{\mathrm{Y}}\right)^2, \qquad \sigma_{\mathrm{X+Y}} = \left|\sigma_{\mathrm{X}} - \sigma_{\mathrm{Y}}\right|; \tag{2.20}$$

$$\rho^{(\mathrm{pe})}_{\mathrm{X,Y}} = 0 : \quad \mathrm{Var}\left[X+Y\right] = \mathrm{Var}\left[X\right] + \mathrm{Var}\left[Y\right], \quad \sigma^2_{\mathrm{X+Y}} = \sigma^2_{\mathrm{X}} + \sigma^2_{\mathrm{Y}}; \text{ and} \tag{2.21}$$

$$\rho^{(\mathrm{pe})}_{\mathrm{X,Y}} = 1 : \quad \mathrm{Var}\left[X+Y\right] = \left(\sigma_{\mathrm{X}} + \sigma_{\mathrm{Y}}\right)^2, \qquad \sigma_{\mathrm{X+Y}} = \sigma_{\mathrm{X}} + \sigma_{\mathrm{Y}}. \tag{2.22}$$

These relations are illustrated in Fig. 2.2. If the RVs X and Y have equal variances and are completely negatively correlated, their sum $(X+Y)$ is a degenerate RV with variance 0, that is a constant [Gut13]. Assuming a completely positive correlation $\rho_{X,Y}^{(pe)}=1$ between the RVs X and Y provides an upper limit for the variance of the sum $(X+Y)$, assuming a completely negative correlation $\rho_{X,Y}^{(pe)}=-1$ provides a lower limit. The variance of the sum of uncorrelated RVs is smaller than in case of positive correlations, the variations partially cancel out.

Third, in variation-aware digital circuit analysis, statistical maximum and minimum operations are frequently performed assuming Gaussian operands $X \sim \mathrm{N}(\mu_X, \sigma_X^2)$ and $Y \sim \mathrm{N}(\mu_Y, \sigma_Y^2)$ [VRK+04, VRK+06]. Artificial examples for the maximum operation for two Gaussian RVs X and Y with different distribution parameters and Pearson's product-moment correlation coefficients $\rho_{X,Y}^{(pe)}$ are depicted in the Q-Q plots in Fig. 2.3 based on sample data. In general, as in Fig. 2.3(a) and (b), non-Gaussian maximum distributions have to be expected, but identical (Fig. 2.3(c)) or significantly distant operands (Fig. 2.3(d)) yield Gaussian maximum distributions. According to [Cla61],

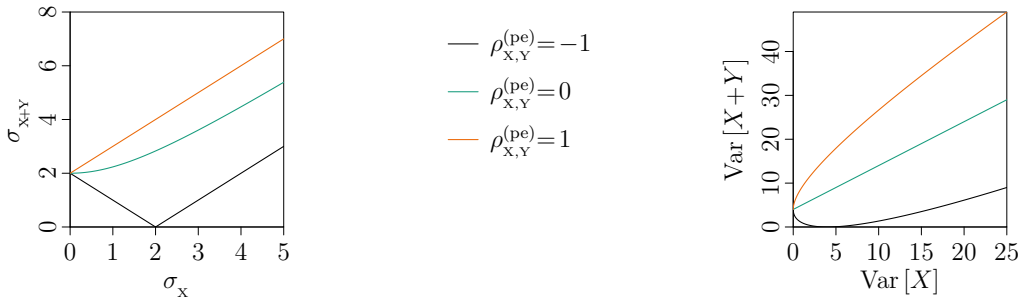

Fig. 2.2: Standard deviations and variances of sums of RVs, $(X+Y)$, with $\mathrm{Var}[Y]=\sigma_Y^2=4$ and different product-moment correlation coefficients $\rho_{X,Y}^{(pe)}$

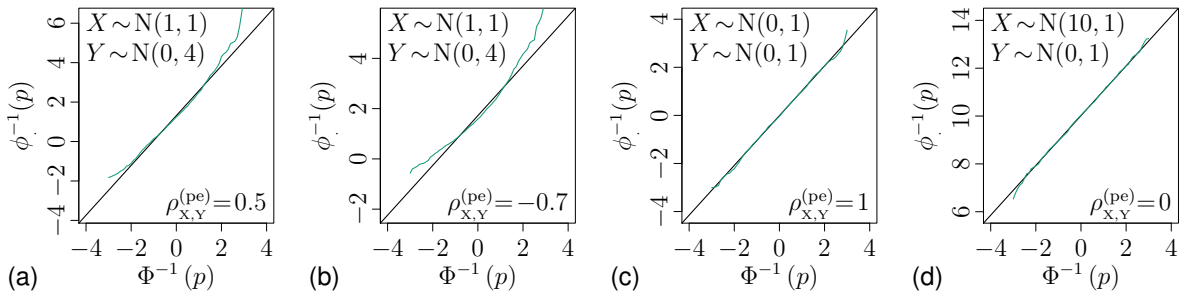

Fig. 2.3: Q-Q plots of maxima of two Gaussian RVs X and Y with different mean values, standard deviations, and product-moment correlation coefficients $\rho_{X,Y}^{(pe)}$; sample size $N=1000$

the first four distribution moments of the maximum $\max[X, Y]$ can be calculated. Additionally, it is claimed that the maximum $\max[X, Y]$ can often be considered Gaussian without introducing large errors.

2.1.4 Statistical Inference and Selected Statistical Tests

Many analysis methods, for example measurements or simulations, can generate sample data $\widetilde{X}$, that is sets of observations $x^{(\mathrm{k})}$. Concluding on the underlying RV X based on the sample $\widetilde{X}$ is referred to as *statistical inference* [Eve06].

An example set of sample data $\widetilde{X}$ is given in Tab. 2.2. The observations $x^{(\mathrm{k})}$ are also referred to as raw or empirical data, and their overall number is called sample size N [Eve06]. From these observations, the ranks $\mathrm{rk}\left(x^{(\mathrm{k})}\right)$, that is the positions of the observations in the ordered sample [HEK09], and the order statistics, that is the ordered observations with $x^{<1>} \leq x^{<2>} \leq \ldots \leq x^{<\mathrm{N}>}$ [Eve06, HEK09], can be derived.

Different methods to visualize sample data are depicted in Fig. 2.4: the histogram, the empirical CDF, and the empirical Q-Q plot [HEK09]. The histogram, which graphically approximates the PDF, is created by counting the observations in predefined intervals. The empirical CDF $\widetilde{\phi}_{\mathrm{x}}(.)$ is derived from the order statistics $x^{<\mathrm{k}>}$ [Dwa70, HEK09]:

$$\widetilde{\phi}_{\mathrm{x}}(x) = \begin{cases} 0 & : x < x^{<1>} \\ 1/N & : x^{<1>} \leq x < x^{<2>} \\ \ldots & \\ (N-1)/N & : x^{<\mathrm{N}-1>} \leq x < x^{<\mathrm{N}>} \\ 1 & : x^{<\mathrm{N}>} \leq x \end{cases} . \tag{2.23}$$

Tab. 2.2: Example sample data: observations $x^{(\mathrm{k})}$, ranks $\mathrm{rk}\left(x^{(\mathrm{k})}\right)$, order statistics $x^{<\mathrm{k}>}$; $N = 15$

k	1	2	3	4	5	6	7	8	9	10	11	12	13	14	15
$x^{(\mathrm{k})}$	0.29	0.57	0.19	0.34	1.85	1.85	0.46	1.17	0.03	0.14	0.15	0.16	0.81	0.30	0.00
$\mathrm{rk}\left(x^{(\mathrm{k})}\right)$	7	11	6	9	15	14	10	13	2	3	4	5	12	8	1
$x^{<\mathrm{k}>}$	0.00	0.03	0.14	0.15	0.16	0.19	0.29	0.30	0.34	0.46	0.57	0.81	1.17	1.85	1.85

In analogy to the theoretical quantile function in (2.2), the empirical quantile function is defined as

$$\widetilde{\phi}_{\mathrm{X}}^{-1}(p) = \inf\left\{x : \widetilde{\phi}_{\mathrm{X}}(x) \geq p\right\} \qquad \text{with} \qquad 0 \leq p \leq 1, \tag{2.24}$$

and methods for its practical evaluation are discussed in [HF96], for instance.

In an empirical Q-Q plot, the order statistics $x^{<\mathrm{k}>}$ are depicted over the corresponding expected quantiles from a reference distribution [HEK09], the standard Gaussian distribution in this thesis.

Sample data $\widetilde{X}$ of the size N allow to compute the sample mean $\widetilde{\mu}_{\mathrm{X}}$, the sample standard deviation $\widetilde{\sigma}_{\mathrm{X}}$, the empirical skew $\widetilde{\alpha}_{\mathrm{X},3}$, and the empirical kurtosis $\widetilde{\alpha}_{\mathrm{X},4}$ [HEK09]:

$$\widetilde{\mu}_{\mathrm{X}} = \frac{1}{N}\sum_{k=1}^{N} x^{(\mathrm{k})}, \tag{2.25}$$

$$\widetilde{\sigma}_{\mathrm{X}}^2 = \frac{1}{N-1}\sum_{k=1}^{N}\left(x^{(\mathrm{k})} - \widetilde{\mu}_{\mathrm{X}}\right)^2 = \frac{1}{N-1}\left[\sum_{k=1}^{N}\left(x^{(\mathrm{k})}\right)^2 - N\cdot\widetilde{\mu}_{\mathrm{X}}^2\right], \tag{2.26}$$

$$\widetilde{\alpha}_{\mathrm{X},3} = \frac{\frac{1}{N}\sum_{k=1}^{N}\left(x^{(\mathrm{k})} - \widetilde{\mu}_{\mathrm{X}}\right)^3}{\sqrt{\left[\frac{1}{N}\sum_{k=1}^{N}\left(x^{(\mathrm{k})} - \widetilde{\mu}_{\mathrm{X}}\right)^2\right]^3}}, \text{ and} \tag{2.27}$$

$$\widetilde{\alpha}_{\mathrm{X},4} = \frac{\frac{1}{N}\sum_{k=1}^{N}\left(x^{(\mathrm{k})} - \widetilde{\mu}_{\mathrm{X}}\right)^4}{\left[\frac{1}{N}\sum_{k=1}^{N}\left(x^{(\mathrm{k})} - \widetilde{\mu}_{\mathrm{X}}\right)^2\right]^2}. \tag{2.28}$$

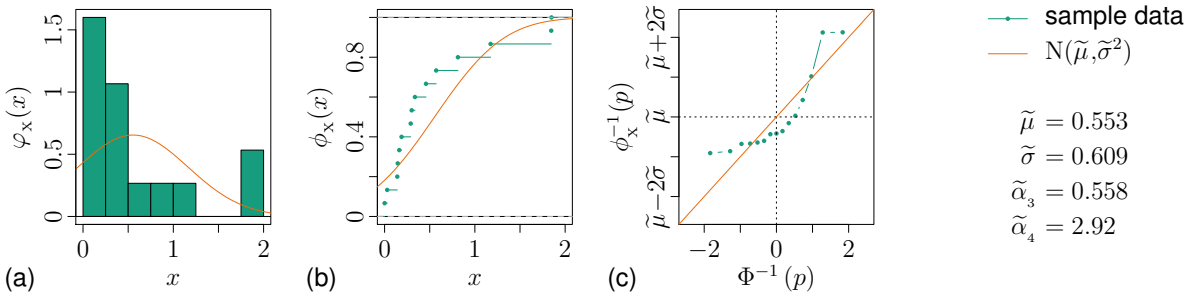

Fig. 2.4: Visualization of sample data from the example in Tab. 2.2 with Gaussian approximation as a reference and empirical characteristic values; (a) histogram, (b) empirical CDF, (c) empirical Q-Q plot

For the sample data in Tab. 2.2, these quantities are added to Fig. 2.4.

Since the sample data $\widetilde{X}$ solely represents a subset of the underlying distribution, (2.25)–(2.28) can only estimate the true distribution characteristics. Furthermore, (2.25)–(2.28) result in single values, which are therefore referred to as *point estimators*. To increase their significance, *confidence intervals* can be derived. They are also referred to as interval estimators and contain the true parameter value with a given probability or confidence level $(1-\alpha_c)$ [Eve06, HEK09]. For instance, for a Gaussian RV X with unknown mean value μ_{x} but known standard deviation σ_{x}, the confidence interval for the mean value can be determined from a sample of the size N as [HEK09]

$$\left[\widetilde{\mu}_{\mathrm{x}} - \frac{\sigma_{\mathrm{x}}}{\sqrt{N}} \cdot \Phi^{-1}\left(1-\alpha_c/2\right) \;,\; \widetilde{\mu}_{\mathrm{x}} + \frac{\sigma_{\mathrm{x}}}{\sqrt{N}} \cdot \Phi^{-1}\left(1-\alpha_c/2\right)\right] \tag{2.29}$$

with the quantile function of the standard Gaussian distribution $\Phi^{-1}\left(.\right)$. The width of this interval,

$$2 \cdot \frac{\sigma_{\mathrm{x}}}{\sqrt{N}} \cdot \Phi^{-1}\left(1-\alpha_c/2\right) \propto \frac{1}{\sqrt{N}}$$

is inversely proportional to the square root of the sample size N. That is, in terms of confidence interval widths, the accuracy of a mean value estimation grows with the square root of the sample size N [LLP06]. This statement can be qualitatively generalized: a rising sample size N increases the significance of statistical inference.

Furthermore, sample data $\widetilde{X}$ can be mapped to predefined probability distributions. One opportunity is to use the method of moments: equating theoretical distribution moments and derived quantities in (2.5)–(2.8) and their empirical counterparts in (2.25)–(2.28) to determine the distribution parameters [Eve06, HEK09]. For example, the sample data $\widetilde{X}$ in Fig. 2.4 can be mapped to a Gaussian distribution $X \sim \mathrm{N}(\mu, \sigma^2)$ with $\mu = 0.553$ and $\sigma = 0.609$, which is added to the graphs in Fig. 2.4 as a reference.

Statistical tests examine sample data for confirming particular assumptions, the so-called null hypotheses [Eve06]. An important test parameter is the confidence level $(1-\alpha_c)$ with α_c, typically 0.05 or 0.1, being the probability that a null hypothesis is rejected although it is true [HEK09]. From numerous statistical tests, *Kolmogorov-Smirnov* (KS) tests and *Shapiro-Wilk* (SW) tests, which are widely available in software, are applied in this thesis

The KS two-sample test compares two samples $\tilde{X}$ and $\tilde{Y}$ [Eve06]. The null-hypothesis, "*the samples $\tilde{X}$ and $\tilde{Y}$ represent the same underlying distribution*" is tested with the maximum absolute difference between the empirical CDFs $\widetilde{\phi}_{\mathrm{X}}(.)$ and $\widetilde{\phi}_{\mathrm{Y}}(.)$ [HEK09]

$$D = \max\left\{\left|\widetilde{\phi}_{\mathrm{X}}(x) - \widetilde{\phi}_{\mathrm{Y}}(x)\right|\right\}, \tag{2.30}$$

while paying attention to the step-wise definition of empirical CDFs in (2.23). If the value of D exceeds a particular threshold D_t, the null-hypothesis is rejected and, hence, the samples $\tilde{X}$ and $\tilde{Y}$ should be assumed to represent different distributions. Otherwise, the null-hypothesis is accepted and the samples $\tilde{X}$ and $\tilde{Y}$ can be considered representing the same distribution [HEK09]. The threshold D_t depends on the confidence level $(1-\alpha_c)$ as well as on the sizes of the samples $\tilde{X}$ and $\tilde{Y}$, and it can be extracted from tables for the particular scenario.

The SW test examines a sample $\tilde{X}$ of the size N with the null-hypothesis "*the sample $\tilde{X}$ represents a Gaussian distribution*". The test statistic [SW65]

$$W = \frac{\left(\sum\limits_{k=1}^{N} a_k \cdot x^{<\mathrm{k}>}\right)^2}{\sum\limits_{k=1}^{N}\left(x^{(\mathrm{k})} - \widetilde{\mu}\right)^2} = \frac{\left(\sum\limits_{k=1}^{N/2} a_{N-k+1} \cdot \left(x^{<\mathrm{N-k+1}>} - x^{<\mathrm{k}>}\right)\right)^2}{\sum\limits_{k=1}^{N}\left(x^{(\mathrm{k})} - \widetilde{\mu}\right)^2} \tag{2.31}$$

is computed with tabulated coefficients a_k, which depend on the sample size N. If the test statistic W exceeds a particular threshold W_t, the null-hypothesis is accepted and the distribution represented by the sample $\tilde{X}$ can be considered Gaussian. Otherwise, the null-hypothesis is rejected and the distribution represented by the sample $\tilde{X}$ should be considered non-Gaussian. Similar to the KS test, the threshold W_t depends on the confidence level $(1-\alpha_c)$ and on the sample size N, and it can be extracted from tables for the particular scenario.[1]

[1] Although the SW test was extended to cover other theoretical distributions as well [Eve06], is is solely applied to test sample data for Gaussianity in this thesis.

2.2 Multivariate Random Variables

2.2.1 Definitions

When n univariate RVs $X_1, X_2, ..., X_n$ have to be considered simultaneously, they can be summarized into a *multivariate RV* or *random vector* [HS12]

$$\boldsymbol{X} = (X_1, X_2, \ldots, X_n)\,. \tag{2.32}$$

The univariate RVs $X_1, X_2, ..., X_n$ are referred to as *random components* in this context [HS12]. A multivariate RV can be described by its joint PDF $\varphi_{\mathbf{x}}(\mathbf{x}) = \varphi_{\mathbf{x}}(x_1, x_2, \ldots, x_n)$ or its joint CDF [Eve06, HE07]

$$\phi_{\mathbf{x}}(\mathbf{x}) = \phi_{\mathbf{x}}(x_1, x_2, \ldots, x_n) = \int_{x_1=-\infty}^{x_1} \int_{x_2=-\infty}^{x_2} \cdots \int_{x_n=-\infty}^{x_n} \varphi_{\mathbf{x}}(\mathbf{x})\ \mathrm{dx_1}\ \mathrm{dx_2}\ \cdots\ \mathrm{dx_n} \tag{2.33}$$

while a joint quantile function does not exist.

The distribution of a random component X_i is referred to as *marginal distribution* and can be handled as a univariate RV according to the principles in Sec. 2.1. The CDF of a marginal distribution can be obtained from the integration [Eve06, HE07]

$$\phi_{\mathrm{X_i}}(x) = \int_{x_1=-\infty}^{\infty} \cdots \int_{x_i=-\infty}^{x} \cdots \int_{x_n=-\infty}^{\infty} \varphi_{\mathbf{x}}(\mathbf{x})\ \mathrm{dx_1}\ \mathrm{dx_2}\ \cdots\ \mathrm{dx_n}. \tag{2.34}$$

To characterize a multivariate RV $\boldsymbol{X}$, the inter-dependencies of its random components are required in addition to the marginal distributions. For two random components X_i and X_j, the covariance $\mathrm{Cov}[X_i, X_j]$ and Pearson's product-moment correlation coefficient $\rho^{(\mathrm{pe})}_{\mathrm{X_i,X_j}}$ were introduced as measures of inter-dependency in (2.18) and (2.19) in Sec. 2.1.3. For an n-dimensional multivariate random RV $\boldsymbol{X}$, (2.18) can be generalized to yield the covariance matrix [HS12]

$$\mathrm{Cov}[\boldsymbol{X}] = \boldsymbol{\Sigma}_{\mathbf{x}} = \mathrm{E}\left[(\boldsymbol{X} - \boldsymbol{\mu}_{\mathbf{x}})\,(\boldsymbol{X} - \boldsymbol{\mu}_{\mathbf{x}})^{\mathrm{T}}\right] = \boldsymbol{\Sigma}_{\mathbf{x}}^{\mathrm{T}}, \tag{2.35}$$

with $\boldsymbol{\Sigma}_{\mathbf{x}}^{\mathrm{T}}$ being the transposed of the matrix $\boldsymbol{\Sigma}_{\mathbf{x}}$. In (2.35), $\boldsymbol{\mu}_{\mathbf{x}} = (\mu_{\mathrm{X_1}}, \mu_{\mathrm{X_2}}, ..., \mu_{\mathrm{X_n}})$ is the mean vector consisting of the mean values of the random components X_i.

The $(n \times n)$ covariance matrix $\mathbf{\Sigma_x}$ is symmetric and positive semi-definite[2]. Its main diagonal elements are the variances of the random components, $\mathbf{\Sigma_{x},}_{ii} = \mathrm{Var}\,[X_i]$; its off-diagonal elements are the corresponding covariances, $\mathbf{\Sigma_{x},}_{ij} = \mathrm{Cov}[X_i, X_j] \;\forall\, i \neq j$ [Eve06, HS12, HEK09].

Scaling covariances by the standard deviations of the respective random components yields Pearson's product moment correlation coefficients $\rho^{(\mathrm{pe})}_{\mathrm{X_i},\mathrm{X_j}}$. Generalizing this fact leads to the $(n \times n)$ *Pearson's product moment correlation matrix* [Eve06, HS12]

$$\mathbf{C_x} = \boldsymbol{\sigma}_{\mathbf{x}}^{-1}\, \mathbf{\Sigma_x}\, \boldsymbol{\sigma}_{\mathbf{x}}^{-1}. \tag{2.36}$$

In (2.36), $\boldsymbol{\sigma}_{\mathbf{x}}$ is the diagonal matrix of the component standard deviations $\sigma_{\mathrm{X_i}}$,

$$\boldsymbol{\sigma}_{\mathbf{x}} = \begin{pmatrix} \sigma_{\mathrm{X_1}} & 0 & \cdots & 0 \\ 0 & \sigma_{\mathrm{X_2}} & \cdots & 0 \\ \vdots & \vdots & \ddots & \vdots \\ 0 & 0 & \cdots & \sigma_{\mathrm{X_n}} \end{pmatrix} \quad \text{such that} \quad \boldsymbol{\sigma}_{\mathbf{x}}^{-1} = \begin{pmatrix} \sigma^{-1}_{\mathrm{X_1}} & 0 & \cdots & 0 \\ 0 & \sigma^{-1}_{\mathrm{X_2}} & \cdots & 0 \\ \vdots & \vdots & \ddots & \vdots \\ 0 & 0 & \cdots & \sigma^{-1}_{\mathrm{X_n}} \end{pmatrix}. \tag{2.37}$$

Pearson's product moment correlation matrix $\mathbf{C_x}$ is symmetric and positive semi-definite. Its main diagonal elements are $\mathbf{C_{x},}_{ii} = 1$; its off-diagonal elements are Pearson's product moment correlation coefficients $\mathbf{C_{x},}_{ij} = \mathbf{C_{x},}_{ji} = \rho^{(\mathrm{pe})}_{\mathrm{X_i},\mathrm{X_j}}$ [Eve06, HS12].

2.2.2 Multivariate Gaussian Distribution and Visualization

An important multivariate distribution is the multivariate Gaussian distribution $\boldsymbol{X}_{\mathbf{G}} \sim \mathbf{N}(\boldsymbol{\mu}_{\mathbf{x_G}}, \mathbf{\Sigma_{x_G}})$ with its mean vector $\boldsymbol{\mu}_{\mathbf{x_G}}$ and its covariance matrix $\mathbf{\Sigma_{x_G}}$. Its joint PDF is defined as [HS12, HE07]

$$\varphi_{\boldsymbol{x}_{\mathbf{G}}}(\mathbf{x}) = \frac{1}{\sqrt{(2\pi)^n \cdot \left|\mathbf{\Sigma_{x_G}}\right|}} \cdot \exp\left[-\frac{1}{2}\left(\mathbf{x} - \boldsymbol{\mu}_{\mathbf{x_G}}\right)^{\mathrm{T}}\, \mathbf{\Sigma}^{-1}_{\mathbf{x_G}}\, \left(\mathbf{x} - \boldsymbol{\mu}_{\mathbf{x_G}}\right)\right], \tag{2.38}$$

whereas $\mathbf{\Sigma}^{-1}_{\mathbf{x_G}}$ and $\left|\mathbf{\Sigma_{x_G}}\right|$ are the inverse and the determinant of the covariance matrix $\mathbf{\Sigma_{x_G}}$. Special cases include the multivariate Gaussian RV $\boldsymbol{X}_{\mathbf{Gu}} \sim \mathbf{N}(\boldsymbol{\mu}_{\mathbf{x_{Gu}}}, \mathbf{\Sigma_{x_{Gu}}})$ with uncorrelated Gaussian components $X_{Gu_i} \sim \mathrm{N}(\mu_{\mathrm{X_{Gu_i}}}, \sigma^2_{\mathrm{X_{Gu_i}}})$; the multivariate Gaus-

[2] Many calculations require the covariance matrix to be positive definite. If required, the algorithm in [Hig02] can be applied to approximate a covariance matrix $\mathbf{\Sigma_x}$ by its nearest positive definite matrix.

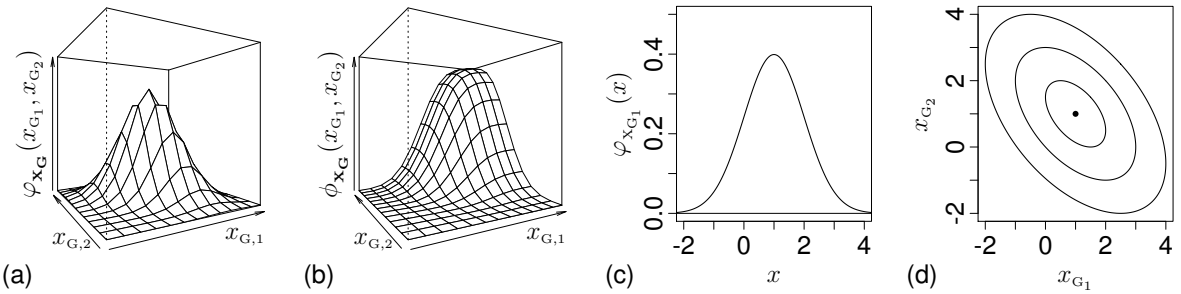

Fig. 2.5: Example of a multivariate Gaussian RV $\boldsymbol{X}_{\mathbf{G}} = (X_{G_1}, X_{G_2})^{\mathrm{T}} \sim \mathbf{N}(\boldsymbol{\mu}_{\mathbf{X_G}}, \boldsymbol{\Sigma}_{\mathbf{X_G}})$ with $\boldsymbol{\mu}_{\mathbf{X_G}} = (1, 1)$ and $\boldsymbol{\Sigma}_{\mathbf{X_G}} = \begin{pmatrix} 1 & -0.5 \\ -0.5 & 1 \end{pmatrix}$; (a) joint PDF; (b) joint CDF; (c) marginal distribution of X_{G_1} (PDF); (d) 1σ-, 2σ-, and 3σ-covariance ellipses

sian RV $\boldsymbol{G} \sim \mathbf{N}(\mathbf{0}, \boldsymbol{\Sigma}_{\mathbf{G}})$ with arbitrarily correlated standard Gaussian components $G_i \sim \mathrm{N}(0, 1)$; and the multivariate standard Gaussian RV $\boldsymbol{G}_{\mathbf{std}} \sim \mathbf{N}(\mathbf{0}, \mathbf{I})$, where $\mathbf{I}$ is the identity matrix, with uncorrelated standard Gaussian components $G_{\mathrm{std}_i} \sim \mathrm{N}(0, 1)$.

As an example, Fig. 2.5 depicts different visualization methods for a two-dimensional Gaussian RV $\boldsymbol{X}_{\mathbf{G}}$: the joint PDF, the joint CDF, a marginal distribution, and covariance ellipses.

2.2.3 Selected Transformations and Calculations

In this thesis, linear transformations, concatenations, and summations are applied to multivariate RVs. To introduce these operations, let $\boldsymbol{X}$, $\boldsymbol{Y}$, and $\boldsymbol{Z}$ be multivariate RVs of the dimensionalities n_x, n_y, and n_z with their mean vectors $\boldsymbol{\mu}_{\mathbf{X}}$, $\boldsymbol{\mu}_{\mathbf{Y}}$, and $\boldsymbol{\mu}_{\mathbf{Z}}$ as well as their covariance matrices $\boldsymbol{\Sigma}_{\mathbf{X}}$, $\boldsymbol{\Sigma}_{\mathbf{Y}}$, and $\boldsymbol{\Sigma}_{\mathbf{Z}}$.

First, the linear transformation

$$\boldsymbol{X} \;\rightarrow\; \mathbf{A}\,\boldsymbol{X}^{\mathrm{T}} + \mathbf{b} \tag{2.39}$$

applies an $(m \times n_x)$ matrix $\mathbf{A}$ and an (m)-vector $\mathbf{b}$. This operation converts the mean vector and covariance matrix of the RV $\boldsymbol{X}$ by [HS12]

$$\boldsymbol{\mu}_{\mathbf{A}\boldsymbol{X}^{\mathbf{T}}+\mathbf{b}} = \mathbf{A}\,\boldsymbol{\mu}_{\mathbf{X}} + \mathbf{b} \qquad \text{and} \tag{2.40}$$

$$\boldsymbol{\Sigma}_{\mathbf{A}\boldsymbol{X}^{\mathrm{T}}+\mathbf{b}} = \mathbf{A}\,\boldsymbol{\Sigma}_{\mathbf{X}}\,\mathbf{A}^{\mathrm{T}}. \tag{2.41}$$

Important linear transformations apply to multivariate Gaussian RVs. The *principal component analysis* (PCA), which is described in App. A.1, transforms a RV $\boldsymbol{X}_{\mathbf{G}} \sim \mathbf{N}(\boldsymbol{\mu}_{\mathbf{X_G}}, \boldsymbol{\Sigma}_{\mathbf{X_G}})$ into a multivariate Gaussian RV $\boldsymbol{X}_{\mathbf{Gu}} \sim \mathbf{N}(\mathbf{0}, \boldsymbol{\Sigma}_{\mathbf{X_{Gu}}})$ with zero means and uncorrelated components $X_{Gu,i}$. Conversely, a multivariate standard Gaussian RV $\boldsymbol{G}_{\mathbf{std}} \sim \mathbf{N}(\mathbf{0}, \mathbf{I})$ can be converted into an arbitrary multivariate Gaussian RV $\boldsymbol{X}_{\mathbf{G}} \sim \mathbf{N}(\boldsymbol{\mu}_{\mathbf{X_G}}, \boldsymbol{\Sigma}_{\mathbf{X_G}})$ with the transformation [Tho13]

$$\boldsymbol{X}_{\mathbf{G}}^{\mathrm{T}} = \mathbf{L}_{\mathbf{X_G}}\, \boldsymbol{G}_{\mathbf{std}}^{\mathrm{T}} + \boldsymbol{\mu}_{\mathbf{X_G}} \qquad \text{with} \qquad \boldsymbol{\Sigma}_{\mathbf{X_G}} = \mathbf{L}_{\mathbf{X_G}}\, \mathbf{L}_{\mathbf{X_G}}^{\mathrm{T}}. \tag{2.42}$$

The matrix $\mathbf{L}_{\mathbf{X_G}}$ in (2.42) can, for instance, be obtained from a Cholesky decomposition of a positive definite covariance matrix $\boldsymbol{\Sigma}_{\mathbf{X_G}}$ [Tho13].

Second, similar to univariate RVs in (2.32), multidimensional RVs $\boldsymbol{X}$ and $\boldsymbol{Y}$ of the dimensionalities n_x and n_y can be concatenated to an $(n_x{+}n_y)$-dimensional RV $(\boldsymbol{X}, \boldsymbol{Y})$. Its mean vector is the concatenation of the mean vectors of the operands, $\boldsymbol{\mu}_{(\boldsymbol{X},\boldsymbol{Y})} = (\boldsymbol{\mu}_{\mathbf{X}}, \boldsymbol{\mu}_{\mathbf{Y}})$. However, to derive the covariance matrix $\boldsymbol{\Sigma}_{(\boldsymbol{X},\boldsymbol{Y})}$, the inter-dependency of the RVs $\boldsymbol{X}$ and $\boldsymbol{Y}$ has to be considered. For this purpose, a generalization of (2.18) or an extension of (2.35) defines the $(n_x \times n_y)$ covariance matrix between the RVs $\boldsymbol{X}$ and $\boldsymbol{Y}$ [HS12],

$$\mathrm{Cov}[\boldsymbol{X}, \boldsymbol{Y}] = \boldsymbol{\Sigma}_{\mathbf{X,Y}} = \mathrm{E}\left[(\boldsymbol{X} - \boldsymbol{\mu}_{\mathbf{X}})\,(\boldsymbol{Y} - \boldsymbol{\mu}_{\mathbf{Y}})^{\mathrm{T}}\right] = \boldsymbol{\Sigma}_{\mathbf{Y,X}}^{\mathrm{T}}. \tag{2.43}$$

The result $\boldsymbol{\Sigma}_{\mathbf{X,Y}} = \mathbf{0}$ identifies the multivariate RVs $\boldsymbol{X}$ and $\boldsymbol{Y}$ to be uncorrelated. The covariance matrix of the concatenation $(\boldsymbol{X}, \boldsymbol{Y})$ reads

$$\boldsymbol{\Sigma}_{(\boldsymbol{X},\boldsymbol{Y})} = \mathrm{Cov}[(\boldsymbol{X}, \boldsymbol{Y})] = \begin{pmatrix} \boldsymbol{\Sigma}_{\mathbf{X}} & \boldsymbol{\Sigma}_{\mathbf{X,Y}} \\ \boldsymbol{\Sigma}_{\mathbf{Y,X}} & \boldsymbol{\Sigma}_{\mathbf{Y}} \end{pmatrix} = \begin{pmatrix} \boldsymbol{\Sigma}_{\mathbf{X}} & \boldsymbol{\Sigma}_{\mathbf{X,Y}} \\ \boldsymbol{\Sigma}_{\mathbf{X,Y}}^{\mathrm{T}} & \boldsymbol{\Sigma}_{\mathbf{Y}} \end{pmatrix}. \tag{2.44}$$

Third, multivariate RVs $\boldsymbol{X}$ and $\boldsymbol{Y}$ of the same dimensionality $n_x = n_y$ can be added. The summation $\boldsymbol{X}+\boldsymbol{Y}$ combines the mean vectors and covariance matrices of the operands to [HS12]

$$\boldsymbol{\mu}_{\mathbf{X+Y}} = \boldsymbol{\mu}_{\mathbf{X}} + \boldsymbol{\mu}_{\mathbf{Y}} \qquad \text{and} \tag{2.45}$$

$$\begin{aligned} \boldsymbol{\Sigma}_{\mathbf{X+Y}} = \mathrm{Cov}[\boldsymbol{X} + \boldsymbol{Y}] &= \boldsymbol{\Sigma}_{\mathbf{X}} + \boldsymbol{\Sigma}_{\mathbf{X,Y}} + \boldsymbol{\Sigma}_{\mathbf{Y,X}} + \boldsymbol{\Sigma}_{\mathbf{Y}} \\ &= \boldsymbol{\Sigma}_{\mathbf{X}} + \boldsymbol{\Sigma}_{\mathbf{X,Y}} + \boldsymbol{\Sigma}_{\mathbf{X,Y}}^{\mathrm{T}} + \boldsymbol{\Sigma}_{\mathbf{Y}}. \end{aligned} \tag{2.46}$$

For uncorrelated RVs $\boldsymbol{X}$ and $\boldsymbol{Y}$, (2.46) simplifies to $\boldsymbol{\Sigma}_{\mathbf{X+Y}} = \boldsymbol{\Sigma}_{\mathbf{X}} + \boldsymbol{\Sigma}_{\mathbf{Y}}$ due to $\boldsymbol{\Sigma}_{\mathbf{X,Y}} = \mathbf{0}$.

Fourth, with three multivariate RVs $\boldsymbol{X}$, $\boldsymbol{Y}$, and $\boldsymbol{Z}$ of equal dimension $n_x = n_y = n_z$, the RV $(\boldsymbol{X}+\boldsymbol{Z}, \boldsymbol{Y}+\boldsymbol{Z})$ combines the aforementioned concatenation and summation. The mean vectors and the covariance matrices of the operands as well as the covariance matrices between the operands have to be regarded to obtain the mean vector and covariance matrix

$$\boldsymbol{\mu}_{(\mathbf{X}+\mathbf{Z},\mathbf{Y}+\mathbf{Z})} = (\boldsymbol{\mu}_{\mathbf{X}} + \boldsymbol{\mu}_{\mathbf{Z}}\ ,\ \boldsymbol{\mu}_{\mathbf{Y}} + \boldsymbol{\mu}_{\mathbf{Z}}) \qquad \text{and} \tag{2.47}$$

$$\boldsymbol{\Sigma}_{(\mathbf{X}+\mathbf{Z},\mathbf{Y}+\mathbf{Z})} = \mathrm{Cov}[(\boldsymbol{X}+\boldsymbol{Z}, \boldsymbol{Y}+\boldsymbol{Z})] = \begin{pmatrix} \boldsymbol{\Sigma}_{\mathbf{X}+\mathbf{Z}} & \boldsymbol{\Sigma}_{\mathbf{X}+\mathbf{Z},\mathbf{Y}+\mathbf{Z}} \\ \boldsymbol{\Sigma}^{\mathrm{T}}_{\mathbf{X}+\mathbf{Z},\mathbf{Y}+\mathbf{Z}} & \boldsymbol{\Sigma}_{\mathbf{Y}+\mathbf{Z}} \end{pmatrix}. \tag{2.48}$$

In (2.48), the covariance matrices $\boldsymbol{\Sigma}_{\mathbf{X}+\mathbf{Z}}$ and $\boldsymbol{\Sigma}_{\mathbf{Y}+\mathbf{Z}}$ can be determined from (2.46), and the remaining entry reads

$$\begin{aligned} \boldsymbol{\Sigma}_{\mathbf{X}+\mathbf{Z},\mathbf{Y}+\mathbf{Z}} &= \mathrm{E}\left[(\boldsymbol{X}-\boldsymbol{\mu}_{\mathbf{X}}+\boldsymbol{Z}-\boldsymbol{\mu}_{\mathbf{Z}})\,(\boldsymbol{Y}-\boldsymbol{\mu}_{\mathbf{Y}}+\boldsymbol{Z}-\boldsymbol{\mu}_{\mathbf{Z}})^{T}\right] \\ &= \boldsymbol{\Sigma}_{\mathbf{X},\mathbf{Y}} + \boldsymbol{\Sigma}_{\mathbf{X},\mathbf{Z}} + \boldsymbol{\Sigma}_{\mathbf{Z},\mathbf{Y}} + \boldsymbol{\Sigma}_{\mathbf{Z}}. \end{aligned} \tag{2.49}$$

If the RVs $\boldsymbol{X}$, $\boldsymbol{Y}$, and $\boldsymbol{Z}$ are uncorrelated, (2.49) simplifies to $\boldsymbol{\Sigma}_{\mathbf{X}+\mathbf{Z},\mathbf{Y}+\mathbf{Z}} = \boldsymbol{\Sigma}_{\mathbf{Z}}$.

2.2.4 Statistical Inference and Statistical Tests

Samples from an n-dimensional multivariate RV $\boldsymbol{X}$ have to be treated as multivariate data $\tilde{\boldsymbol{X}}$ of the sample size N. Consequently, random observations have to be considered as n-dimensional vectors $\boldsymbol{x}^{(\mathrm{k})}$ [Eve06, HE07]. The properties of the marginal distributions can be derived according to the principles in Sec. 2.1.4. Furthermore, the sample data $\tilde{\boldsymbol{X}}$ allow estimating Pearson's product moment correlation coefficients for arbitrary random components X_i and X_j as [Eve06, HE07]

$$\widetilde{\rho}^{(\mathrm{pe})}_{\mathrm{X_i},\mathrm{X_j}} = \frac{\sum\limits_{k=1}^{N}\left(x_i^{(\mathrm{k})} - \widetilde{\mu}_{\mathrm{X_i}}\right)\left(x_j^{(\mathrm{k})} - \widetilde{\mu}_{\mathrm{X_j}}\right)}{\sqrt{\sum\limits_{k=1}^{N}\left(x_i^{(\mathrm{k})} - \widetilde{\mu}_{\mathrm{X_i}}\right)^2 \sum\limits_{k=1}^{N}\left(x_j^{(\mathrm{k})} - \widetilde{\mu}_{\mathrm{X_j}}\right)^2}} \tag{2.50}$$

and, consequently, constructing the empirical product-moment correlation matrix.

Replacing the observations $x_i^{(\mathrm{k})}$ and $x_j^{(\mathrm{k})}$ in (2.50) by their ranks $\mathrm{rk}\left(x_i^{(\mathrm{k})}\right)$ and $\mathrm{rk}\left(x_j^{(\mathrm{k})}\right)$ leads to an estimator for *Spearman's rank correlation coefficient* $\rho^{(\mathrm{sp})}_{\mathrm{X_i\,X_j}}$, which is also

referred to as fractile correlation [Fac]. With $d_{ij}{}^{(\mathrm{k})} = \mathrm{rk}\left(x_i^{(\mathrm{k})}\right) - \mathrm{rk}\left(x_j^{(\mathrm{k})}\right)$ being the difference in the ranks of the k-th observations of X_i and X_j, it is computed as [Eve06, HE07]

$$\widetilde{\rho}^{(\mathrm{sp})}_{\mathrm{X_i},\mathrm{X_j}} = 1 - \frac{6 \cdot \sum_{k=1}^{N} \left[\mathrm{rk}\left(x_i^{(\mathrm{k})}\right) - \mathrm{rk}\left(x_j^{(\mathrm{k})}\right)\right]^2}{N(N^2-1)} = 1 - \frac{6 \sum_{k=1}^{N} \left(d_{ij}^{(k)}\right)^2}{N(N^2-1)}. \tag{2.51}$$

Spearman's rank correlation coefficient lies in the interval $-1 \leq \rho^{(\mathrm{sp})}_{\mathrm{X_i},\mathrm{X_j}} \leq 1$. It measures the monotonicity in the dependency of X_i and X_j: $\rho^{(\mathrm{sp})}_{\mathrm{X_i},\mathrm{X_j}} = \pm 1$ indicate strictly monotonic increasing and decreasing dependencies, and $\rho^{(\mathrm{sp})}_{\mathrm{X_i},\mathrm{X_j}} = 0$ indicates uncorrelated components [HEK09]. The coefficients $\rho^{(\mathrm{sp})}_{\mathrm{X_i},\mathrm{X_j}}$ can be summarized in the symmetric $(n \times n)$ *Spearman's rank correlation matrix* $\mathbf{R}$ with $R_{ii} = 1$ and $R_{ij} = R_{ji} = \widetilde{\rho}^{(\mathrm{sp})}_{\mathrm{X_i},\mathrm{X_j}}$.

The combination of Spearman's rank correlation matrix and the marginal distributions of all components X_i characterizes an arbitrarily complex multivariate RV $\boldsymbol{X}$ [Fac, PQH04]. This is an important general approach since analytical expressions for joint PDFs $\varphi_{\boldsymbol{X}}(.)$ or joint CDFs $\phi_{\boldsymbol{X}}(.)$ only exist for certain distribution types, such as the multivariate Gaussian distribution, or for low-dimensional RVs [Fac].

As every estimation, (2.51) is subject to statistical inaccuracies due to the limited information available in the sample data $\tilde{\boldsymbol{X}}$. However, a significance test can eliminate non-significant values: with a confidence level $(1-\alpha_c)$ and a sufficiently large[3] sample size N, an estimated Spearman's rank correlation coefficient $\widetilde{\rho}^{(\mathrm{sp})}_{\mathrm{X_i},\mathrm{X_j}}$ is considered significantly different from 0 if [Haz95, Po11]

$$\left|\widetilde{\rho}^{(\mathrm{sp})}_{\mathrm{X_i},\mathrm{X_j}}\right| > \frac{\Phi^{-1}\left(1-\alpha_c/2\right)}{\sqrt{N-1}}. \tag{2.52}$$

The boundary between significant and insignificant estimators for Spearman's rank correlation coefficient $\widetilde{\rho}^{(\mathrm{sp})}_{\mathrm{X_i},\mathrm{X_j}}$ defined by (2.52) is illustrated in Fig. 2.6 for the confidence level $(1-\alpha_c) = 0.95$.

The visualizations of a two-dimensional RV in Fig. 2.5 are not applicable to data with higher dimensionality. Instead, empirical multivariate data can be visualized in scatterplot matrices. As demonstrated in the example in Fig. 2.7, they depict the pair-wise scatter plots of the random components of a multivariate RV $\boldsymbol{X}$ in a square grid [Eve06]. In this thesis, the main diagonals of scatterplot matrices are usually filled

[3] The constraint $N > 10$ from [Po11] does not cause practical limitations for the studies in this thesis.

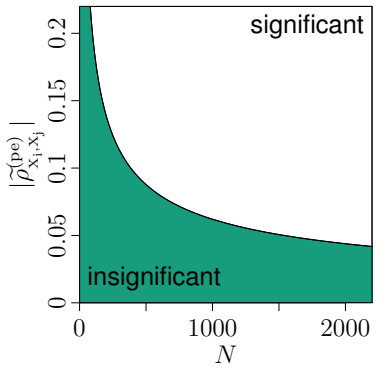

Fig. 2.6: Illustration of boundary between significant and insignificant estimators $\widetilde{\rho}^{(\mathrm{sp})}_{\mathrm{X_i},\mathrm{X_j}}$ for rank correlation coefficients depending on sample size N; confidence level $(1-\alpha_c)=0.95$

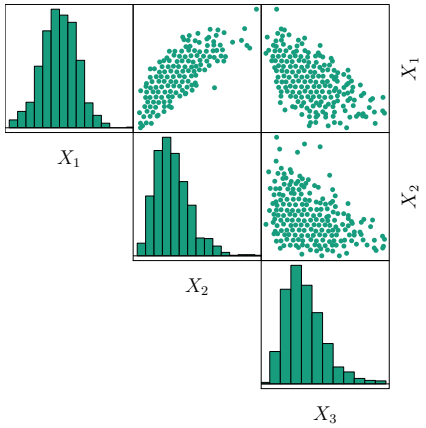

Fig. 2.7: Scatterplot matrix for multivariate data illustration with example data; off-diagonal graphs depict scatter plots of random components with plots in a column sharing the abscissas and plots in a row sharing the ordinates; lower triangular left empty since it is redundant to the upper triangular; graphs on main diagonal can depict marginal distributions of random components in the respective columns as additional information

with visualizations of the marginal distributions, such as PDF plots, CDF plots, or Q-Q plots to provide additional information.

2.3 Generation of Random Samples

Besides the description of RVs and statistical inference, the generation of random samples is an important topic in the context of this thesis. Introductory remarks and a method to draw random samples of arbitrary multivariate RVs $\boldsymbol{X}$ are presented in the following sections.

2.3.1 Introductory Remarks

The computer-based generation of pseudo-random numbers usually applies modulo operations (mod) [Leh51, Tho13]. With an initial value, the *random seed* $u^{(0)}$, a sample point $u^{(\mathrm{k})}$ with $k \geq 1$ can be generated from its predecessor $u^{(\mathrm{k}-1)}$ by [Tho13]

$$u^{(\mathrm{k})} = \frac{(a \cdot u^{(\mathrm{k}-1)} + b) \mod m}{m}, \tag{2.53}$$

yielding a sample $\tilde{U}$ from a uniform RV $U \sim \mathrm{U}(0,1)$. The parameters a, b, and m have to be adequately set to achieve a reasonable sample quality [Tho13].

The uniform sample $\tilde{U}$ can be converted to a sample $\tilde{X}$ of an arbitrary RV X with its CDF $\phi_{\mathrm{X}}(.)$ by choosing $x^{(\mathrm{k})}$ such that $\phi_{\mathrm{X}}(x^{(\mathrm{k})}) = u^{(\mathrm{k})}$ [Tho13]. This conversion is most efficient when the quantile function $\phi_{\mathrm{X}}^{-1}(.)$ is analytically available, that is when $x^{(\mathrm{k})}$ can be directly calculated as $x^{(\mathrm{k})} = \phi_{\mathrm{X}}^{-1}(u^{(\mathrm{k})})$.

For certain RVs, more appropriate methods for efficient random sampling have been developed. An important example is the generation of standard Gaussian samples $\tilde{G}$ from the RV $G \sim \mathrm{N}(0,1)$ [Tho13]. These samples can be re-ordered to sample data $\tilde{\boldsymbol{G}}_{\mathbf{std}}$ of a multivariate standard Gaussian RV $\boldsymbol{G}_{\boldsymbol{std}} = \mathbf{N}(\mathbf{0}, \mathbf{I})$. By applying (2.42) in Sec. 2.2.3, this sample is transformed into a correlated Gaussian sample $\tilde{\boldsymbol{X}}_{\mathbf{G}}$ from a multivariate Gaussian RV $\boldsymbol{X}_{\mathbf{G}} \sim \mathbf{N}(\boldsymbol{\mu}_{\mathbf{X_G}}, \boldsymbol{\Sigma}_{\mathbf{X_G}})$ with arbitrary mean vector $\boldsymbol{\mu}_{\mathbf{X_G}}$ and covariance matrix $\boldsymbol{\Sigma}_{\mathbf{X_G}}$ [Tho13]. However, this transformation requires the potentially computationally expensive decomposition of the target covariance matrix $\boldsymbol{\Sigma}_{\mathbf{X_G}} = \mathbf{L}_{\mathbf{X_G}} \mathbf{L}_{\mathbf{X_G}}^{\mathrm{T}}$.

In this thesis, standard *Monte Carlo* (MC) sampling, the random sample generation based on the underlying parameter distributions without further processing, is applied. More advanced sampling techniques are listed and briefly explained in App. A.2.

2.3.2 Generation of Multivariate Random Samples

An approach to characterize an n-dimensional RV $\boldsymbol{X}$ is to combine its marginal distributions and its Spearman's rank correlation matrix $\mathbf{R}_{\mathbf{X}}$. Given such a description, the following four-step algorithm can be applied to draw random samples $\tilde{\boldsymbol{X}}$ of the size N [Fac, PQH04]. Fig. 2.8 depicts the procedure for a two-dimensional example.

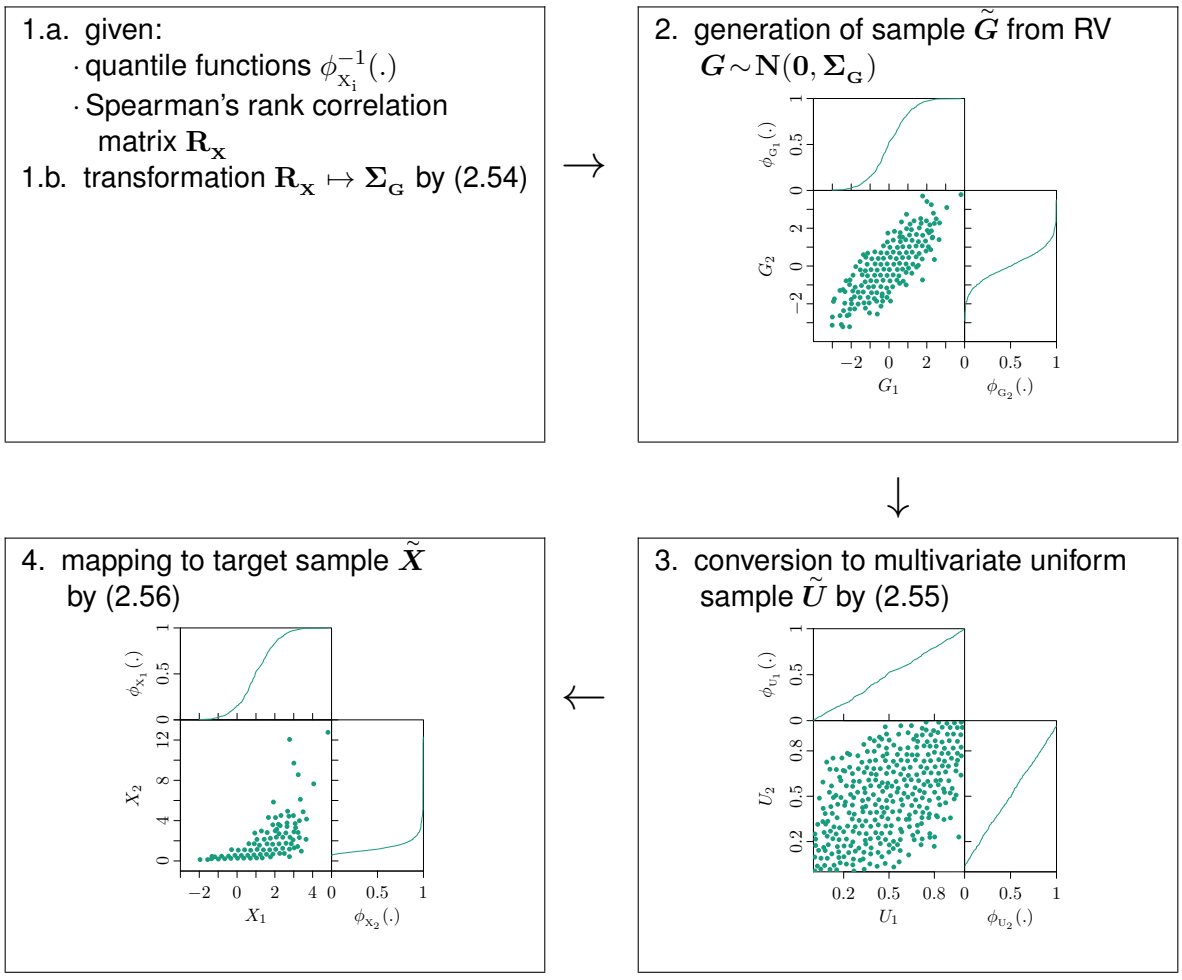

Fig. 2.8: Generation of multivariate random samples for an $n=2$-dimensional RV $\boldsymbol{X}$: $X_1 \sim \mathrm{N}(1,1)$ and $X_2 \sim \mathrm{L}(0.75, 0.75)$, $\mathbf{R_X} = \begin{pmatrix} 1 & 0.75 \\ 0.75 & 1 \end{pmatrix}$, $N = 1000$

1. *Conversion of Spearman's rank correlation matrix* $\mathbf{R_X}$ *into a matrix* $\mathbf{\Sigma_G}$ by applying the element by element calculation [Fac, PQH04]

$$\mathbf{\Sigma_{G},}_{ij} = 2 \cdot \sin\left(\frac{\pi}{6} \cdot \mathbf{R_{X},}_{ij}\right) \tag{2.54}$$

   with $-1 \leq \mathbf{\Sigma_{G},}_{ij} \leq 1$ by $-1 \leq \mathbf{R_{X},}_{ij} \leq 1$ and $\mathbf{\Sigma_{G},}_{ii} = 1$ by $\mathbf{R_{X},}_{ii} = 1$.

   For multivariate Gaussian RVs, the transformation (2.54) connects Spearman's rank correlation matrix and Pearson's product moment correlation matrix with negligible errors [Fac, HP36, PQH04].

2. *Generation of random samples* $\tilde{G}$ *of the size* N *from the multivariate Gaussian RV* $G \sim \mathbf{N}(\mathbf{0}, \mathbf{\Sigma_G})$ by applying the principles in Sec. 2.3.

Having zero means and the covariance matrix $\mathbf{\Sigma_G}$ determined from (2.54), the RV $\boldsymbol{G}$ consists of n correlated standard Gaussian components $G_i \sim \mathrm{N}(0,1)$. In this case, (2.54) connects Spearman's rank correlation coefficients and Pearson's product moment correlation coefficients. In addition, Pearson's product moment correlation matrix and the covariance matrix $\mathbf{\Sigma_G}$ coincide. Hence, the sample $\tilde{\boldsymbol{G}}$ resembles the target rank correlation matrix $\mathbf{R_X}$ apart from statistical inaccuracies.

Mind that correlated Gaussian sampling requires a potentially costly decomposition of the target covariance matrix, $\mathbf{\Sigma_G} = \mathbf{L_G}\,\mathbf{L_G}^{\mathrm{T}}$. For this decomposition, the matrix $\mathbf{\Sigma_G}$ has to be positive semi-definite [PQH04]. If necessary, the algorithm in [Hig02] can convert the matrix $\mathbf{\Sigma_G}$ into the nearest positive definite matrix for this purpose.

3. *Transformation of the correlated multivariate Gaussian sample $\tilde{\boldsymbol{G}}$ into a correlated multivariate uniform sample $\tilde{\boldsymbol{U}}$* by applying the standard Gaussian CDF $\Phi(.)$ to each realization of each random component,

$$u_i{}^{(\mathrm{k})} = \Phi\left(g_i{}^{(\mathrm{k})}\right) \quad \forall\ i \in \{1,n\},\ k \in \{1,N\}, \tag{2.55}$$

which results in samples $\tilde{U}_i$ of uniform distributions $\mathrm{U}(0,1)$.

Since the standard Gaussian CDF $\Phi(.)$ is strictly monotonically increasing, (2.55) does not alter Spearman's rank correlation coefficients. Hence, apart from statistical inaccuracies, the sample $\tilde{\boldsymbol{U}}$ resembles the target rank correlation matrix $\mathbf{R_X}$ as well.

4. *Generation of the target sample $\tilde{\boldsymbol{X}}$ from the correlated multivariate uniform sample $\tilde{\boldsymbol{U}}$ by CDF mapping,* that is by applying the corresponding quantile function to each realization of each random component $\tilde{U}_i$,

$$x_i{}^{(\mathrm{k})} = \phi_{\mathrm{X_i}}^{-1}(u_i{}^{(\mathrm{k})}) \quad \forall\ i \in \{1,n\},\ k \in \{1,N\}. \tag{2.56}$$

Clearly, the conversions (2.56) can be performed most efficiently when the quantile functions $\phi_{\mathrm{X_i}}^{-1}(.)$ are analytically available.

In analogy to Step 3., as the conversion (2.56) is strictly monotonically increasing, it does not alter Spearman's rank correlation coefficients. Consequently, the sample $\tilde{\boldsymbol{X}}$ features the target rank correlation matrix $\mathbf{R_X}$ and its components follow marginal distributions defined by the quantile functions $\phi_{\mathrm{X_i}}^{-1}(.)$. Therefore, the sample $\tilde{\boldsymbol{X}}$ of the size N represents the RV $\boldsymbol{X}$.

2.4 Principles of Variability Abstraction

The principle of variability abstraction is illustrated in Fig. 2.9: a functional block transforms an n_x-dimensional RV $\boldsymbol{X}$ into an n_z-dimensional RV $\boldsymbol{Z}$ via a function $\mathbf{h}(.)$. While the distribution of the RV $\boldsymbol{X}$ can be assumed to be known, properties of the RV $\boldsymbol{Z}$ have to be determined.

In principle, dedicated analyses, such as simulations, allow the point wise evaluation of the mapping $\mathbf{h}(.)$, but they may cause unreasonable computational costs. An interim abstraction layer can be introduced and described by an n_y-dimensional RV $\boldsymbol{Y}$ to increase the efficiency. The RV $\boldsymbol{Y}$ can be obtained from a transformation $\mathbf{f}(.)$ of the RV $\boldsymbol{X}$ and mapped to the RV $\boldsymbol{Z}$ via the function $\mathbf{g}(.)$.[4]

The mapping $\mathbf{g}(.)$ is known and, depending on the particular application scenario, may be analytically available. In contrast, the function $\mathbf{f}(.)$ is known but usually not analytically available. Nevertheless, it can be evaluated point wise at reasonable costs, for example by simulations. In particular, examining random samples $\tilde{\boldsymbol{X}}$ in a MC simulation yields sample data $\tilde{\boldsymbol{Y}}$ of the RV $\boldsymbol{Y}$.

Under these assumptions, the properties of the RV $\boldsymbol{Z}$ can be derived by two approaches. First, the mapping $\mathbf{f}(.)$ can be approximated by an arbitrary analytical approach $\tilde{\mathbf{f}}(.)$, which connects the sample data $\tilde{\boldsymbol{X}}$ and $\tilde{\boldsymbol{Y}}$. This model can be used to approximate the mapping function

$$\boldsymbol{Z} = \mathbf{h}(\boldsymbol{X}) \approx \mathbf{g}\left((\tilde{\mathbf{f}}(\boldsymbol{X})\right) \tag{2.57}$$

to analyze the impact of the RV $\boldsymbol{X}$ on the RV $\boldsymbol{Z}$ if the function $\mathbf{g}(.)$ is analytically available. Otherwise, an appropriate approximation $\tilde{\mathbf{g}}(.)$ of the mapping $\mathbf{g}(.)$ has to be used in (2.57). Second, the sample data $\tilde{\boldsymbol{Y}}$ can be used to infer on the underlying RV

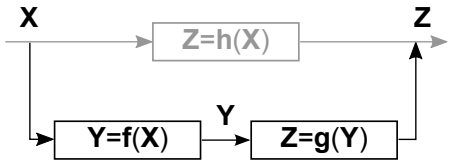

Fig. 2.9: Principle problem of parameter transformations in modeling and abstraction

[4] Usually, the RVs obtained by $\mathbf{f}(.)$ and used in $\mathbf{g}(.)$ are different but interlinked. This fact is neglected here for illustration purposes.

$\boldsymbol{Y}$, that is to approximate its distribution. Based on this description, sample data $\tilde{\boldsymbol{Y}}$ can be generated and transformed via the function $\mathrm{g}(.)$ to obtain sample data $\tilde{\boldsymbol{Z}}$ for inferring on the RV $\boldsymbol{Z}$. This approach does not require exact or approximate analytical expressions for the mappings $\mathrm{f}(.)$ and $\mathrm{g}(.)$

These abstraction principles will guide the review of the state of the art in Chap. 3. Since it appears more universal by not relying on analytical mappings $\mathrm{f}(.)$ and $\mathrm{g}(.)$, the development of a multivariate modeling approach in Chap. 4 will apply the second approach, the generation of sample data and the subsequent inference on the corresponding RVs.

2.5 Summary

Selected principles of statistics were introduced in this chapter. Univariate and multivariate RVs and their description and visualization will be basic modules in the remainder of this thesis. Furthermore, statistical inference and generation of random samples provide interfaces to empirical data. They will be of particular importance to abstract variability information and transfer them between different hierarchical levels in IC design and analysis.

3 State of the Art to Handle Variability in Integrated Circuit Design and Analysis

Already in 2007, it was reported that guard banding and yield loss needed to be traded off and statistical methods were required in circuit design to considerably benefit from new technology nodes [Kah07]. Consequently, a variety of methods and tools for variability handling on different levels of abstraction have been developed. In this chapter, they are reviewed based on the abstraction levels, models, and analysis approaches illustrated in Fig. 3.1. These levels were introduced to handle the complexity in IC design and analysis with hierarchical approaches since physical level approaches cannot be used to analyze entire ICs due to their excessive computational requirements [CFGR06, GR00, RERB13].

After the definition of terms in Sec. 3.1, the general approaches of corner models and statistical models are introduced in Sec. 3.2. Sec. 3.3 discusses how variability observed in measurements or device simulations can be transferred to variability-aware device compact models for circuit simulations. Based on them, standard cell models for gate level analyses, bit cell models for memories, and behavioral models for simulations of analog blocks can be constructed. The Secs. 3.4–3.6 introduce how variability is incorporated in these models and analyses.

For the remainder of this thesis, conclusions are drawn from the state of the art in Sec. 3.7. They reveal that variability is still an apparent challenge in IC design and guide the research documented in Chap. 4 and Chap. 5 of this thesis.

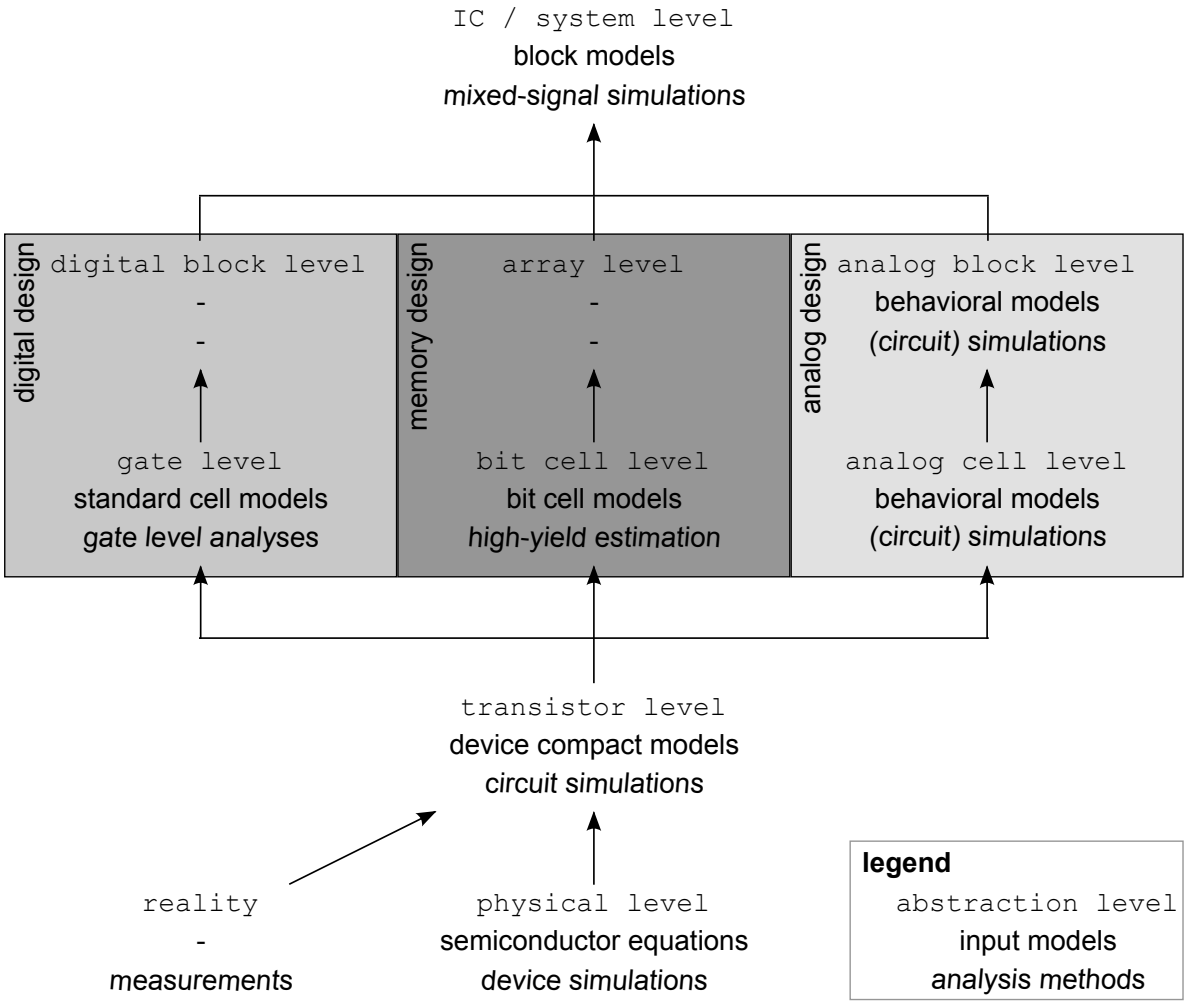

Fig. 3.1: Abstraction levels for variability including required models and analysis approaches to define terms used throughout this chapter, "-" means no dedicated model or analysis approach; level of detail increases from top to bottom; adapted and extended from [ITR11a] and Fig. 1.4

3.1 Definition of Terms

In principle, an IC is characterized by n_z performance parameters z, which form the n_z-dimensional *performance space* $\mathbb{R}_{\mathbf{Z}}$ [SS97][1]. For each performance parameter z_j, a lower and an upper specification boundary, LSB_j and USB_j, define the design target. Together, the specification boundaries create the *tolerance region* $\mathbb{R}_{\mathbf{T}} \subset \mathbb{R}_{\mathbf{Z}}$. It is the part of the performance space $\mathbb{R}_{\mathbf{Z}}$ where all performance specifications are met

[1] For example, performance parameters of a transistor may contain its threshold voltage, leakage current, and maximum drain current; performance parameters of a standard cell include its delay, static power consumption, and dynamic energies; performance parameters of a digital circuit include its operating frequency and power consumption.

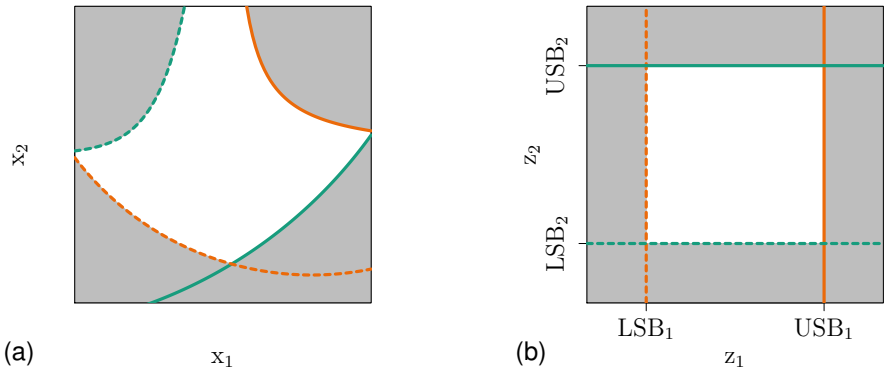

Fig. 3.2: Illustration of (a) input parameter space $\mathbb{R}_{\mathbf{X}}$ and (b) performance space $\mathbb{R}_{\mathbf{Z}}$ as well as region of acceptability and tolerance region (non-shaded) for two performance parameters z_1 and z_2; line colors and types of boundaries of region of acceptability and tolerance region correlate

[SS97]. Fig. 3.2(b) depicts a two-dimensional performance space $\mathbb{R}_{\mathbf{Z}}$ and an assumed tolerance region $\mathbb{R}_{\mathbf{T}}$ as an example.

The performance parameters $\boldsymbol{z}$ are impacted by input parameters. Mathematically, this can be described via a usually very complex mapping $\mathbf{h}(.)$, which is schematically illustrated in Fig. 3.3(a). The input parameters can be classified into *design parameters* $\boldsymbol{x}_{\mathrm{d}}$, *environmental parameters* $\boldsymbol{x}_{\mathrm{e}}$, and *process parameters* $\boldsymbol{x}$ [AGW94, MBDG13]. While designers tune the design parameters $\boldsymbol{x}_{\mathrm{d}}$ to meet the performance specifications, the operating conditions, such as temperature and supply voltage, define the environmental parameters $\boldsymbol{x}_{\mathrm{e}}$. This thesis assumes design parameters and environmental parameters parameters to be fixed. Instead, it focuses on the process parameters, which capture the impact of process variations and atomic-level fluctuations. In consequence, process parameters will be referred to as input parameters $\boldsymbol{x}$ in the remainder of this thesis. They span the n_x-dimensional *input parameter space* $\mathbb{R}_{\mathbf{X}}$ [SS97]. To

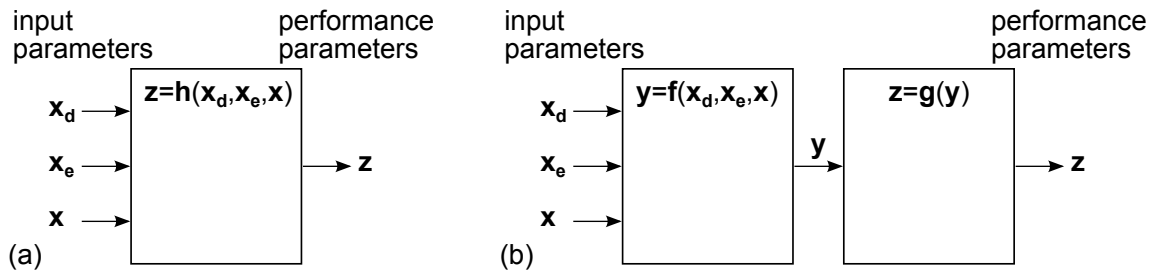

Fig. 3.3: (a) Illustration of design parameters $\boldsymbol{x}_{\mathrm{d}}$, environmental parameters $\boldsymbol{x}_{\mathrm{e}}$, as well as process parameters $\boldsymbol{x}$ and their impact on performance parameters $\boldsymbol{z}$; (b) introduction of interim hierarchical level

capture variability, input parameters are assumed to be described in terms of an n_x-dimensional RV $\boldsymbol{X}$. Consequently, the mapping $\mathbf{h}(.)$ in Fig. 3.3 transforms the RV $\boldsymbol{X}$ into an n_z-dimensional RV $\boldsymbol{Z}$, which characterizes the performance parameter variability. This fact can be taken into account by applying the principles introduced in Chap. 2. To hierarchically cope with complexity issues, one or multiple interim abstraction levels can be inserted, which was introduced in Sec. 2.4 and which is indicated in Fig. 3.3(b). An interim level is assumed to be modeled by an n_y-dimensional RV $\boldsymbol{Y}$.

Theoretically, the inverse mapping $\mathbf{h}^{-1}(.)$ projects the specification boundaries into the input parameter space $\mathbb{R}_{\mathbf{X}}$, which is illustrated for two input parameters in Fig. 3.2. In particular, it transforms the tolerance region $\mathbb{R}_{\mathbf{T}}$ into the *region of acceptability* $\mathbb{R}_{\mathbf{A}} \subset \mathbb{R}_{\mathbf{X}}$ [SS97], which summarizes all combinations of input parameters $\boldsymbol{x}$ that fulfill all performance specifications [SS97]. From the projected specification boundaries, information on *parametric yields* can be derived as important figures of merit for the impact of process variations and atomic-level fluctuations in IC design [SS97]. The partial parametric yield Ψ_{i} quantifies the fraction of circuits fulfilling the specification i; the parametric yield Ψ quantifies the fraction of circuits fulfilling all performance specifications.

3.2 Corner Models and Statistical Models

This section outlines corner models and statistical models as general approaches to describe variability. For completeness, it also considers environmental parameters $\boldsymbol{x}_{\mathrm{e}}$. While environmental parameters $\boldsymbol{x}_{\mathrm{e}}$ are subject to changes during circuit operation, process parameters $\boldsymbol{x}$ are constant after circuit manufacturing when degradation effects are neglected, as in this thesis. Environmental and process parameters are also referred to as *deterministic* and *statistical parameters* [ZSH+12]. Their distinction and the derived modeling approaches are illustrated in Fig. 3.4.

Environmental parameters, such as supply voltage and temperature, can be defined in terms of intervals. A correct functionality is required for all combinations of environmental parameters $\boldsymbol{x}_{\mathrm{e}}$ within these ranges [ZSH+12]. When their mapping to the performance parameters, $\boldsymbol{z} = \mathbf{h}_{\mathbf{e}}(\boldsymbol{x}_{\mathrm{e}})$, is assumed monotonic, the extreme performance parameter combinations are observed for the extreme combinations of environmental parameters $\boldsymbol{x}_{\mathrm{e}}$, which are obtained from the interval boundaries and referred to as

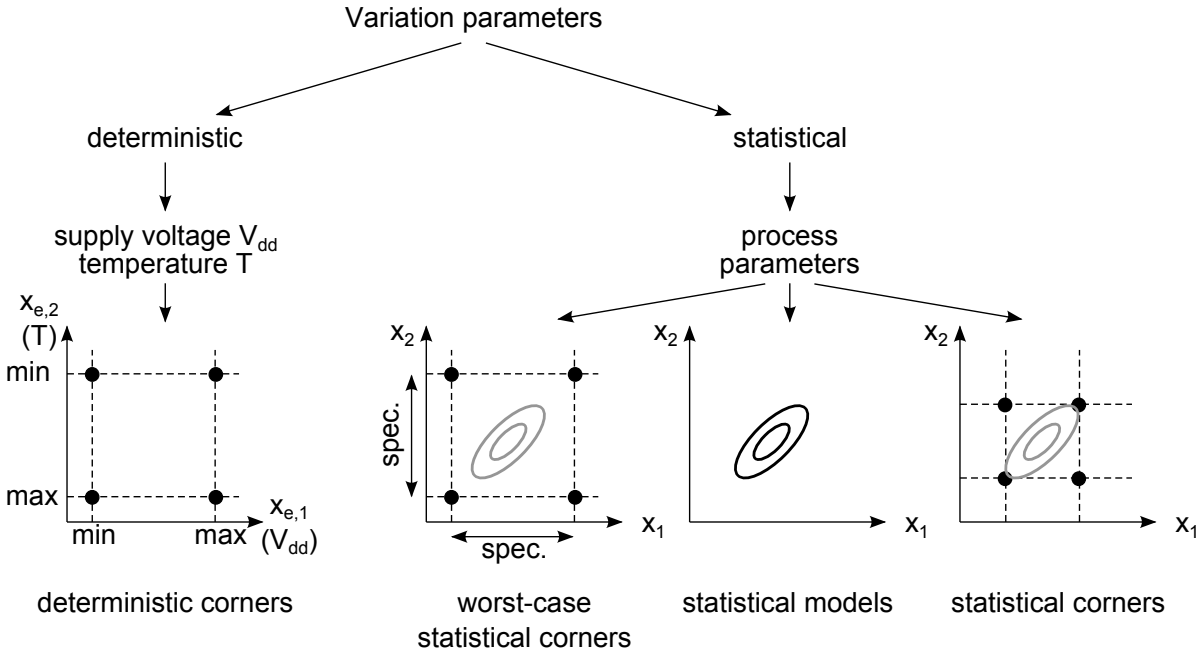

Fig. 3.4: Deterministic and statistical parameters with corresponding corner models and statistical models; statistical parameters are assumed Gaussian with the covariance ellipses provide as references for worst-case statistical corners and statistical corners

deterministic corners $\boldsymbol{x}_{\mathbf{det}}^{(\mathrm{corner})}$. Under the assumption of a monotonic mapping $\mathbf{h_e}(.)$, it is sufficient to only consider the deterministic corners for circuit verification.

In contrast, to capture variability, process parameters $\boldsymbol{x}$ are described as an n_x-dimensional RV $\boldsymbol{X}$, that is by a *statistical model*. An example statistical model is a multivariate Gaussian distribution $\boldsymbol{X} \sim \mathbf{N}(\boldsymbol{\mu}, \boldsymbol{\Sigma})$ [BCSS08, ONB08, Sah10], which is illustrated by the covariance ellipses in Fig. 3.4. Such a description can contain information on global and local variations and achieve a high accuracy.

Commonly, a statistical model is the input to *Monte Carlo* (MC) analyses, which are based on random samples $\tilde{\boldsymbol{X}}$ from the RV $\boldsymbol{X}$. They can be generated following the principles in Sec. 2.3 or App. A.2. Potentially expensive simulations evaluate each sample point $\boldsymbol{x}^{(\mathrm{k})}$ to obtain a sample $\tilde{\boldsymbol{Z}}$ of the circuit performance parameters. This sample can be used to infer on the properties of the RV $\boldsymbol{Z}$ describing the performance variability or to estimate the parametric yield Ψ [Sah10], for example. However, to achieve a reasonable significance in a MC analysis, a large sample size N may be required and cause an immense computational effort.

Corner models are an approach to reduce this effort by providing a compact set of parameter combinations for efficient circuit verification. As a simplification, they assume monotonic mappings between process parameters and performance parameters, $\boldsymbol{z}=\mathbf{h}(\boldsymbol{x})$. In this case, as for deterministic corners, extreme performance parameters are obtained at the extreme process parameter combinations [ONB08]. However, due to their statistical nature, extreme process parameter combinations are more difficult to define than deterministic corners with their predefined intervals for environmental parameters [ONB08, ZSH+12]. One approach is combining the most extreme allowed statistical parameters, which can be derived from the process specifications, into *worst-case statistical corners* $\boldsymbol{x}_{\mathbf{stat,wc}}^{(\mathrm{corner})}$ [Sah10]. As indicated in Fig. 3.4, worst-case statistical corners may be far off the real parameter distribution, making them very unlikely. In addition, they over-estimate the spread in the process parameters so that they are very pessimistic.

In contrast, *statistical corners* are directly derived from the statistical model: each parameter x_i is shifted by k standard deviations $\sigma_{\mathrm{X_i}}$ from its mean value $\mu_{\mathrm{X_i}}$ [Sah10],

$$x_{i;\mathrm{stat}}^{(\mathrm{corner})} = \mu_{\mathrm{X_i}} \pm k \cdot \sigma_{\mathrm{X_i}}. \tag{3.1}$$

Statistical corners $\boldsymbol{x}_{\mathbf{stat}}^{(\mathrm{corner})}$ are the combinations of these corner values for multiple input parameters. As indicated in Fig. 3.4, they are closer to the real parameter distribution so that they better represent a statistical model than worst-case statistical corners. Under the assumption of monotonic mappings $\boldsymbol{z}=\mathbf{h}(\boldsymbol{x})$, extreme performance parameter combinations are observed at the statistical corners. The definition in (3.1), however, implies that statistical corners do no represent parameter limits. Instead, more extreme values may occur with a small probability of occurrence [ONB08].

While statistical corners can reduce the complexity by simplifications, a variety of disadvantages was reported.

1. Corners are created by all extreme combinations of input parameters $\boldsymbol{x}$. For n_x parameters with lower and upper corner values, 2^{n_x} corners can be defined. This leads to 4 corners for $n_x=2$ parameters as in Fig. 3.4 and more than 1000 corners for $n_x=10$ parameters already. To provide a reasonable number of parameter combinations to be analyzed, the number of corners has to be reduced. While different corners may result in the extreme values of different performance parameters, for instance timing and leakage power of digital circuits [BC09], such a reduction without waiving important scenarios appears challenging [SSK+09].

2. The simultaneous deflection of parameters into a particular corner ignores real parameter correlations, which may lead to extremely unlikely statistical corners. This can be observed in Fig. 3.4, where the upper left and lower right statistical corners are far off the distribution of the input parameters x_1 and x_2. The impact of this effect dramatically grows with the number of input parameters n_x.
3. Applied to multiple instances or circuit elements, such as transistors or logic gates, statistical corners deflect all instances or elements in the same manner. Hence, they neglect local variability and introduce inaccuracies [LLP06, YTG10].
4. Corner cases do not represent the context-specific extreme circuit performance [BCSS08, LLP06, SSK+09] if the assumption of monotonic mappings $\mathbf{h}(.)$ is wrong.

All these disadvantages can be observed throughout the hierarchical levels in IC design when corner models are transferred to higher levels of abstraction.

Corner models and statistical models are universal approaches to model variability. In IC design and analysis, they are applied to standard models, such as device compact models or standard cell models, as well as custom models, such as bit cell performance models and analog behavioral models. For this purpose, a subset or all coefficients of these are considered statistical parameters and described by a corner model or a statistical model.

3.3 Device Compact Models

Device compact models abstract the physics of devices by describing their electrical behaviors. They consist of equations that connect pin voltages and currents depending on geometry information as well as environmental conditions. Hence, device compact models can be efficiently evaluated in circuit simulations [Cou12].

According to the naming conventions in Sec. 3.1, physical level parameters are considered as the vector of input parameters $\boldsymbol{x}$; model parameters are considered as a vector $\boldsymbol{y}$; and the electrical behavior is considered as a vector of performance parameters $\boldsymbol{z}$ in this section.

A simple example for an NFET or PFET compact model is the equation [MK86]

$$I_d = \mu \cdot C_{ox} \cdot \frac{W}{L} \cdot \left[(V_{gs} - V_{th}) \cdot V_{ds} - \frac{V_{ds}^2}{2} \right]. \tag{3.2}$$

It relates the static drain current I_d to the applied gate-source and drain-source voltages, V_{gs} and V_{ds}. The performance parameters $\boldsymbol{z}$ may be a set of drain currents I_d at different bias conditions. The device length L and width W are instance parameters; the mobility μ, the gate capacitance per unit area C_{ox}, and the threshold voltage V_{th} are the model parameters, which can be summarized in a vector $\boldsymbol{y}$.

Although they are related to the underlying physics, compact model parameters $\boldsymbol{y}$ usually cannot be directly determined via a mapping $\boldsymbol{y}=\mathbf{f}(\boldsymbol{x})$. Instead, as indicated in Fig. 3.5, they are derived from performance parameters during *parameter extraction*: the model parameters $\boldsymbol{y}$ are adjusted until the mapping $\boldsymbol{z}=\mathrm{g}(\boldsymbol{y})$ well represents the measured electrical device behavior. The device-specific model parameters are summarized in *model cards* to be accessed and evaluated by circuit simulators.

Since a simple model, such as (3.2), cannot capture all physical effects in modern semiconductor technologies, more detailed *field effect transistor* (FET) compact models with dedicated extraction procedures have been developed [CMC, DH12]. From the selection of FET compact models in Tab. 3.1, the *Berkeley short-channel insulated gate field effect transistor model* (BSIM) can be considered most prevalent.

Process variations and atomic-level fluctuations stem from the physical level where their sources can be modeled as an n_x-dimensional RV $\boldsymbol{X}$. They manifest themselves in electrical device performance variability, which can then be considered an n_z-

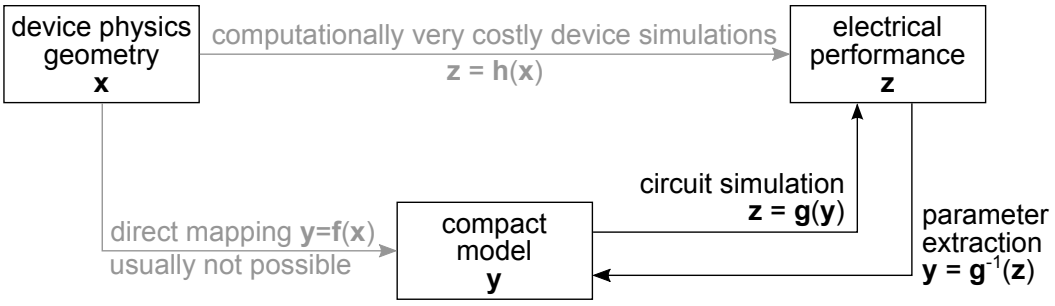

Fig. 3.5: Device compact models in context; relations in gray cannot be efficiently evaluated

Tab. 3.1: Overview of selected FET compact models for bulk processes, *silicon on insulator* (SOI) technologies, and high-voltage technologies [CMC, DH12]

Technology / Application	**Models**
Bulk	BSIM3, BSIM4, BSIM5, BSIM6; PSP; HiSIM; EKV
SOI	BSIMSOI; HiSIM_SOI
High-Voltage	HiSIM_HV

dimensional RV $\boldsymbol{Z}$. To make these variations available in circuit simulations, variability information has to be transferred to (selected) compact model parameters, which can be modeled as an n_y-dimensional RV $\boldsymbol{Y}$. A selection of previously published approaches for variability-aware FET compact modeling is summarized in Tab. 3.2. Differences can be obtained in the selections of compact model parameters and in the specific definitions, such as using Gaussian or non-Gaussian distributions. Hence, a standard to capture variability in FET compact models has not been developed yet.

Independent of the underlying compact model and the set of parameters that captures variability, statistical device compact modeling strategies differ in the generation of sample data $\tilde{\boldsymbol{Z}}$ of electrical device performance parameters and their transfer to statistical device compact models described by the RV $\boldsymbol{Y}$, which is illustrated in Fig. 3.6. Sample data generation is usually based on measurements of single devices, device arrays, or small circuits, such as *ring oscillator*s (ROs) [CDM+10, KGB+11, MAW+11, MLSG10, ONB08, Sah10, YTG10]. In industrial environments, extensive sample data $\tilde{\boldsymbol{Z}}$ are usually available from process monitoring [PG11, YTG10]. Alternatively, when feasible physical-level models of devices and variation sources are available, sample data $\tilde{\boldsymbol{Z}}$ can be obtained from runtime-intensive statistical device simulations. Variability information can be transferred to statistical device compact models in terms of a RV $\boldsymbol{Y}$ by two approaches. First, originating at a single typical compact model, centering and variation mapping yield a multivariate Gaussian model $\boldsymbol{Y} \sim \mathbf{N}(\boldsymbol{\mu}_{\mathbf{Y}}, \boldsymbol{\Sigma}_{\mathbf{Y}})$. Second, the conventional extraction of an ensemble of compact models yields sample data $\tilde{\boldsymbol{Y}}$, which can be used to infer on the RV $\boldsymbol{Y}$.

Tab. 3.2: Approaches for statistical transistor compact modeling

Reference	Compact Model	Varied Parameters	Distributions
[REO+06]	BSIM3v3	vth0, u0, xl, xw, nsub, tox, cgdo, cgso, cgbo, rsh, cj	Gaussian
[ONB08], pp. 163	SPICE Level 3	vth, u0, theta, eta	Gaussian
[Sah10]	BSIM4	tox, xl, xw, vth0, u0, nsub, nch, rsh	presumably Gaussian
[YTG10]	EKV	tox, nsub, u0, dl, dw	Gaussian
[CDM+10]	BSIM4	vth0, u0, nfactor, voff, minv, rdsw, dsub	Gaussian
	PSP	nsub0, cfl, alp1l1, u0, cs0, ct0, rsw1	Gaussian
[KDC+10]	PSP	nsub0, cfl, alpl, u0, cs0, ct0, rsw1	non-Gaussian
Sec. 5.1	BSIM4	vth0, rdsw, nfactor, voff, u0, dsub, vsat	non-Gaussian

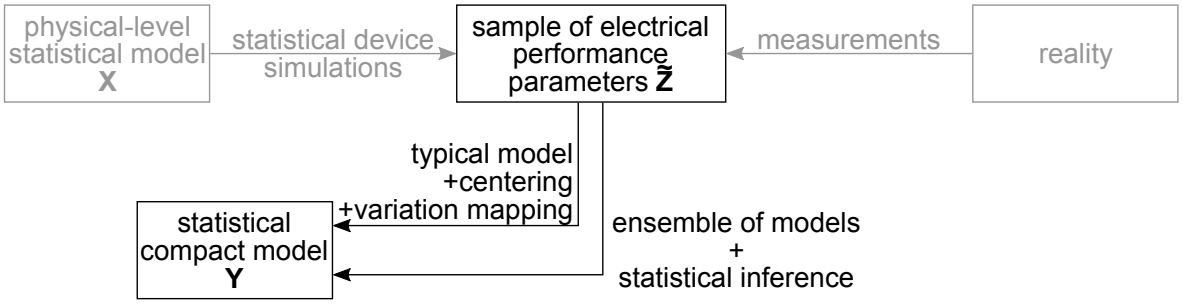

Fig. 3.6: Overview on statistical device compact modeling strategies

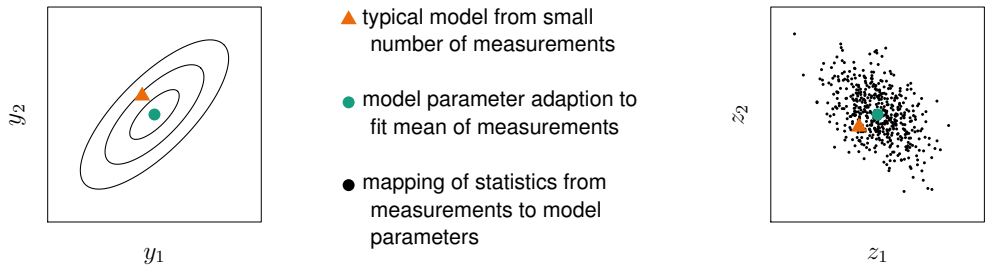

Fig. 3.7: Procedure for statistical device model extraction based on *backward propagation of variance* (BPV); (1) typical set of model parameters extracted from typical electrical performance; (2) adaption of model parameters to meet mean measurement results (3) mapping of statistics from electrical performance to model parameters applying BPV

The approach of centering and variation mapping is less computationally expensive. Therefore, it can be efficiently re-used when manufacturing processes change, and it is usually applied in industry [MLSG10, SM09]. From the sample $\tilde{\boldsymbol{Z}}$ of electrical performance parameters, the mean vector $\widetilde{\boldsymbol{\mu}}_{\mathbf{Z}}$ and the covariance matrix $\widetilde{\boldsymbol{\Sigma}}_{\mathbf{Z}}$ can be estimated applying the principles in Sec. 2.1 and 2.2. Note that the empirical standard deviations of the components Z_j, $\widetilde{\sigma}_{Z_j}$, are parts of the empirical covariance matrix $\widetilde{\boldsymbol{\Sigma}}_{\mathbf{Z}}$. If necessary, the mean vector of the RV $\boldsymbol{Y}$, $\boldsymbol{\mu}_{\mathbf{Y}}$, is tuned until it emulates the mean electrical performance $\widetilde{\boldsymbol{\mu}}_{\mathbf{Z}}$. This multi-criteria optimization, which originates at the typical model, can be solved by a least squares approach [SM09], for instance. Variation mapping is based on the assumption of a linear mapping function

$$\boldsymbol{z} = \boldsymbol{\mu}_{\mathbf{Z}} + \mathrm{S}\,(\boldsymbol{y} - \boldsymbol{\mu}_{\mathbf{Y}})\,, \tag{3.3}$$

which is justified for small variations [DM03]. The $(n_z \times n_y)$ sensitivity matrix S in (3.3) with $\mathrm{S}_{ji} = \partial z_j / \partial y_i$ can be obtained from circuit simulations. According to (2.41) in

Sec. 2.2.3, (3.3) relates the covariance matrix of the RV $\boldsymbol{Y}$, $\boldsymbol{\Sigma}_{\mathbf{Y}}$, and the empirical covariance matrix of electrical performance $\widetilde{\boldsymbol{\Sigma}}_{\mathbf{Z}}$ by the equation

$$\widetilde{\boldsymbol{\Sigma}}_{\mathbf{Z}} = \mathbf{S} \cdot \boldsymbol{\Sigma}_{\mathbf{Y}} \cdot \mathbf{S}^{\mathrm{T}}. \tag{3.4}$$

Transferring covariance information from performance parameters to model parameters by solving (3.4) for the covariance matrix $\boldsymbol{\Sigma}_{\mathbf{Y}}$ is referred to as *backward propagation of variance* (BPV). With the mean vector $\boldsymbol{\mu}_{\mathbf{Y}}$ and the covariance matrix $\boldsymbol{\Sigma}_{\mathbf{Y}}$, the RV $\boldsymbol{Y}$ is then assumed multivariate Gaussian $\boldsymbol{Y} \sim \mathrm{N}(\boldsymbol{\mu}_{\mathbf{Y}}, \boldsymbol{\Sigma}_{\mathbf{Y}})$. In [PG11], (3.4) is directly solved to explicitly consider correlations between electrical performance parameters and between model parameters.

Practical applications often use simplifications, however. In [DM03], the components of the RV $\boldsymbol{Y}$, Y_i, are assumed uncorrelated Gaussians and electrical performance parameter correlations are neglected, so that (3.4) simplifies to the equation system

$$\left.\begin{array}{rcl} \sum\limits_i \mathbf{S}_{1\mathrm{i}}^2 \; \sigma_{\mathrm{Y_i}}^2 & = & \widetilde{\sigma}_{\mathrm{Z_j}}^2 \\ \cdots & & \\ \sum\limits_i \mathbf{S}_{1\mathrm{n_y}}^2 \; \sigma_{\mathrm{Y_i}}^2 & = & \widetilde{\sigma}_{\mathrm{Z_{n_z}}}^2 \end{array}\right\} \quad \begin{pmatrix} \mathbf{S}_{11}^2 & \mathbf{S}_{12}^2 & \cdots & \mathbf{S}_{1\mathrm{n_y}}^2 \\ \vdots & \vdots & \cdots & \vdots \\ \mathbf{S}_{\mathrm{n_z}1}^2 & \mathbf{S}_{\mathrm{n_y}2}^2 & \cdots & \mathbf{S}_{\mathrm{n_z n_y}}^2 \end{pmatrix} \cdot \begin{pmatrix} \sigma_{\mathrm{Y_1}}^2 \\ \cdots \\ \sigma_{\mathrm{Y_{n_y}}}^2 \end{pmatrix} = \begin{pmatrix} \widetilde{\sigma}_{\mathrm{Z_1}}^2 \\ \cdots \\ \widetilde{\sigma}_{\mathrm{Z_{n_z}}}^2 \end{pmatrix}, \tag{3.5}$$

which has to be evaluated for the model parameter standard deviations $\sigma_{\mathrm{Y_i}}$. In [MLSG10, SLM+10], electrical performance parameter correlations are taken into account by evaluating

$$\forall j \neq k: \quad \widetilde{\boldsymbol{\Sigma}}_{\mathbf{Z},jk} = \widetilde{\boldsymbol{\Sigma}}_{\mathbf{Z},kj} = \sum_i \mathbf{S}_{ji} \cdot \mathbf{S}_{ki} \cdot \sigma_{\mathrm{Y_i}}^2 \tag{3.6}$$

in addition to (3.5) to determine the standard deviations $\sigma_{\mathrm{Y_i}}$ of the model parameters, which are still assumed uncorrelated Gaussians. Model parameters with known standard deviations $\sigma_{\mathrm{Y_i}}$, for example the oxide thickness with a dedicated measurement procedure, may be considered constant in (3.5) and (3.6) [MLSG10, SM09, SLM+10]. Furthermore, a quadratic mapping [MLSG10, SM09],

$$\forall j: \quad z_j = \mu_{\mathrm{Z_j}} + \sum_i \mathbf{S}_{j,i} \cdot (y_i - \mu_{\mathrm{Y_i}}) + \sum_{i,k} \mathbf{S}_{j,ik}^* \cdot (y_i - \mu_{\mathrm{Y_i}}) \cdot (y_k - \mu_{\mathrm{Y_k}}) \tag{3.7}$$

$$\text{with} \quad \mathbf{S}_{j,ik}^* = \frac{1}{2} \cdot \frac{\partial^2 z_j}{\partial y_i \, \partial y_k},$$

results in a *quadratic backward propagation of variance* (QBPV), which may overcome the accuracy limitations of the linear mapping (3.3). After adapting (3.5) and (3.6) to additionally capture the skews of the electrical performance parameter distributions, the mapping (3.7) supports non-Gaussian electrical performance parameters but still assumes uncorrelated Gaussian model parameters Y_i.

To correctly describe variability, global and local variations have to be captured [SM09]. While global variations do not depend on device geometries, the geometry dependence of local variations has to be taken into account [DM03]. Nevertheless, both variation types can be extracted with the discussed BPV approaches based on suitable sample data $\tilde{\boldsymbol{Z}}$ [MLSG10].

The second approach to extract statistical device compact models is based on an ensemble of model cards. From single-device electrical performance parameters, a separate model card is extracted for each device. With significant computational effort, sample data $\tilde{\boldsymbol{Y}}$ of the compact model parameters that capture variability is generated to infer on the underlying RV $\boldsymbol{Y}$ [CDM+10, KDC+10, MAW+11]. Neglecting global variations but introducing random local variations from atomic-level fluctuations in terms of a RV $\boldsymbol{X}$ at the physical level, $N=200$ microscopically different $35\,nm$ square NFETs were analyzed by device simulations in [CDM+10]. Their electrical behaviors were mapped to $N=200$ model cards. For BSIM4 and PSP compact models, the authors found that, while keeping most model parameters constant, capturing variability by 7 model parameters provided a good compromise between model complexity and accuracy. From the $n_y=7$-dimensional sample data $\tilde{\boldsymbol{Y}}$ of the size $N=200$, they observed correlated and non-Gaussian random components Y_i and concluded that a novel modeling approach for variability was required. A potential solution was proposed in [KDC+10]: each random component Y_i was described by a third-order polynomial of a standard Gaussian RV $G_i \sim \mathrm{N}(0,1)$ [Fle78],

$$Y_i = c_{i,0} + c_{i,1} \cdot G_i + c_{i,2} \cdot G_i^2 + c_{i,3} \cdot G_i^3, \tag{3.8}$$

with the coefficients $c_{i,0}$, $c_{i,1}$, $c_{i,2}$, and $c_{i,3}$. These coefficients were determined by matching the theoretical and the empirical mean value, variance, skew, and kurtosis per model parameter Y_i. While the theoretical characteristics can be obtained from (3.8) using (2.5)–(2.8) in Sec. 2.1.1, their empirical counterparts can be derived from the sample $\tilde{\boldsymbol{Y}}$ using (2.25)–(2.28) in Sec. 2.1.4. Furthermore, Pearson's correlation coefficients $\widetilde{\rho}^{(\mathrm{pe})}_{\mathrm{Y_i,Y_j}}$ between the model parameters Y_i and Y_j were estimated from the

sample data $\tilde{\boldsymbol{Y}}$ by applying (2.50) and transformed to the required correlations between the standard Gaussian components G_i and G_j by solving [KDC+10]

$$\widetilde{\rho}^{(\mathrm{pe})}_{\mathrm{Y_i},\mathrm{Y_j}} = c_{i,0} \cdot \Big(c_{j,0} + c_{j,2} + c_{i,1}\, c_{j,1}\, \rho^{(\mathrm{pe})}_{\mathrm{G_i},\mathrm{G_j}} + 3c_{i,3}\, c_{j,1}\, \rho^{(\mathrm{pe})}_{\mathrm{G_i},\mathrm{G_j}} + 3c_{i,1}\, c_{j,3}\, \rho^{(\mathrm{pe})}_{\mathrm{G_i},\mathrm{G_j}} + 9c_{i,3}\, c_{j,3}\, \rho^{(\mathrm{pe})}_{\mathrm{G_i},\mathrm{G_j}} + 6c_{i,3}\, c_{j,3}\, {\rho^{(\mathrm{pe})}_{\mathrm{G_i},\mathrm{G_j}}}^{3} + c_{i,2}\, c_{j,0} + c_{j,2} + 2c_{j,2}\, {\rho^{(\mathrm{pe})}_{\mathrm{G_i},\mathrm{G_j}}}^{2} \Big) \tag{3.9}$$

for Pearson's correlation coefficients $\rho^{(\mathrm{pe})}_{\mathrm{G_i},\mathrm{G_j}}$ for all combinations of $i \neq j$. In combination, (3.8) and (3.9) yield statistical device models with non-Gaussian and correlated components Y_i as transformations of correlated standard Gaussian components G_i. This approach is utilized in industrial software for device compact modeling [Gol].

3.4 Digital Design and Standard Cell Models

Transistor-level implementations of complete digital circuits are usually infeasible in terms of complexity. However, transistor-level implementations of basic logic functionality, such as inverters or NAND and NOR gates, appear appropriate. These logic gates, which serve as an interim abstraction layer, are referred to as *standard cells* and stored in technology-specific *standard cell libraries* [BC09].

Digital design is usually based on a functional circuit description in a *hardware description language* (HDL), such as *Verilog® HDL* [Ver06] or *Very High Speed Integrated Circuit Hardware Description Language* (VHDL) [VHD09b]. A highly automated chain of transformation steps instantiates available standard cells to translate this description into a circuit layout: synthesis maps the circuit functionality onto standard cells; placement defines their locations on the die area; and routing realizes the physical interconnects [Bha02, BC09]. Since these steps handle logic gates, the corresponding abstraction layer is referred to as *gate level*.

The performance parameters of digital circuits include circuit timing and power consumption, and they are summarized in a vector of performance parameters $\boldsymbol{z}$ in this section. To consider them during design, the automated transformation steps are based on and followed by dedicated analysis approaches at the gate level. For this purpose, information on standard cell properties, such as propagation delay, dynamic energy, or leakage power, have to be available in a standard cell library. These quantities, which are treated as vector $\boldsymbol{y}$ in this section, are obtained from circuit simulations

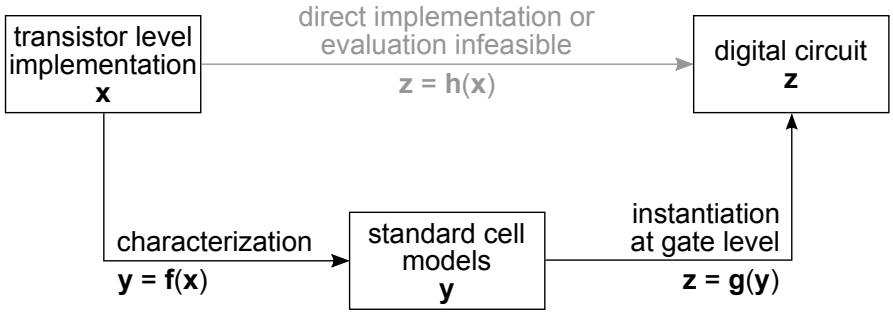

Fig. 3.8: Standard cells as an abstraction layer in digital design

of standard cells during *characterization* [BC09]. Since transistor-level parameters can be tuned to adapt standard cell performance quantities, they may be treated as input parameters $\boldsymbol{x}$ in this section. Overall, Fig. 3.8 illustrates the different abstraction layers in digital design.

Timing can be considered the most important performance parameter of a digital block. Within and after each of the automated transformation steps in the design flow, it is verified by the *static timing analysis* (STA), an efficient gate level analysis method that can be considered as a part of the mapping $\boldsymbol{z}=\mathrm{g}(\boldsymbol{y})$ in Fig. 3.8. While the details of STA are documented elsewhere, for instance in [BC09, Sap04], the AND3 gate in Fig. 3.9(a) serves as an example to introduce its basic principles.

The STA neglects the logic functionality by abstracting standard cells and consequently the whole digital block by a timing graph as in Fig. 3.9(b). This graph contains standard cell and, potentially, interconnect delays[2] on its edges [Sap04]. Then, signal arrival times are computed. In Fig. 3.9, the arrival times at the AND3 input pins $i1$, $i2$, and $i3$, AT_{i1}, AT_{i2}, and AT_{i3}, are assumed to be known from user-defined constraints or

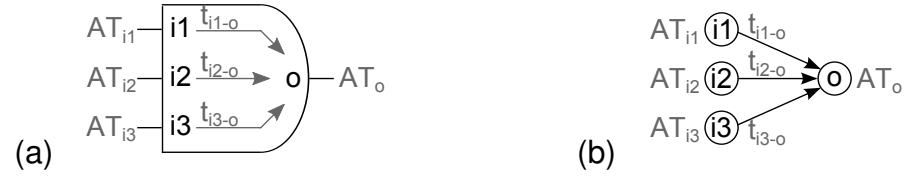

Fig. 3.9: Principles of *static timing analysis* (STA); (a) AND3 gate; (b) timing graph

[2]Detailed modeling approaches for standard cell and interconnect delays are beyond the scope of this thesis but, for instance, discussed in [BC09, DH12, Kno12, Sap04].

previous STA steps. The signal arrival times at the AND3 output pin o with respect to a specific switching event at a specific input pin [BC09],

$$\mathrm{AT}_o^{(i1)} = \mathrm{AT}_{i1} + t_{\mathrm{i1-o}}, \quad \mathrm{AT}_o^{(i2)} = \mathrm{AT}_{i2} + t_{\mathrm{i2-o}}, \quad \text{and} \quad \mathrm{AT}_o^{(i3)} = \mathrm{AT}_{i3} + t_{\mathrm{i3-o}}, \tag{3.10}$$

are computed from signal arrival times and the corresponding standard cell propagation delays from the standard cell library, $t_{\mathrm{i1-o}}$, $t_{\mathrm{i2-o}}$, and $t_{\mathrm{i3-o}}$. While the path-based STA propagates the arrival times at the AND3 output pin o separately through the subsequent stages of the timing graph, the block-based STA only propagates their maximum or minimum,

$$\mathrm{AT}_o = \max\left\{\mathrm{AT}_o^{(i1)}, \mathrm{AT}_o^{(i2)}, \mathrm{AT}_o^{(i3)}\right\} \quad \text{or} \quad \mathrm{AT}_o = \min\left\{\mathrm{AT}_o^{(i1)}, \mathrm{AT}_o^{(i2)}, \mathrm{AT}_o^{(i3)}\right\}, \tag{3.11}$$

through the subsequent stages depending on performing setup or hold checks and treating clock or data signals [DH12, ONB08]. Due to its increased efficiency, block-based STA is the industry standard. Summation as well as maximum or minimum operations are the basic calculations in STA.

Besides timing, circuit leakage power is an important performance characteristic of a digital block. For each standard cell, state-dependent leakage power values are determined in the circuit simulations during characterization [FF02, XLL04]. At the gate level, the leakage power of a digital block is calculated as the sum of the leakage power values of all standard cell instances [FF02, XLL04]. The dependency on logic states can be considered by including the results of logic simulations. They can be used as weighting factors in leakage power summations [FF02] or to identify minimum and maximum leakage power states based on optimization techniques [CVB04, XLL04].

The performance parameters $\boldsymbol{z}$ of digital blocks vary due to process variations and atomic-level fluctuations. To take these effects into account, variability information needs to be abstracted from transistor level parameters $\boldsymbol{x}$ to standard cell performance parameters $\boldsymbol{y}$ for gate level analyses, such as STA or leakage computations.

For this purpose, corner-based approaches are most straightforward. Standard cells are characterized for the corner cases of transistor level parameters $\boldsymbol{x}$, either worst-case statistical corners or, usually, statistical corners. This is assumed to result in extreme standard cell performance parameters $\boldsymbol{y}^{(\mathrm{corner})}$. However, corner-based gate level analysis approaches suffer from the disadvantages discussed in Sec. 3.2: pessimism in propagation delays [BCSS08, Sap04]; difficulties in defining a reasonable

set of corners without waiving important scenarios [ONB08, SSK+09]; and neglecting local variations that tend to partially cancel out along timing paths. Consequently, corner-based STA results are pessimistic by over-estimating the spread in circuit timing [BCSS08, DH12, ONB08, Sap04, SSK+09]. A simulation study of a full adder with independent threshold voltage variations reported up to $>25\,\%$ errors for variations of $\sigma/\mu = 10\,\%$ and up to $>40\,\%$ errors for variations of $\sigma/\mu = 15\,\%$ for corner-based STA [MAW+11]. Counteracting this pessimism by large design margins increases the die area, power consumption, and design time [VCBS11]. Accordingly, by more accurate approaches, timing margins may be relaxed and die areas, power consumptions, as well as design times may be reduced [BCSS08].

Fig. 3.10 arranges advanced approaches to consider variability in STA. As an extension to corner-based STA, *on-chip variations* (OCV) techniques take into account local variability. The actual OCV approach multiplies all standard cell propagation delays $t_{\mathrm{i-o}}$ with a constant derating factor to determine a percentage path delay variation [BC09, SSK+09]. To improve OCV, *advanced on-chip variations* (AOCV) defines derating factors based on logic path lengths and physical distances. Thus, it reduces the analysis pessimism by capturing that local variability tends to average out along timing paths [SSK+09, Wal09]. AOCV is the industry standard for technology nodes down to approximately $20\,nm$ but still considered pessimistic and costly [Tec12]. For the $16\,nm$ or the $14\,nm$ technology node, the *parametric on-chip variations* (POCV) approach gains importance [Spe12]. It adds cell and net-specific delay variations assuming Gaussian distributions [MLMC09, Tec12].

Based on statistical standard cell propagation delay models in terms of a multi-dimensional RV $\boldsymbol{Y}_{\mathrm{d}}$, the *statistical static timing analysis* (SSTA) offers an im-

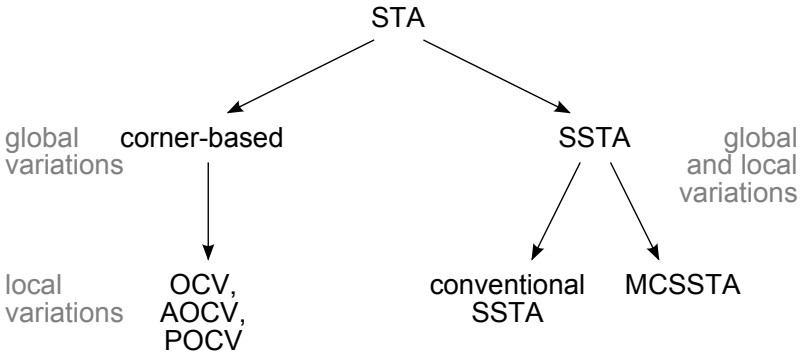

Fig. 3.10: Survey of approaches to consider variability during *static timing analysis* (STA)

proved accuracy. In its conventional form, it applies a *canonical delay model* [VRK+04, VRK+06],

$$Y^*_{d;j} = t_{i-o,j} + \sum_{i=1}^{n_g} s_{g;ji} \cdot X_{g,i} + s_{l;j} \cdot X_{l;j} \implies Y_{d;j} = t_{i-o,j} + \mathbf{s_{g;j}}\, \boldsymbol{X}_{\mathbf{g}} + s_{l;j}\, X_{l;j}, \quad (3.12)$$

to each component of the RV $\boldsymbol{Y}_{\mathbf{d}}$. In (3.12), $t_{\mathrm{i-o,j}}$ is the nominal propagation delay of instance j. The n_g-dimensional RV $\boldsymbol{X}_{\mathbf{g}}$ represents the statistical transistor level model describing global transistor level variations with the corresponding instance-specific sensitivity vector $\mathbf{s_{g;j}}$. The instance-specific univariate RV $X_{l;j}$ describes the local transistor level variations with the corresponding sensitivity $s_{l;j}$. In [VRK+04, VRK+06], all global transistor level variation parameters $X_{g,i}$ and the instance-specific RV $X_{l;j} \sim \mathrm{N}(0,1)$ are assumed uncorrelated standard Gaussian RVs. Accordingly, as introduced in Sec. 2.1.3, each propagation delay $Y_{d;j}$ in (3.12) is a Gaussian RVs with its mean value $t_{\mathrm{i-o,j}}$. The propagation delays of different standard cell instances are correlated due equal global transistor level parameters $\boldsymbol{X}_{\mathbf{g}}$ being applied to all instances. Signal arrival times determined in (3.10) and (3.11) are mapped to the canonical form in (3.12), that is to Gaussian RVs, accepting the potential errors for statistical maximum and minimum operations [VRK+04, VRK+06]. Different developments improve the usability of the conventional SSTA by reducing its run times. Reversible statistical maximum and minimum operations enable an incremental SSTA [SVV+12] and intelligent operand ordering and processing in [KSP+13] achieves run time improvements of about $60\,\%$ in statistical maximum and minimum operations. To further enhance the SSTA, the sensitivities $\mathbf{s_{g;j}}$ and $s_{l;j}$ can be treated as linear functions of environmental parameters, such as the supply voltage V_{dd}, to capture deterministic variations derived from deterministic corners [ZSH+12]. To incorporate local across-chip variations, the die area can be partitioned into grids and (3.12) can be extended to [LCXS13]

$$Y_j = t_{i-o,j} + \mathbf{s_{g;j}}\, \boldsymbol{X}_{\mathbf{g}} + \mathbf{s_{sp;j}}\, \boldsymbol{X}_{\mathbf{sp}} + s_{l;j}\, X_{l;j}. \quad (3.13)$$

The n_{sp}-dimensional RV $\boldsymbol{X}_{\mathbf{sp}}$ is a statistical transistor level model representing local variations that apply to all instances in a specific grid cell with instance-specific sensitivity vectors $\mathbf{s_{sp;j}}$ to account for spatial local correlations. Furthermore, a hierarchical timing model extraction adapts the SSTA to large digital designs [LCXS13].

Nevertheless, the disadvantages of the conventional SSTA are often criticized.

1. When variability gains importance, the canonical delay model (3.12), which is justified for relatively small variations only, becomes inaccurate [BCSS08, DH12, DMD+07].
2. The Gaussian approximations of the results of statistical maximum and minimum operations introduce inaccuracies by ignoring the skewness [BCSS08, VCBS11].

Non-linear and non-Gaussian SSTA approaches may solve these issues. For instance, the quadratic model in [CXH07],

$$Y^*_{d;j} = t_{\mathrm{i-o,j}} + \sum_{i=1}^{n_g} \left(s_{g;j,i} \cdot X_{g,i} + s_{g2;j,i} \cdot X^2_{g,i} \right) + s_{l;j} \cdot X_{l;j} + s_{l2;j} \cdot X^2_{l;j} \tag{3.14}$$

with quadratic sensitivities $s_{g2;j,i}$ and $s_{l2;j}$, assumes the RV $X_{l;j}$ to be Gaussian but allows arbitrary distributions for the global components $X_{g,i}$. In [CGX+12], the last term in (3.14) is skipped. Applying (3.14) to sum, maximum, and minimum operations increases the SSTA accuracy at the costs of efficiency.

Instead of propagating canonical or higher-order delay models, such as (3.12)–(3.14), *Monte Carlo-based statistical static timing analysis* (MCSSTA) methods [BCSS08, VCBS11] are based on sample data. Sampling from the RVs $\boldsymbol{X}_{\mathbf{g}}$ and $X_{l;j}$, which model transistor level parameters, and from the RVs $\boldsymbol{Y}_{\mathbf{d;j}}$, which model standard cell propagation delays, can be distinguished. The first approach is demonstrated in [VCBS11], where the canonical delay model (3.12) is assumed. The transistor level parameters in the RVs $\boldsymbol{X}_{\mathbf{g}}$ and $X_{l;j}$ are assumed Gaussian. Random samples $\tilde{\boldsymbol{X}}_{\mathbf{g}}$ and $\tilde{X}_{l,j}$ are applied to generate samples of the propagation delays $\tilde{Y}_{d;j}$ to be sequentially processed by the standard STA in (3.10) and (3.11). The combination of stratified sampling, quasi-MC, and latin hypercube sampling significantly improves the sampling efficiency. Furthermore, pruning unimportant stages and intelligently re-using sample points enable an incremental analysis [VCBS11]. The second approach, directly sampling from standard cell propagation delays, is referred to as *probabilistic timing analysis* [BCSS08]. Sample data $\tilde{Y}_{d;j}$ can be obtained from standard cell libraries, which contain multiple instances per cell to capture variability [DMD+07, MAW+11, PMM+07]. Sets of digital blocks are obtained by randomly assigning standard cell realizations from the library to instances in the circuit under investigation. They can be analyzed with standard tools and approaches, such as standard STA. For example, the simulation study in [MAW+11] demonstrates MCSSTA with 500 random instances of 4 standard cells and achieves a high accuracy with respect to circuit level MC reference simulations. Furthermore, the probabilistic library is shown to suit efficient and accurate

statistical gate level power analyses. However, finding a feasible compromise between library size and accuracy of probabilistic MCSSTA appears challenging.

While timing variability appears to be mainly considered in digital design, dynamic and static power consumption including their variations are important circuit performance characteristics as well. In [DEH10], VHDL [VHD09b] simulations are run and the conventional SSTA approach with the canonical delay model in (3.12) is adapted to dynamic power to perform a statistical gate level dynamic power analysis. More effort has been spent on statistical gate level leakage analyses, which treat standard cell leakage power distributions as a multivariate RV $\boldsymbol{Y}_{\mathbf{leak}}$. It is common to analytically model the leakage power variation of instance j in the form [SSA+05]

$$Y_{leak_j} = \exp\left(a_{j,0} + \sum_{i=1}^{n_g} a_{g;j,i} \cdot X_{g,i} + a_{l;j} \cdot X_{l;j}\right), \tag{3.15}$$

with $\exp(a_{j,0})$ being the nominal leakage power, $\boldsymbol{X}_{\mathbf{g}}$ being an n_g-dimensional RV modeling global transistor level variation parameters with the corresponding instance-specific sensitivity vector $\mathbf{a_{g;j}}$, and $X_{l;j}$ being an instance-specific univariate RV modeling local variations with the corresponding sensitivity $a_{l;j}$. Assuming the underlying transistor level parameters $\boldsymbol{X}_{\mathbf{g}}$ and $X_{l;j}$ to be Gaussian, different variation sources are taken into account: for example transistor length and oxide thickness variations in [CS05] or transistor length and threshold voltage variations in [SSA+05]. These approaches result in log-normal standard cell leakage power distributions so that the circuit leakage power distribution can be calculated as the sum of log-normal distributions. In [CS05], the logic states of each standard cell instance are assumed equally probable, but the state dependency of leakage power can be considered as in nominal leakage power analyses, for example in [CVB04, FF02, XLL04]. A quadratic dependency of standard cell leakage power on transistor length variations extends (3.15) to increase its accuracy [AMG12]. Assuming equally probable logic states as well as Gaussian transistor length and threshold voltage variations, the circuit leakage power distribution is estimated from a sampling-based analysis.

However, proper circuit design needs to simultaneously take into account multiple circuit performance parameters, such as timing, dynamic power, and leakage power, including their variations. For this purpose, the methods behind MCSSTA with sampled standard cell performance parameters allow statistical gate level analyses of circuit timing and power consumption using standard tools [DMD+07, MAW+11, PMM+07].

As an alternative, [BVG08, SSA+05] combine SSTA and statistical leakage power analyses to simultaneously examine digital block timing and leakage power. The underlying process parameters in the analytical standard cell performance models are assumed to be Gaussian. While [SSA+05] combines the approaches in (3.12) and (3.15), [BVG08] applies second-order polynomials for standard cell timing and the logarithm of standard cell leakage power. In [CGO+07], behavioral standard cell models describe the distributions of standard cell delays, leakage power values, and potentially other performance parameters depending on design, environmental, and process parameters. Based on these models, dedicated simulations allow to examine circuit timing and power consumption.

During circuit optimization, the different performance characteristics and their variability have to be traded off. For instance, in [BV08], standard cell sizes are optimized to minimize the mean value and the variance of the circuit leakage power distribution while an acceptable circuit timing is verified with a simplified delay model. The approaches in [MDO05, MDOZ07, HKK13] originate from a high performance and high leakage power circuit implementation. Standard cells are subsequently re-sized or replaced by lower leakage cells to reduce the circuit leakage power as long as the timing constraints are met. In principle, [MDO05, MDOZ07] apply the standard cell performance models in (3.12) and (3.15) and utilize power-delay sensitivities to drive the optimization. In contrast, the cell contributions to timing yield are the optimization criteria in [HKK13].

3.5 Memory Design and Bit Cell Models

This section on memory design focuses on *static random access memories* (SRAMs), which are dedicated structures for on-chip data storage. As illustrated in Fig. 3.11(a), they consist of control logic and bit cells, which are connected to an array structure. The transistor-level schematic in Fig. 3.11(b) depicts an SRAM bit cell from six FETs, which form two cross-coupled inverters and two access transistors [ARA13, ONB08].

From a complexity perspective, it is infeasible to analyze the SRAM array performance parameters z based on circuit simulations and transistor-level parameters x. Instead, according to the SRAM structure, bit cells are introduced as an interim abstraction layer. Their performance parameters y can be efficiently obtained from circuit simulations. Bit cells with the worst performance parameters y are assumed to dominate the SRAM

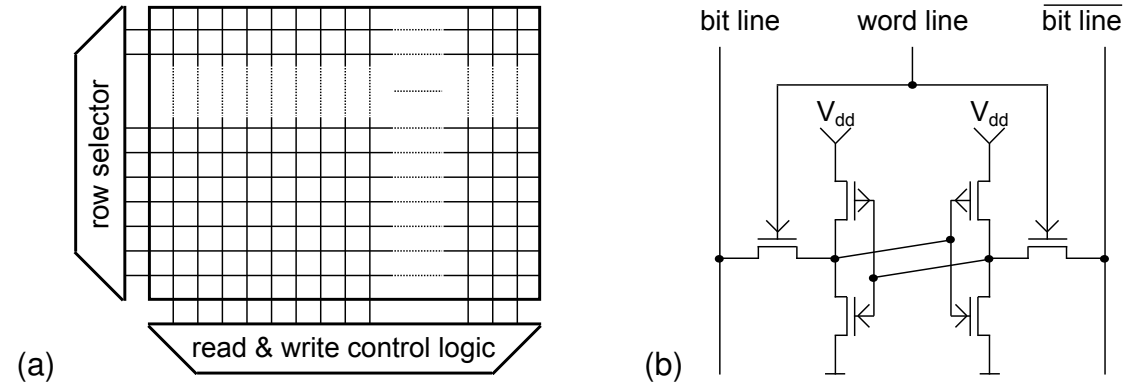

Fig. 3.11: *Static random access memory* (SRAM); (a) array structure with one bit cell at each crossing of rows and columns (simplified from [ARA13]); (b) bit cell schematic [ARA13]

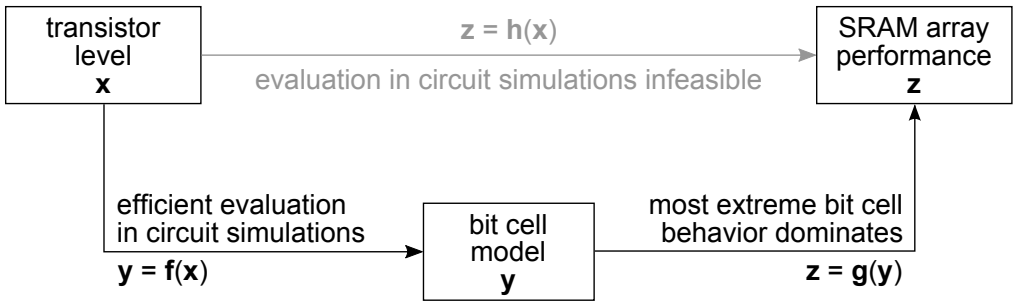

Fig. 3.12: Hierarchical levels in SRAM design

array performance parameters z. Fig. 3.12 illustrates the interactions between the hierarchical levels.

Obviously, SRAMs are affected by variability from process variations and atomic-level fluctuations. Potential failure mechanisms are documented in [ARA13], for example. Different aspects make SRAMs especially susceptible to variability and require a special treatment.

- SRAM bit cells are designed with the minimum allowed feature sizes to achieve a high integration density [ARA13]. These geometries and the cross-coupled architecture make SRAM bit cells extremely sensitive to variations, especially to local fluctuations that cannot be captured by corner-based analysis approaches [ARA13, ONB08, SR10].
- An SRAM array consists of up to several million bit cell instances. This large number makes statistically rare bit cells important. Their extreme performance parameters y dominate the SRAM array performance parameters z with their specifications [ARA13, SR10].

Tab. 3.3: Examples for required bit cell failure rates $\mathrm{FR}_{\mathrm{bit}} = 1 - \Psi_{\mathrm{bit}}$ to achieve pre-defined array yields Ψ_{array} at selected array sizes n according to (3.16)

n	Ψ_{array}		
	0.90	**0.95**	**0.99**
100	$1.05e$-03	$5.13e$-04	$1.00e$-04
1000	$1.05e$-04	$5.13e$-05	$1.01e$-05
10000	$1.05e$-05	$5.13e$-06	$1.01e$-06

While SRAMs are typically analyzed based on circuit simulations for bit cells, yield or failure rate requirements, Ψ or $\mathrm{FR} = 1 - \Psi$ are defined for arrays. Without redundancy, for an n-bit array, bit cell and array yields and failure rates can be converted by [SR09, SR10]

$$\mathrm{FR}_{\mathrm{array}} = 1 - (1 - \mathrm{FR}_{\mathrm{bit}})^n \;\Leftrightarrow\; \mathrm{FR}_{\mathrm{bit}} = 1 - (1 - \mathrm{FR}_{\mathrm{array}})^{1/n} \;\Leftrightarrow\; \Psi_{\mathrm{array}} = {\Psi_{\mathrm{bit}}}^n, \quad (3.16)$$

which assumes bit cells to be uncorrelated. The example conversions in Tab. 3.3 indicate that very low bit cell failure rates $\mathrm{FR}_{\mathrm{bit}}$ or, accordingly, very high bit cell yields Ψ_{bit} have to be verified in circuit simulation-based analyses. This already holds for moderate array yield requirements and relatively small array sizes as in Tab. 3.3. In reality, redundancy is introduced in SRAM arrays to account for potential bit cell failures and to relax the bit cell yield requirements. In this case, (3.16) cannot be used to relate bit cell and array yields but, for instance, the Poisson yield model provides an alternative [SR09, SR10].

To estimate the required very high bit cell yield values Ψ_{bit}, standard MC circuit simulations based on statistical device compact models with their parameters $\boldsymbol{X}$ require an enormous sample size N and hence a tremendous computational effort [ONB08, SR09, SR10]. The following sections introduce more efficient approaches: *worst-case point* (WCP)-based high yield estimation, *High-Sigma Monte Carlo* (HSMC), and *statistical blockade* (SB).

3.5.1 Worst Case Point Analysis

Also referred to as *most probable points* [SR10] or *most probable failure points* [ARA13], *worst-case points* (WCPs) are an approach for circuit analysis and optimization [AGW94]. A particular application is estimating high yield values, which makes them appropriate for SRAM bit cell analyses.

For bit cells, the WCP $\boldsymbol{x}_{\mathrm{j}}^{(\mathrm{WCP})}$ is the set of transistor level parameters $\boldsymbol{x}$ that fulfills two properties: (a) the corresponding bit cell performance parameter y_j exactly hits its specification boundary and (b) of all combinations of input parameters fulfilling (a), the set $\boldsymbol{x}_{\mathrm{j}}^{(\mathrm{WCP})}$ is the most probable. If the input parameters are modeled as a multivariate Gaussian RV $\boldsymbol{X}$ with independent components X_i, the WCP $\boldsymbol{x}_{\mathrm{j}}^{(\mathrm{WCP})}$ is closest to the nominal or mean point $\boldsymbol{\mu}_{\mathbf{X}}$ of all points fulfilling (a) [AGW94]. Recall that a multivariate Gaussian RV can be transformed into a multivariate Gaussian RV with uncorrelated components by *principal component analysis* (PCA), see App. A.1. The vector from the nominal point to the WCP is denoted *worst-case vector* (WCV), and its length is referred to as *worst-case distance* (WCD) β_j^{wc} [AGW94].

Determining a WCP $\boldsymbol{x}_{\mathrm{j}}^{(\mathrm{WCP})}$ is a non-linear optimization problem, which was proposed to be solved based on sequential quadratic programming [AGW94] to reduce the computational effort compared with MC simulations. With this point, the corresponding specification boundary of the bit cell performance parameter y_j can be approximately projected from the bit cell performance space $\mathbb{R}_{\mathbf{Y}}$ into the transistor level parameter space $\mathbb{R}_{\mathbf{X}}$. As illustrated in Fig. 3.13(a), the projected specification boundary is the hyperplane perpendicular to the WCV through the WCP $\boldsymbol{x}_{\mathrm{j}}^{(\mathrm{WCP})}$ [AGW94]. When this procedure is repeated for all specification boundaries, the region of acceptability can be approximated. As indicated in Fig. 3.13(b), the true region of acceptability may be overestimated or underestimated by this approach.

With properly scaled Gaussian transistor-level parameters with zero means and unit variances, $X_i \sim \mathrm{N}(0,1)$, the partial parametric bit cell yield $\Psi_{\mathrm{bit,j}}$ for the specification j

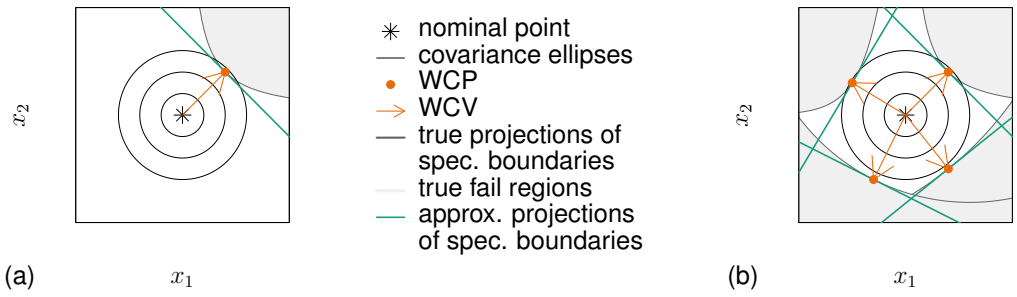

Fig. 3.13: Interpretation of WCPs; (a) first specification only; (b) all specifications; variation parameters X_i are assumed independent Gaussian; illustrations based on Fig. 3.2 in Sec. 3.1

Tab. 3.4: Example conversions between failure rate $\mathrm{FR}_{\mathrm{bit,j}} = 1 - \Psi_{\mathrm{bit,j}}$ and *worst-case distance* (WCD) β_j^{wc} applying (3.17), $\kappa = 1$

$\mathrm{FR}_{\mathrm{bit,j}}$	0.5	0.1587	$2.275e$-02	1.350-03	$3.167e$-05	$2.867e$-07	$9.866e$-10
β_j^{wc}	0	1	2	3	4	5	6

can be estimated from the corresponding WCD β_j^{wc} by applying the standard Gaussian CDF $\Phi(.)$ [AGW94],

$$\Psi_{\mathrm{bit,j}} \approx \Phi\left(\kappa_j \cdot \beta_j^{\mathrm{wc}}\right) \quad \text{with} \quad \kappa_j = \begin{cases} 1 & \text{nominal point fulfills spec. j} \\ -1 & \text{nominal point misses spec. j} \end{cases}. \tag{3.17}$$

Tab. 3.4 lists examples for the transformation (3.17). As results of simulation studies, WCDs of, for instance, $\beta_j^{\mathrm{wc}} = 5$ or $\beta_j^{\mathrm{wc}} = 6$ can be better distinguished than bit cell failure rates of $\mathrm{FR}_{\mathrm{bit,j}} = 2.867e$-$07$ or $\mathrm{FR}_{\mathrm{bit,j}} = 9.866e$-$10$. In addition, compared with MCs simulations, the much higher computational efficiency [AGW94] makes WCP-based SRAM bit cell analyses promising.

The approximate region of acceptability, such as in Fig. 3.13(b), allows efficient MC-based bit cell yield estimations [AGW94]. Transistor-level parameter samples $\tilde{\boldsymbol{X}}$ are generated and classified as pass or fail without any simulation. The overall bit cell yield Ψ_{bit} is simply the percentage of passing samples. Although the region of acceptability is approximated, this yield estimate can be considered fairly accurate [AGW94].

Due to their efficiency, WCP-based methods are applied in commercial tools. They offer efficient analyses and optimizations of, for instance, SRAM bit cells or analog cells based on multivariate Gaussian transistor-level parameters [AGW94, Liu14, Mun].

3.5.2 High-Sigma Monte Carlo and Statistical Blockade

Instead of approximating the region of acceptability, *High-Sigma Monte Carlo* (HSMC) [MBDG13] and *statistical blockade* (SB) [SWCR08, SR09, SR10] are methods that focus on the tails of bit cell performance parameter distributions to take extreme events into account. To introduce them, a particular performance parameter y is assumed to be modeled as a RV Y with its CDF $\phi_{\mathrm{Y}}(.)$. HSMC and SB are based on an initial N_a-sample MC circuit simulation, which evaluates a sample of transistor level parameters $\tilde{\boldsymbol{X}}^{(a)}$ to obtain a corresponding sample of bit cell performance parameters $\tilde{Y}^{(a)}$.

HSMC generates an ordering model from the initial samples $\tilde{\boldsymbol{X}}^{(a)}$ and $\tilde{Y}^{(a)}$. With this model, an additional and potentially very large sample of transistor-level parameters $\tilde{\boldsymbol{X}}^{(b*)}$ of size N_b can be evaluated to estimate the corresponding bit cell performance parameter sample $\tilde{Y}^{(b*)}$ without further circuit simulations [MBDG13]. The ranks of the bit cell performance parameter sample $\tilde{Y}^{(b*)}$ are used to re-order the transistor-level parameter sample $\tilde{\boldsymbol{X}}^{(b*)}$. This results in a transistor-level parameter sample $\tilde{\boldsymbol{X}}^{(b)}$ which, according to the model, yields an ordered[3] bit cell performance parameter sample $\tilde{\boldsymbol{Y}}^{(b)}$. The sample points in $\tilde{\boldsymbol{X}}^{(b)}$ are simulated in sequence, and these simulation results can be used to improve the ordering model. The analysis stops when sufficient information on the tail of the bit cell performance parameter distribution has been gained. For example, this is achieved if all N_{fail} sample points failing the specification have been simulated. The partial parametric yield for performance parameter y and the considered specification can then be derived as [MBDG13]

$$\Psi = 1 - \frac{N_{\text{fail}}}{N_b}. \tag{3.18}$$

Apparently, such an analysis can be applied to multiple bit cell performance parameters and specifications sequentially.

As an alternative, SB focuses on modeling the upper tail of a bit cell performance parameter distribution[4]. It is based on the conditional probability [Uo11], which defines the probability that the performance parameter y is smaller than a given value $y_1 > y_t$ by the equation [SR09, SR10]

$$\text{Prob}\left[Y < y_1\right] = \phi_{\text{Y}}(y_1) = \left[1 - \phi_{\text{Y}}(y_t)\right] \cdot \phi_{[\text{y}_\text{t}]}(y_1 - y_t) + \phi_{\text{Y}}(y_t). \tag{3.19}$$

In (3.19), y_t is an arbitrary threshold and $\phi_{[\text{y}_\text{t}]}(y_1 - y_t)$ is the probability of $y_t \leq Y < y_1$ under the condition $y_1 > y_t$. From the initial samples $\tilde{\boldsymbol{X}}^{(a)}$ and $\tilde{Y}^{(a)}$, SB estimates the bit cell performance parameter CDF $\widetilde{\phi}_{\text{Y}}(y)$, derives the thresholds y_t and $y_c < y_t$, and generates a classification or blockade filter using data mining techniques [SR07, SWCR08, SR09, SR10]. An initial sample of the size $N_a = 1000$ as well as the thresholds y_c and y_t such that $\widetilde{\phi}_{\text{Y}}(y_c) = 0.97$ and $\widetilde{\phi}_{\text{Y}}(y_t) = 0.99$ were proposed in

[3] Using the ranks in ascending order has to be used to examine a lower distribution tails; using the ranks in descending order has to be used to examine an upper distribution tail.

[4] However, it can also be applied to lower tails, which can be converted to upper tails by a multiplication with -1 [SR07].

[SR09, SR10]. The classification filter evaluates a potentially very large sample of transistor-level parameters $\tilde{\boldsymbol{X}}^{(b*)}$ by predicting the corresponding bit cell performance parameter sample $\tilde{Y}^{(b*)}$ without additional simulations. It flags sample points as important when the filter predicts the performance parameters y to exceed the threshold y_c, which is applied instead of y_t to account for potential model inaccuracies. The important points form the input parameter sample $\tilde{\boldsymbol{X}}^{(b)}$ of size N_{extr}, which is evaluated in further circuit simulations to obtain the sample $\tilde{Y}^{(b)}$ of extreme bit cell performance parameter values from comparably few simulations [SR07, SR09, SR10]. The sample $\tilde{Y}^{(b)}$ is mapped to the *generalized Pareto distribution* with its CDF [SR07, SR09, SR10]

$$\phi_{[y_t]}(y_1) = \phi(z) = \begin{cases} 1 - \left(1 - \zeta \cdot \frac{z}{\beta}\right)^{1/\zeta} & \zeta \neq 0 \\ 1 - \exp\left(-\frac{z}{\beta}\right) & \zeta = 0 \end{cases} \quad \text{with} \quad z = y_1 - t \geq 0. \tag{3.20}$$

The distribution parameters ζ and β can be tuned such that (3.20) well describes the sample $\tilde{Y}^{(b)}$. With these steps, the unknown quantities on the right-hand side of (3.19) can be determined. When an upper specification boundary is used as the threshold y_1 in (3.19), SB allows to estimate high partial parametric bit cell yields Ψ_{bit}. Compared with MC circuit simulations, SB can achieve $10\,X\ -100\,X$ speed ups [SR07, SR09]. The approach can be applied to multiple performance parameters and specifications sequentially with separate classification filters. Furthermore, its recursive application can yield about $10^4\,X$ speed ups compared with standard MC circuit simulations when estimating extremely high bit cell yield values Ψ_{bit} [SWCR08, SR10].

3.6 Analog Design and Behavioral Models

Although many signal processing tasks are performed by digital circuits, analog blocks will remain important parts of mixed-signal systems. Examples include amplifiers, filters, and converters for signal processing or stable oscillators and voltage as well as current sources as internal references [GR00]. In principle, analog circuit design comprises three basic steps, which are closely linked and accompanied by verification [GR00, RERB13], usually in terms of circuit simulations.

1. The basic structure of the circuit schematic is defined during topology selection. Devices and potential sub-cells are chosen, arranged, and connected. Topology

selection is usually based on the designer's experience but can be assisted by design tools [GR00, MBDG13, RDL+09].

2. The design parameters, mainly the device geometries, are tuned during circuit sizing [GR00, MBDG13, RERB13]. An initial phase and optimization phases can be distinguished to meet the analog block performance specifications over operating corners and to improve the parametric yield Ψ in the presence of variability. Optimization algorithms based on performance models [AGW94, GR00, MBDG13] and commercial tools [Cad14, Mun] allow automatic circuit sizing.
3. During layout generation, the sized devices are placed and routed to prepare mask generation and circuit manufacturing. While layouts of analog blocks have mainly been created manually, template-based [CFGR06, GR00], generator-based [RERB13], or constraint-based [SEGS11] automatic approaches have been evolved. Layout parasitics, mainly resistances and capacitances of interconnects, can be extracted and fed back to circuit sizing [CFGR06, RDL+09].

The complexity of state-of-the-art analog blocks is a challenge for analog circuit design. The transistor-level implementation of an analog block is difficult, and its verification by circuit simulations may be computationally very expensive. In common practice, both aspects can be tackled by the introduction of hierarchy: analog blocks are divided into analog cells, and analog cells may be further sub-divided [CFGR06, GR00, GP06, RERB13]. As an example, a particular analog block is a particle and radiation detector front-end. It can be implemented by instantiating several analog cells: a filter stage and operational amplifiers [GR00]. The operational amplifiers can be sub-divided into a differential input stage, an output stage, and potential interim amplification stages [CFGR06, Jun06, SEGS11, TS02]. Analog cells can be designed and verified stand-alone, before they are connected to form an analog block.

The hierarchical analysis of analog blocks benefits from higher-level models [GR00, GP06, Niz12]. Selected approaches to represent analog cells are briefly introduced in Tab. 3.5. From this selection of models with different purposes as well as levels of complexity and accuracy, performance models usually describe quantities that characterize an analog cell. In contrast, macro models as well as analog behavioral models can be used in efficient circuit simulations; functional models can be used in system-level simulations. The following discussions focus on analog behavioral models for two reasons. First, functional models better suit the abstraction of analog blocks, a hierarchical level, which is beyond the scope of this thesis. Second, macro models can be used as parts of behavioral models if properly implemented [JS06].

Tab. 3.5: Representations and models of analog cells [DGS03, Dur98, GR00, GP06, Vog12]

Representation	Explanation and Purpose
Transistor level circuits	For circuit implementation, active (transistors, diodes) and passive (resistors, capacitors, etc.) devices and their interconnections are defined in terms of schematics and layouts. Circuit simulators allow verification.
Macro models	Macro models, also referred to as equivalent circuits, are simplified circuit descriptions of analog cells. They are based on primitive devices and controlled voltage or current sources, which are available in a particular circuit simulator syntax. Macro models mimic the behavior of an analog cell for efficient verification using circuit simulators.
(Analog) Behavioral models	Behavioral models are implemented in an analog HDL, such as *VHDL-AMS* [VHD09a] or *Verilog-AMS* with its sub-set *Verilog-A* [Acc14]. They abstract analog cells or blocks by describing the relations between pin voltages and currents. They can replace the corresponding transistor level circuits to speed up circuit simulations.
Functional models	Functional models describe the outputs of analog cells or blocks based on their inputs in a signal-flow like manner. They can be used in system level analyses, for example to derive cell specifications from block specifications.
Performance models	Performance models approximate the performance parameters of analog cells $\boldsymbol{y}$, such as bandwidth or gain, as functions of input parameters $\boldsymbol{x}$. Hence, they describe particular quantities that characterize a circuit implementation. When the input parameters are design parameters $\boldsymbol{x}_\mathrm{d}$, such as transistor lengths and widths, performance models can be used for circuit sizing. To evaluate performance models in circuit simulations or system level simulations, they have to be transformed to behavioral models or functional models, however.

Fig. 3.14 illustrates the introduction of analog behavioral models to abstract a transistor level circuit. The behavioral model coefficients $\boldsymbol{y}$ are determined from circuit simulations that evaluate sets of transistor level parameters $\boldsymbol{x}$. Instantiating a behavioral model in a further simulation to obtain the analog block performance parameters $\boldsymbol{z}$ is much less computationally expensive than directly examining transistor level parameters $\boldsymbol{x}$ for the whole analog block. For single analog cells, evaluating analog behavioral models can be expected to yield $10\,X$ to $50\,X$ speed-ups compared with circuit simulations [Vog12].

To implement analog behavioral models in an analog HDL, numerical, symbolical, and analytical approaches can be applied and combined with macro models [JS06]. Some approaches and tools offer an automatic model derivation. In [MG05], for example, the transient behaviors of analog cells are mapped to compact non-linear differen-

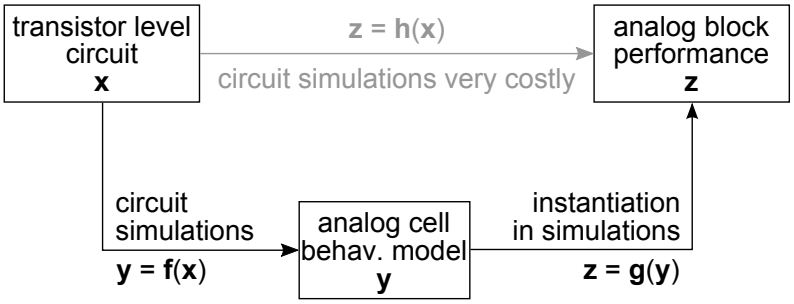

Fig. 3.14: Abstraction in analog design

tial equations applying a modification of genetic programming. Furthermore, [Fra] takes circuit structures into account to describe analog cells by systems of non-linear symbolic differential-algebraic equations. Subsequent model order reductions ensure reasonable model complexities. However, in general, the generation of analog behavioral models is a complex procedure, which consists of specification, definition, implementation, validation, and documentation [JS06]. Since analog behavioral modeling appears difficult and hard to automate, it seems to be rarely used in industrial designs [GR00, LBC+11b, Vog12].

Nevertheless, a variety of behavioral models is available for basic analog cells. For example, without considering a power supply pin and close to functional models, [Dur98] demonstrates analog behavioral models of various analog cells, for instance analog arithmetic, differentiators and integrators, or sample-and-hold circuits. Commercial design environments, such as [Cada], offer behavioral models of numerous basic analog cells without power supply pins. Based on an equivalent circuit, a behavioral model template of an operational amplifier is set up in [Sab16]. The automatic model calibration captures the dependency on operating conditions, for instance supply voltage and bias current. Their impact is included in a *Verilog-A* implementation by a table-based approach. Behavioral passband models of a low noise amplifier as well as a modulator and a demodulator are presented in [Che12]. These models take into account noise as a non-ideal effect. In contrast, [Vog12] demonstrates behavioral models of a programmable-gain amplifier and of an operational amplifier including their power supplies.

However, these model examples focus on the nominal behavior of analog cells. Extensions are required to capture variability from process variations and atomic-level fluctuations. Selected examples from literature are introduced in the following. Although not considering process variations, the behavioral model of a single photon

avalanche diode in [GMP11] demonstrates how the inherent statistical nature of the physics in this semiconductor structure can be described in *Verilog-A* syntax with Gaussian and exponential distributions. In [AKWW09, Ali09], a behavioral model of a voltage-controlled oscillator is discussed. It combines table models for design space exploration and Gaussian variations of the tabulated coefficients. Variability leads to an ensemble of cell behaviors, which can be enclosed by behavioral models with interval-valued parameters. These parameters can be found by support vector machine-based optimizations [KOB14]. Furthermore, linear [KC96, LBC+11a, SH10] or second-order [HHPP15, KLLH09] sensitivity information, which is similar to the SSTA for digital circuits in Sec. 3.4, can be applied to include variability information into behavioral models. That is, the coefficients y of behavioral models are approximated as linear or second-order functions of process parameters x, which may be arbitrarily distributed, for sampling-based model evaluations. Response surface approximations are more general and may improve the accuracy of this mapping [Mun]. Nevertheless, variability-aware analog behavioral models do not appear to be widely applied.

3.7 Conclusions

Variability has been and will remain an issue in IC design and analysis. Hence, multiple approaches address these effects and their impacts. The review in this chapter reveals that besides the still widely used corner-based approaches to tackle global variations, different methods to additionally capture local variations exists. In the state of the art, however, several issues can be detected.

1. In the different domains of variability modeling, different approaches are applied, which appear tailored to particular problems. Examples are the *backward propagation of variance* (BPV) to extract statistical device compact models, the *statistical static timing analysis* (SSTA) to verify the timing of digital circuits, and the high-yield estimation methods to analyze memories. Thus, none of these approaches can be applied universally.
2. Many approaches make simplifying assumptions, for instance linear approximations and Gaussian distributions. When non-Gaussian parameters are considered, the approaches are application-specific: *non-linear power models* (NPMs) in device compact modeling, quadratic mapping functions and non-Gaussian parameters in *statistical static timing analysis* (SSTA) or analog behavioral models, or generalized Pareto distributions in *statistical blockade* (SB).

3. For statistical device compact models, a standard on which model parameters capture variability has not been established yet. Instead, different authors propose different sets of parameters based on the underlying compact models and technologies. Due to potential confidentiality issues, it can be expected that not all variability-aware compact modeling approaches will be made public.
4. The missing standards for variability-aware device compact models and the potential confidentiality concerns may hinder a wide-spread application of analytical approximations of model coefficients y on transistor level parameters x, for instance to describe the variations in standard cell performance parameters or analog behavioral model coefficients. Furthermore, whether linear functions, higher-order polynomials, or response surface models in general, analytical approximations have to be treated carefully to prevent the introduction of inaccuracies.

In addition, some techniques that consider variability do not appear to be widely applied. In particular, this holds for variability-aware analog behavioral models. Furthermore, in digital design, corner-based *static timing analysis* (STA) combined with *on-chip variations* (OCV) approaches appears to be performed more frequently than *statistical static timing analysis* (SSTA). In the design community, there does not seem to be a common agreement on an optimum timing analysis method [TAU13].

Special attention should be paid to non-Gaussian distributions, which were considered difficult to model at a reasonable complexity, for instance in [LLP06]. Gaussian variations in characteristics of the manufacturing process, that is at the physical level, have to be expected to cause significantly non-Gaussian transistor level parameter distributions [LKBF09]. Their abstraction in the design flow will yield further non-Gaussian parameter distributions.

Consequently and conforming with [Mir12], advanced methods and tools for variability handling in IC design and analysis are required to supplement existing approaches. As a potential solution, a multivariate probabilistic modeling approach is developed in the subsequent chapter of this thesis. This approach addresses the issues listed above to consistently transfer variability information between different levels of abstraction in IC design and analysis.

4 A Probabilistic Model for Integrated Circuit Analysis

A variety of methods is available to address variability in different domains of IC design and analysis. According to their review in Chap. 3, missing universality, simplifying assumptions, and potential confidentiality concerns are their disadvantages. To improve the variability considerations in IC design, a novel modeling approach is introduced in this thesis. It is intended for solving the issues of the state of the art, which were listed in Sec. 3.7.

For this purpose, a statistical model is developed. In agreement with the conventions in [BCSS08], the denotation *probabilistic model* is used throughout this thesis. Variability is modeled by multivariate RVs, which take into account global and local variations and offer the following advantages over the state of the art.

1. Variability from process variations and atomic-level fluctuations is modeled by a unique approach, which can be applied in different domains and at different levels of abstraction. The approach can be applied to extend an arbitrary underlying model: standard models, such as device compact models or standard cell performance models, as well as custom models, such as bit cell performance models or analog behavioral models. In particular, selected or all parameters of the underlying model are treated as multivariate RVs. The scenarios in Tab. 4.1 outline selected application cases.
2. The approach is not based on analytical approximations that relate selected parameters on different levels of abstraction. Therefore, it avoids confidentiality concerns by not requiring explicit dependencies on transistor level parameters and potential inaccuracies by not assuming particular analytical mappings.
3. When the probabilistic model is adequately defined, it can simultaneously capture non-Gaussian and correlated parameters to achieve a high accuracy. The evaluation of such a model allows the joint analysis of multiple circuit performance parameters, for example digital circuit timing and power consumption, including their inter-dependencies.

Tab. 4.1: Selected scenarios for probabilistic modeling

Design Domain	Level of abstraction	Application examples
All	**Transistor level**	Extensions of nominal compact models of active or passive devices
Digital	**Gate level**	Extensions of arbitrary nominal standard cell models
Memory	**SRAM bit cell level**	SRAM bit cell models based on bit cell performance models
Analog	**Analog cell level**	Extensions of nominal behavioral models of analog cells

The essentials for probabilistic modeling are introduced in Fig. 4.1. The goal is to define a probabilistic model at an interim abstraction layer, which was considered a multivariate RV $\boldsymbol{Y}$ in Sec. 2.4 and Chap. 3. A proper statistical model, which is indicated by the RV $\boldsymbol{X}$, is assumed to be available at a lower level of abstraction. During characterization, random samples $\tilde{\boldsymbol{X}}_{\mathrm{char}}$ of this RV are generated and evaluated in MC simulations to obtain sample data $\tilde{\boldsymbol{Y}}_{\mathrm{char}}$. This complies with pointwise evaluations of the mapping $\mathrm{f}(.)$. According to its definition, the model is calibrated based on the characterization data $\tilde{\boldsymbol{Y}}_{\mathrm{char}}$. To analyze the impact of variability at a higher level of abstraction, which is indicated by the RV $\boldsymbol{Z}$ in Fig. 4.1, random samples $\tilde{\boldsymbol{Y}}$ are generated from the probabilistic model, and the pointwise evaluation of the mapping $\mathrm{g}(.)$ in dedicated analyses yields sample data $\tilde{\boldsymbol{Z}}$ to infer on the RV $\boldsymbol{Z}$. If required, this sequence can be repeated for an arbitrary number of abstraction levels.

From the aforementioned essentials, three tasks can be derived to properly establish a probabilistic model: model definition, characterization and model calibration, as well as generation of random sample. They will be addressed in Secs. 4.1–4.3.

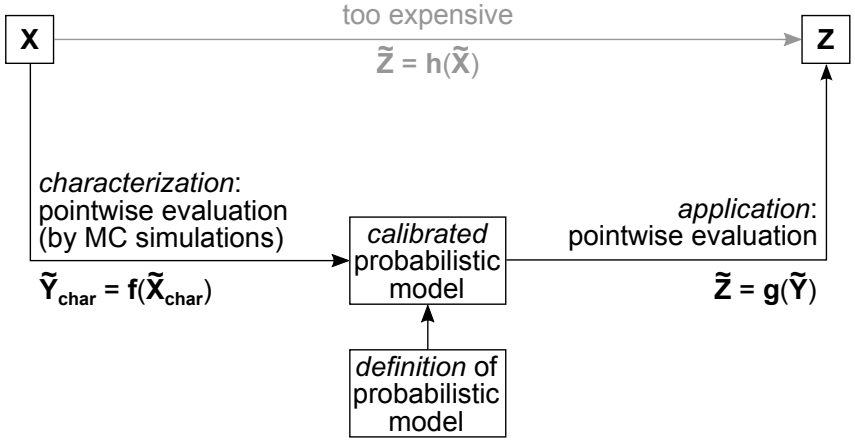

Fig. 4.1: Essentials for probabilistic modeling

4.1 Model Definition

4.1.1 Preliminaries

In Chap. 2, the combination of the marginal distributions of all random components Y_i and Spearman's rank correlation matrix $\mathbf{R}_{\mathbf{Y}}$ was outlined as a general and flexible approach to describe a multivariate RV $\boldsymbol{Y}$. Consequently, this description method is used as a basis to define probabilistic models in this thesis.

As a specific constraint in IC design, a finite set of circuit elements is available as basic building blocks at each level of abstraction. A circuit is realized by multiply instantiating these elements to meet the desired functionality. For example, at the transistor level, an inverter can be created by connecting one NFET instance and one PFET instance. Tab. 4.2 summarizes further scenarios, most of which will be considered in the application scenarios in Chap. 5.

For the sake of clarity, the following discussions are limited to two circuit elements A and B. Nevertheless, the modeling method scales to an arbitrary number of elements. The variability of element A is assumed to be captured by n_A random components, which can be described as an n_A-dimensional RV $\boldsymbol{Y}_{\mathbf{A}}$. Analogously, the variability of element B is assumed to be captured by n_B random components, which can be described as an n_B-dimensional RV $\boldsymbol{Y}_{\mathbf{B}}$.

At an arbitrary level of abstraction, a particular circuit consists of m_A instances of element A and m_B instances of element B, $A^{[1]}, ..., A^{[\mathrm{m_A}]}$ and $B^{[1]}, ..., B^{[\mathrm{m_B}]}$. The distribution of the RV $\boldsymbol{Y}_{\mathbf{A}}$ is assumed to apply to all instances of element A, which are then modeled by the RVs $\boldsymbol{Y}_{\mathbf{A}}^{[1]}, ..., \boldsymbol{Y}_{\mathbf{A}}^{[\mathrm{m_A}]}$. Analogously, the distribution of the RV $\boldsymbol{Y}_{\mathbf{B}}$ is

Tab. 4.2: Examples for circuits with their circuit elements and instances on selected levels of abstraction; N_{array} is the size of an SRAM array in bit

Level	Circuit example	Elements and Instances	Reference
Transistor level	**SRAM bit cell**	4 NFET instances, 2 PFET instances	Fig. 3.11(b)
Gate level	**AND4 circuit**	2 NAND2 instances, 1 NOR2 instance	Fig. 5.11(a)
	NAND4 circuit	2 NAND2 instances, 1 NOR2 instance, 1 inverter instance	Fig. 5.11(b)
	oscillators	k inverter instances, k NAND2 instances, or k NOR2 instances	Fig. 5.13
Bit cell level	**SRAM array**	N_{array} bit cell instances and control logic	Sec. 3.5

assumed to apply to all instances of element B, which are then modeled by the RVs $\boldsymbol{Y}_{\mathbf{B}}^{[1]}, ..., \boldsymbol{Y}_{\mathbf{B}}^{[\mathrm{m_B}]}$.

With these assumptions, the probabilistic model has to contain the descriptions of the RVs $\boldsymbol{Y}_{\mathbf{A}}$ and $\boldsymbol{Y}_{\mathbf{B}}$ including statistical inter-dependencies between arbitrary instances of the elements A and B.

4.1.2 Modeling Marginal Distributions

One task in probabilistic modeling is the description of the marginal distributions, that is of all components Y_{A_i} and Y_{B_j} of the RVs $\boldsymbol{Y}_{\mathbf{A}}$ and $\boldsymbol{Y}_{\mathbf{B}}$ above. For simplicity, they are represented by a univariate RV Y in this section. A variety of probability distributions is available to describe its distribution. Examples are the Gaussian distribution $\mathrm{N}(\mu, \sigma^2)$, the uniform distribution $\mathrm{U}(a, b)$, and the lognormal distribution $\mathrm{L}(m, \sigma_l)$, which were introduced in Sec. 2.1.2. While the lognormal distribution offers at least some flexibility in terms of distribution shape, which is characterized by the skew $\alpha_{\mathrm{Y},3}$ and the kurtosis $\alpha_{\mathrm{Y},4}$, Gaussian and uniform distributions have a fixed shape. The assumption of Gaussian distributions in the methods in Chap. 3 is often criticized since the fixed shape does not necessarily represent the underlying data with a high accuracy.

To increase the flexibility, a more general approach is required to model marginal distributions. The following core items can be identified as having to be addressed.

1. The probability distribution has to support a wide range of distribution shapes, that is it has to be flexible in terms of skew $\alpha_{\mathrm{Y},3}$ and kurtosis $\alpha_{\mathrm{Y},4}$.
2. A reasonable number of distribution coefficients is required to compactly store the probability distribution.
3. Preferably, an analytical quantile function $\phi_{\mathrm{Y}}^{-1}(.)$ should be available to support the efficient implementation of the sampling algorithm introduced in Sec. 2.3.2.

4.1.2.1 Choice of a Probability Distribution

As introduced in Sec. 2.1.1, the skew $\alpha_{\mathrm{Y},3}$ and the kurtosis $\alpha_{\mathrm{Y},4}$ measure the shape of the distribution of a univariate RV Y. A valid probability distribution satisfies the relation [KD00]

$$\alpha_{\mathrm{Y},4} > 1 + \alpha_{\mathrm{Y},3}^2, \tag{4.1}$$

Fig. 4.2: Examples of distribution shapes in terms of skew $\alpha_{Y,3}$ and kurtosis $\alpha_{Y,4}$; adapted from [KD00] with data of selected probability distributions from [FEHP11]; PDFs and CDF of selected distributions are shown in Fig. 4.3 in Sec. 4.1.2.2; impossible region derived from (4.1) shaded in dark gray; approximate range covered by *Generalized Lambda Distribution* (GLD) derived from (4.3) shaded in light gray; (a) linear scale; (b) logarithmic scale – note that symmetric distributions with $\alpha_{Y,3} = 0$ cannot be displayed in logarithmic scale

which is illustrated in Fig. 4.2. The skews and kurtoses of selected probability distributions are added to the graphs. While points indicate fixed-shape distributions, lines indicate distributions with some flexibility in their shapes. However, the illustrated distributions cover only a small range of possible distribution shapes. In contrast, this thesis aims at an approach that supports various distribution shapes by allowing flexible combinations of skews and kurtoses.

Piecewise linear CDFs $\phi_Y(.)$, PDFs $\varphi_Y(.)$, or quantile functions $\phi_Y^{-1}(.)$, which are based on pointwise definitions, are candidates to model marginal distributions. However, storing potentially large numbers of data points for a sufficient accuracy appears inefficient and hard to implement, for example in *process design kit*s (PDKs).

A variety of approaches to analytically describe probability distributions with arbitrary shapes was compiled in [Tad80]:

- the Fleishman transformation based on [Fle78],
- the Johnson system based on [Joh49],
- the Tadikamalla-Johnson system published in [TJ82],
- the *Generalized Lambda Distribution* (GLD) based on [RS74] and later discussed in [KD00],
- the Schmeiser-Deutsch system based on [SD77],
- and the Burr system of distributions based on [Bur42].
- Furthermore, the Pearson system of distributions [Pol79] is mentioned.

While more detailed information on these distributions and families of distributions can be found in App. B.1, they are rated below.

The Pearson system of distributions, the Johnson system, the Tadikamalla-Johnson system, and the Schmeiser-Deutsch system cover the entire plane of possible combinations of skews $\alpha_{\mathrm{Y},3}$ and kurtoses $\alpha_{\mathrm{Y},4}$. Nonetheless, like the generalized Pareto distribution, which was introduced with *statistical blockade* (SB) in (3.20), these distributions apply distinctions of cases in their analytical definitions [Joh49, Pol79, SD77, Tad80, TJ82]. This makes them difficult to implement into circuit analysis tools, for instance into circuit simulators, so that they are not considered suitable for simulation studies in this thesis. The other distributions and systems mentioned above cover a wide and nearly equivalent range of possible distribution shapes. The Burr system of distributions is dismissed for using several different functional forms [Bur42, Tad80].

The Fleishman transformation, which is applied to statistical device compact modeling [KDC+10], was introduced in (3.8) in Sec. 3.3. It describes a univariate RV Y by a third-order polynomial of a standard Gaussian RV $G \sim \mathrm{N}(0,1)$ with four coefficients [Fle78]. It was criticized for neither supporting all possible distribution shapes nor having a closed-form PDF $\varphi_{\mathrm{Y}}(.)$, CDF $\phi_{\mathrm{Y}}(.)$, or quantile function $\phi_{\mathrm{Y}}^{-1}(.)$ [Tad80]. The last fact hinders its efficient application in the sampling approach in Sec. 2.3.2. However, as introduced in (3.9) in Sec. 3.3, a dedicated approach can capture the correlations in multiple univariate RVs, which are modeled by the Fleishman transformation [HS99, KDC+10, VM83].

The GLD is defined by a quantile function $\phi_{\mathrm{Y}}^{-1}(.)$ with four coefficients [RS74, Tad80] so that it can be efficiently applied in the sampling algorithm in Sec. 2.3.2. It does not introduce any disadvantages compared with the Fleishman transformation by supporting nearly the same range of distribution shapes and by having the same number of coefficients. Indeed, the GLD addresses all identified core items to model marginal distributions. Hence, it will be used in this thesis and further investigated in the following section.

4.1.2.2 The Generalized Lambda Distribution

The *Generalized Lambda Distribution* (GLD) is a probability distribution that is capable of approximating a variety of distribution shapes. For a univariate RV Y, the

Generalized Lambda Distribution in parametrization after Ramberg and Schmeiser [RS74] (GLD-RS)[1] is defined by its quantile function [RS74, Tad80, KD00]

$$y = \phi_{\mathrm{Y}}^{-1}(u) = \lambda_1 + \frac{u^{\lambda_3} - (1-u)^{\lambda_4}}{\lambda_2} \qquad \text{with} \qquad 0 \leq u \leq 1. \tag{4.2}$$

With four distribution coefficients for location (λ_1), scale (λ_2), and shape (λ_3 and λ_4), the GLD-RS compactly characterizes the RV Y.

According to numerical experiments, a valid GLD-RS (4.2) yields skews $\alpha_{\mathrm{Y},3}$ and kurtoses $\alpha_{\mathrm{Y},4}$ that underlie the constraint [KD00]

$$\alpha_{\mathrm{Y},4} \geq 1.8 \cdot \alpha_{\mathrm{Y},3}^2 + 1.8. \tag{4.3}$$

The resulting wide range of GLD-RS shapes is illustrated in Fig. 4.2 in Sec. 4.1.2.1. Even though many theoretical distributions are included, there are potential combinations of skews $\alpha_{\mathrm{Y},3}$ and kurtoses $\alpha_{\mathrm{Y},4}$ that cannot be realized. An example is the chi-squared distribution with 1 degree of freedom with the skew $\alpha_{\mathrm{Y},3} = \sqrt{8}$ and the kurtosis $\alpha_{\mathrm{Y},4} = 15$ [FEHP11].

While the location coefficient λ_1 may be an arbitrary real number, restrictions apply to the coefficients for scale and shape: (4.2) yields a valid distribution if [RS74, KD00]

- $\lambda_3 \leq -1$ and $\lambda_4 \geq 1$;
- $\lambda_3 \geq 1$ and $\lambda_4 \leq -1$;
- $\lambda_3 \geq 0$ and $\lambda_4 \geq 0$;
- $\lambda_3 \leq 0$ and $\lambda_4 \leq 0$;
- $-1 < \lambda_3 < 0$ and $\lambda_4 > 1$ and $\dfrac{(1-\lambda_3)^{1-\lambda_3} \cdot (\lambda_4 - 1)^{\lambda_4 - 1}}{(\lambda_4 - \lambda_3)^{\lambda_4 - \lambda_3}} < -\dfrac{\lambda_3}{\lambda_4}$; or
- $-1 < \lambda_3 < 0$ and $\lambda_4 > 1$ and $\dfrac{(1-\lambda_4)^{1-\lambda_4} \cdot (\lambda_3 - 1)^{\lambda_3 - 1}}{(\lambda_3 - \lambda_4)^{\lambda_3 - \lambda_4}} < -\dfrac{\lambda_4}{\lambda_3}$.

Additionally, the shape coefficient λ_2 has to have the same sign as the numerator in the second summand in (4.2). Consequently, the regions for valid GLD-RSs defined by (4.2) are separated in the plane of the shape coefficients λ_3 and λ_4.

These restrictions on the coefficients λ_3 and λ_4 for valid GLD-RSs were criticized and led to the development of an alternative parametrization, the *Generalized Lambda*

[1] The denotation was introduced in [KM99] after J.S. Ramberg and B.W. Schmeiser, the authors of [RS74].

Distribution in parametrization after Freimer, Kollia, Mudholkar, and Lin [FKML88] (GLD-FKML)[2]. It is defined by the quantile function

$$y = \phi_{\mathrm{Y}}^{-1}(u) = \lambda_1 + \frac{\frac{u^{\lambda_3}-1}{\lambda_3} - \frac{(1-u)^{\lambda_4}-1}{\lambda_4}}{\lambda_2} \quad \text{with} \quad \lambda_2 > 0 \quad \text{and} \quad 0 \le u \le 1 \tag{4.4}$$

and supports a similar range of distribution shapes as the GLD-RS [FKML88, KM99]. If the gap between the GLD range and all possible distribution shapes causes problems in variability modeling for IC design and analysis, an alternative approach to model marginal distributions might have to be found.

The GLD-FKML yields valid probability distributions for arbitrary real location and shape coefficients λ_1, λ_3, and λ_4 [FKML88, KM99]. Since it overcomes the disadvantages of the GLD-RS, it will be used for the further considerations and denoted by $\mathrm{GLD}(\lambda_1, \lambda_2, \lambda_3, \lambda_4)$ in this thesis.

The support of the GLD-FKML can be derived from its definition in (4.4) by $y_{\min} = \phi_{\mathrm{Y}}^{-1}(0)$ and $y_{\max} = \phi_{\mathrm{Y}}^{-1}(1)$ [FKML88]:

$$y_{\min} = \begin{cases} \lambda_1 - \frac{1}{\lambda_2 \lambda_3} & : \lambda_3 > 0 \\ -\infty & : \lambda_3 \le 0 \end{cases} \quad \text{and} \quad y_{\max} = \begin{cases} \lambda_1 + \frac{1}{\lambda_2 \lambda_4} & : \lambda_4 > 0 \\ \infty & : \lambda_4 \le 0 \end{cases} \tag{4.5}$$

The GLD-FKML approximations of selected probability distributions in the PDF and CDF plots in Fig. 4.3 demonstrate the flexibility and accuracy that can be

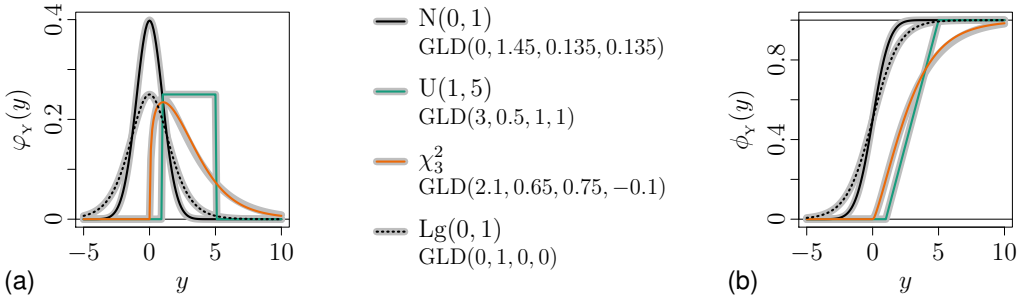

Fig. 4.3: GLD-FKML (defined by (4.4)) approximations of selected distributions (gray plots in background) with data from [FKML88, KM99]; (a) PDF; (b) CDF; χ^2_3: chi-squared distribution with 3 degrees of freedom; $\mathrm{Lg}(0, 1)$: standard logistic distribution

[2]The denotation was introduced in [KM99] after M. Freimer, G. Kollia, G.S. Mudholkar, and T. Lin, the authors of [FKML88]

achieved. One example in Fig. 4.3 is the standard Gaussian distribution $\mathrm{N}(0,1)$ with its GLD-FKML approximation $\mathrm{GLD}(0, 1.45, 0.135, 0.135)$ [FKML88][3]. By (4.5), this approximation is valid for $-5.1 \leq y \leq 5.1$. While this restriction will be negligible in most scenarios, it may be a disadvantage in special applications, which may require an alternative approach to model marginal distributions.

Nevertheless, marginal distributions will be modeled by GLD-FKMLs in this thesis because of their flexibility in terms of distribution shapes, their compactness, and their analytically available quantile functions.

4.1.3 Modeling Correlations

While the previous section introduced an approach to model marginal distributions, this section focuses on correlations. They are expressed in terms of Spearman's rank correlation coefficients, which were introduced in Sec. 2.2.4.

Recall that for the sake of simplicity, this discussion is limited to two circuit elements A and B, for which variability is modeled by n_A- and n_B-dimensional distributions. As introduced in Sec. 4.1.1, these elements are multiply instantiated in a circuit. An example with 3 instances of element A and 2 instances of element B is illustrated in Fig. 4.4. The variability of this particular circuit can be expressed by the RV

$$\boldsymbol{Y} = \left(\boldsymbol{Y}_{\mathbf{A}}^{[1]}, \boldsymbol{Y}_{\mathbf{A}}^{[2]}, \boldsymbol{Y}_{\mathbf{A}}^{[3]}, \boldsymbol{Y}_{\mathbf{B}}^{[1]}, \boldsymbol{Y}_{\mathbf{B}}^{[2]} \right), \tag{4.6}$$

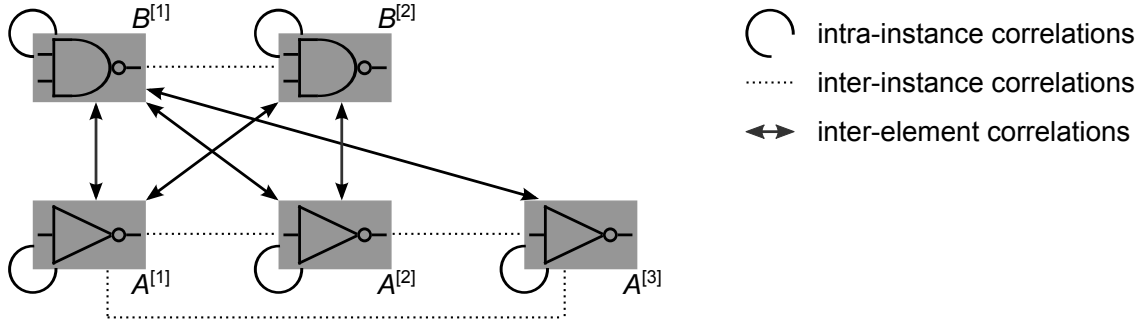

Fig. 4.4: Distinction of correlations in probabilistic modeling for circuit elements A and B; representing 3 inverter instances and 2 NAND2 instances at gate level for illustration purposes

[3] In [KM99], $\mathrm{GLD}(0, 1.45, 0.15, 0.15)$ was reported. However $\lambda_3 = \lambda_4 = 0.135$ from [FKML88] yields a slightly better approximation

which concatenates the multivariate RVs that describe the variability of each instance. The RVs $\boldsymbol{Y}_{\mathbf{A}}^{[1]}$, $\boldsymbol{Y}_{\mathbf{A}}^{[2]}$, and $\boldsymbol{Y}_{\mathbf{A}}^{[3]}$ model the variability of the instances of element A, and they follow the same distribution. Analogously, this applies to the RVs $\boldsymbol{Y}_{\mathbf{B}}^{[1]}$ and $\boldsymbol{Y}_{\mathbf{B}}^{[2]}$.

According to the discussion on the concatenation of multivariate RVs in Sec. 2.2.3, correlations within the RVs that model the variability of each instance as well as their inter-dependencies are required to describe a RV, such as the one defined by (4.6)[4]. Based on this fact and as illustrated in Fig. 4.4, correlations are divided into three categories in this thesis: *intra-instance correlations*, *inter-instance correlations*, *and inter-element correlations*.

Intra-instance correlations model the inter-dependencies within a particular instance. Mathematically, they are represented by the $(n_A \times n_A)$ Spearman's rank correlation matrix $\mathbf{R}_{\mathbf{A}}$ and the $(n_B \times n_B)$ Spearman's rank correlation matrix $\mathbf{R}_{\mathbf{B}}$. Spearman's rank correlation matrix $\mathbf{R}_{\mathbf{A}}$ applies to all instances of element A; Spearman's rank correlation matrix $\mathbf{R}_{\mathbf{B}}$ applies to all instances of element B. Note that the matrices $\mathbf{R}_{\mathbf{A}}$ and $\mathbf{R}_{\mathbf{B}}$ are symmetric.

Inter-instance correlations model the inter-dependencies between different instances of the same element. In IC design and analysis, they occur since all instances are equally effected by global variations but individually effected by local variations. Mathematically, inter-instance correlations are represented by the symmetric $(n_A \times n_A)$ matrix of Spearman's rank correlation coefficients $\mathbf{R}_{\mathbf{A},\mathbf{A}}$, which is assumed to equally apply to all combinations of instances of element A, and the symmetric $(n_B \times n_B)$ matrix of Spearman's rank correlation coefficients $\mathbf{R}_{\mathbf{B},\mathbf{B}}$, which is assumed to equally apply to all combinations of instances of element B.

Inter-element correlations model the inter-dependencies between instances of different elements. In IC design, they occur since global variation contributions equally effect all instances of all elements. Mathematically, inter-element correlations are represented by the $(n_A \times n_B)$ matrix of Spearman's rank correlation coefficients $\mathbf{R}_{\mathbf{A},\mathbf{B}}$, which is assumed to equally apply to all combinations of instances of the elements A and B.

As an example, the inverter and NAND2 instances in Fig. 4.4 are considered. Intra-instance correlations capture the fact that a faster inverter tends to have a higher leakage power. Inter-instance correlations capture the fact that if one inverter instance is fast, another inverter instance in this circuit tends to be fast as well due to global

[4]While Sec. 2.2.3 focused on covariance matrices, the principles can directly be transferred to Spearman's rank correlation matrices because (2.54) in Sec. 2.3.2 allows their conversion into each other.

variations. Inter-element correlations capture the fact that if an inverter instance is fast, a NAND2 instance tends to be fast as well due to global variations.

With intra-instance, inter-instance, and inter-element correlations, the Spearman's rank correlation matrix for the RV $\boldsymbol{Y}$ in (4.6) can be expressed as

$$\mathbf{R}_{\mathbf{Y}} = \begin{pmatrix} \mathbf{R}_{\mathbf{A}} & \mathbf{R}_{\mathbf{A},\mathbf{A}} & \mathbf{R}_{\mathbf{A},\mathbf{A}} & \mathbf{R}_{\mathbf{A},\mathbf{B}} & \mathbf{R}_{\mathbf{A},\mathbf{B}} \\ \mathbf{R}_{\mathbf{A},\mathbf{A}} & \mathbf{R}_{\mathbf{A}} & \mathbf{R}_{\mathbf{A},\mathbf{A}} & \mathbf{R}_{\mathbf{A},\mathbf{B}} & \mathbf{R}_{\mathbf{A},\mathbf{B}} \\ \mathbf{R}_{\mathbf{A},\mathbf{A}} & \mathbf{R}_{\mathbf{A},\mathbf{A}} & \mathbf{R}_{\mathbf{A}} & \mathbf{R}_{\mathbf{A},\mathbf{B}} & \mathbf{R}_{\mathbf{A},\mathbf{B}} \\ \mathbf{R}_{\mathbf{A},\mathbf{B}}^{\mathrm{T}} & \mathbf{R}_{\mathbf{A},\mathbf{B}}^{\mathrm{T}} & \mathbf{R}_{\mathbf{A},\mathbf{B}}^{\mathrm{T}} & \mathbf{R}_{\mathbf{B}} & \mathbf{R}_{\mathbf{B},\mathbf{B}} \\ \mathbf{R}_{\mathbf{A},\mathbf{B}}^{\mathrm{T}} & \mathbf{R}_{\mathbf{A},\mathbf{B}}^{\mathrm{T}} & \mathbf{R}_{\mathbf{A},\mathbf{B}}^{\mathrm{T}} & \mathbf{R}_{\mathbf{B},\mathbf{B}} & \mathbf{R}_{\mathbf{B}} \end{pmatrix}. \tag{4.7}$$

This approach neglects spatial local correlations, which might occur in IC design. In the future, they could be considered by definitions of intra-instance, inter-instance, and inter-element correlations, which are based on the physical locations of the corresponding instances.

In summary, to capture global and local variations and the resulting inter-dependencies, probabilistic models have to contain intra-instance, inter-instance, and inter-element correlations in terms of matrices of Spearman's rank correlation coefficients.

4.1.4 Summary

The proposed probabilistic models are based on instantiations of a finite set of circuit elements in IC design. The variability of each element is modeled by a multivariate distribution, which is applied to all instances of this element. To describe this distribution, the marginal distributions of all random components are modeled by the GLD-FKMLs, and Spearman's rank correlation matrices capture the intra-instance correlations. To capture the fact that global variations equally effect all instances, inter-instance correlations and inter-element correlations represent the inter-dependencies between different instances. By neglecting spatial local correlations, inter-instance correlations can be equally applied to all combinations of instances of a particular element and inter-element correlations can be equally applied to all combinations of instances of two different elements. The variability of a particular circuit can then be described by a multivariate RV that concatenates the RVs that model the variability of each instance. In contrast to the discussion above, this approach is not limited to two circuit elements. It scales naturally to an arbitrary number of elements and instances.

4.2 Characterization and Model Calibration

Characterization denotes the process of the generation of sample data $\tilde{\boldsymbol{Y}}_{\mathbf{char}}$ of a RV $\boldsymbol{Y}_{\mathbf{char}}$ to derive probabilistic models. *Model calibration* means to quantify the models, which will be split into the approximation of marginal distributions and the determination of Spearman's rank correlation coefficients and matrices in this section.

As for the model definition in Sec. 4.1, the discussion on characterization and model calibration is based on two circuit elements A and B for simplicity. The approach can be extended to further elements, however. For illustration purposes, App. B.3 demonstrates an example for the model calibration based on sample data.

4.2.1 Characterization

According to Fig. 4.1, characterization is based on simulations. They evaluate sample data $\tilde{\boldsymbol{X}}_{\mathbf{char}}$ of a RV $\boldsymbol{X}_{\mathbf{char}}$, which describes variability at a lower level of abstraction, to obtain sample data $\tilde{\boldsymbol{Y}}_{\mathbf{char}}$ of a RV $\boldsymbol{Y}_{\mathbf{char}}$ at a higher level of abstraction. Examples are device simulations to determine device compact models [CDM+10] or circuit simulations to determine standard cell performance parameters, such as delay times and power consumptions [DMD+07, PMM+07].

The definition of probabilistic models in Sec. 4.1 requires the characterization to provide data for each marginal distribution as well as information on intra-instance, inter-instance, and inter-element correlations to approximate statistical inter-dependencies. The RV

$$\boldsymbol{Y}_{\mathbf{char}} = \left(\boldsymbol{Y}_{\mathbf{A}}^{[1]}, \boldsymbol{Y}_{\mathbf{A}}^{[2]}, \boldsymbol{Y}_{\mathbf{B}}^{[1]}, \boldsymbol{Y}_{\mathbf{B}}^{[2]} \right) \tag{4.8}$$

with its Spearman's rank correlation matrix

$$\mathbf{R}_{\mathbf{Y}_{\mathrm{char}}} = \begin{pmatrix} \mathbf{R}_{\mathbf{A}} & \mathbf{R}_{\mathbf{A,A}} & \mathbf{R}_{\mathbf{A,B}} & \mathbf{R}_{\mathbf{A,B}} \\ \mathbf{R}_{\mathbf{A,A}} & \mathbf{R}_{\mathbf{A}} & \mathbf{R}_{\mathbf{A,B}} & \mathbf{R}_{\mathbf{A,B}} \\ \mathbf{R}_{\mathbf{A,B}}^{\mathrm{T}} & \mathbf{R}_{\mathbf{A,B}}^{\mathrm{T}} & \mathbf{R}_{\mathbf{B}} & \mathbf{R}_{\mathbf{B,B}} \\ \mathbf{R}_{\mathbf{A,B}}^{\mathrm{T}} & \mathbf{R}_{\mathbf{A,B}}^{\mathrm{T}} & \mathbf{R}_{\mathbf{B,B}} & \mathbf{R}_{\mathbf{B}} \end{pmatrix} \tag{4.9}$$

fulfills these requirements with the least possible complexity. In contrast, the RV $\left(\boldsymbol{Y}_{\mathbf{A}}^{[1]}, \boldsymbol{Y}_{\mathbf{B}}^{[1]}\right)$ is less complex, but it does not contain intra-instance correlations, which are expressed by the matrices $\mathbf{R}_{\mathbf{A},\mathbf{A}}$ and $\mathbf{R}_{\mathbf{B},\mathbf{B}}$ in (4.9). This result can easily be generalized to more than two elements: the characterization has to generate sample data for two instances per circuit element under consideration.

The data generation during characterization requires appropriate inputs in terms of sample data $\tilde{\boldsymbol{X}}_{\mathbf{char}}$: equal global but independent local variation parameters have to be applied to all instances, which are taken into account. Then, the characterization results in sample data $\tilde{\boldsymbol{Y}}_{\mathbf{char}} = \left(\tilde{\boldsymbol{Y}}_{\mathbf{A}}^{[1]}, \tilde{\boldsymbol{Y}}_{\mathbf{A}}^{[2]}, \tilde{\boldsymbol{Y}}_{\mathbf{B}}^{[1]}, \tilde{\boldsymbol{Y}}_{\mathbf{B}}^{[2]}\right)$ that represents the RV $\boldsymbol{Y}_{\mathbf{char}}$ in (4.8).

4.2.2 GLD-FKML Approximation of Marginal Distributions

The first step of model calibration is to approximate the marginal distributions. For this purpose, each component of the characterization sample data $\tilde{\boldsymbol{Y}}_{\mathbf{char}}$, has to be mapped to a GLD-FKML. For simplicity, the sample $\tilde{Y}$ of a univariate RV Y is assumed to represent an arbitrary random component of the characterization data $\tilde{\boldsymbol{Y}}_{\mathbf{char}}$.

As for all computations in this thesis, the open-source statistics software *R* [R C14] is used. Its dedicated package *gld* [KDK14] handles the GLD-RS and the GLD-FKML, and it provides the function *starship* for mapping sample data $\tilde{Y}$ to corresponding GLD coefficients. As discussed in Sec. 4.1, this thesis focuses on the GLD-FKML. Originally, the starship method has been applied to a RV Y, which could be transformed into a Gaussian RV $X_G \sim \mathrm{N}(\mu, \sigma^2)$ by a mapping $f_{Y-X_G}(.)$ and vice versa, such as the Johnson system of distributions, which is briefly introduced in App. B.1 [Owe88]. Therein, the mapping $f_{Y-X_G}(.)$ converts sample data $\tilde{Y}$ to sample data $\tilde{X}_G$, which is tested for Gaussianity by *Shapiro-Wilk* (SW) tests. An optimization tunes the coefficients of the mapping until the sample data $\tilde{X}_G$ is closest to Gaussian with respect to the SW tests. The resulting coefficients then describe the RV Y [Owe88].

Instead of transforming a Gaussian RV G, the GLD-FKML expresses the RV $Y \sim \mathrm{GLD}(\lambda_1, \lambda_2, \lambda_3, \lambda_4)$ as a transformation of a uniform RV $U \sim \mathrm{U}(0, 1)$. Therefore, the starship method needs to be adapted for an application to GLD-FKMLs. Numerically, (4.4) is inverted to convert a sample $\tilde{Y}$ of the RV Y into a sample $\tilde{U}$. The starship approach implemented in [KDK14] optimizes the GLD coefficients λ_1, λ_2, λ_3, and λ_4

until this numerical inversion yields sample data $\tilde{U}$, which are closest to uniform. The uniformity of the sample data $\tilde{U}$ is tested by Anderson-Darling tests [AD52].

The *R* function *FitGLD* has been implemented for this thesis to improve the performance when approximating large samples $\tilde{Y}$ by GLD-FKMLs. The respective source code is appended in App. B.2. If the sample size N is sufficiently small, $N \leq 100$, the starship method from [KDK14] is used. Otherwise, the starship method from [KDK14] determines the GLD-FKML coefficients for the empirical quantiles $\widetilde{\phi}_{\mathrm{Y}}^{-1}(0.01)$, $\widetilde{\phi}_{\mathrm{Y}}^{-1}(0.02)$, ..., $\widetilde{\phi}_{\mathrm{Y}}^{-1}(0.99)$, which are estimated from the sample data $\tilde{Y}$. These coefficients are then used as the starting point for an optimization, which adapts the coefficients of the GLD-FKML quantile function $\phi_{\mathrm{Y}}^{-1}(.)$ to minimize its deviations from the empirical quantile function $\widetilde{\phi}_{\mathrm{Y}}^{-1}(.)$. Although this thesis focuses on applications of the GLD-FKML, the implemented function *FitGLD* supports both GLD-RS and GLD-FKML.

These principles can be sequentially applied to map all random components of multivariate sample data to GLD-FKMLs, that is to approximate all marginal distributions. The assumption that all instances of a particular circuit element can be described by the same distribution implicates redundancy in the characterization sample data $\tilde{\boldsymbol{Y}}_{\mathbf{char}}$, which contains empirical data of two instances per element. To make best use of the available information, the *R* function *FitGLD* is sequentially applied to interim univariate sample data: the component by component union of the i-th components of the sample data $\tilde{\boldsymbol{Y}}_{\mathbf{A}}^{[1]}$ and $\tilde{\boldsymbol{Y}}_{\mathbf{A}}^{[2]}$ for $i \in \{1, 2, ..., n_A\}$ as well as the component by component union of the j-th components of the sample data $\tilde{\boldsymbol{Y}}_{\mathbf{B}}^{[1]}$ and $\tilde{\boldsymbol{Y}}_{\mathbf{B}}^{[2]}$ for $j \in \{1, 2, ..., n_B\}$.

4.2.3 Determination of Correlations

The second step of model calibration is to capture the correlations. From the characterization sample data $\tilde{\boldsymbol{Y}}_{\mathbf{char}}$, Spearman's rank correlation coefficients can be estimated by (2.51) in Sec. 2.2.4 and summarized in matrix form:

$$\widetilde{\mathbf{R}}_{\mathbf{Y_{char}}} = \begin{pmatrix} \widetilde{\mathbf{R}}_{\boldsymbol{A}^{[1]}} & \widetilde{\mathbf{R}}_{\boldsymbol{A}^{[1]},\boldsymbol{A}^{[2]}} & \widetilde{\mathbf{R}}_{\boldsymbol{A}^{[1]},\boldsymbol{B}^{[1]}} & \widetilde{\mathbf{R}}_{\boldsymbol{A}^{[1]},\boldsymbol{B}^{[2]}} \\ \widetilde{\mathbf{R}}_{\boldsymbol{A}^{[2]},\boldsymbol{A}^{[1]}} & \widetilde{\mathbf{R}}_{\boldsymbol{A}^{[2]}} & \widetilde{\mathbf{R}}_{\boldsymbol{A}^{[2]},\boldsymbol{B}^{[1]}} & \widetilde{\mathbf{R}}_{\boldsymbol{A}^{[2]},\boldsymbol{B}^{[2]}} \\ \widetilde{\mathbf{R}}_{\boldsymbol{B}^{[1]},\boldsymbol{A}^{[1]}} & \widetilde{\mathbf{R}}_{\boldsymbol{B}^{[1]},\boldsymbol{A}^{[2]}} & \widetilde{\mathbf{R}}_{\boldsymbol{B}^{[1]}} & \widetilde{\mathbf{R}}_{\boldsymbol{B}^{[1]},\boldsymbol{B}^{[2]}} \\ \widetilde{\mathbf{R}}_{\boldsymbol{B}^{[2]},\boldsymbol{A}^{[1]}} & \widetilde{\mathbf{R}}_{\boldsymbol{B}^{[2]},\boldsymbol{A}^{[2]}} & \widetilde{\mathbf{R}}_{\boldsymbol{B}^{[2]},\boldsymbol{B}^{[1]}} & \widetilde{\mathbf{R}}_{\boldsymbol{B}^{[2]}} \end{pmatrix}. \tag{4.10}$$

This form can only be obtained under the assumption that all instances of a particular element can be described by the same distribution.

To evaluate all information in the sample data $\widetilde{\boldsymbol{Y}}_{\mathbf{char}}$, intra-instance, inter-instance, and inter-element correlations are derived from all available instances:

$$\begin{aligned}
\mathbf{R}_{\mathbf{A}} &= \frac{1}{2}\left(\widetilde{\mathbf{R}}_{\boldsymbol{A}^{[1]}} + \widetilde{\mathbf{R}}_{\boldsymbol{A}^{[2]}}\right) \text{ and} \\
\mathbf{R}_{\mathbf{B}} &= \frac{1}{2}\left(\widetilde{\mathbf{R}}_{\boldsymbol{B}^{[1]}} + \widetilde{\mathbf{R}}_{\boldsymbol{B}^{[2]}}\right); \qquad (4.11) \\
\mathbf{R}_{\mathbf{A},\mathbf{A}} &= \frac{1}{2}\left(\widetilde{\mathbf{R}}_{\boldsymbol{A}^{[1]},\boldsymbol{A}^{[2]}} + \widetilde{\mathbf{R}}_{\boldsymbol{A}^{[2]},\boldsymbol{A}^{[1]}}\right) \text{ and} \\
\mathbf{R}_{\mathbf{B},\mathbf{B}} &= \frac{1}{2}\left(\widetilde{\mathbf{R}}_{\boldsymbol{B}^{[1]},\boldsymbol{B}^{[2]}} + \widetilde{\mathbf{R}}_{\boldsymbol{B}^{[2]},\boldsymbol{B}^{[1]}}\right) \text{; as well as} \qquad (4.12) \\
\mathbf{R}_{\mathbf{A},\mathbf{B}} &= \frac{1}{4}\left(\widetilde{\mathbf{R}}_{\boldsymbol{A}^{[1]},\boldsymbol{B}^{[1]}} + \widetilde{\mathbf{R}}_{\boldsymbol{A}^{[1]},\boldsymbol{B}^{[2]}} + \widetilde{\mathbf{R}}_{\boldsymbol{A}^{[2]},\boldsymbol{B}^{[1]}} + \widetilde{\mathbf{R}}_{\boldsymbol{A}^{[2]},\boldsymbol{B}^{[2]}}\right). \qquad (4.13)
\end{aligned}$$

Estimating Spearman's rank correlation matrix $\widetilde{\mathbf{R}}_{\mathbf{Y}_{\mathbf{char}}}$ of the RV $\boldsymbol{Y}_{\mathbf{char}}$ and applying (4.11)–(4.13) can easily be implemented in the statistics software *R* . The calculations are followed by significance tests, which were introduced in Sec. 2.2.4, to waive insignificant correlations.

4.3 Generation of Random Samples

According to their definition in Sec. 4.1, probabilistic models consist of multivariate RVs that describe the variability of all instances of element A and multivariate RVs that describe the variability of all instances of element B. They combine Spearman's rank correlation matrices for intra-instance correlations and GLD-FKML approximations of the marginal distributions of all random components. In addition, inter-instance and inter-element rank correlation matrices capture the inter-dependencies between instances of the same element and between instances of different elements.

To utilize these information in a circuit analysis step, the generation of random samples from probabilistic models is an apparent approach. In this section, two sampling approaches are presented and compared to each other with respect to accuracy and performance. As in the previous sections, the discussion is limited to two circuit elements A and B for simplicity. Nevertheless, the principles scale to an arbitrary number of elements.

4.3.1 Conventional Approach

The conventional approach for random sampling directly applies the four-step algorithm in Sec. 2.3.2: the conversion of Spearman's rank correlation matrix $\mathbf{R}_{\mathbf{Y}}$ into a covariance matrix $\mathbf{\Sigma}_{\mathbf{G}}$, the generation of correlated Gaussian samples $\tilde{\boldsymbol{G}}$, the transformation into uniform components $\tilde{\boldsymbol{U}}$, and the transformation into the target sample $\tilde{\boldsymbol{Y}}$. By the standard Gaussian CDF and the quantile functions of the marginal distributions, the transformations into uniform samples $\tilde{\boldsymbol{U}}$ and into the target samples $\tilde{\boldsymbol{Y}}$ in the steps 3 and 4 of this algorithm are uncomplicated.

To analyze a particular circuit, a circuit-specific RV $\boldsymbol{Y}$, which models the variability of the circuit under consideration, has to be defined with its rank correlation matrix $\mathbf{R}_{\mathbf{Y}}$ and the GLD-FKML descriptions of the marginal distributions. In general, a circuit consists of m_A instances of element A and m_B instances of element B, so that this RV reads

$$\boldsymbol{Y} = \left(\overbrace{\boldsymbol{Y}_{\mathbf{A}}^{[1]}, \boldsymbol{Y}_{\mathbf{A}}^{[2]}, \ldots, \boldsymbol{Y}_{\mathbf{A}}^{[\mathrm{m_A}]}}^{m_A \text{ instances of element } A}, \overbrace{\boldsymbol{Y}_{\mathbf{B}}^{[1]}, \boldsymbol{Y}_{\mathbf{B}}^{[2]}, \ldots, \boldsymbol{Y}_{\mathbf{B}}^{[\mathrm{m_B}]}}^{m_B \text{ instances of element } B} \right) . \tag{4.14}$$

The corresponding GLD-FKML coefficients from the probabilistic models describe the marginal distributions of all components. From the matrices for intra-instance, inter-instance, and inter-element correlations, the circuit-specific Spearman's rank correlation matrix

$$\mathbf{R}_{\mathbf{Y}} = \left(\begin{array}{cccc|cccc} \overbrace{\mathbf{R}_{\mathbf{A}} & \mathbf{R}_{\mathbf{A,A}} & \cdots & \mathbf{R}_{\mathbf{A,A}}}^{m_A \text{ instances of element } A} & \overbrace{\mathbf{R}_{\mathbf{A,B}} & \mathbf{R}_{\mathbf{A,B}} & \cdots & \mathbf{R}_{\mathbf{A,B}}}^{m_B \text{ instances of element } B} \\ \mathbf{R}_{\mathbf{A,A}} & \mathbf{R}_{\mathbf{A}} & \cdots & \mathbf{R}_{\mathbf{A,A}} & \mathbf{R}_{\mathbf{A,B}} & \mathbf{R}_{\mathbf{A,B}} & \cdots & \mathbf{R}_{\mathbf{A,B}} \\ \vdots & \vdots & \ddots & \vdots & \vdots & \vdots & \ddots & \vdots \\ \mathbf{R}_{\mathbf{A,A}} & \mathbf{R}_{\mathbf{A,A}} & \cdots & \mathbf{R}_{\mathbf{A}} & \mathbf{R}_{\mathbf{A,B}} & \mathbf{R}_{\mathbf{A,B}} & \cdots & \mathbf{R}_{\mathbf{A,B}} \\ \hline \mathbf{R}_{\mathbf{A,B}}^{\mathrm{T}} & \mathbf{R}_{\mathbf{A,B}}^{\mathrm{T}} & \cdots & \mathbf{R}_{\mathbf{A,B}}^{\mathrm{T}} & \mathbf{R}_{\mathbf{B}} & \mathbf{R}_{\mathbf{B,B}} & \cdots & \mathbf{R}_{\mathbf{B,B}} \\ \mathbf{R}_{\mathbf{A,B}}^{\mathrm{T}} & \mathbf{R}_{\mathbf{A,B}}^{\mathrm{T}} & \cdots & \mathbf{R}_{\mathbf{A,B}}^{\mathrm{T}} & \mathbf{R}_{\mathbf{B,B}} & \mathbf{R}_{\mathbf{B}} & \cdots & \mathbf{R}_{\mathbf{B,B}} \\ \vdots & \vdots & \ddots & \vdots & \vdots & \vdots & \ddots & \vdots \\ \mathbf{R}_{\mathbf{A,B}}^{\mathrm{T}} & \mathbf{R}_{\mathbf{A,B}}^{\mathrm{T}} & \cdots & \mathbf{R}_{\mathbf{A,B}}^{\mathrm{T}} & \mathbf{R}_{\mathbf{B,B}} & \mathbf{R}_{\mathbf{B,B}} & \cdots & \mathbf{R}_{\mathbf{B}} \end{array} \right) \begin{array}{l} \left. \begin{array}{c} \\ \\ \\ \\ \end{array} \right\} m_A \text{ instances of element } A \\ \left. \begin{array}{c} \\ \\ \\ \\ \end{array} \right\} m_B \text{ instances of element } B \end{array} \tag{4.15}$$

has to be constructed as an important input to the sampling algorithm in Sec. 2.3.2.

In step 1 of the sampling algorithm in Sec. 2.3.2, the element by element transformation (2.54) is applied to determine the covariance matrix

$$\boldsymbol{\Sigma}_{\mathbf{G}} = \left(\begin{array}{cccc|cccc} \overbrace{\boldsymbol{\Sigma}_{\mathbf{A}} & \boldsymbol{\Sigma}_{\mathbf{A,A}} & \cdots & \boldsymbol{\Sigma}_{\mathbf{A,A}}}^{m_A \text{ instances of element } A} & \overbrace{\boldsymbol{\Sigma}_{\mathbf{A,B}} & \boldsymbol{\Sigma}_{\mathbf{A,B}} & \cdots & \boldsymbol{\Sigma}_{\mathbf{A,B}}}^{m_B \text{ instances of element } B} \\ \boldsymbol{\Sigma}_{\mathbf{A,A}} & \boldsymbol{\Sigma}_{\mathbf{A}} & \cdots & \boldsymbol{\Sigma}_{\mathbf{A,A}} & \boldsymbol{\Sigma}_{\mathbf{A,B}} & \boldsymbol{\Sigma}_{\mathbf{A,B}} & \cdots & \boldsymbol{\Sigma}_{\mathbf{A,B}} \\ \vdots & \vdots & \ddots & \vdots & \vdots & \vdots & \ddots & \vdots \\ \boldsymbol{\Sigma}_{\mathbf{A,A}} & \boldsymbol{\Sigma}_{\mathbf{A,A}} & \cdots & \boldsymbol{\Sigma}_{\mathbf{A}} & \boldsymbol{\Sigma}_{\mathbf{A,B}} & \boldsymbol{\Sigma}_{\mathbf{A,B}} & \cdots & \boldsymbol{\Sigma}_{\mathbf{A,B}} \\ \hline \boldsymbol{\Sigma}_{\mathbf{A,B}}^{\mathrm{T}} & \boldsymbol{\Sigma}_{\mathbf{A,B}}^{\mathrm{T}} & \cdots & \boldsymbol{\Sigma}_{\mathbf{A,B}}^{\mathrm{T}} & \boldsymbol{\Sigma}_{\mathbf{B}} & \boldsymbol{\Sigma}_{\mathbf{B,B}} & \cdots & \boldsymbol{\Sigma}_{\mathbf{B,B}} \\ \boldsymbol{\Sigma}_{\mathbf{A,B}}^{\mathrm{T}} & \boldsymbol{\Sigma}_{\mathbf{A,B}}^{\mathrm{T}} & \cdots & \boldsymbol{\Sigma}_{\mathbf{A,B}}^{\mathrm{T}} & \boldsymbol{\Sigma}_{\mathbf{B,B}} & \boldsymbol{\Sigma}_{\mathbf{B}} & \cdots & \boldsymbol{\Sigma}_{\mathbf{B,B}} \\ \vdots & \vdots & \ddots & \vdots & \vdots & \vdots & \ddots & \vdots \\ \boldsymbol{\Sigma}_{\mathbf{A,B}}^{\mathrm{T}} & \boldsymbol{\Sigma}_{\mathbf{A,B}}^{\mathrm{T}} & \cdots & \boldsymbol{\Sigma}_{\mathbf{A,B}}^{\mathrm{T}} & \boldsymbol{\Sigma}_{\mathbf{B,B}} & \boldsymbol{\Sigma}_{\mathbf{B,B}} & \cdots & \boldsymbol{\Sigma}_{\mathbf{B}} \end{array} \right) \begin{array}{l} \left. \begin{array}{c} \\ \\ \\ \\ \end{array} \right\} m_A \text{ instances of element } A \\ \left. \begin{array}{c} \\ \\ \\ \\ \end{array} \right\} m_B \text{ instances of element } B \end{array} \tag{4.16}$$

from Spearman's rank correlation matrix $\mathbf{R}_{\mathbf{Y}}$. Alternatively, the covariance matrix $\boldsymbol{\Sigma}_{\mathbf{G}}$ can directly be constructed from the previously transformed intra-instance, inter-instance, and inter-element rank correlation matrices $\boldsymbol{\Sigma}_{\mathbf{A}}$, $\boldsymbol{\Sigma}_{\mathbf{B}}$, $\boldsymbol{\Sigma}_{\mathbf{A,A}}$, $\boldsymbol{\Sigma}_{\mathbf{B,B}}$ and $\boldsymbol{\Sigma}_{\mathbf{A,B}}$.

In Step 2 of the sampling algorithm in Sec. 2.3.2, random samples have to be generated from a multivariate Gaussian RV $\boldsymbol{G} \sim \mathrm{N}(\mathbf{0}, \boldsymbol{\Sigma}_{\mathbf{G}})$. As introduced in Sec. 2.3.1, this requires a decomposition of the covariance matrix $\boldsymbol{\Sigma}_{\mathbf{G}} = \mathbf{L}_{\mathbf{G}} \mathbf{L}_{\mathbf{G}}^{\mathrm{T}}$, for instance its Cholesky decomposition.

Three related disadvantages make this sampling approach impractical. First, the RV $\boldsymbol{Y}$ is specific for a particular circuit under consideration. That is, it has to be redefined after each change in the design of this circuit. Second, the dimensionality of the RV $\boldsymbol{Y}$ rapidly grows with the number of instances per element and with the number of components in the RVs $\boldsymbol{Y}_{\mathbf{A}}^{[\mathrm{k}]}$, $k = 1, ..., n_A$ and $\boldsymbol{Y}_{\mathbf{B}}^{[\mathrm{l}]}$, $l = 1, ..., n_B$. Third, especially for complex circuits with many instances, the decomposition of the covariance matrix $\boldsymbol{\Sigma}_{\mathbf{G}}$ causes significant computational costs.

4.3.2 Improved Approach

To overcome the disadvantages of the conventional sampling approach in Sec. 4.3.1, an alternative method is proposed in this section.

Assuming that a circuit contains m instances of element A and m instances of element B, the RV $\boldsymbol{Y}^*$ that models the variability of this particular circuit can be specified as

$$\boldsymbol{Y}^* = \left(\overbrace{\boldsymbol{Y}_{\mathbf{A}}^{[1]}, \boldsymbol{Y}_{\mathbf{B}}^{[1]}}^{\substack{1^{st}\text{ instance}\\ \text{per element}}} \quad , \quad \overbrace{\boldsymbol{Y}_{\mathbf{A}}^{[2]}, \boldsymbol{Y}_{\mathbf{B}}^{[2]}}^{\substack{2^{nd}\text{ instance}\\ \text{per element}}} \quad , \quad \dots \quad , \quad \overbrace{\boldsymbol{Y}_{\mathbf{A}}^{[\mathrm{m}]}, \boldsymbol{Y}_{\mathbf{B}}^{[\mathrm{m}]}}^{\substack{m^{th}\text{ instance}\\ \text{per element}}} \right). \tag{4.17}$$

Thus, random samples $\tilde{\boldsymbol{G}}^*$ of the multivariate Gaussian RV

$$\boldsymbol{G}^* = \left(\overbrace{\boldsymbol{G}_{\mathbf{A}}^{[1]}, \boldsymbol{G}_{\mathbf{B}}^{[1]}}^{\substack{1^{st}\text{ instance}\\ \text{per element}}} \quad , \quad \overbrace{\boldsymbol{G}_{\mathbf{A}}^{[2]}, \boldsymbol{G}_{\mathbf{B}}^{[2]}}^{\substack{2^{nd}\text{ instance}\\ \text{per element}}} \quad , \quad \dots \quad , \quad \overbrace{\boldsymbol{G}_{\mathbf{A}}^{[\mathrm{m}]}, \boldsymbol{G}_{\mathbf{B}}^{[\mathrm{m}]}}^{\substack{m^{th}\text{ instance}\\ \text{per element}}} \right) \sim \mathbf{N}(\mathbf{0}, \boldsymbol{\Sigma}_{\mathbf{G}^*}) \tag{4.18}$$

have to be generated in Step 2 of the algorithm in Sec. 2.3.2. Its covariance matrix

$$\boldsymbol{\Sigma}_{\mathbf{G}^*} = \left(\begin{array}{cccccc} \overbrace{\phantom{\boldsymbol{\Sigma}_{\mathbf{A}}}}^{\substack{1^{st}\text{ instance}\\ \text{per element}}} & & \overbrace{\phantom{\boldsymbol{\Sigma}_{\mathbf{A}}}}^{\substack{2^{nd}\text{ instance}\\ \text{per element}}} & & & \overbrace{\phantom{\boldsymbol{\Sigma}_{\mathbf{A}}}}^{\substack{m^{th}\text{ instance}\\ \text{per element}}} \\ \boldsymbol{\Sigma}_{\mathbf{A}} & \boldsymbol{\Sigma}_{\mathbf{A,B}} & \boldsymbol{\Sigma}_{\mathbf{A,A}} & \boldsymbol{\Sigma}_{\mathbf{A,B}} & \cdots & \boldsymbol{\Sigma}_{\mathbf{A,A}} & \boldsymbol{\Sigma}_{\mathbf{A,B}} \\ \boldsymbol{\Sigma}_{\mathbf{A,B}}^{\mathrm{T}} & \boldsymbol{\Sigma}_{\mathbf{B}} & \boldsymbol{\Sigma}_{\mathbf{A,B}}^{\mathrm{T}} & \boldsymbol{\Sigma}_{\mathbf{B,B}} & \cdots & \boldsymbol{\Sigma}_{\mathbf{A,B}}^{\mathrm{T}} & \boldsymbol{\Sigma}_{\mathbf{B,B}} \\ \boldsymbol{\Sigma}_{\mathbf{A,A}} & \boldsymbol{\Sigma}_{\mathbf{A,B}} & \boldsymbol{\Sigma}_{\mathbf{A}} & \boldsymbol{\Sigma}_{\mathbf{A,B}} & \cdots & \boldsymbol{\Sigma}_{\mathbf{A,A}} & \boldsymbol{\Sigma}_{\mathbf{A,B}} \\ \boldsymbol{\Sigma}_{\mathbf{A,B}}^{\mathrm{T}} & \boldsymbol{\Sigma}_{\mathbf{B,B}} & \boldsymbol{\Sigma}_{\mathbf{A,B}}^{\mathrm{T}} & \boldsymbol{\Sigma}_{\mathbf{B}} & \cdots & \boldsymbol{\Sigma}_{\mathbf{A,B}}^{\mathrm{T}} & \boldsymbol{\Sigma}_{\mathbf{B,B}} \\ \vdots & \vdots & \vdots & \vdots & \ddots & \vdots & \vdots \\ \boldsymbol{\Sigma}_{\mathbf{A,A}} & \boldsymbol{\Sigma}_{\mathbf{B,B}} & \boldsymbol{\Sigma}_{\mathbf{A,A}} & \boldsymbol{\Sigma}_{\mathbf{B,B}} & \cdots & \boldsymbol{\Sigma}_{\mathbf{A}} & \boldsymbol{\Sigma}_{\mathbf{A,B}} \\ \boldsymbol{\Sigma}_{\mathbf{A,B}}^{\mathrm{T}} & \boldsymbol{\Sigma}_{\mathbf{B,B}} & \boldsymbol{\Sigma}_{\mathbf{A,B}}^{\mathrm{T}} & \boldsymbol{\Sigma}_{\mathbf{B,B}} & \cdots & \boldsymbol{\Sigma}_{\mathbf{A,B}}^{\mathrm{T}} & \boldsymbol{\Sigma}_{\mathbf{B}} \end{array} \right) \tag{4.19}$$

$$= \left(\begin{array}{ccccc} \boldsymbol{\Sigma}_{\mathbf{i}} & \boldsymbol{\Sigma}_{\mathbf{ii}} & \cdots & \boldsymbol{\Sigma}_{\mathbf{ii}} \\ \boldsymbol{\Sigma}_{\mathbf{ii}} & \boldsymbol{\Sigma}_{\mathbf{i}} & \cdots & \boldsymbol{\Sigma}_{\mathbf{ii}} \\ \vdots & \vdots & \ddots & \vdots \\ \boldsymbol{\Sigma}_{\mathbf{ii}} & \boldsymbol{\Sigma}_{\mathbf{ii}} & \cdots & \boldsymbol{\Sigma}_{\mathbf{i}} \end{array} \right) \tag{4.20}$$

has a block structure with

$$\boldsymbol{\Sigma}_{\mathbf{i}} = \begin{pmatrix} \boldsymbol{\Sigma}_{\mathbf{A}} & \boldsymbol{\Sigma}_{\mathbf{A,B}} \\ \boldsymbol{\Sigma}_{\mathbf{A,B}}^{\mathrm{T}} & \boldsymbol{\Sigma}_{\mathbf{B}} \end{pmatrix} \quad \text{and} \quad \boldsymbol{\Sigma}_{\mathbf{ii}} = \begin{pmatrix} \boldsymbol{\Sigma}_{\mathbf{A,A}} & \boldsymbol{\Sigma}_{\mathbf{A,B}} \\ \boldsymbol{\Sigma}_{\mathbf{A,B}}^{\mathrm{T}} & \boldsymbol{\Sigma}_{\mathbf{B,B}} \end{pmatrix}. \tag{4.21}$$

This structure allows a decomposition into independent “global” and “local” parts:

$$\boldsymbol{\Sigma}_{\mathbf{G}^*} = \underbrace{\overbrace{\begin{pmatrix} \boldsymbol{\Sigma}_{\mathbf{glob}} & \boldsymbol{\Sigma}_{\mathbf{glob}} & \cdots & \boldsymbol{\Sigma}_{\mathbf{glob}} \\ \boldsymbol{\Sigma}_{\mathbf{glob}} & \boldsymbol{\Sigma}_{\mathbf{glob}} & \cdots & \boldsymbol{\Sigma}_{\mathbf{glob}} \\ \vdots & \vdots & \ddots & \vdots \\ \boldsymbol{\Sigma}_{\mathbf{glob}} & \boldsymbol{\Sigma}_{\mathbf{glob}} & \cdots & \boldsymbol{\Sigma}_{\mathbf{glob}} \end{pmatrix}}^{m \text{ times}}}_{\text{“global part”}} + \underbrace{\overbrace{\begin{pmatrix} \boldsymbol{\Sigma}_{\mathbf{loc}} & \mathbf{0} & \cdots & \mathbf{0} \\ \mathbf{0} & \boldsymbol{\Sigma}_{\mathbf{loc}} & \cdots & \mathbf{0} \\ \vdots & \vdots & \ddots & \vdots \\ \mathbf{0} & \mathbf{0} & \cdots & \boldsymbol{\Sigma}_{\mathbf{loc}} \end{pmatrix}}^{m \text{ times}}}_{\text{“local part”}} \tag{4.22}$$

with

$$\boldsymbol{\Sigma}_{\mathbf{glob}} = \boldsymbol{\Sigma}_{\mathbf{ii}} = \begin{pmatrix} \boldsymbol{\Sigma}_{\mathbf{A,A}} & \boldsymbol{\Sigma}_{\mathbf{A,B}} \\ \boldsymbol{\Sigma}_{\mathbf{A,B}}^{\mathrm{T}} & \boldsymbol{\Sigma}_{\mathbf{B,B}} \end{pmatrix} \quad \text{and} \tag{4.23}$$

$$\boldsymbol{\Sigma}_{\mathbf{loc}} = \boldsymbol{\Sigma}_{\mathbf{i}} - \boldsymbol{\Sigma}_{\mathbf{ii}} = \begin{pmatrix} \boldsymbol{\Sigma}_{\mathbf{A}} - \boldsymbol{\Sigma}_{\mathbf{A,A}} & \mathbf{0} \\ \mathbf{0} & \boldsymbol{\Sigma}_{\mathbf{B}} - \boldsymbol{\Sigma}_{\mathbf{B,B}} \end{pmatrix}. \tag{4.24}$$

This decomposition implies that the global RV

$$\boldsymbol{G}_{\mathbf{glob}} = \left(\boldsymbol{G}_{\mathbf{A}}^{[\mathrm{glob}]}, \boldsymbol{G}_{\mathbf{B}}^{[\mathrm{glob}]} \right) \sim \mathbf{N}(\mathbf{0}, \boldsymbol{\Sigma}_{\mathbf{glob}}), \tag{4.25}$$

which contains entries for each circuit element, equally applies to all instances. Furthermore, the local RV

$$\boldsymbol{G}_{\mathbf{loc}} = \left(\overbrace{\boldsymbol{G}_{\mathbf{A}}^{[\mathrm{loc:1}]}, \boldsymbol{G}_{\mathbf{B}}^{[\mathrm{loc:1}]}}^{\substack{1^{st} \text{ instance} \\ \text{per element}}}, \overbrace{\boldsymbol{G}_{\mathbf{A}}^{[\mathrm{loc:2}]}, \boldsymbol{G}_{\mathbf{B}}^{[\mathrm{loc:2}]}}^{\substack{2^{nd} \text{ instance} \\ \text{per element}}}, \ \ldots \ , \overbrace{\boldsymbol{G}_{\mathbf{A}}^{[\mathrm{loc:m}]}, \boldsymbol{G}_{\mathbf{B}}^{[\mathrm{loc:m}]}}^{\substack{m^{th} \text{ instance} \\ \text{per element}}} \right) \sim \mathbf{N}(\mathbf{0}, \boldsymbol{\Sigma}_{\mathbf{loc}}) \tag{4.26}$$

resolves into instance-specific independent RVs: the n_A-dimensional RV $\boldsymbol{G}_{\mathbf{A}}^{[\mathrm{loc:k}]} \sim \mathbf{N}(\mathbf{0}, \boldsymbol{\Sigma}_{\mathbf{A}} - \boldsymbol{\Sigma}_{\mathbf{A,A}})$ describes the local variability contribution of the k-th instance of element A and the n_B-dimensional RV $\boldsymbol{G}_{\mathbf{B}}^{[\mathrm{loc:l}]} \sim \mathbf{N}(\mathbf{0}, \boldsymbol{\Sigma}_{\mathbf{B}} - \boldsymbol{\Sigma}_{\mathbf{B,B}})$ describes the local variability contribution of the l-th instance of element B.

In summary, the improved sampling approach divides the complex correlated Gaussian sampling in the conventional approach in Sec. 4.3.1 into smaller and less expensive sub-tasks:

- the generation of a sample $\tilde{\boldsymbol{G}}_{\mathbf{glob}}$ from the RV $\boldsymbol{G}_{\mathbf{glob}} \sim \mathbf{N}(\mathbf{0}, \boldsymbol{\Sigma}_{\mathbf{glob}})$, which requires the covariance matrix $\boldsymbol{\Sigma}_{\mathbf{glob}}$ to be decomposed only once;
- the generation of a sample $\tilde{\boldsymbol{G}}_{\mathbf{A}}^{[loc:k]}$ from the RV $\boldsymbol{G}_{\mathbf{A}}^{[\mathrm{loc:k}]} \sim \mathbf{N}(\mathbf{0}, \boldsymbol{\Sigma}_{\mathbf{A}} - \boldsymbol{\Sigma}_{\mathbf{A,A}})$ for each instance k of element A, which requires the covariance matrix $(\boldsymbol{\Sigma}_{\mathbf{A}} - \boldsymbol{\Sigma}_{\mathbf{A,A}})$ to be decomposed once;
- and the generation of a sample $\tilde{\boldsymbol{G}}_{\mathbf{B}}^{[loc:l]}$ from the RV $\boldsymbol{G}_{\mathbf{B}}^{[\mathrm{loc:l}]} \sim \mathbf{N}(\mathbf{0}, \boldsymbol{\Sigma}_{\mathbf{B}} - \boldsymbol{\Sigma}_{\mathbf{B,B}})$ for each instance l of element B, which requires the covariance matrix $(\boldsymbol{\Sigma}_{\mathbf{B}} - \boldsymbol{\Sigma}_{\mathbf{B,B}})$ to be decomposed once.

The required sample $\tilde{\boldsymbol{G}}^*$ can then be obtained from

$$\tilde{\boldsymbol{G}}^* = \left(\overbrace{\tilde{\boldsymbol{G}}_{\mathbf{A}}^{[\mathrm{glob}]} + \tilde{\boldsymbol{G}}_{\mathbf{A}}^{[\mathrm{loc:1}]}}^{1^{st} \text{ instance of element A}}, \overbrace{\tilde{\boldsymbol{G}}_{\mathbf{B}}^{[\mathrm{glob}]} + \tilde{\boldsymbol{G}}_{\mathbf{B}}^{[\mathrm{loc:1}]}}^{1^{st} \text{ instance of element B}}, \right.$$

$$\overbrace{\tilde{\boldsymbol{G}}_{\mathbf{A}}^{[\mathrm{glob}]} + \tilde{\boldsymbol{G}}_{\mathbf{A}}^{[\mathrm{loc:2}]}}^{2^{nd} \text{ instance of element A}}, \overbrace{\tilde{\boldsymbol{G}}_{\mathbf{B}}^{[\mathrm{glob}]} + \tilde{\boldsymbol{G}}_{\mathbf{B}}^{[\mathrm{loc:2}]}}^{2^{nd} \text{ instance of element B}}, \tag{4.27}$$

$$\dots,$$

$$\left. \overbrace{\tilde{\boldsymbol{G}}_{\mathbf{A}}^{[\mathrm{glob}]} + \tilde{\boldsymbol{G}}_{\mathbf{A}}^{[\mathrm{loc:m}]}}^{m^{th} \text{ instance of element A}}, \overbrace{\tilde{\boldsymbol{G}}_{\mathbf{B}}^{[\mathrm{glob}]} + \tilde{\boldsymbol{G}}_{\mathbf{B}}^{[\mathrm{loc:m}]}}^{m^{th} \text{ instance of element B}} \right).$$

This approach is not limited to exactly m instances per circuit element. Instead, it extends naturally to arbitrary numbers of circuit elements with arbitrary and potentially different numbers of instances. The fact that it leads to correct intra-instance, inter-instance, and inter-element correlations is proved in App. B.4.

As in the conventional approach in Sec. 4.3.2, the Steps 3 and 4 of the basic sampling algorithm in Sec. 2.3.2, the transformation into uniform samples $\tilde{\boldsymbol{U}}$ and into the target samples $\tilde{\boldsymbol{Y}}$, are straightforward.

4.3.3 Performance Comparison

To compare the accuracy and the performance of the conventional approach and the improved approach for correlated Gaussian sampling, two hypothetic circuit elements are considered: an element A with $n_A = 3$ components and an element B with $n_B = 2$ components. The intra-instance, inter-instance, and inter-element rank correlation matrices are arbitrarily chosen,

$$\mathbf{R_A} = \begin{pmatrix} 1 & -0.35 & -0.39 \\ -0.35 & 1 & -0.42 \\ -0.39 & -0.42 & 1 \end{pmatrix}, \quad \mathbf{R_{A,A}} = \begin{pmatrix} 0.63 & -0.11 & -0.39 \\ -0.11 & 0.66 & -0.27 \\ -0.39 & -0.27 & 0.73 \end{pmatrix},$$

$$\mathbf{R_B} = \begin{pmatrix} 1 & 0.6 \\ 0.6 & 1 \end{pmatrix}, \quad \mathbf{R_{B,B}} = \begin{pmatrix} 0.89 & 0.56 \\ 0.56 & 0.78 \end{pmatrix}, \text{ and } \quad \mathbf{R_{A,B}} = \begin{pmatrix} 0.42 & 0.27 \\ -0.4 & -0.17 \\ -0.15 & -0.25 \end{pmatrix},$$

such that the resulting covariance matrices

$$\mathbf{\Sigma_{glob}} = \begin{pmatrix} 0.65 & -0.12 & -0.41 & 0.44 & 0.28 \\ -0.12 & 0.68 & -0.28 & -0.42 & -0.18 \\ -0.41 & -0.28 & 0.75 & -0.16 & -0.26 \\ 0.44 & -0.42 & -0.16 & 0.9 & 0.58 \\ 0.28 & -0.18 & -0.26 & 0.58 & 0.79 \end{pmatrix},$$

$$(\mathbf{\Sigma_A} - \mathbf{\Sigma_{A,A}}) = \begin{pmatrix} 0.35 & -0.24 & 0 \\ -0.24 & 0.32 & -0.16 \\ 0 & -0.16 & 0.25 \end{pmatrix}, \text{ and } \quad (\mathbf{\Sigma_B} - \mathbf{\Sigma_{B,B}}) = \begin{pmatrix} 0.1 & 0.04 \\ 0.04 & 0.21 \end{pmatrix}$$

are positive definite. Gaussian RVs $\boldsymbol{G}_\mathbf{i}$ with corresponding theoretical covariance matrices $\mathbf{\Sigma_{G_i}}$ are constructed for different numbers of instances of elements A and B, $m_A \in \{1, 2, 5, 10, 20, 50, 100, 200, 500, 1000\}$ and $m_B \in \{0, 1, 2, 5, 10, 20, 50, 100, 200, 500, 1000\}$. For different sample sizes, $N_1 = 100$ and $N_2 = 1000$, corresponding random samples $\tilde{\boldsymbol{G}}_\mathbf{i}$ and $\tilde{\boldsymbol{G}}_\mathbf{i}^*$ are generated by applying the conventional approach and the improved sampling approach, respectively. The maximum absolute deviations in the observed covariance matrices, $\max\{|\widetilde{\mathbf{\Sigma}}_{\mathbf{G_i}} - \mathbf{\Sigma_{G_i}}|\}$ and $\max\{|\widetilde{\mathbf{\Sigma}}_{\mathbf{G_i^*}} - \mathbf{\Sigma_{G_i}}|\}$, as well as the required run times for correlated Gaussian sampling T_s are recorded in this study, which is conducted on a standard server computer.

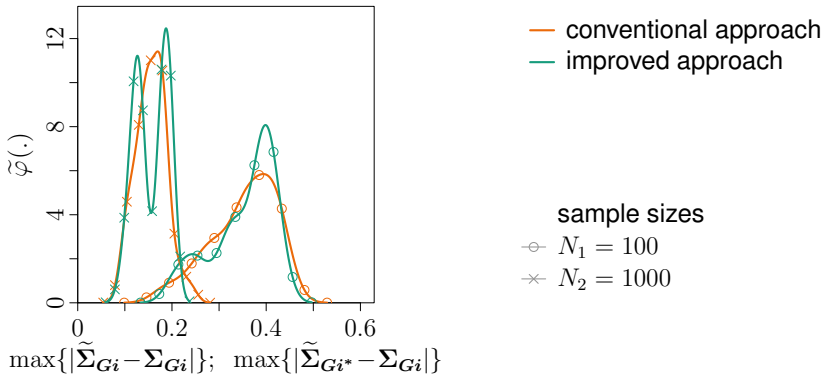

Fig. 4.5: Maximum errors in sample covariance matrices $\widetilde{\Sigma}$ with respect to theoretical covariance matrices Σ for conventional and improved sampling approaches

With respect to the maximum absolute deviations in the observed covariance matrices in Fig. 4.5, the conventional approach and the improved approach perform similarly in terms of accuracy. As expected, the deviations between theoretical and empirical covariance matrices decrease when the sample size grows from $N_1 = 100$ to $N_2 = 1000$. Consequently, the improved algorithm can be considered equivalent to the conventional approach in terms of the sample quality[5].

However, the comparisons of the required run times T_s in Fig. 4.6 reveal significant differences between the sampling approaches. The computational effort for the conventional approach only marginally depends on the sample size N. Instead, it is essentially influenced by the numbers of circuit elements and instances, that is by the particular circuit under consideration, for which the specific RV $\boldsymbol{Y}$ with its rank correlation matrix $\mathbf{R}_{\boldsymbol{Y}}$ or the corresponding covariance matrix $\boldsymbol{\Sigma}_{\mathbf{G}}$ has to be constructed from the probabilistic model. In this analysis, for $m_A = 1000$ instances of element A and $m_B = 0$ instances of element B, that is without inter-element correlations, the run times for correlated Gaussian sampling applying the conventional approach are $237\,s$ for $N_1 = 100$ samples and $247\,s$ for $N_2 = 1000$ samples. For $m_A = m_B = 1000$ instances of both elements A and B, the run times are $809\,s$ for $N_1 = 100$ samples and $892\,s$ for $N_2 = 1000$ samples, for example.

Contrarily, the computational effort for the improved approach depends on both the sample size N and the circuit under consideration with its number of circuit elements

[5]The maximum absolute deviations of up to 0.8 appear large when considering $-1 \leq \boldsymbol{\Sigma}_{\mathbf{G},ij} \leq 1$. They result from the fact that, in this study, the matrix $\boldsymbol{\Sigma}_{\mathbf{G}}$ grows up to a dimensionality of (5000×5000) for $m_A = m_B = 1000$ instances of each element A and B so that it may contain too many inter-dependencies to be accurately captured in samples of the size $N_1 = 100$ or $N_2 = 1000$.

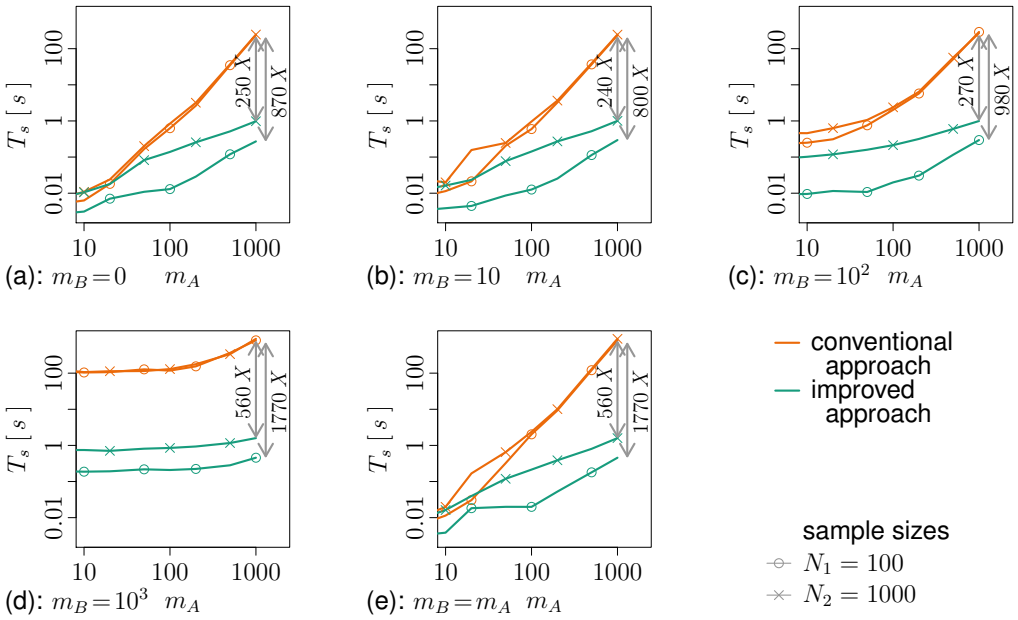

Fig. 4.6: Performance comparison of conventional and improved sampling approaches for two circuit elements A and B with different numbers of instances m_A and m_B as well as different sample sizes $N_1 = 100$ and $N_2 = 1000$

and instances. While amount of data to process is proportional to the sample size N, the number of circuit elements defines the dimensionality of the global covariance matrix $\boldsymbol{G}_{\mathbf{glob}}$ in (4.23), and the number of instances per circuit element defines the amount of required instance-specific local samples $\tilde{\boldsymbol{G}}_{\mathbf{A}}^{[\mathrm{loc:k}]}$ and $\tilde{\boldsymbol{G}}_{\mathbf{B}}^{[\mathrm{loc:l}]}$. In the performance analysis, for $m_A = 1000$ instances of element A and $m_B = 0$ instances of element B, the run times for Gaussian sampling by the improved approach are $0.27\,s$ for $N_1 = 100$ samples and $0.98\,s$ for $N_2 = 1000$ samples, complying with $870\,X$ and $250\,X$ speed-ups over the conventional approach. For $m_A = m_B = 1000$ instances of each element A and B, the required run times of $0.46\,s$ for $N_1 = 100$ samples and $1.6\,s$ for $N_2 = 1000$ samples correspond to $1170\,X$ and $560\,X$ speed-ups.

In summary, the conventional approach and the improved approach are equivalent in terms of sample quality. However, in contrast to the conventional approach, the improved approach keeps the run times for correlated Gaussian sampling reasonable with $T_s < 2\,s$ in this study. Compared with the conventional approach, the improved approach accelerates the sample generation by up to more than three orders of magnitude. Consequently, the improved approach allows a wide-spread application of sampling-based evaluations of the probabilistic GLD-FKML models.

4.4 Generalization to Arbitrary Numbers of Elements

The discussions in the previous sections of this chapter were limited to two circuit elements A and B. In this section, the generalization to an arbitrary number of elements is explained by introducing an additional circuit element C.

According to the definition of probabilistic models in Sec. 4.1, the variability of this element can be described by an n_C-dimensional distribution with GLD-FKML approximations of marginal distributions and intra-instance correlations in terms of the $(n_C \times n_C)$ Spearman's rank correlation matrix $\mathbf{R}_{\mathbf{C}}$. In addition, the probabilistic model needs to be extended to capture intra-instance correlations of element C in the $(n_C \times n_C)$ matrix of Spearman's rank correlation coefficients $\mathbf{R}_{\mathbf{C,C}}$ and to capture inter-element correlations between the elements A and C as well as B and C in the $(n_A \times n_C)$ matrix $\mathbf{R}_{\mathbf{A,C}}$ and the $(n_B \times n_C)$ matrix $\mathbf{R}_{\mathbf{B,C}}$. Note that the matrices for quantifying correlations can be transformed into the matrices $\mathbf{\Sigma}_{\mathbf{C}}$, $\mathbf{\Sigma}_{\mathbf{C,C}}$, $\mathbf{\Sigma}_{\mathbf{A,C}}$, and $\mathbf{\Sigma}_{\mathbf{B,C}}$ by the element by element calculation (2.54).

To calibrate this extended model, the characterization data has to contain information on two instances for each element A, B, and C. That is, the required characterization sample reads

$$\tilde{\boldsymbol{Y}}_{\mathbf{char}} = \left(\tilde{\boldsymbol{Y}}_{\mathbf{A}}^{[1]}, \tilde{\boldsymbol{Y}}_{\mathbf{A}}^{[2]}, \tilde{\boldsymbol{Y}}_{\mathbf{B}}^{[1]}, \tilde{\boldsymbol{Y}}_{\mathbf{B}}^{[2]}, \tilde{\boldsymbol{Y}}_{\mathbf{C}}^{[1]}, \tilde{\boldsymbol{Y}}_{\mathbf{C}}^{[2]} \right)$$

in this case. Based on this sample data, the model can be calibrated by applying the principles in Sec. 4.2.2 and Sec. 4.2.3 to all elements.

The generation of random samples from the probabilistic model is then straightforward. The conventional approach applies m_C instances of element C according to the circuit under investigation. In the improved approach, the global RV $\boldsymbol{G}_{\mathbf{glob}}$ in (4.25) needs to be extended to

$$\boldsymbol{G}_{\mathbf{glob}} = \left(\boldsymbol{G}_{\mathbf{A}}^{[\mathrm{glob}]}, \boldsymbol{G}_{\mathbf{B}}^{[\mathrm{glob}]}, \boldsymbol{G}_{\mathbf{C}}^{[\mathrm{glob}]} \right) \sim \mathbf{N}(\mathbf{0}, \mathbf{\Sigma}_{\mathbf{glob}}) \quad \text{with} \quad \mathbf{\Sigma}_{\mathbf{glob}} = \begin{pmatrix} \mathbf{\Sigma}_{\mathbf{A,A}} & \mathbf{\Sigma}_{\mathbf{A,B}} & \mathbf{\Sigma}_{\mathbf{A,C}} \\ \mathbf{\Sigma}_{\mathbf{A,B}}^{\mathrm{T}} & \mathbf{\Sigma}_{\mathbf{B,B}} & \mathbf{\Sigma}_{\mathbf{B,C}} \\ \mathbf{\Sigma}_{\mathbf{A,C}}^{\mathrm{T}} & \mathbf{\Sigma}_{\mathbf{B,C}}^{\mathrm{T}} & \mathbf{\Sigma}_{\mathbf{C,C}} \end{pmatrix}.$$

In addition, instance-specific independent RVs $\boldsymbol{G}_{\mathbf{C}}^{[\mathrm{loc:k}]} \sim \mathbf{N}(\mathbf{0}, \mathbf{\Sigma}_{\mathbf{C}} - \mathbf{\Sigma}_{\mathbf{C,C}})$ have to be introduced to model the local variations of each instance k of element C.

The repetition of the aforementioned procedure extends the probabilistic modeling approach to arbitrary numbers of elements.

4.5 Summary and Conclusions

In this section, Chap. 4 is summarized and some conclusions are drawn. To illustrate the statements, an example for model calibration and random sample generation is presented in App. B.3.

1. At an arbitrary level of abstraction, probabilistic models can capture the variability of the available circuit elements by describing selected components of the underlying models by multivariate distributions.
2. The applied combination of Spearman's rank correlation matrices and GLD-FKML approximations of marginal distributions allows a high flexibility for capturing arbitrary correlations and almost arbitrary distribution shapes.
3. Considering the fact that ICs consist of instances of a finite number of circuit elements, the variability of each instance is modeled as a multivariate RV. All instances of a particular circuit element are assumed to follow the same multivariate distribution.
4. The correlations within an instance are described by intra-instance correlation matrices. Inter-instance and inter-element correlations describe the inter-dependencies between different instances of a particular circuit element and between instances of different circuit elements. They are equally applied to all combinations of instances, which neglects spatial local correlations but captures global and local variability.
5. To calibrate a fully statistical probabilistic model, sample data $\tilde{\boldsymbol{Y}}_{\mathbf{char}}$ from a RV

   $$\boldsymbol{Y}_{\mathbf{char}} = \left(\boldsymbol{Y}_{\mathbf{A}}^{[1]}, \boldsymbol{Y}_{\mathbf{A}}^{[2]}, \boldsymbol{Y}_{\mathbf{B}}^{[1]}, \boldsymbol{Y}_{\mathbf{B}}^{[2]}, \boldsymbol{Y}_{\mathbf{C}}^{[1]}, \boldsymbol{Y}_{\mathbf{C}}^{[2]}, \ldots \right),$$

   which contains two instances per circuit element needs to be gained from characterization. To correctly extract all correlation components, identical global but independent local variation parameters $\tilde{\boldsymbol{X}}_{\mathbf{char}}$ have to be applied to all instances during characterization.
6. To optimally use the available information in the characterization data $\tilde{\boldsymbol{Y}}_{\mathbf{char}}$, the correlation matrices are extracted by applying (4.11)–(4.13). Marginal distributions

are approximated from unions of sample data of corresponding components of both instances per element.

7. To generate random samples from a probabilistic model, the RV $\boldsymbol{Y}$ that describes the variability of a particular circuit under consideration has to be constructed from the model. Then, the sampling algorithm in Sec. 2.3.2 can be applied.

8. Random sampling by the conventional approach in Sec. 4.3.1 requires the construction of the circuit-specific Spearman's rank correlation matrix $\mathbf{R}_{\mathrm{Y}}$ from the intra-instance, inter-instance, and inter-element matrices as well as its conversion to the covariance matrix $\boldsymbol{\Sigma}_{\mathrm{G}}$ by (2.54). The interim step of random Gaussian sampling from the RV $\boldsymbol{G} \sim \mathrm{N}(\mathbf{0}, \boldsymbol{\Sigma}_{\mathrm{G}})$ requires a decomposition of this covariance matrix, $\boldsymbol{\Sigma}_{\mathrm{G}} = \mathbf{L}_{\mathrm{G}}\, \mathbf{L}_{\mathrm{G}}^{\mathrm{T}}$, which may be computationally very expensive. These disadvantages impede an efficient application of the conventional sampling approach.

9. The improved sampling approach in Sec. 4.3.2 divides the complex conventional sampling method into smaller sub-tasks. It requires the construction and decomposition of (a) a global covariance matrix $\boldsymbol{\Sigma}_{\mathrm{glob}}$, which contains the inter-instance and inter-element correlations of one instance of all available circuit elements, as well as of (b) instance-specific local covariance matrices, which are identical for all instances of a particular circuit element. This approach allows an implementation of probabilistic models into standard tools, such as circuit simulators. Furthermore, without introducing errors with respect to the conventional approach, it keeps the computational effort for the generation of correlated Gaussian samples reasonable. Both aspects support the application of probabilistic models in sampling-based circuit analyses.

5 Application Scenarios

In this chapter, the modeling approach proposed in Chap. 4 is applied to multiple application scenarios. They are chosen to cover a broad range of the abstraction levels discussed in Chap. 3, which is demonstrated in Fig. 5.1. In particular, device compact models, standard cell performance models and adapted gate level analyses,

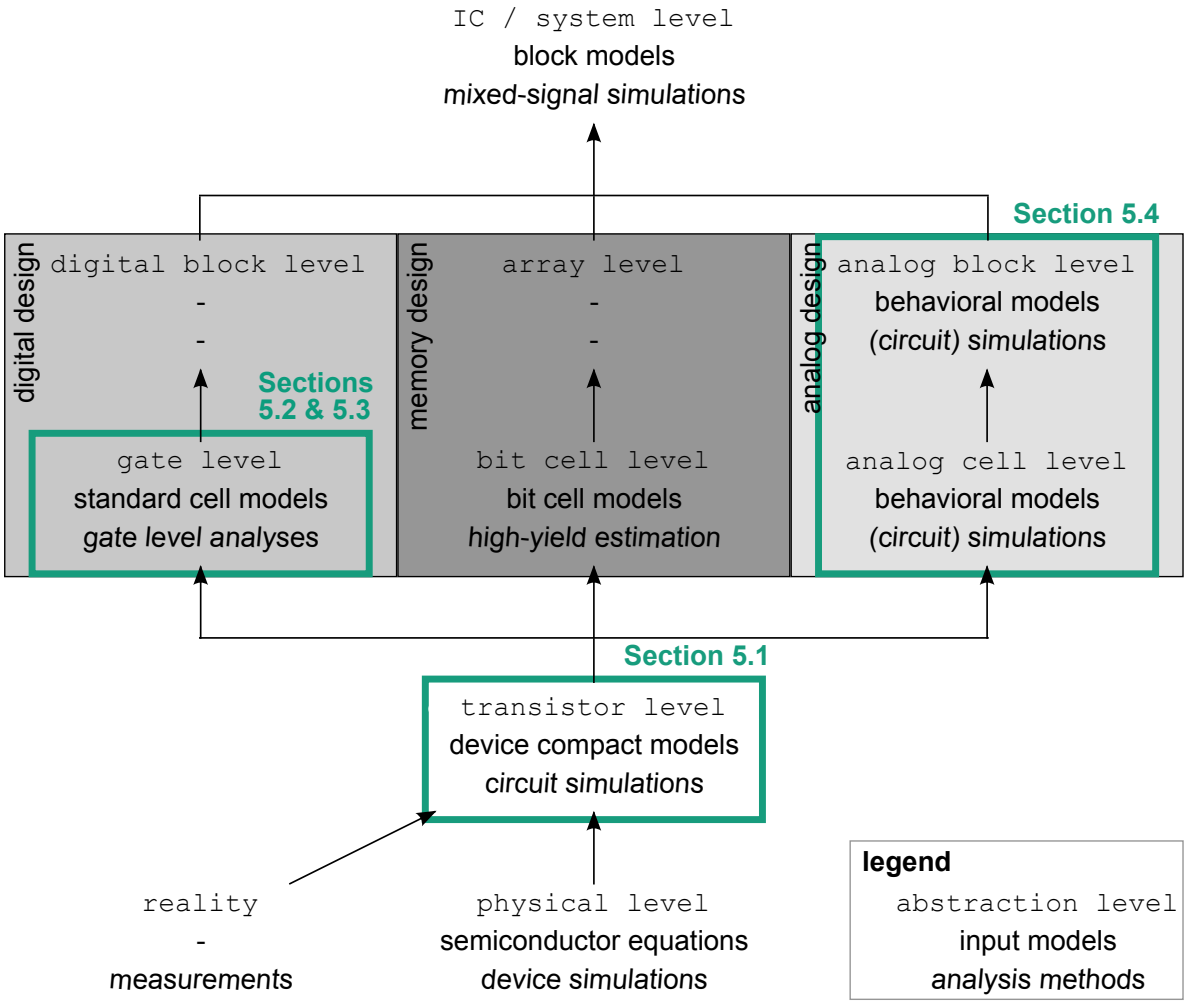

Fig. 5.1: Allocation of application scenarios in abstraction levels from Fig. 3.1 in Sec. 3

as well as behavioral models of analog cells demonstrate the applicability and the universality of the modeling approach, which is based on GLD-FKML approximations of marginal distributions and Spearman's rank correlation matrices. To evaluate the benefits of considering non-Gaussian and correlated random components, Gaussian models are taken into account for comparisons.

5.1 Probabilistic Device Compact Modeling and Monte Carlo Circuit Simulation

5.1.1 Origin and Characterization

A particular task in modeling IC variability is the transfer of variability information into variation-aware device compact models. For this purpose, Sec. 3.3 has discussed the *backward propagation of variance* (BPV), which maps observed fluctuations in electrical device performance parameters to variations in selected compact model parameters, and statistical device simulations, from which ensembles of model cards can be generated to infer on the underlying distributions.

The scenario in this section is based on statistical device simulations. They were performed at the University of Glasgow with the Glasgow atomistic 3D drift-diffusion device simulator to analyze $35\,nm$ square NFET and PFET devices in a poly-silicon gate technology. Neglecting global variations but introducing random local variations, $N_{char} = 200$ microscopically different NFET and PFET instances were simulated, and their individual behaviors were mapped to BSIM4 device compact models. While most compact model parameters were kept constant, $n = 7$ parameters were varied to capture the variability [LSJ+11, LSJ+16]:

- the long-channel threshold voltage at zero body bias $\mathrm{vth0}$,
- the zero-bias source and drain resistance rdsw,
- the subthreshold swing factor $\mathrm{nfactor}$,
- the offset voltage in subthreshold regime voff,
- the low-field carrier mobility $\mathrm{u0}$,
- the coefficient for drain-induced barrier lowering dsub, and
- the saturation velocity vsat [M+09, M+11].

These parameters can be considered $n_y = 7$-dimensional RVs $\boldsymbol{Y}_{\mathrm{N}}$ and $\boldsymbol{Y}_{\mathrm{P}}$, which represent the variability of the NFET and the PFET. Their suitable descriptions allow an evaluation of variability in MC circuit simulations [LSJ+11, LSJ+16]. The device simulation study, which corresponds to the characterization in the context of this thesis, generated $N_{\mathrm{char}} = 200$-sample characterization data $\tilde{\boldsymbol{Y}}_{\mathbf{char}} = \left(\tilde{\boldsymbol{Y}}_{\mathbf{N,char}}, \tilde{\boldsymbol{Y}}_{\mathbf{P,char}}\right)$ to calibrate the probabilistic device models.

5.1.2 Model Calibration

Approximating marginal distributions is one task to calibrate variation-aware device compact models. To check whether the probabilistic GLD-FKML modeling approach is justified, the components of the characterization data $\tilde{\boldsymbol{Y}}_{\mathbf{N,char}}$ and $\tilde{\boldsymbol{Y}}_{\mathbf{P,char}}$ are checked for Gaussian distributions. For this purpose, *Shapiro-Wilk* (SW) tests, which were introduced in Sec. 2.1.4, are performed with $(1-\alpha_c) = 0.95$ confidence level. The test results are summarized in Tab. 5.1, and they reveal that only some components are Gaussian: the long-channel threshold voltage at zero body bias $\mathrm{vth0}$, the zero-bias source and drain resistance rdsw, and the offset voltage in subthreshold regime voff for the NFET as well as the long-channel threshold voltage at zero body bias $\mathrm{vth0}$ and the saturation velocity vsat for the PFET. The remaining components are significantly non-Gaussian, which is further underlined by the Q-Q plots in App. C.1.1 and a selection of them in Fig. 5.2. These interim results justify a modeling approach that supports non-Gaussian distributions, such as the probabilistic GLD-FKML model proposed in this thesis.

Tab. 5.1: Statistical tests for device parameter distributions from characterization data; SW tests with results **+**: *Gaussian* and –: *non-Gaussian*; KS tests comparing characterization data and GLD-FKML approximations of marginal distributions with results **o**: *accurate approximation* and x: *inaccurate approximation*; confidence level $(1-\alpha_c) = 0.05$; cf. TABLE I in [LSJ+16]

Parameter	NFET		PFET	
	SW test	KS test	SW test	KS test
vth0	**+**	**o**	**+**	**o**
rdsw	**+**	**o**	-	**o**
nfactor	-	**o**	-	**o**
voff	**+**	**o**	-	**o**
u0	-	**o**	-	**o**
dsub	-	**o**	-	**o**
vsat	-	**o**	**+**	**o**

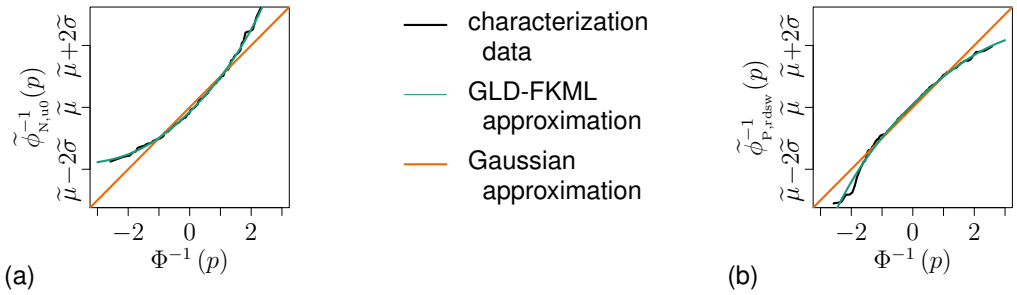

Fig. 5.2: Q-Q plots of (a) NFET $\mathrm{u0}$ and (b) PFET rdsw; compare Fig. 2 in [LSJ+16]

The components of the characterization data are mapped to GLD-FKMLs with the *R* function *FitGLD* in App. B.2. This is in contrast to [LSJ+11], which applies the GLD-RS defined in (4.2). The GLD-FKML approximations are added to the Q-Q plots in Fig. 5.2 and App. C.1.1, and they appear to represent the characterization data well. To verify the accuracy, the characterization data are compared with $N_s = 1000$ random samples from the GLD-FKML approximations by *Kolmogorov-Smirnov* (KS) tests with a $(1-\alpha_c) = 0.95$ confidence level. As discussed in Sec. 2.1.4, these tests reveal whether the characterization data and the samples from the GLD-FKML approximations represent the same distributions, that is whether the GLD-FKML approximations accurately describe the characterization data. According to their results, which are additionally listed in Tab. 5.1, the KS tests confirm the accuracy of the GLD-FKML approximations, which holds for the NFET and the PFET as well as for Gaussian and non-Gaussian components.

In addition to the marginal distributions, probabilistic models need to capture the correlations in the characterization data. Since global variations were neglected in the device simulation study, inter-instance and inter-element correlations do not exist, that is $\mathbf{R}_{\mathbf{N,N}} = \mathbf{\Sigma}_{\mathbf{N,N}} = \mathbf{0}$, $\mathbf{R}_{\mathbf{P,P}} = \mathbf{\Sigma}_{\mathbf{P,P}} = \mathbf{0}$, and $\mathbf{R}_{\mathbf{N,P}} = \mathbf{\Sigma}_{\mathbf{N,P}} = \mathbf{0}$. Accordingly, in this scenario, the intra-instance correlations for the NFET and the PFET have to be taken into account solely. Applying (2.51) in Sec. 2.2.4 to the characterization data $\tilde{\boldsymbol{Y}}_{\mathbf{char}}$, the Spearman's rank correlation matrices $\mathbf{R}_{\mathbf{N}}$ and $\mathbf{R}_{\mathbf{P}}$ are estimated. Due to the sample size $N_{\mathrm{char}} = 200$, Spearman's rank correlation coefficients $\left|\widetilde{\rho}^{(\mathrm{sp})}\right| \leq 0.139$ are considered insignificant according to (2.52). It is straightforward to convert Spearman's rank correlation matrices into covariance matrices for the improved sampling approach introduced in Sec. 4.3.2.

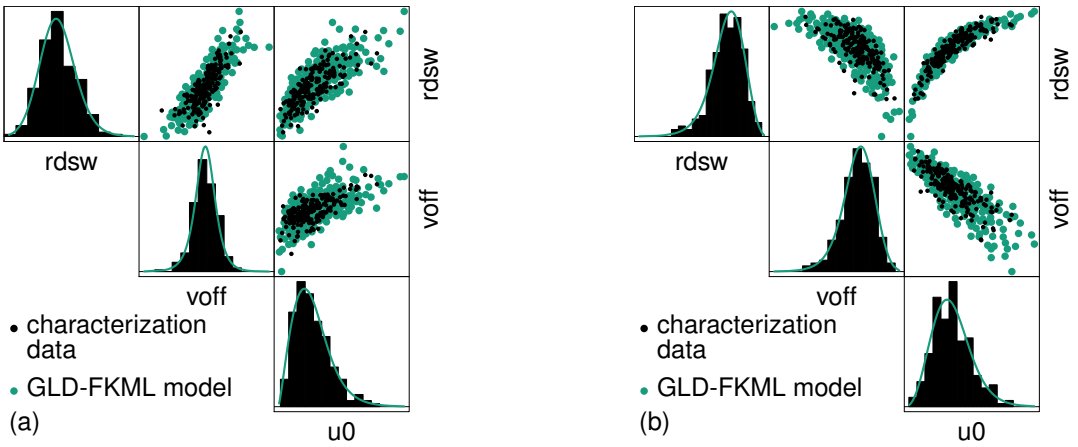

Fig. 5.3: Partial scatterplot matrices for selected parameters of (a) NFET and (b) PFET probabilistic models; compare Fig. 5 in [LSJ+16]

With the GLD-FKML approximations of the marginal distributions and the correlation matrices, the probabilistic NFET and PFET models are completely calibrated. The scatterplot matrices for selected components in Fig. 5.3 and for all model components in App. C.1.2 contrast the characterization data with $N_s = 1000$ samples from the probabilistic GLD-FKML models. Their good agreement for marginal distributions and clusters of points attests the high modeling accuracy.

5.1.3 Model Implementation Outline

To efficiently evaluate probabilistic device compact models in sampling-based MC circuit simulations, they have to be implemented into the respective simulators with *Synopsys HSPICE*® [Syn15] being chosen for demonstration purposes in this section. While the complete implementation of the models calibrated in Sec. 5.1.2 is omitted, a simplified NFET model serves as an illustration example. It is assumed that the BSIM4 parameters $\mathrm{vth0}$ and $\mathrm{u0}$ capture the device variability. They can be modeled as a $n_y = 2$-dimensional RV $\boldsymbol{Y}_{\mathrm{N}}$ with their GLD-FKML approximations of the marginal distributions, $Y_{\mathrm{N,vth0}} \sim \mathrm{GLD}(\lambda_{v1}, \lambda_{v2}, \lambda_{v3}, \lambda_{v4})$ and $Y_{\mathrm{N,u0}} \sim \mathrm{GLD}(\lambda_{u1}, \lambda_{u2}, \lambda_{u3}, \lambda_{u4})$, as well as the intra-instance Spearman's rank correlation matrix

$$\mathbf{R}_{\mathrm{N}} = \begin{pmatrix} 1 & 0.7859 \\ 0.7859 & 1 \end{pmatrix},$$

which is arbitrarily chosen such that the element by element transformation (2.54) in Sec. 2.3.2 yields a valid covariance matrix $\mathbf{\Sigma_N}$. Furthermore, as in Sec. 5.1.2, there are no inter-instance correlations, that is $\mathbf{R_{N,N}} = \mathbf{\Sigma_{N,N}} = \mathbf{0}$, or inter-element correlations to potential further circuit elements. Under these assumptions, the principles for the improved sampling approach in Sec. 4.3.2 lead to

$$\begin{aligned} &\text{the } (2\times 2) \text{ global covariance matrix} && \mathbf{\Sigma_{glob}} = \mathbf{0} && \text{and} \\ &\text{the local covariance matrix for the NFET} && (\mathbf{\Sigma_N} - \mathbf{\Sigma_{N,N}}) = \begin{pmatrix} 1 & 0.8 \\ 0.8 & 1 \end{pmatrix}. \end{aligned}$$

Since a circuit simulator generates uncorrelated random numbers, for correlated Gaussian sampling with the target covariance matrix $(\mathbf{\Sigma_N} - \mathbf{\Sigma_{N,N}})$, this matrix has to be decomposed, for instance by the Cholesky decomposition [Tho13],

$$(\mathbf{\Sigma_N} - \mathbf{\Sigma_{N,N}}) = \mathbf{L_N}\mathbf{L_N^T} \qquad \Longrightarrow \qquad \mathbf{L_N} = \begin{pmatrix} 1 & 0 \\ 0.8 & 0.6 \end{pmatrix}.$$

With the matrix $\mathbf{L_N}$, the required correlated Gaussian sampling can be realized. In addition, the Steps 3 and 4 of the sampling algorithm in Sec. 2.3.2 require implementations of the standard Gaussian CDF $\Phi(.)$ and the GLD-FKML quantile function (4.4). While the GLD-FKML quantile function can directly be implemented into *HSPICE*, the standard Gaussian CDF $\Phi(.)$ has to be approximated. Based on the formula [AA08]

$$\Phi(x) \approx \frac{1}{2} + \frac{1}{2}\sqrt{1 - \exp\left(-\sqrt{\frac{\pi}{8}}x^2\right)} \qquad \text{for} \qquad x > 0, \tag{5.1}$$

the relation

$$\Phi(x) \approx \frac{1}{2} + \frac{1}{2}\,\mathrm{sgn}(x)\,\sqrt{1 - \exp\left(-\sqrt{\frac{\pi}{8}}x^2\right)}, \tag{5.2}$$

with the sign operator $\mathrm{sgn}(.)$, is implemented.

In combination, these information can be converted into *HSPICE* syntax. An example implementation of the probabilistic NFET model is proposed in Fig. 5.4. The analytically available GLD-FKML quantile function (4.4) supports an efficient model evaluation.

```
******** definitions of functions
**** standard Gaussian CDF - based on [AA08]
.param sqrt_pi_by_8 = '0.6266571' $ sqrt(pi/8)
.param pnorm(z) = '1/2 + 1/2 * sgn(z) * sqrt(1-exp(-sqrt_pi_by_8*z*z))'
**** quantile function of GLD-FKML
.param qgl(u,L1,L2,L3,L4)='L1 + 1/L2 * ((pwr(u,L3)-1)/L3-(pwr(1-u,L4)-1)/L4)'
**** force local parameter scooping
.option parhier=LOCAL

******** NFET subckt model
.subckt NFET d g s b L=<L> W=<W>
  **** declaration of GLD-FKLM parameters
  .param lambda_v1=... lambda_v2=... lambda_v3=... lambda_v4=...
  .param lambda_u1=... lambda_u2=... lambda_u3=... lambda_u4=...
  **** correlated Gaussian sampling
  ** independent standard Gaussian sampling
  .param c1_=agauss(0,1,1)          c2_=agauss(0,1,1)
  .param c1=c1_                     c2=c2_
  ** transformation to correlated Gaussians
  .param z_vth0='1*c1'              z_u0='0.8*c1+0.6*c2'
  **** map to correlated uniforms - step 3 of algorithm in Sec. 4.1
  .param u_vth0='pnorm(z_vth0)'     u_u0='pnorm(z_u0)'
  **** map to marginal distributions - step 4 of algorithm in Sec. 4.1
  .param vth0= 'qgl(u_vth0,lambda_v1,lambda_v2,lambda_v3,lambda_v4)'
  .param u0  = 'qgl(u_u0,  lambda_u1,lambda_u2,lambda_u3,lambda_u4)'
  **** device instantiation
  m1 d g s b nfet0 L='L' L='W'
  **** model card
  .model nfet0 nmos vth0='vth0' u0='u0'
  + $ remaining model card parameters
.ends
```

Fig. 5.4: Example for *HSPICE* implementation of probabilistic NFET model; slightly improved efficiency in 'pnorm(z)' compared to [LSJ+16]

5.1.4 Model Evaluation in Monte Carlo Circuit Simulations

Device compact models with their statistical extensions are the basis for *Monte Carlo* (MC) circuit simulations. To enable these simulations with a high efficiency, the probabilistic models derived in Sec. 5.1.2 have to be implemented into circuit simulators, for example following the outline in Sec. 5.1.3.

To evaluate the accuracy of the probabilistic GLD-FKML models, the following simulation scenarios are considered. The corresponding simulation netlists are available in App. C.1.3.

1. *Single devices* – For a constant drain-to-source voltage $|V_{ds}| = 1\,V$, the static performance parameters of an NFET and a PFET are determined. In particular, the off-current I_{off} and the on-current I_{on} are measured at gate-to-source voltages of $V_{gs} = 0$ and $V_{gs} = V_{dd}$.
2. *Standard cell* – An NFET and a PFET are connected to form an inverter. At the supply voltage $V_{dd} = 1\,V$, the inverter performance parameters are analyzed without a load at the output pin: the state-dependent leakage power consumptions for the input pin at logic 0 and at logic 1 as well as the rise and fall delays for a linear input voltage waveform switching from 0 to 1 and vice versa within $t = 1\,ps$.
3. *Small-scale digital circuit*
   A NAND2 instance and two inverter instances are connected to a three-stage *ring oscillator* (RO). The oscillation can be enabled and disabled by a control signal which is connected to the NAND2 input pin b. The leakage power in idle mode as well as the oscillation frequency are the observed performance parameters.

In addition to the probabilistic GLD-FKML models, uncorrelated Gaussian models, that is NFET and PFET models with uncorrelated Gaussian components, and correlated Gaussian models, that is NFET and PFET models with correlated Gaussian components, are derived from the characterization data for comparison purposes. For each simulation scenario, the figures of merit are obtained from $N_s = 5000$-sample MC circuit simulations applying the different models. Reference data is generated by $N_{\mathrm{ref}} = 200$-sample circuit simulations, which apply random permutations of the characterization data $\tilde{\boldsymbol{Y}}_{\mathbf{N,char}}$ and $\tilde{\boldsymbol{Y}}_{\mathbf{P,char}}$.

The Q-Q plots in Fig. 5.5 and Fig. 5.6 as well as in App. C.1.4 visualize the obtained distributions of the figures of merit. Furthermore, KS tests with $(1-\alpha_c) = 0.95$ confi-

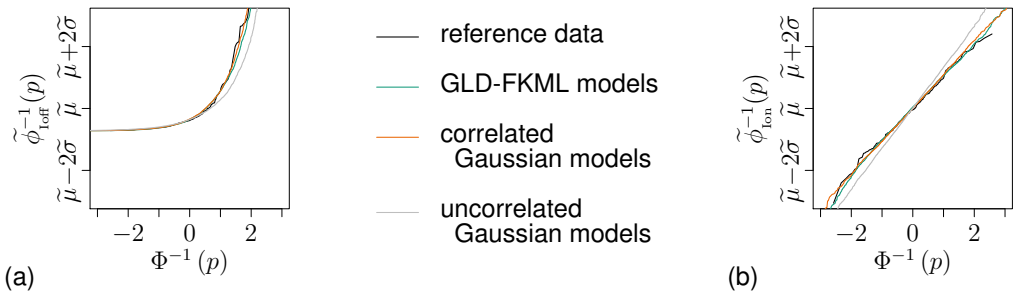

Fig. 5.5: Q-Q plots of static NFET performance parameters; (a) off-current; (b) on-current

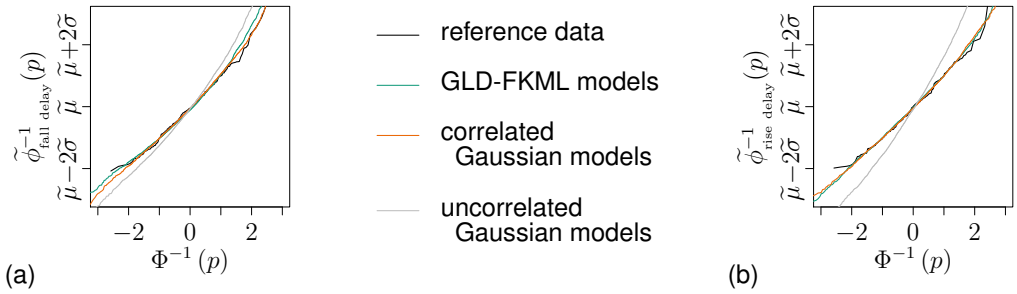

Fig. 5.6: Q-Q plots of inverter propagation delay distributions; (a) fall delay; (b) rise delay

Tab. 5.2: Statistical tests to evaluate MC circuit simulation results: KS test comparing the $N_{\mathrm{ref}} = 200$-sample reference data with results of $N_s = 5000$-sample MC circuit simulations with results **o**: *sample data from same distribution* and x: *sample data from different distributions*; test results for MC circuit simulations with uncorrelated Gaussian models, correlated Gaussian models, and probabilistic GLD-FKML models; confidence level $(1-\alpha_c) = 0.95$

Testcase	Performance parameter	uncorrelated Gaussian models	correlated Gaussian models	probabilistic GLD-FKML models
NFET	I_{off}	**o**	**o**	**o**
	I_{on}	**o**	**o**	**o**
PFET	I_{off}	**o**	**o**	**o**
	I_{on}	x	**o**	**o**
Inverter	fall delay	**o**	**o**	**o**
	rise delay	x	**o**	**o**
	leakage ($a = 0$)	**o**	**o**	**o**
	leakage ($a = 1$)	**o**	**o**	**o**
RO	leakage power	**o**	**o**	**o**
	frequency	x	**o**	**o**

dence levels compare them with the reference data. When the null-hypothesis, "*the samples represent the same distribution*", is accepted, the models can be considered accurate. However, due to the small sample size of the characterization data and, consequently, the reference data for the MC circuit simulations, $N_{\mathrm{char}} = N_{\mathrm{ref}} = 200$, the KS tests are not very distinguishing. Nevertheless, their results in Tab. 5.2 can reveal major model inaccuracies.

For a considerable fraction of the simulation scenarios, uncorrelated Gaussian models introduce inaccuracies: the distributions of the PFET on-current, the inverter rise delay, and the RO frequency significantly differ from the reference data, which is further illustrated by the corresponding Q-Q plots in Fig. 5.6 and App. C.1.4. These figures of

merit are closely related since the PFET drain current mainly determines the inverter rise delay, which is an important contributor to the RO period and hence the RO frequency. In addition, slight but insignificant deviations between the distributions of the NFET on-current and the inverter fall delay can be observed when comparing the results of simulations with uncorrelated Gaussian models and the reference data in the Q-Q plots in Fig. 5.5 and Fig. 5.6.

In contrast, correlated Gaussian models and probabilistic GLD-FKML models perform equally well in the simulation scenarios: the determined distributions of the figures of merit do not significantly differ from the reference data. This is confirmed by the KS test results in Tab. 5.2 and by the Q-Q plots in Fig. 5.5, Fig. 5.6, and App. C.1.4.

5.1.5 Results of the Compact Modeling Scenario

A variety of conclusions can be drawn from the probabilistic device compact modeling scenario [LSJ+11, LSJ+16].

First, a considerable number of random components may be non-Gaussian so that more general approximation methods are necessary and justified. The GLD-FKML in (4.4) is an appropriate solution since it accurately represents marginal distributions of various shapes, which can be obtained from the characterization data.

Second, most components of probabilistic models are correlated. The correlations have to be captured to achieve a reasonable accuracy in analyses based on probabilistic models, which is demonstrated by the errors introduced by uncorrelated Gaussian models in the simulation scenarios.

Third, probabilistic GLD-FKML models are able to represent the characterization data in terms of correlated and potentially non-Gaussian components.

Fourth, the required modeling accuracy may depend on the simulation scenarios for model applications. Although they are inaccurate, uncorrelated Gaussian models can lead to feasible simulation results in particular scenarios, for example when determining the NFET and PFET off-current distributions. In general, however, they have to be treated with caution. Furthermore, the fact that correlated Gaussian models and probabilistic GLD-FKML models perform equally well in the simulation scenarios leads to the conclusion that, at least to a certain extent, some non-Gaussian components may be represented by Gaussian distributions.

5.2 Probabilistic Standard Cell Performance Modeling & Statistical Gate Level Digital Circuit Analysis

To efficiently evaluate variability information in digital circuit design and analysis, they need to be transferred from the transistor level to higher levels of abstraction, in particular to the gate level. This section demonstrates how probabilistic GLD-FKML models can be applied for this purpose. Based on [LJH+13, LSJ+14, LSJ+16], statistical standard cell characterization is outlined, probabilistic models are derived for selected standard cells in a preliminary $28\,nm$ technology, and the principles of statistical gate level analyses based on probabilistic standard cell models are introduced.

5.2.1 Statistical Standard Cell Characterization

To be accessed by dedicated digital circuit design and analysis tools, the standard cell performance parameters are stored in libraries that contain particular models, for example non-linear delay models or current source models [BC09, KJS12]. During characterization, the standard cell performance parameters, that is the standard cell responses to different input signals and output loads, are obtained from circuit simulations.

In the conventional standard cell characterization flow, which is schematically depicted in Fig. 5.7(a), standard cell models are generated considering different combinations of environmental conditions and process parameters. Applying deterministic and

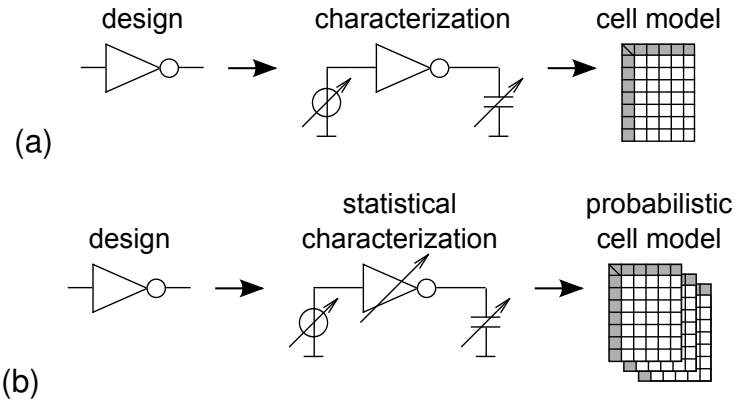

Fig. 5.7: Flow for standard cell modeling; (a) conventional method; (b) extension to generate probabilistic standard cell models

worst-case statistical corners or statistical corners, it is assumed to obtain the extreme standard cell behaviors, so-called corner models. To enable probabilistic modeling, according to the discussions in Sec. 4.2, the characterization methodology needs to be modified: MC circuit simulations replace corner simulations to mimic process variations and atomic-level fluctuations and two instances per standard cell under consideration with identical global but independent local variation parameters have to be analyzed. This statistical standard cell characterization, which is illustrated in Fig. 5.7(b), evaluates statistical device models and generates sample characterization data $\tilde{\boldsymbol{Y}}_{\mathbf{char}}$ for calibrating probabilistic models. The method creates a significant computational effort, which is required to derive the complete probabilistic GLD-FKML models, nevertheless.

5.2.2 Probabilistic Modeling of Selected Standard Cells

The probabilistic modeling of standard cells is demonstrated at five standard cells in a preliminary $28\,nm$ technology, an AND2 gate ($\mathrm{AN2}$), a buffer (BUF), an inverter (INV), a NAND2 gate ($\mathrm{ND2}$), and a NOR2 gate ($\mathrm{NR2}$), with selected static and dynamic performance parameters [LSJ+14, LSJ+16].

1. *Static performance parameters* – For all static input signal combinations, the state-dependent leakage power is obtained. Consequently, the buffer and the inverter are analyzed at the input pin signals $a=0$ and $a=1$; the AND2 gate, the NAND2 gate, and the NOR2 gate are analyzed at the input pin signal combinations $a=b=0$, $a=0$ and $b=1$, $a=1$ and $b=0$, as well as $a=b=1$.
2. *Dynamic performance parameters* – In this study, delays and dynamic energies are the considered dynamic standard cell performance parameters. Simultaneously switching input signals are not considered. Exponential voltage sources switch the input pins under analysis from logic 0 to logic 1 and vice versa with two time constants, $\tau=2.5\,ps$ and $\tau=5\,ps$, and two different output loads, $C_L=5\,fF$ and $C_L=10\,fF$, are combined to 4 fall delays and 4 rise delays as well as 4 fall energies and 4 rise energies for each input pin of the standard cells. For the AND2, the NAND2, and the NOR2 gate, the second input pin is kept constant at the logic level that allows the switching event to propagate through the standard cell.

In summary, this study includes 144 performance parameters. For the buffer and the inverter, 2 leakage power values, 8 delays, and 8 dynamic energies are taken into account. For the AND2 gate, the NAND2 gate, and the NOR2 gate, 4 leakage power

values, 16 delays, and 16 dynamic energies are considered. The statistical standard cell characterization generates sample data

$$\tilde{\boldsymbol{Y}}_{\mathbf{char}} = \left(\tilde{\boldsymbol{Y}}^{[1]}_{\mathbf{AN2}}, \tilde{\boldsymbol{Y}}^{[2]}_{\mathbf{AN2}}, \tilde{\boldsymbol{Y}}^{[1]}_{\mathbf{BUF}}, \tilde{\boldsymbol{Y}}^{[2]}_{\mathbf{BUF}}, \tilde{\boldsymbol{Y}}^{[1]}_{\mathbf{INV}}, \tilde{\boldsymbol{Y}}^{[2]}_{\mathbf{INV}}, \tilde{\boldsymbol{Y}}^{[1]}_{\mathbf{ND2}}, \tilde{\boldsymbol{Y}}^{[2]}_{\mathbf{ND2}}, \tilde{\boldsymbol{Y}}^{[1]}_{\mathbf{NR2}}, \tilde{\boldsymbol{Y}}^{[2]}_{\mathbf{NR2}} \right). \tag{5.3}$$

The sample size is arbitrarily set to $N_{\mathrm{char}} = 1000$ to allow a sufficient significance of the modeling results [LSJ+14, LSJ+16].

As a first evaluation step, SW tests with $(1-\alpha_c) = 0.95$ confidence level test the characterization data $\tilde{\boldsymbol{Y}}_{\mathbf{char}}$ for Gaussian distributions. The test results are listed in App. C.2 and summarized in the bar plots in Fig. 5.8. They reveal that only 28 dynamic energy distributions, that is $44\,\%$ of the dynamic energy distributions, can be considered Gaussian. They are all fall energy distributions of the inverter, the NAND2 gate, and the NOR2 gate; all NAND2 rise energy distributions related to the input pin a; the AND2 fall energy distributions related to input pin b at $\tau = 5\,ps$; and the AND2 rise energy distributions related to input pin a at $\tau = 2.5\,ps$. Contrastingly, the remaining standard cell performance parameter distributions are significantly non-Gaussian: the leakage power distributions, as expected and already taken into account in the state of the art; all delay distributions; and the remaining $56\,\%$ of the dynamic energy

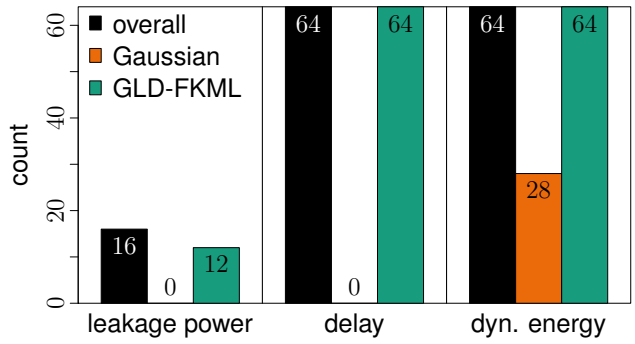

Fig. 5.8: Statistical test results for standard cell performance parameter distributions; bar plots of numbers of overall components, numbers of valid Gaussian approximations according to SW tests, and numbers of valid GLD-FKML approximations according to KS tests grouped by leakage power, delay, and dynamic energy; confidence level $(1-\alpha_c) = 0.95$; interpretation example: there are 64 distributions of dynamic energies in the sample $\tilde{\boldsymbol{Y}}_{\mathbf{char}}$, 28 of them can be considered Gaussian, and all of them can accurately be approximated by GLD-FKMLs; compare Fig. 3 in [LSJ+14] and see Fig. 8 in [LSJ+16]

distributions. This confirms the criticism of the state of the art and justifies a more advanced modeling approach, such as the GLD-FKML in (4.4).

All standard cell performance parameter distributions are approximated by GLD-FKMLs by applying the *R* function *FitGLD* in App. B.2. From the selected modeling results that are illustrated in the Q-Q plots in Fig. 5.9, a good agreement between the characterization data and the GLD-FKML approximations can be observed for non-Gaussian distributions, such as in Fig. 5.9(a)–(d), and for Gaussian distributions, such as dynamic energy distribution in Fig. 5.9(e) [LJH+13, LSJ+14, LSJ+16].

KS tests with $(1-\alpha_c)=0.95$ confidence level investigate the GLD-FKML approximations by comparing $N_s=10^5$ samples from the approximations with the characterization data. The corresponding test results are added to the tables in App. C.2 and the bar plots in Fig. 5.8. They confirm that the GLD-FKML approximations accurately represent all delay and dynamic energy distributions as well as $75\,\%$ of the leakage power distributions. However, four leakage power distributions, that is $25\,\%$, cannot be accurately approximated: the buffer leakage power distribution for the input $\mathrm{a}=1$, the NAND2 leakage power distributions for the inputs $\mathrm{a}=0$ and $\mathrm{b}=1$ as well as $\mathrm{a}=1$ and $\mathrm{b}=0$, and the NOR2 leakage power distribution for the inputs $\mathrm{a}=\mathrm{b}=0$. Representative for these distributions, Fig. 5.9(c) depicts the buffer leakage power distribution

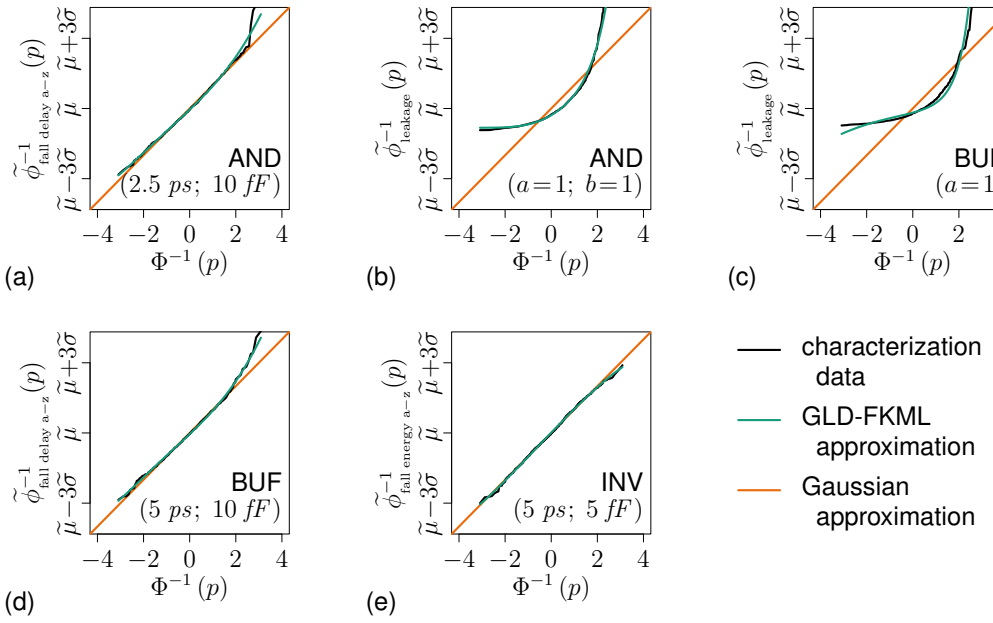

Fig. 5.9: Selected standard cell performance parameter distributions and their approximations; compare Fig. 9 in [LSJ+16]

for the input $\mathrm{a}=1$. Since slight deviations between the characterization data and the GLD-FKML approximation can only be observed in the lower distribution tails, that is for low leakage power values, they can be considered less critical. In conclusion, while the assumption of Gaussian distributions is often wrong, the GLD-FKML is an approach that adequately models the characterization data without prior data transformations.

The second important task in probabilistic modeling is to preserve correlations. Applying (4.11)–(4.13) in Sec. 4.2, the intra-instance Spearman's rank correlation matrices $\mathbf{R}_{\mathbf{AN2}}$, $\mathbf{R}_{\mathbf{BUF}}$, $\mathbf{R}_{\mathbf{INV}}$, $\mathbf{R}_{\mathbf{ND2}}$, and $\mathbf{R}_{\mathbf{NR2}}$; the inter-instance correlation matrices $\mathbf{R}_{\mathbf{AN2,AN2}}$, $\mathbf{R}_{\mathbf{BUF,BUF}}$, $\mathbf{R}_{\mathbf{INV,INV}}$, $\mathbf{R}_{\mathbf{ND2,ND2}}$, and $\mathbf{R}_{\mathbf{NR2,NR2}}$; as well as the inter-element correlation matrices, such as $\mathbf{R}_{\mathbf{AN2,BUF}}$ or $\mathbf{R}_{\mathbf{AN2,INV}}$, can be determined. Subsequently, to support the improved sampling approach in Sec. 4.3.2, these matrices are converted into the corresponding covariance matrices.

For a selected set of performance parameters, test sample data from the probabilistic standard cell models of the size $N_s=1000$ are contrasted with the characterization data in the scatterplot matrix in Fig. 5.10. The good agreement of the clusters of points indicates the high accuracy in the correlations captured by the probabilistic GLD-FKML standard cell performance models: intra-instance correlations, such as within the inverter instance $\mathrm{INV}^{[1]}$ or within the buffer instance $\mathrm{BUF}^{[1]}$; inter-instance correlations, such as between the inverter instances $\mathrm{INV}^{[1]}$ and $\mathrm{INV}^{[2]}$; as well as inter-element correlations, such as between the inverter instances $\mathrm{INV}^{[1]}$ or $\mathrm{INV}^{[2]}$ and the buffer instance $\mathrm{BUF}^{[1]}$. Quantitatively, the maximum absolute differences between the rank correlation coefficients derived from the characterization data and the test sample data are in the range of 0.05 to 0.07 and hence very small. They can be reduced below 0.02 by increasing the test sample size N_s by an order of magnitude.

In summary, the probabilistic GLD-FKML models describe the standard cell performance variability with a high accuracy. This includes marginal distributions, supporting non-Gaussian and Gaussian components without prior data transformations, as well as intra-instance, inter-instance, and inter-element correlations [LJH+13, LSJ+14, LSJ+16].

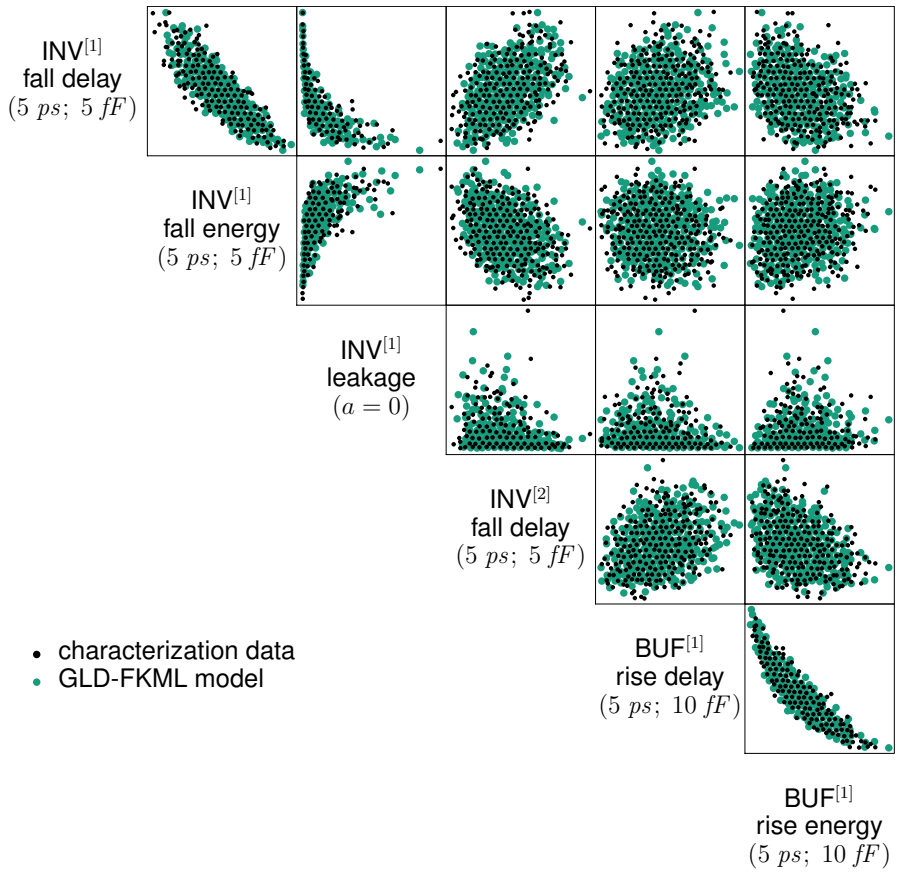

Fig. 5.10: Scatterplot matrix of selected standard cell performance parameter distributions; arbitrary units; $^{[k]}$ identifies instance k of the respective logic gate; INV: inverter; BUF: buffer; see Fig. 4 in [LSJ+14]

5.2.3 Outline of Statistical Gate Level Analyses

To evaluate probabilistic standard cell performance models in statistical gate level analyses, the underlying analysis approaches have to be adapted. The basic procedures are illustrated at the circuits in Fig. 5.11: an AND4 circuit, which is composed of two NAND2 instances $\mathrm{ND2}^{[1]}$ and $\mathrm{ND2}^{[2]}$ as well as a NOR2 instance $\mathrm{NR2}^{[1]}$, and a NAND4 circuit, which is composed of an AND4 circuit and an inverter instance $\mathrm{INV}^{[1]}$.

As an example, the circuit leakage power consumption is investigated. As introduced in Sec. 3.4, in a gate level analysis, it is computed as the sum of the state-dependent leakage power consumptions of all standard cell instances. In particular, for the static circuit input signals $A=D=1$ and $B=C=0$ with their resulting internal logic states being added to Fig. 5.11, the circuit leakage power consumptions are [LSJ+16]

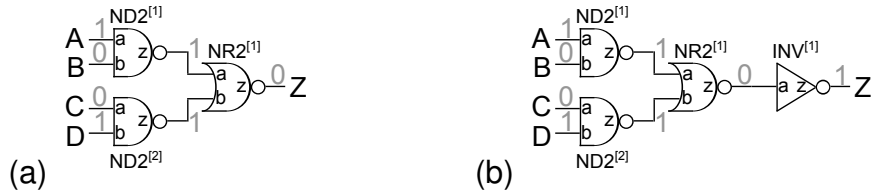

Fig. 5.11: Gate level schematics of (a) an AND4 circuit and (b) a NAND4 circuit; $^{[k]}$ identifies instance k of the corresponding cell; compare Fig. 5 in [LSJ+14] and Fig. 11 in [LSJ+16]

$$P_{\text{leak; AND4}}^{(\text{A=D=1, B=C=0})} = P_{\text{leak; ND2}^{[1]}}^{(\text{a=1,b=0})} + P_{\text{leak; ND2}^{[2]}}^{(\text{a=0,b=1})} + P_{\text{leak; NR2}^{[1]}}^{(\text{a=1,b=1})} \qquad \text{and} \tag{5.4}$$

$$P_{\text{leak; NAND4}}^{(\text{A=D=1, B=C=0})} = P_{\text{leak; ND2}^{[1]}}^{(\text{a=1,b=0})} + P_{\text{leak; ND2}^{[2]}}^{(\text{a=0,b=1})} + P_{\text{leak; NR2}^{[1]}}^{(\text{a=1,b=1})} + P_{\text{leak; INV}^{[1]}}^{(\text{a=0})}. \tag{5.5}$$

In (5.4) and (5.5), $P_{\text{leak; ND2}^{[1]}}^{(\text{a=1,b=0})}$ is the leakage power of the NAND2 instance ND2$^{[1]}$ at its inputs $a=1$ and $b=0$, and the remaining quantities are defined analogously. When accounting for variability by applying the probabilistic standard cell performance models derived in Sec. 5.2.2, the variability of the AND4 circuit and the NAND4 circuit can be described by the RVs

$$\boldsymbol{Y}_{\mathbf{AND4}} = \left(\boldsymbol{Y}_{\mathbf{ND2}}^{[1]}, \boldsymbol{Y}_{\mathbf{ND2}}^{[2]}, \boldsymbol{Y}_{\mathbf{NR2}}^{[1]}\right) \qquad \text{and} \tag{5.6}$$

$$\boldsymbol{Y}_{\mathbf{NAND4}} = \left(\boldsymbol{Y}_{\mathbf{ND2}}^{[1]}, \boldsymbol{Y}_{\mathbf{ND2}}^{[2]}, \boldsymbol{Y}_{\mathbf{NR2}}^{[1]}, \boldsymbol{Y}_{\mathbf{INV}}^{[1]}\right). \tag{5.7}$$

From these RVs, random samples $\tilde{\boldsymbol{Y}}_{\mathbf{AND4}}$ and $\tilde{\boldsymbol{Y}}_{\mathbf{NAND4}}$ of the size N_{gate} can be generated to enable sampling-based statistical gate level analyses. For the small example circuits, the conventional sampling approach in Sec. 4.3.1 can be used. It is based on the Spearman's rank correlation matrices [LSJ+14, LSJ+16]

$$\mathbf{R}_{\mathbf{Y}_{\mathbf{AND4}}} = \begin{pmatrix} \mathbf{R}_{\mathbf{ND2}} & \mathbf{R}_{\mathbf{ND2}} & \mathbf{R}_{\mathbf{NR2}} \\ \mathbf{R}_{\mathbf{ND2,ND2}} & \mathbf{R}_{\mathbf{ND2}} & \mathbf{R}_{\mathbf{ND2}} \\ \mathbf{R}_{\mathbf{ND2,NR2}}^{\mathrm{T}} & \mathbf{R}_{\mathbf{ND2,NR2}}^{\mathrm{T}} & \mathbf{R}_{\mathbf{NR2}} \end{pmatrix} \qquad \text{and} \tag{5.8}$$

$$\mathbf{R}_{\mathbf{Y}_{\mathbf{NAND4}}} = \begin{pmatrix} \mathbf{R}_{\mathbf{ND2}} & \mathbf{R}_{\mathbf{ND2}} & \mathbf{R}_{\mathbf{NR2}} & \mathbf{R}_{\mathbf{ND2,INV}} \\ \mathbf{R}_{\mathbf{ND2,ND2}} & \mathbf{R}_{\mathbf{ND2}} & \mathbf{R}_{\mathbf{ND2}} & \mathbf{R}_{\mathbf{ND2,INV}} \\ \mathbf{R}_{\mathbf{ND2,NR2}}^{\mathrm{T}} & \mathbf{R}_{\mathbf{ND2,NR2}}^{\mathrm{T}} & \mathbf{R}_{\mathbf{NR2}} & \mathbf{R}_{\mathbf{NR2,INV}} \\ \mathbf{R}_{\mathbf{ND2,INV}}^{\mathrm{T}} & \mathbf{R}_{\mathbf{ND2,INV}}^{\mathrm{T}} & \mathbf{R}_{\mathbf{NR2,INV}}^{\mathrm{T}} & \mathbf{R}_{\mathbf{INV}} \end{pmatrix}. \tag{5.9}$$

However, in general, the improved sampling approach in Sec. 4.3.2 is preferred to achieve a reasonable computational effort.

Since the samples $\tilde{\boldsymbol{Y}}_{\mathbf{AND4}}$ and $\tilde{\boldsymbol{Y}}_{\mathbf{NAND4}}$ contain more information than required for the leakage power analysis applying (5.4) or (5.5), the corresponding components have to be extracted: the leakage power of the NAND2 instance $\mathrm{ND2}^{[1]}$ at the input signal combination $a=1$ and $b=0$, the leakage power of the NAND2 instance $\mathrm{ND2}^{[2]}$ at the input signal combination $a=0$ and $b=1$, the leakage power of the NOR2 instance $\mathrm{NR2}^{[1]}$ at the input signal combination $a=1$ and $b=1$, and the leakage power of the inverter instance $\mathrm{INV}^{[1]}$ at the input signal $a=0$ for the NAND4 circuit. With them, (5.4) and (5.5) can be applied to all sample points, embodying sampling-based statistical gate level leakage power analyses. The sample size N_{gate} can be chosen relatively large since the gate level calculations are computationally inexpensive.

Fig. 5.12 compares $N_{\mathrm{gate}}=1000$-sample statistical gate level leakage power analysis results and $N_{\mathrm{ref}}=1000$-sample MC reference circuit simulations for the AND4 and NAND4 scenarios outlined in Fig. 5.11. Their good agreements demonstrate that probabilistic standard cell performance models can be successfully applied in statistical gate level analyses, in principle. This holds for the conventional approach and the improved approach for correlated Gaussian sampling, which do not reveal significant differences in their analysis results.

Being close to the reference data, the important advantage of the illustrated statistical gate level analysis is its efficiency. While the $N_{\mathrm{ref}}=1000$-sample reference simulations for the NAND4 circuit leakage power analysis take slightly more than $30\,s$, the $N_{\mathrm{gate}}=1000$-sample gate level analyses finish in approximately $1.7\,s$ applying the

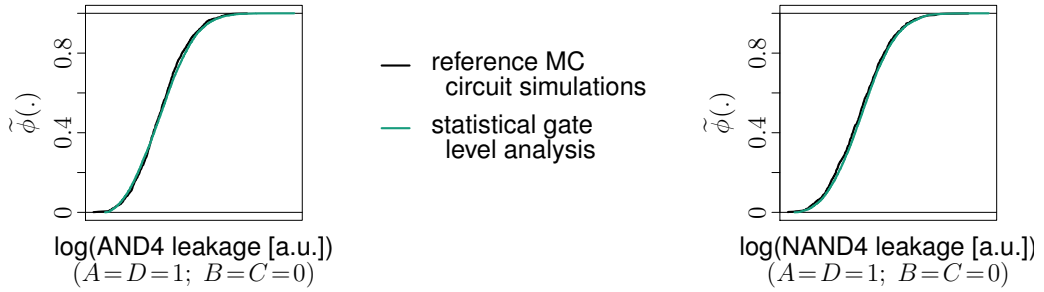

Fig. 5.12: AND4 and NAND4 leakage power distributions for the input signal combination $A=D=1$ and $B=C=0$ determined by statistical gate level analyses (improved approach for correlated Gaussian sampling) and MC reference circuit simulations; $N_{\mathrm{gate}}=N_{\mathrm{ref}}=1000$; compare Fig. 6 in [LSJ+14] and Fig. 12 in [LSJ+16]

conventional approach and in approximately $0.4\,s$ applying the improved approach for correlated Gaussian sampling, corresponding to speed-ups of $18\,X$ and $75\,X$ on a standard notebook computer. When the sample size for the gate level analysis is increased to $N_{\mathrm{gate}} = 10^4$, the analysis run times grow to $2.8\,s$ for the conventional sampling approach and $2\,s$ for the improved sampling approach, corresponding to speed-ups of $11\,X$ and $15\,X$. The differences in the run times applying the conventional and the improved approach for correlated Gaussian sampling are reduced with a growing gate level sample size N_{gate}. The reasons are the low complexity of the test circuits and the computational effort for mapping uniform components to the target marginal distributions via the GLD-FKML in (4.4) in step 4 of the sampling algorithm in Sec. 2.3.2, which is not negligible in this scenario.

If desired, other performance parameters can be extracted from the samples $\tilde{\boldsymbol{Y}}_{\mathbf{AND4}}$ and $\tilde{\boldsymbol{Y}}_{\mathbf{NAND4}}$ in (5.6) and (5.7). For example, summing the corresponding standard cell delays and dynamic energies results in the circuit propagation delay and dynamic energy consumption for a particular input signal switching event. In combination, these computations allow a joint gate level analysis of digital circuit performance variability including marginal distributions and correlations [LJH+13, LSJ+14, LSJ+16].

To reduce the complexity, the circuit-specific RVs $\boldsymbol{Y}_{\mathbf{AND4}}$ and $\boldsymbol{Y}_{\mathbf{NAND4}}$ can be constructed from the standard cell performance parameters that are required for a particular analysis only. This approach can significantly improve the analysis efficiency but neglects potential correlations of circuit performance parameters.

5.2.4 Results of the Standard Cell Modeling Scenario

After extending the conventional standard cell characterization to the statistical standard cell characterization, the probabilistic GLD-FKML modeling approach can be applied to standard cell performance models. The investigation of five standard cells in a preliminary $28\,nm$ technology reveals that most standard cell performance parameters are significantly non-Gaussian [LSJ+14, LSJ+16] so that the assumption of Gaussian distributions is wrong. However, GLD-FKML approximations usually well represent the characterization data without requiring non-linear transformations. A proper selection of the units of measurements, for instance ps for delay times, fJ for dynamic energies, and nW for leakage power values, is numerically beneficial when the *R* function *FitGLD* fits marginal distributions to GLD-FKMLs. In addition, probabilis-

tic GLD-FKML standard cell models accurately capture intra-instance, inter-instance, and inter-element correlations from the characterization data.

To apply probabilistic GLD-FKML standard cell models in statistical gate level analyses of digital circuits, the underlying analysis approaches have to be extended to generate and evaluate sample data from the models. While solutions to particular scenarios can be implemented, some challenges remain to be solved on the way to an application of probabilistic GLD-FKML models in standard digital circuit design and analysis tools. First, the circuit environment defines the input waveforms and output loads for a particular standard cell instance. Usually, table-based models, such as the non-linear delay model or current-source models [BC09, KJS12], capture the standard cell behaviors for multiple combinations of these variables, which makes statistical standard cell characterization computationally expensive. Second, how the table-based standard cell performance models can be extended to capture GLD-FKML approximations of marginal distributions as well as intra-instance, inter-instance, and inter-element correlations, remains a subject for future research. Third, standard digital circuit design and analysis tools do not necessarily enable an implementation of the approach in Sec. 2.3.2 to generate sample data for statistical gate level analyses. Consequently, standard tools cannot apply probabilistic GLD-FKML standard cell performance models up to now.

However, in a particular circuit under investigation, the input signals and output loads for each standard cell instance are known from their driving cells and fanout cones. Therefore, circuit-specific probabilistic models can be derived, for instance from the sequential circuit simulation of stages in a timing path [SKS08a, SKS08b], and applied in circuit analyses. In terms of efficiency, such an approach benefits from regular circuit structures in which many standard cell instances share their circuit environment, that is driving cells and output loads. Digital ROs, which will be detailed in Sec. 5.3, are examples for this scenario.

5.3 Statistical Digital Ring Oscillator Analysis

In this section, the variability information provided by probabilistic standard cell models are evaluated in efficient gate level analyses of digital *ring oscillator*s (ROs), which are particular digital circuits with regular structures. They consist of k stages, an odd number of inverting plus an arbitrary number of non-inverting stages, in principle. In

practice, however, ROs are usually composed of k instances of a particular inverting standard cell. Fig. 5.13 depicts two examples: an inverter-based digital RO and a NAND2-based digital RO. As the previous section, this study is based on a preliminary $28\,nm$ technology [LSJ+16].

5.3.1 Analysis Approach

The RO performance parameters are its oscillation frequency f, its on-power P_{on}, that is its power consumption when oscillating, and its off-power P_{off}, that is its power consumption in idle mode if appropriate. As indicated by the schematic signal waveforms in Fig. 5.14, per oscillation, each instance is switched from logic 0 to logic 1 and vice versa. Consequently, the oscillation period T_{RO}, the reciprocal of the oscillation frequency f, can be calculated as the sum of the rise and fall delays, $t_{\mathrm{r;[i]}}$ and $t_{\mathrm{f;[i]}}$, of all oscillator stages [LSJ+16],

$$T_{\mathrm{RO}} = \frac{1}{f} = \sum_{i=1}^{k} \left(t_{\mathrm{r;[i]}} + t_{\mathrm{f;[i]}} \right) . \tag{5.10}$$

If necessary, wiring delays can be added to (5.10).

For these switching events, the dynamic rise and fall energies, $W_{\mathrm{r;[i]}}$ and $W_{\mathrm{f;[i]}}$, are required at each stage i. In addition, between the switching events, each standard

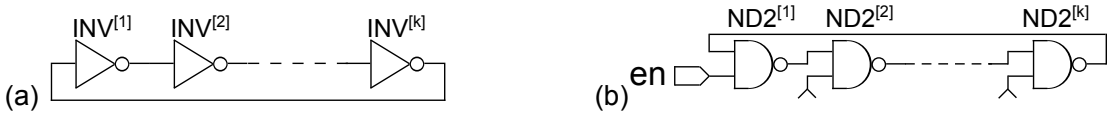

Fig. 5.13: Gate level schematics; (a) inverter-based RO; (b) NAND2-based RO

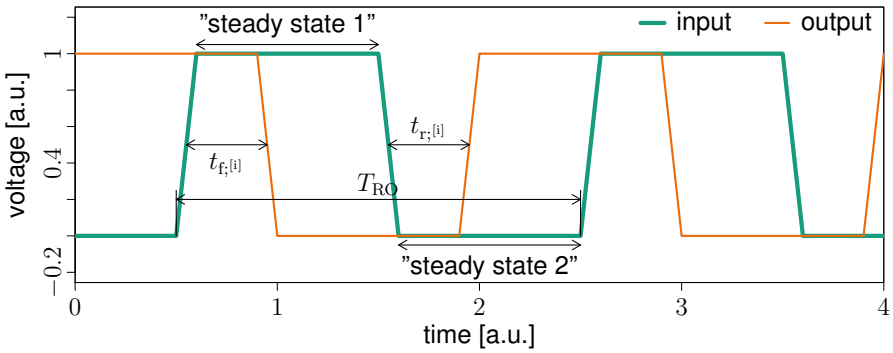

Fig. 5.14: Schematic input and output signal waveforms at stage i of a RO

cell instance has two “steady states” in which leakage power $P^{(\mathrm{st1})}_{\mathrm{leak};[\mathrm{i}]}$ and $P^{(\mathrm{st2})}_{\mathrm{leak};[\mathrm{i}]}$ is consumed. Neglecting signal transition times, it can be assumed that both “steady states” last for half of the oscillation period T_{RO}. In summary, the total energy required per oscillation W_{on} and the on-power P_{on} can be calculated from [LSJ+16]

$$W_{\mathrm{on}} = \sum_{i=1}^{k} \left(W_{\mathrm{r};[\mathrm{i}]} + W_{\mathrm{f};[\mathrm{i}]} \right) + \frac{T_{\mathrm{RO}}}{2} \left(\sum_{i=1}^{k} \left(P^{(\mathrm{st1})}_{\mathrm{leak};[\mathrm{i}]} + P^{(\mathrm{st2})}_{\mathrm{leak};[\mathrm{i}]} \right) \right) \qquad \text{and} \tag{5.11}$$

$$P_{\mathrm{on}} = \frac{W_{\mathrm{on}}}{T_{\mathrm{RO}}} = W_{\mathrm{on}} \cdot f. \tag{5.12}$$

Most digital ROs, such as the NAND2-based RO in Fig. 5.13(b), can be enabled and disabled via a control signal. When disabled, all stages are forced into static states so that each instance consumes state-dependent leakage power $P^{(\mathrm{state})}_{\mathrm{leak};[\mathrm{i}]}$. The RO off-power P_{off} can then be calculated as the sum of the stage leakage power consumptions [LSJ+16]:

$$P_{\mathrm{off}} = \sum_{i=1}^{k} P^{(\mathrm{state})}_{\mathrm{leak};[\mathrm{i}]}. \tag{5.13}$$

In summary, (5.10)–(5.13) provide a general basis for gate-level digital RO performance evaluations. However, some details directly depend on the structure and the configuration of the RO under consideration. First, the switching events depend on the connected standard cell pins. Second, the particular connection of the stages and potential additional loads determine input signal waveforms and output loads at each instance. Third, the logic states for leakage power consumptions of each instance are specific for a certain RO implementation.

5.3.2 Characterization and Model Calibration

As already introduced, a specialty of most digital ROs is their regular structure: many stages have the same circuit environments in terms of driving cells and output loads. Examples are the inverter-based RO and the NAND2-based RO in Fig. 5.13. Further test scenarios in this section are ROs composed of NOR2 instances.

In these application cases, each stage can be considered an instance of a single standard cell model containing delays and dynamic energies for this particular circuit

environment as well as static leakage power values. The standard cell model can directly be derived from a MC circuit simulation of a RO. During statistical characterization of the standard cell instances in the ROs in Fig. 5.13, $k=9$ stage oscillators provide the best trade-offs between characterization effort and model accuracy: the characterization data is determined from 2 stages, and the remaining 7 stages slow down the oscillation to achieve full signal swings, which are mandatory for a reasonable model accuracy. These simulations generate the characterization data

$$\begin{aligned} \tilde{\boldsymbol{Y}}_{\mathbf{char,INV}} &= \left(\tilde{\boldsymbol{Y}}^{[1]}_{\mathbf{INV}}, \tilde{\boldsymbol{Y}}^{[2]}_{\mathbf{INV}}\right), \tilde{\boldsymbol{Y}}_{\mathbf{char,ND2}} = \left(\tilde{\boldsymbol{Y}}^{[1]}_{\mathbf{ND2}}, \tilde{\boldsymbol{Y}}^{[2]}_{\mathbf{ND2}}\right), \text{and} \\ \tilde{\boldsymbol{Y}}_{\mathbf{char,NR2}} &= \left(\tilde{\boldsymbol{Y}}^{[1]}_{\mathbf{NR2}}, \tilde{\boldsymbol{Y}}^{[2]}_{\mathbf{NR2}}\right) \end{aligned} \tag{5.14}$$

with the sample sizes $N_{\mathrm{char}} \in \{200, 500, 1000\}$ as inputs to calibrate the RO-internal inverter, NAND2, and NOR2 models. For the inverter instances, state-dependent leakage power consumption is not taken into account.

SW tests with $(1-\alpha_c)=0.95$ confidence level are performed to test the characterization data for Gaussian distributions. For the $N_{\mathrm{char}}=200$-sample characterization data, the test results are summarized in Tab. 5.3. They reveal that the distributions of the dynamic energies, the NAND2 delays, as well as the NOR2 delays can be considered Gaussian while the inverter delays as well as all leakage power distributions cannot. For the larger characterization sample sizes $N_{\mathrm{char}}=500$ and $N_{\mathrm{char}}=1000$, smaller

Tab. 5.3: Results of statistical tests for $N_{\mathrm{char}}=200$-sample characterization data; SW tests of components of characterization data with results **+**: *Gaussian* and –: *non-Gaussian*; KS tests comparing characterization data and GLD-FKML approximations of marginal distributions with results **o**: *accurate approximation* and x: *inaccurate approximation*; confidence level $(1-\alpha_c)=0.05$; compare TABLE II in [LSJ+16]

Performance parameter	**Inverter**		**NAND2**		**NOR2**	
	SW test	**KS test**	**SW test**	**KS test**	**SW test**	**KS test**
t_{r}	–	**o**	**+**	**o**	**+**	**o**
t_{f}	–	**o**	**+**	**o**	**+**	**o**
W_{r}	**+**	**o**	**+**	**o**	**+**	**o**
W_{f}	**+**	**o**	**+**	**o**	**+**	**o**
$P_{\mathrm{leak}}^{(\mathrm{a=0,b=0})}$			–	**o**	–	**o**
$P_{\mathrm{leak}}^{(\mathrm{a=0,b=1})}$			–	**o**	–	**o**
$P_{\mathrm{leak}}^{(\mathrm{a=1,b=0})}$			–	x	–	**o**
$P_{\mathrm{leak}}^{(\mathrm{a=1,b=1})}$			–	**o**	–	**o**

deviations become significant. The test results in App. C.3.1 reveal that the NAND2 delays, the NOR2 rise delay, and the NAND2 rise energy tend to be slightly non-Gaussian as well.

Practically independent of their shapes and without prior data transformations, the marginal distributions can be approximated by GLD-FKMLs for the different characterization sample sizes. The model accuracy is evaluated by KS tests that compare the characterization data with $N_s = N_{\mathrm{char}}$ samples from the GLD-FKML approximations at a $(1-\alpha_c) = 0.95$ confidence level. The test results in Tab. 5.3 and App. C.3.1 attest the high modeling accuracy for delay, dynamic energy, and leakage power distributions. The only exception is the NAND2 leakage power at the inputs $a = 1$ and $b = 0$, $P_{\mathrm{leak}}^{(a=1,b=0)}$.

The Q-Q plots of the NAND2 performance parameter distributions on the diagonal of the scatterplot matrix in Fig. 5.15 illustrate the accuracy of the GLD-FKML approximations of the Gaussian and the non-Gaussian components. This statement also holds for the NAND2 leakage power distribution at the inputs $a = 1$ and $b = 0$ for which the GLD-FKML approximation is reported inaccurate by the KS test. In contrast, while describing the delay and the dynamic energy distributions without large deviations, Gaussian approximations of the standard cell leakage power distributions over-estimate the lower tails and under-estimate the upper tails.

In addition to the marginal distributions, intra-instance and inter-instance correlations are extracted from the characterization data. Being representative for all models derived in this section, the scatterplot matrix of the NAND2 performance parameters in Fig. 5.15 indicates that the probabilistic GLD-FKML model well captures the correlations in the characterization data. These results also apply to the performance parameters of the RO-internal inverters and NOR2 gates with the corresponding scatterplot matrices being illustrated in App. C.3.2.

5.3.3 Application Examples with Accuracy and Performance Evaluations

Instances of the inverter (INV), the NAND2 gate ($\mathrm{ND2}$), or the NOR2 gate ($\mathrm{NR2}$) can be connected to digital ROs of different lengths according to Fig. 5.13. Similar to the NAND2-based ROs, the NOR2-based ROs can be enabled and disabled via a control signal connected to the input pin b of the first stage, and the input pins b of the

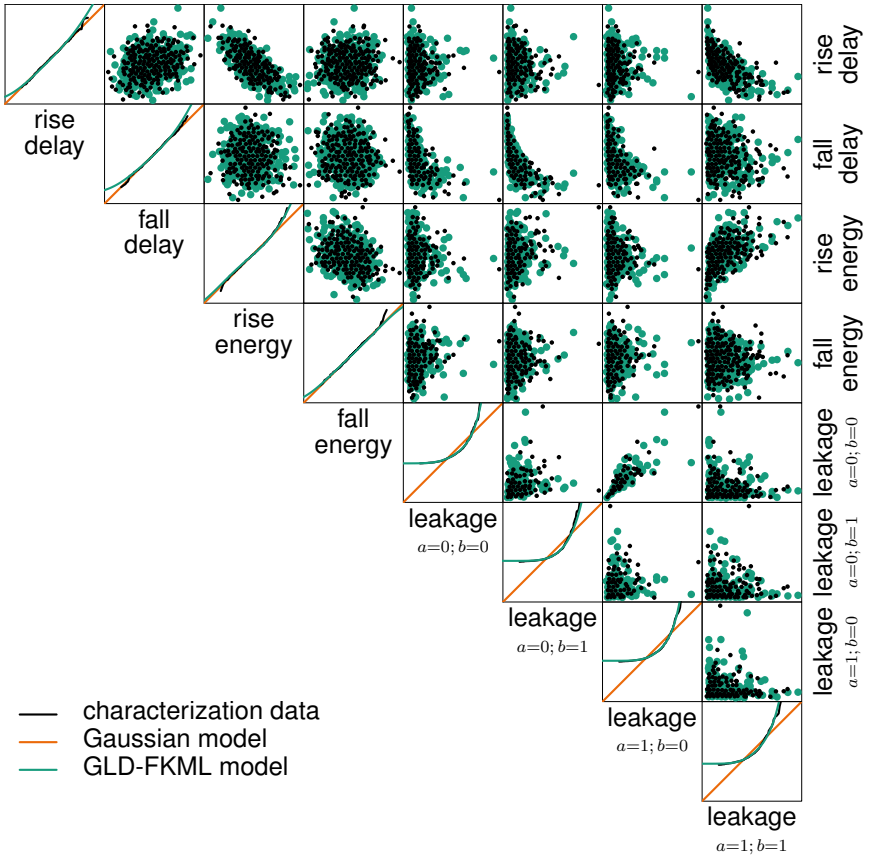

Fig. 5.15: RO-internal probabilistic NAND2 model; $N_{\mathrm{char}} = 500$; Gaussian approximations and GLD-FKML approximations of marginal distributions; scatter plots from $N_s = 500$ samples from NAND2 model; correlations in Gaussian model not shown

remaining stages are tied to logic 0. In this study, the numbers of stages are varied from $k = 3$ to $k = 69$.

While reference data are obtained from very costly $N_{\mathrm{ref}} = 200$-sample MC circuit simulations, a statistical gate level RO analysis can drastically reduce this effort. After generating sample data of standard cell performance parameters from the probabilistic standard cell models, (5.10)–(5.13) can be evaluated per sample to obtain sample data of the RO performance parameters: the frequency f, the on-power P_{on}, and the off-power P_{off}. While the off-power of any inverter-based RO is neglected in this study, (5.13) needs to be adapted to the NAND2-based ROs and the NOR2-based ROs to consider the corresponding static states in idle mode [LSJ+16]: the calculation

$$P_{\mathrm{off}} = P^{(\mathrm{a=1,b=0})}_{\mathrm{leak;ND2}^{[1]}} + \sum_{i=1}^{k/2} P^{(\mathrm{a=1,b=1})}_{\mathrm{leak;ND2}^{[2i]}} + \sum_{i=1}^{k/2} P^{(\mathrm{a=0,b=1})}_{\mathrm{leak;ND2}^{[2i+1]}} \tag{5.15}$$

has to be applied to the NAND2-based ROs; the calculation

$$P_{\text{off}} = P_{\text{leak;NR2}^{[1]}}^{(\text{a=0,b=1})} + \sum_{i=1}^{k/2} P_{\text{leak;NR2}^{[2i]}}^{(\text{a=0,b=0})} + \sum_{i=1}^{k/2} P_{\text{leak;NR2}^{[2i+1]}}^{(\text{a=1,b=0})} \tag{5.16}$$

has to be applied to the NOR2-based ROs. Due to the efficient generation of random samples from the probabilistic models, a large sample size N_{gate} can be used in the gate level analyses to ensure a reasonable accuracy. It is arbitrarily set to $N_{\text{gate}} = 10^4$.

The gate level analyses are performed with probabilistic GLD-FKML and correlated Gaussian standard cell performance models for comparison purposes. Selected but representative RO analysis results are summarized in the scatterplot matrices in Fig. 5.16. For the probabilistic GLD-FKML models and the reference MC circuit simulation results, the Q-Q plots demonstrate a good agreement in the marginal distributions, and the scatter plots demonstrate a good agreement in the correlations

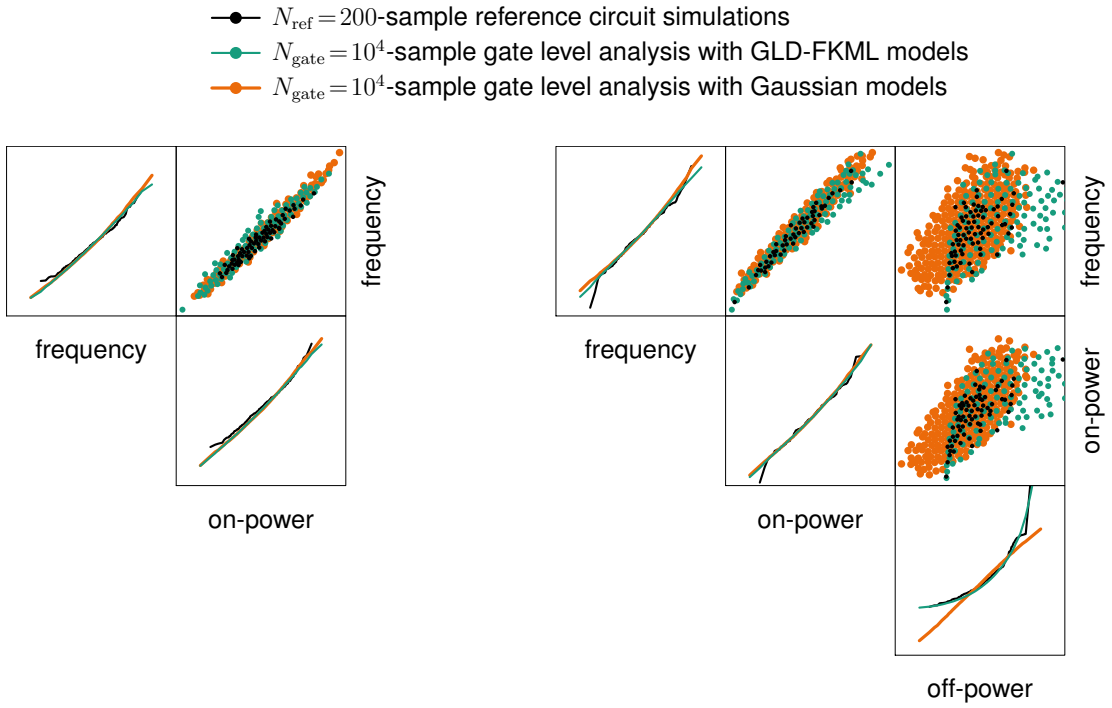

(a) (b)

Fig. 5.16: Example scatterplot matrices of performance parameters of (a) the $k = 55$-stage inverter-based RO and (b) the $k = 57$-stage NAND2-based RO; Q-Q plots of marginal distributions on main diagonal; characterization sample size (a) $N_{char} = 200$ and (b) $N_{char} = 1000$; compare Figs. 15 and 16 in [LSJ+16]

of the RO performance parameters. Hence, statistical gate level digital RO analyses based on probabilistic GLD-FKML models yield accurate results. However, correlated Gaussian models appear to be feasible to determine the RO frequency and on-power distributions as well, but they do not suit off-power computations.

To evaluate the analysis accuracy, KS tests with a $(1-\alpha_c)=0.95$ confidence level compare the gate level analysis results with the reference MC circuit simulation results. The test results are visualized in App. C.3.3 and summarized in Tab. 5.4. As indicated in Fig. 5.16, correlated Gaussian models and probabilistic GLD-FKML models perform similarly in RO frequency and on-power computations even if the stage delay or dynamic energy distributions are slightly non-Gaussian. However, accurately representing a slightly larger ratio of the reference distributions, the probabilistic GLD-FKML models appear more accurate. Nevertheless, the inaccuracies in Gaussian models for standard cell leakage power distributions transfer to significant errors in statistical gate level leakage power analyses. As in Fig. 5.16(b), the upper tails of the RO off-power distributions are under-estimated and the lower tails are over-estimated, corresponding to too optimistic analysis results with even unphysical negative values being obtained. In contrast, the RO off-power computations applying probabilistic GLD-FKML models appear to be feasible in the majority of the scenarios. The demonstrated universality of probabilistic GLD-FKML models, which can be equally applied to multiple performance parameters without requiring non-linear data transformations, is their major benefit with respect to Gaussian modeling approaches.

Tab. 5.4: Summary of $(1-\alpha_c)=0.95$-confidence level KS tests for RO performance parameter distributions; comparison of $N_{\mathrm{ref}}=200$-sample circuit simulation results and $N_{\mathrm{gate}}=10^4$-sample statistical gate level analysis results based on correlated Gaussian models and probabilistic GLD-FKML models; ratio of accepted null-hypotheses indicating ratio of accurate gate level analyses in $\%$

$\mathbf{N_{char}}$	**RO performance parameter**	**Gaussian models**			**GLD-FKML models**		
		INV	NAND2	NOR2	INV	NAND2	NOR2
200	f	62	88	76	74	88	82
	P_{on}	15	88	59	24	88	59
	P_{off}	–	9	12	–	41	62
500	f	91	85	74	94	88	82
	P_{on}	68	88	79	76	88	76
	P_{off}	–	0	3	–	35	53
1000	f	91	74	71	94	79	82
	P_{on}	47	76	59	71	79	74
	P_{off}	–	0	0	–	47	50

Due to the errors of Gaussian models in leakage power analyses, the accuracy of the gate level RO analyses is further evaluated for the probabilistic GLD-FKML models only. The percentage errors of mean values μ and standard deviations σ,

$$\mathrm{err}_\mu = 100\,\% \cdot \left(\frac{\widetilde{\mu}_{\mathrm{gate}}}{\widetilde{\mu}_{\mathrm{ref}}} - 1 \right) \qquad \text{and} \qquad \mathrm{err}_\sigma = 100\,\% \cdot \left(\frac{\widetilde{\sigma}_{\mathrm{gate}}}{\widetilde{\sigma}_{\mathrm{ref}}} - 1 \right), \tag{5.17}$$

relate the results of the $N_{\mathrm{gate}} = 10^4$-sample gate level analyses with their mean values $\widetilde{\mu}_{\mathrm{gate}}$ and standard deviations $\widetilde{\sigma}_{\mathrm{gate}}$ to the $N_{\mathrm{ref}} = 200$-sample reference circuit simulation results mean values $\widetilde{\mu}_{\mathrm{ref}}$ and standard deviations $\widetilde{\sigma}_{\mathrm{ref}}$.

To take into account that the reference sample size $N_{\mathrm{ref}} = 200$ is not very large, confidence intervals are constructed for the standard deviations $\widetilde{\sigma}_{\mathrm{ref}}$. Assuming a Gaussian distribution, the true value of the standard deviation σ_{ref} lies in the interval [Bur74]

$$\left[\widetilde{\sigma}_{\mathrm{ref}} \cdot \sqrt{\frac{N_{\mathrm{ref}} - 1}{\chi^2_{1-\alpha_c/2;N_{\mathrm{ref}}-1}}} \,,\, \widetilde{\sigma}_{\mathrm{ref}} \cdot \sqrt{\frac{N_{\mathrm{ref}} - 1}{\chi^2_{\alpha_c/2;N_{\mathrm{ref}}-1}}} \right] \tag{5.18}$$

with $(1-\alpha_c)$ being the confidence level and $\chi^2_{a;b}$ being the a-quantile of the chi square distribution with b degrees of freedom. With $(1-\alpha_c) = 0.95$ and $N_{\mathrm{ref}} = 200$, (5.18) translates to acceptable errors of

$$\mathrm{err}_\sigma \in [-8.9\,\% \;,\; 10.9\,\%]\,. \tag{5.19}$$

Being tailored to Gaussian distributions, the confidence interval in (5.18) may be inaccurate for non-Gaussian distributions, such as the RO off-power P_{off}.

For different numbers of RO stages $3 \leq k \leq 69$, the evolutions of the statistical gate level RO analyses with respect to the reference circuit simulations are depicted in Fig. 5.17 and Fig. 5.18. From the graphs, multiple conclusions can be drawn [LSJ+16].

(I) The statistical gate level analysis approach with the probabilistic GLD-FKML models from Sec. 5.3.2 introduces considerable errors for $k = 3$-stage ROs. These ROs are too fast to allow full signal swings, which is a particular case simply not covered by the probabilistic standard cell models derived from $k = 9$-stage ROs.

(II) The modeling and analysis approaches are not affected by systematic errors for $k > 3$ stages. This is indicated by the errors in mean values and standard deviations, err_μ and err_σ, which scatter around 0.

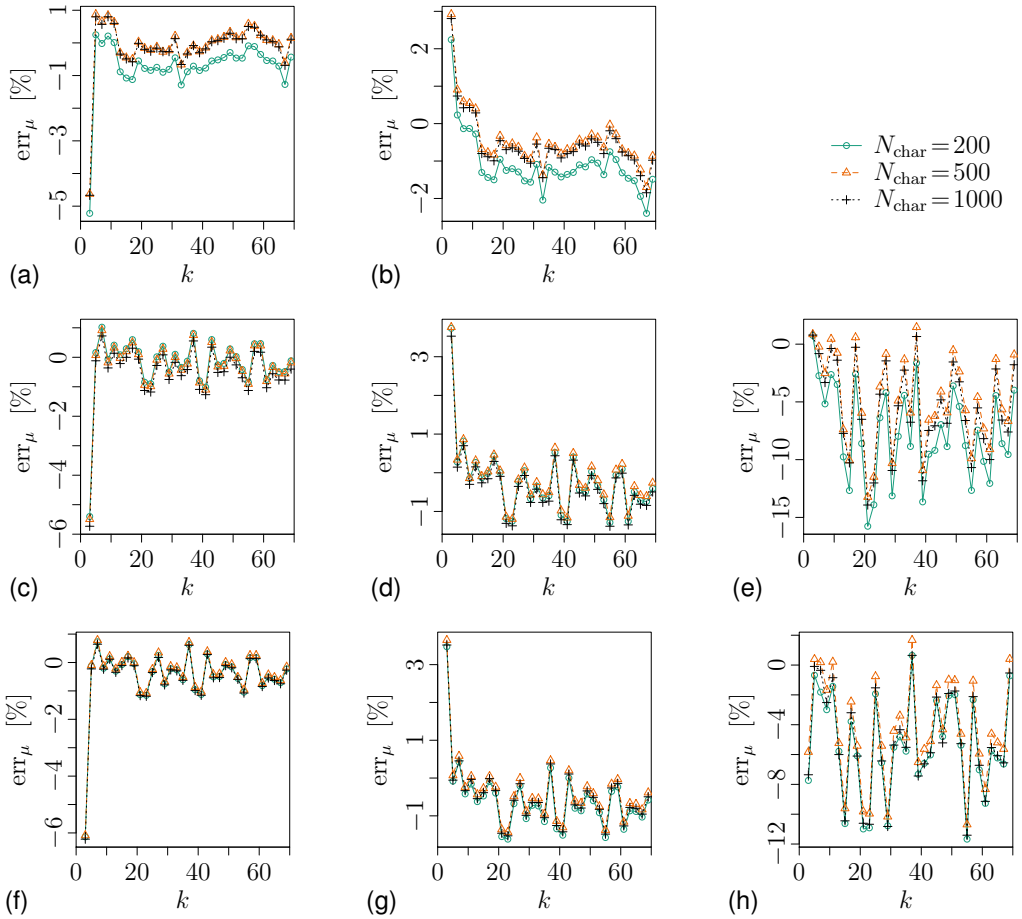

Fig. 5.17: Mean value errors err_μ of statistical gate level RO analyses depending on number of stages k according to (5.17); top: inverter-based RO with (a) frequency f and (b) on-power P_{on} center: NAND2-based RO with (c) frequency f, (d) on-power P_{on}, and (e) off-power P_{off}; bottom: NOR2-based RO with (f) frequency f, (g) on-power P_{on}, and (h) off-power P_{off}; compare Fig. 17 in [LSJ+16]

(III) For ROs with $k > 3$ stages, statistical gate level analyses based on probabilistic GLD-FKML models well represent the dynamic RO performance parameter distributions, that is the oscillation frequency f and the on-power P_{on}, with respect to the reference data. The errors in the mean values are within $|\text{err}_\mu| < 2\,\%$ and often even better. Furthermore, the majority of the standard deviations σ_{gate} is inside the confidence interval derived from the reference data by (5.18). Increasing the characterization sample size N_{char} from $N_{\text{char}} = 200$ to $N_{\text{char}} = 500$ can slightly improve the analysis errors, but a further increase to $N_{\text{char}} = 1000$ only causes additional computational effort without effecting the analysis accuracy, which is additionally underlined by the ratios in Tab. 5.4.

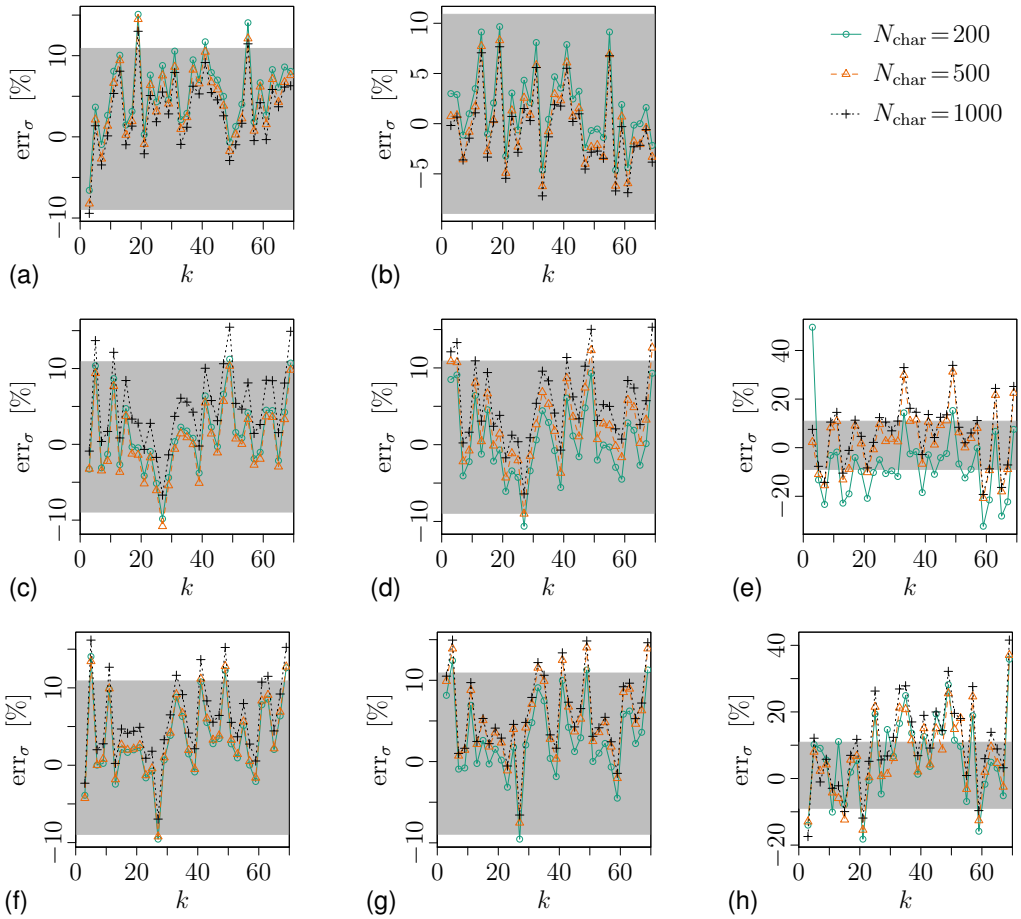

Fig. 5.18: Standard deviation errors err_σ of statistical gate level RO analyses depending on number of stages k according to (5.17); confidence intervals from (5.19) shaded; top: inverter-based RO with (a) frequency f and (b) on-power P_{on} center: NAND2-based RO with (c) frequency f, (d) on-power P_{on}, and (e) off-power P_{off}; bottom: NOR2-based RO with (f) frequency f, (g) on-power P_{on}, and (h) off-power P_{off}; compare Fig. 17 in [LSJ+16]

(IV) The errors of gate level off-power analyses are larger than the errors for the dynamic RO performance parameters: the errors in the mean values are within $[-15\,\%\ ,\ 5\,\%]$, the errors in the standard deviations may even be larger. However, mean values and standard deviations alone are not convincing for the off-power distributions due to their significantly non-Gaussian shapes, which cause the standard deviation confidence intervals in (5.18) to be inaccurate. Optical inspections of the off-power distributions reveal that the gate level analysis well approximates the reference data from MC circuit simulations. For example, for the off-power distribution for the $k = 57$-stage NAND2-based RO at $N_{\text{char}} = 10^3$, the mean error is $\text{err}_\mu = -5.5\,\%$ and the standard deviation error is $\text{err}_\mu = 11\,\%$ although the Q-Q plots of the off-power

distributions from the reference circuit simulations and the gate level analysis with probabilistic GLD-FKML models in Fig. 5.16(b) coincide. Rare extremely large stage leakage power values, which are covered in the probabilistic models and potentially replicated in the gate level analysis, are the reasons for these large errors. A rising characterization sample size N_{char} can increase the number of these large stage leakage power values and, therefore, does not necessarily improve the gate level analysis accuracy.

The reference MC circuit simulations are very time consuming. With the sample size $N_{\mathrm{ref}} = 200$, for example, the simulations of the 19-stage ROs take approximately $31\,min$ for the inverter-based RO, $36\,min$ for the NAND2-based RO, and $40\,min$ for the NOR2-based RO on a 4-core machine with $32\,GB$ RAM. These simulation times increase to nearly $8\,h$, $9.5\,h$, and $10\,h$ for the 69-stage ROs.

The run times of the proposed RO analysis approach with probabilistic models are dominated by the standard cell characterization, N_{char}-sample circuit simulations of $k = 9$-stage ROs, which take approximately $4\,min\ \ 35\,s$ for the inverter-based RO, $7\,min\ \ 25\,s$ for the NAND2-based RO, and $8\,min$ for the NOR2-based RO at $N_{\mathrm{char}} = 200$ samples. Obviously, the major parameter to adapt the computational costs is the characterization sample size N_{char}. According to the accuracy evaluations above, the sample size $N_{\mathrm{char}} = 200$ appears sufficient. Rising this number to $N_{\mathrm{char}} = 500$ may be beneficial from an accuracy perspective, but further rising this number to $N_{\mathrm{char}} = 1000$ only increases the computational effort.

While correlated Gaussian models can be extracted virtually instantly from the characterization data, the GLD-FKML approximation of a single stage performance parameter takes less than $15\,s$, practically independent of the characterization sample size N_{char}. Finally, with the sample size $N_{\mathrm{gate}} = 10^4$, the statistical gate level RO analyses finish in less than $30\,s$ for the inverter-based ROs and in less than $1\,min$ for the other oscillators. The run times of the statistical gate level analyses applying correlated Gaussian models and probabilistic GLD-FKML models do not significantly differ.

In summary, the statistical gate level RO analyses combining characterizations, model calibrations, and gate level computations achieve significant speed-ups with respect to the reference MC circuit simulations. Separated for the different ROs, their evolutions over the number of stages k are illustrated in Fig. 5.19. With the characterization sample size $N_{\mathrm{char}} = 200$ and probabilistic GLD-FKML models, the gate level analyses are more efficient than the $N_{\mathrm{ref}} = 200$-sample reference simulations at $k \geq 11$ stages for

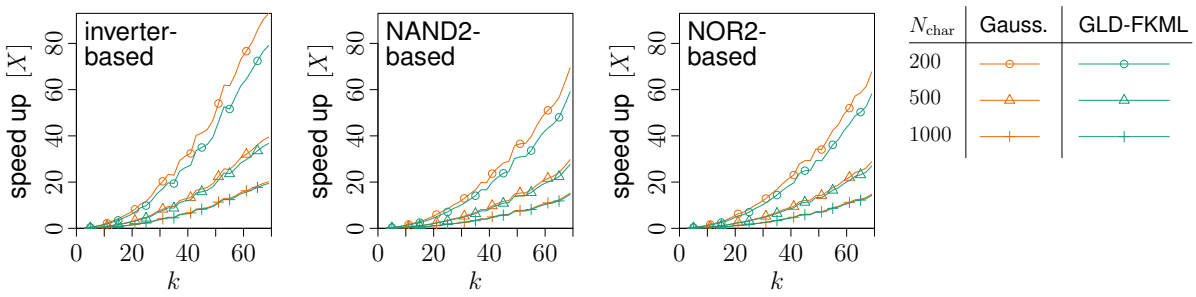

Fig. 5.19: Speed ups of statistical gate level RO analyses compared with MC SPICE reference simulations ($N_{\mathrm{ref}} = 200$); compare Fig. 18 in [LSJ+16]

the inverter-based ROs and the NAND2-based ROs and at $k \geq 13$ stages for the NOR2-based ROs. For the $k = 69$-stage ROs, the analysis run times can be reduced to $6\ min$ for the inverter-based RO, $9\ min\ \ 45\ s$ for the NAND2-based RO, and $10\ min\ \ 20\ s$ for the NOR2-based RO, corresponding to maximum speed-ups of $79\ X$, $59\ X$, and $58\ X$. The trends in the graphs in Fig. 5.19 additionally indicate that the speed-ups further rise with a growing number of stages k and that applying correlated Gaussian models does not lead to a significant performance gain compared with probabilistic GLD-FKML models when the characterization sample size is $N_{\mathrm{char}} \geq 200$.

5.3.4 Results of Ring Oscillator Scenarios

Due to their regular structures with certain standard cells being multiply instantiated, digital ROs are scenarios that allow an efficient application of probabilistic standard cell performance models in statistical gate level analyses.

In contrast to the previous application examples, many standard cell performance parameters of RO-internal instances extracted from MC circuit simulations of 9-stage ROs can be considered Gaussian, at least at the smaller characterization sample size $N_{\mathrm{char}} = 200$: dynamic energies as well as NAND2 and NOR2 delay times. Increasing the characterization sample size, however, reveals that many of these parameters tend to be slightly non-Gaussian as well. In addition, as expected, the leakage power distributions are non-Gaussian. Independent of marginal distributions being Gaussian or non-Gaussian, the obtained standard cell performance variations can be accurately described by probabilistic GLD-FKML models. Besides marginal distributions, these models also capture intra-instance and inter-instance correlations.

The statistical gate level digital RO analyses defined by (5.10)–(5.13) can be performed with correlated Gaussian models and probabilistic GLD-FKML models. While Gaussian models are slightly more efficient, they lead to wrong results in RO off-power distributions, but perform as accurate as GLD-FKML models when examining RO frequency and on-power distributions. Especially for the inverter-based ROs with non-Gaussian stage delays, it can be concluded that it is acceptable to approximate slightly non-Gaussian distributions by Gaussian distributions. To what extent such an approximation is acceptable remains as a topic for future research.

With the probabilistic GLD-FKML standard cell models, the statistical gate level analyses achieved up to $79\,X$ speed-ups compared with MC circuit simulations. A further gain in efficiency can be expected for ROs with $k > 69$ stages, exceeding the maximum number in this study. The analysis accuracy is sufficient for the relatively small characterization sample size $N_{\mathrm{char}} = 200$ already. A higher effort in characterization does not necessarily increase the accuracy of the gate level analyses.

5.4 Probabilistic Analog Behavioral Models

In this section, the probabilistic GLD-FKML modeling approach is transferred to behavioral models of analog cells [LHE+15]. Hence, the range of application scenarios is extended beyond device compact modeling and standard cell performance modeling. The derived models are implemented in *Verilog-A* [Acc14] syntax to be evaluated in *Cadence® Spectre® Circuit Simulator* [Cadb] for demonstration purposes. After a brief discussion of the principles in Sec. 5.4.1, further details are presented at a voltage divider example in Sec. 5.4.2, and the model accuracy and efficiency are evaluated at a bandgap voltage reference circuit in Sec. 5.4.3.

5.4.1 Principles

As introduced in Sec. 3.6, an analog behavioral model connects the pin voltages and currents of an analog cell by equations. Characterizing such a model corresponds to determining the model coefficients. For this purpose, the circuit schematic of the analog cell is instantiated in a testbench that sweeps the variables in the model equations and observes the circuit responses. The determined quantities allow to fit

the model coefficients. In principle, this procedure can be performed for the nominal behavior and for corner cases to obtain different sets of fixed model coefficients.

To introduce variability information into probabilistic analog behavioral models, the characterization needs to perform MC circuit simulations to generate characterization sample data $\tilde{\boldsymbol{Y}}_{\mathbf{char}}$. As discussed in Sec. 4.2 and demonstrated for digital standard cells in Sec. 5.2.1 and Sec. 5.3.2, two instances per analog cell under consideration have to be characterized to derive the complete probabilistic model including marginal distributions as well as intra-instance, inter-instance, and inter-element correlations.

Similar to the device compact models in Sec. 5.1.3, probabilistic analog behavioral models can be implemented to be accessed by circuit simulators, for instance. This requires an approximation of the standard Gaussian CDF, such as (5.2) based on [AA08], and the GLD-FKML quantile function (4.4) to be available. An approach to implement and access probabilistic analog behavioral models is outlined at the voltage divider example in Sec. 5.4.2.

5.4.2 Voltage Divider Example

Behavioral Model and Assumed Variability

To illustrate probabilistic analog behavioral modeling and to extend the discussion in [LHE+15], Fig. 5.20 depicts a the schematic of a simple voltage divider circuit with a corresponding testbench. Applying *Kirchhoff's laws*, for example, the equations

$$V_2 = \frac{1}{1+\frac{R_1}{R_2}} \cdot V_1 - \frac{1}{\frac{1}{R_1}+\frac{1}{R_2}} \cdot I_2 = Y_{\mathrm{vd}_1} \cdot V_1 + Y_{\mathrm{vd}_2} \cdot I_2 \qquad \text{and} \tag{5.20}$$

$$I_1 = \frac{1}{R_1+R_2} \cdot V_1 + \frac{1}{1+\frac{R_1}{R_2}} \cdot I_2 = Y_{\mathrm{vd}_3} \cdot V_1 + Y_{\mathrm{vd}_1} \cdot I_2 \qquad \text{with} \tag{5.21}$$

$$Y_{\mathrm{vd}_1} = \frac{1}{1+\frac{R_1}{R_2}} \ , \qquad Y_{\mathrm{vd}_2} = -\frac{1}{\frac{1}{R_1}+\frac{1}{R_2}} \ , \text{ and } \qquad Y_{\mathrm{vd}_3} = \frac{1}{R_1+R_2} \tag{5.22}$$

can be derived as the behavioral model that relates the output voltage V_2 and the current consumption I_1 to the supply voltage V_1 and the output current I_2 with the coefficients Y_{vd_1}, Y_{vd_2}, and Y_{vd_3}.

A potential implementation of (5.20)–(5.22) as an analog behavioral voltage divider model in *Verilog-A* syntax is demonstrated in Fig. 5.21.

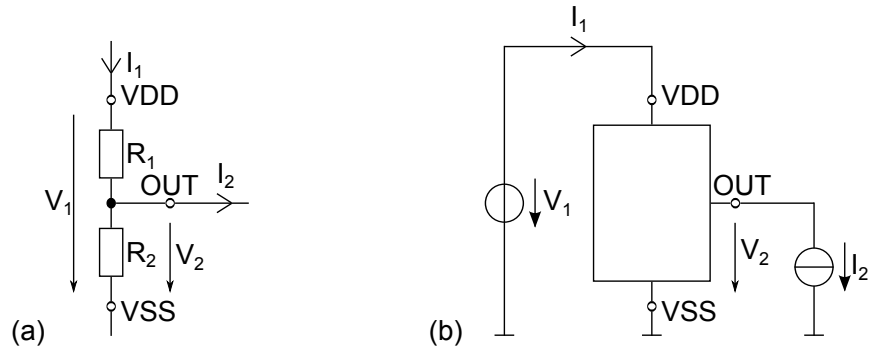

Fig. 5.20: Voltage divider; (a) circuit schematic; (b) simulation testbench for characterization

```
‘include "constants.vams"
‘include "disciplines.vams"
module voltage_divider_va (VDD, VSS, OUT);
 // pins
 inout VDD, VSS, OUT;
 electrical VDD, VSS, OUT;
 // declarations
 real Yvd1, Yvd2, Yvd3;
 // catch resistance values from Spectre
 (* cds_inherited_parameter *) parameter real R1=0;
 (* cds_inherited_parameter *) parameter real R2=0;
 // analog behavior
 analog begin
  @(initial_step) begin
   // assignment of model parameters
   Yvd1 = 1 / (1+R1/R2);
   Yvd2 = -1 / (1/R1+1/R2);
   Yvd3 = 1 / (R1+R2);
  end // initial step
  V(OUT,VSS)<+Yvd1*V(VDD,VSS)+Yvd2*I(VSS,OUT);
  I(VDD,VSS)<+Yvd3*V(VDD,VSS)+Yvd1*I(VSS,OUT);
 end
endmodule
```

Fig. 5.21: Implementation example of voltage divider model in *Verilog-A* syntax

```
parameters R1=1k R2=2k
statistics {
 // R1 = R1_nom + dR1_glob + dR1_loc
 // with R1_nom=1k, dR1_glob~N(0,80^2),
 // and dR1_loc~N(0,60^2);
 // R2 = R2_nom + dR2_glob + dR2_loc
 // with R2_nom=2k, dR2_glob~N(0,160^2),
 // and dR2_loc~N(0,120^2);
 // dR1_glob and dR2_glob global
 // (equal for all instances) and
 // correlated with product-moment
 // correlation coefficient 0.4;
 // dR1_loc and dR2_loc local
 // (instance-specific)
 process {
  vary R1 dist=gauss std=80 percent=no
  vary R2 dist=gauss std=160 percent=no
 }
 correlate param=[R1 R2] cc=0.4
 mismatch {
  vary R1 dist=gauss std=60 percent=no
  vary R2 dist=gauss std=120 percent=no
 }
}
```

Fig. 5.22: Assumed statistics section for resistor variability

The model characterization can be performed by circuit simulations with the testbench in Fig. 5.20(b). While the supply voltage V_1 and the output current I_2 are swept, the output voltage V_2 and the current consumption I_1 are observed to fit the model coefficients Y_{vd_1}, Y_{vd_2}, and Y_{vd_3} in (5.20) and (5.21). As a more efficient alternative for this particular voltage divider scenario, (5.22) can be directly evaluated.

Global and local variability are assumed to cause variations in the resistances R_1 and R_2. For illustration purposes and according to the *Spectre* statistics section in Fig. 5.22, they are modeled as

$$R_1 = \left(\mu_{\mathrm{R1}} + R_{\mathrm{glob},1} + R_{\mathrm{loc},1}\right)\ \Omega \qquad \text{and} \qquad R_2 = \left(\mu_{\mathrm{R2}} + R_{\mathrm{glob},2} + R_{\mathrm{loc},2}\right)\ \Omega \quad (5.23)$$

with $\mu_{\mathrm{R1}} = 1000$ and $\mu_{\mathrm{R2}} = 2000$; correlated Gaussian RVs $R_{\mathrm{glob},1} \sim \mathrm{N}(0, 80^2)$ and $R_{\mathrm{glob},2} \sim \mathrm{N}(0, 160^2)$ with $\rho^{(\mathrm{pe})}_{\mathrm{R_{glob,1}},\mathrm{R_{glob,2}}} = 0.4$ applying to all instances of the resistors R_1 and R_2; as well as instance-specific independent Gaussian RVs $R_{\mathrm{loc},1} \sim \mathrm{N}(0, 60^2)$ and $R_{\mathrm{loc},2} \sim \mathrm{N}(0, 120^2)$.

Probabilistic Model Characterization and Calibration

To introduce variability information into the behavioral voltage divider model (5.20)–(5.22), the model coefficients Y_{vd_1}, Y_{vd_2}, and Y_{vd_3} have to be treated as the components of an $n_y = 3$-dimensional RV $\boldsymbol{Y}_{\mathbf{vd}}$. To derive a probabilistic GLD-FKML description of this RV, sample data $\tilde{\boldsymbol{Y}}_{\mathbf{char}} = \left(\tilde{\boldsymbol{Y}}^{[1]}_{\mathbf{vd}}, \tilde{\boldsymbol{Y}}^{[2]}_{\mathbf{vd}} \right)$ has to be generated during characterization from two voltage divider instances. For example, this can be efficiently done by drawing random samples of the resistances R_1 and R_2 and evaluating (5.22) for two instances. In this section, the characterization sample size is arbitrarily set to $N_{\mathrm{char}} = 1000$.

The characterization data maps to the GLD-FKML approximations of the marginal distributions $Y_{\mathrm{vd}_1} \sim GLD(0.669, 58.5, 0.0447, 0.113)$, $Y_{\mathrm{vd}_2} \sim GLD(-666, 0.0261, 0.139, 0.151)$, and $Y_{\mathrm{vd}_3} \sim GLD(3.31 \cdot 10^{-4}, 5.08 \cdot 10^{4}, 0.255, 0.0678)$ as well as the intra-instance Spearman's rank correlation matrix $\mathbf{R}_{\mathbf{vd}}$ and the inter-instance Spearman's rank correlation matrix $\mathbf{R}_{\mathbf{vd,vd}}$

$$\mathbf{R}_{\mathbf{vd}} = \begin{pmatrix} 1 & 0.206 & -0.262 \\ 0.206 & 1 & 0.868 \\ -0.262 & 0.868 & 1 \end{pmatrix} \quad \text{and} \tag{5.24}$$

$$\mathbf{R}_{\mathbf{vd,vd}} = \begin{pmatrix} 0.541 & 0.112 & -0.155 \\ 0.112 & 0.703 & 0.638 \\ -0.155 & 0.638 & 0.711 \end{pmatrix}. \tag{5.25}$$

Since the voltage divider is taken into account as a single element, inter-element correlations do not exist.

The scatterplot matrix in Fig. 5.23 illustrates the modeling results in terms of marginal distributions as well as intra-element and inter-element correlations. While a Gaussian approximation of the coefficient Y_{vd_3} is not feasible, the probabilistic GLD-FKML model accurately represents the characterization data.

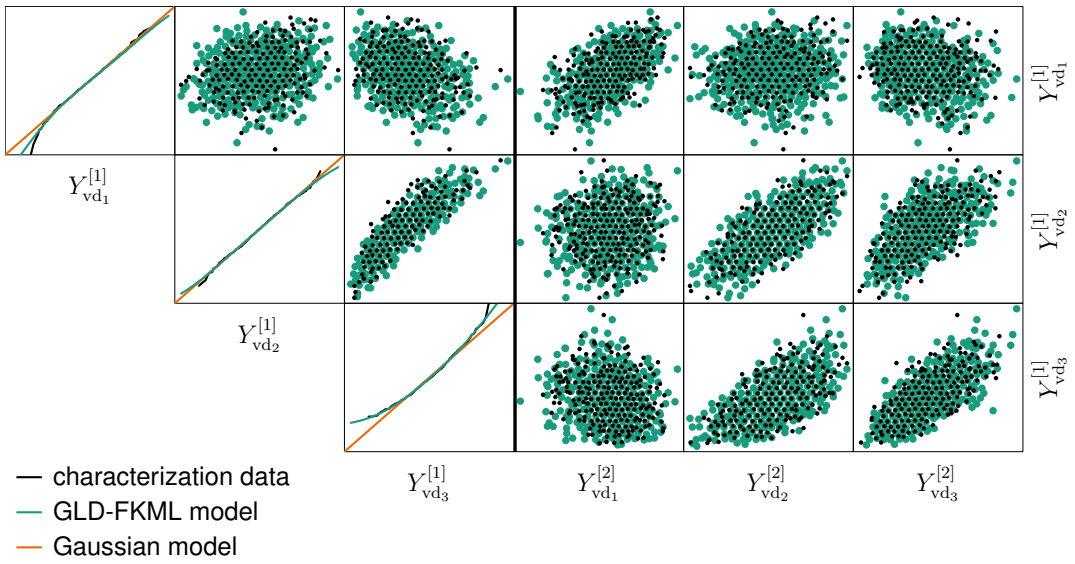

Fig. 5.23: Probabilistic voltage divider model; left part: Q-Q plots for marginal distributions and scatter plots for intra-instance correlations; right part: scatter plots for inter-instance correlations between voltage divider instances 1 and 2; scatter plots from $N_s = 1000$ samples from probabilistic GLD-FKML models and $N_{\mathrm{char}} = 1000$-sample characterization data

Model Implementation and Application

To apply the probabilistic voltage divider model in *Spectre* simulations, the behavioral voltage divider model in Fig. 5.21 has to be extended, and the corresponding statistics section has to be implemented.

From the Spearman's rank correlation sub-matrices in (5.24) and (5.25), the global and the local covariance matrices for the improved sampling algorithm can be derived applying the principles in Sec. 4.3.2:

$$\mathbf{\Sigma}_{\mathbf{glob}} = \begin{pmatrix} 0.559 & 0.117 & -0.162 \\ 0.117 & 0.72 & 0.655 \\ -0.162 & 0.655 & 0.728 \end{pmatrix} \quad \text{and} \tag{5.26}$$

$$\left(\mathbf{\Sigma}_{\mathbf{vd}} - \mathbf{\Sigma}_{\mathbf{vd,vd}}\right) = \begin{pmatrix} 0.441 & 0.099 & -0.111 \\ 0.099 & 0.281 & 0.223 \\ -0.111 & 0.223 & 0.273 \end{pmatrix}. \tag{5.27}$$

To implement the probabilistic behavioral voltage divider model in *Verilog-A* syntax to be used in *Spectre*, the global covariance matrix $\mathbf{\Sigma}_{\mathbf{glob}}$ needs to be converted into the global correlation matrix $\mathbf{C}_{\mathbf{glob}}$ by applying (2.36) in Sec. 2.2.1,

$$\mathbf{C}_{\mathbf{glob}} = \begin{pmatrix} 1 & 0.184 & -0.253 \\ 0.184 & 1 & 0.904 \\ -0.253 & 0.904 & 1 \end{pmatrix}, \tag{5.28}$$

and the local covariance matrix $\left(\mathbf{\Sigma}_{\mathbf{vd}} - \mathbf{\Sigma}_{\mathbf{vd,vd}}\right)$ needs to be decomposed, for instance by applying the Cholesky decomposition

$$\left(\mathbf{\Sigma}_{\mathbf{vd}} - \mathbf{\Sigma}_{\mathbf{vd,vd}}\right) = \mathbf{L}_{\mathbf{vd}}\,\mathbf{L}_{\mathbf{vd}}^{\mathrm{T}} \quad \Longrightarrow \quad \mathbf{L}_{\mathbf{vd}} = \begin{pmatrix} 0.664 & 0 & 0 \\ 0.148 & 0.509 & 0 \\ -0.167 & 0.487 & 0.086 \end{pmatrix}. \tag{5.29}$$

App. C.4.1 demonstrates a potential solution to the model implementation tasks.

The *Spectre* testbench in Fig. 5.25 presents the access of the probabilistic behavioral voltage divider model and the statistics section. From $N = 500$-sample MC simula-

```
simulator lang=spectre
//// load statistics and model
include "./statistics.scs"
ahdl_include "./voltage_divider.va"
//// voltage divider instances
i_va_1 (v1_vdd 0 v1_out) voltage_divider_va
i_va_2 (v2_vdd 0 v2_out) voltage_divider_va
//// supply voltage and output corrent
parameters V1=5 I2=1m
Vdd_v1  (v1_vdd 0) vsource dc=V1
Iout_v1 (v1_out 0) isource dc=I2
Vdd_v2  (v2_vdd 0) vsource dc=V1
Iout_v2 (v2_out 0) isource dc=I2
//// simulator commands
mc1 montecarlo numruns=500 seed=2 variations=all sampling=standard \
  donominal=no scalarfile="./mcdata" \
  {
    dc1 dc
}
//// output statement - export output voltages and supply currents
print Vdd,Iout,v(v1_out),-i(Vdd_v1),v(v2_out),-i(Vdd_v2),name=dc1 addto="sim.out"
```

Fig. 5.24: *Spectre* testbench for probabilistic voltage divider model evaluation; two instances at supply voltage $V_1 = 5\ V$ and output current $I_2 = 1\ mA$

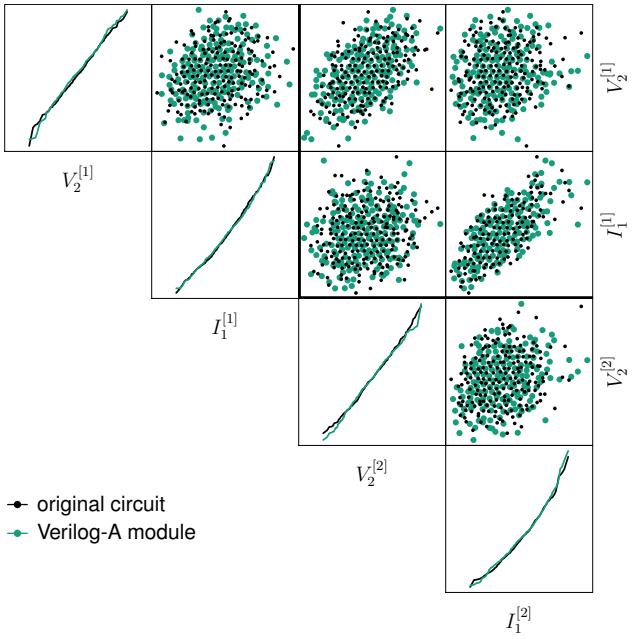

Fig. 5.25: Results of $N = 500$-sample MC voltage divider simulations; comparison of distributions of output voltage V_2 and supply current I_1 for two instances of original circuit and probabilistic *Verilog-A* model at supply voltages $V_1 = 5\ V$ and output currents $I_2 = 1\ mA$; Q-Q plots of marginal distributions; scatter plots for intra-instance correlations and inter-instance correlations (first and second row in third and fourth column)

tions, it determines the responses of two voltage divider instances to supply voltages $V_1 = 5\ V$ and output currents $I_2 = 1\ mA$. Fig. 5.25 depicts their output voltages V_2 and supply currents I_1 and compares them with the results from MC circuit simulations of two instances of the original circuit in Fig. 5.20(a) with variations from Fig. 5.22. The good agreement of marginal distributions as well as intra-instance and inter-instance correlations demonstrates the applicability of the probabilistic behavioral voltage divider model and validates its correctness. However, for this scenario, a behavioral model does not improve the simulation efficiency: the $N = 500$-sample MC simulations finish in about $6\,s$ on a standard workstation for both circuit representations.

5.4.3 Bandgap Voltage Reference Circuit

While the voltage divider example in Sec. 5.4.2 illustrates the principles of probabilistic analog behavioral modeling, a bandgap voltage reference circuit in an industrial $0.35\,\mu m$ technology [aA16] is used as a more realistic test vehicle to rate the model

accuracy and efficiency. The circuit and a corresponding testbench are depicted in Fig. 5.26.

Analog Behavioral Model and Characterization

Using the notations in Fig. 5.26, an approach for an analog behavioral modeling expresses the output voltage V_{ref} and the current consumption I_{dd} as functions of the supply voltage V_{dd}, the output current I_{ref}, and the temperature T. The equations [LHE+15]

$$\left(\frac{V_{\mathrm{ref}}-V_{\mathrm{ref},0}}{V_{\mathrm{ref},0}}\right) = Y_{\mathrm{bg}_1} + Y_{\mathrm{bg}_2}\left(\frac{V_{\mathrm{dd}}-V_{\mathrm{dd},0}}{V_{\mathrm{dd},0}}\right) + Y_{\mathrm{bg}_3}\left(\frac{T-T_0}{T_0}\right) + Y_{\mathrm{bg}_4}\left(\frac{T-T_0}{T_0}\right)^2 + Y_{\mathrm{bg}_5}\left(\frac{I_{\mathrm{ref}}-I_{\mathrm{ref},0}}{I_{\mathrm{ref},0}}\right) + Y_{\mathrm{bg}_6}\left(\frac{V_{\mathrm{dd}}-V_{\mathrm{dd},0}}{V_{\mathrm{dd},0}}\right)\left(\frac{T-T_0}{T_0}\right) \quad \text{and} \tag{5.30}$$

$$\left(\frac{I_{\mathrm{dd}}-I_{\mathrm{dd},0}}{I_{\mathrm{dd},0}}\right) = Y_{\mathrm{bg}_7} + Y_{\mathrm{bg}_8}\left(\frac{V_{\mathrm{dd}}-V_{\mathrm{dd},0}}{V_{\mathrm{dd},0}}\right) + Y_{\mathrm{bg}_9}\left(\frac{T-T_0}{T_0}\right) + Y_{\mathrm{bg}_{10}}\left(\frac{T-T_0}{T_0}\right)^2 \tag{5.31}$$

with their coefficients $Y_{\mathrm{bg}_1},\ldots,Y_{\mathrm{bg}_{10}}$ provide a reasonable trade-off between model complexity and accuracy for supply voltages $3.0\ V \leq V_{\mathrm{dd}} \leq 3.6\ V$, temperatures $-40\,^{\circ}C \leq T \leq 160\,^{\circ}C$, and output currents $1\,nA \leq I_{\mathrm{ref}} \leq 1\,\mu A$. In (5.30) and (5.31), $V_{\mathrm{ref},0}$ and $I_{\mathrm{dd},0}$ are the reference output voltage and the reference current consumption obtained at the reference supply voltage $V_{\mathrm{dd},0} = 3.3\ V$, the reference temperature

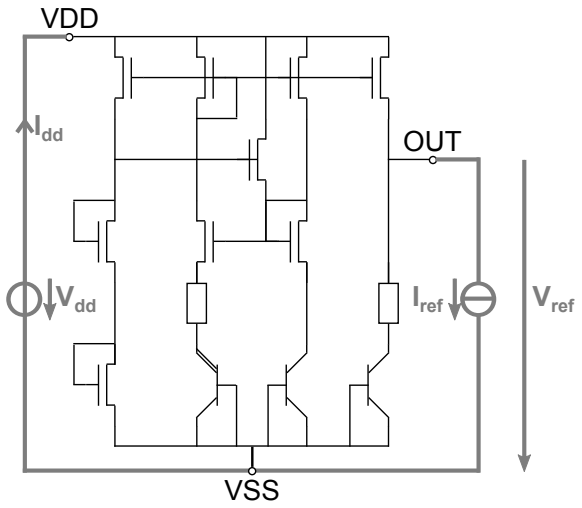

Fig. 5.26: Schematic of bandgap voltage reference circuit (black) with corresponding voltage and current sources for simulations (bold gray)

$T_0 = 27\,^\circ C$, and the reference output current $I_{\mathrm{ref},0} = 100\,nA$. The behavioral model defined by (5.30) and (5.31) can be implemented into *Verilog-A* in analogy to the voltage divider model in Sec. 5.4.2.

The characterization needs to apply the voltage and current sources depicted in Fig. 5.26 to the bandgap schematic in circuit simulations. Observing the output voltage V_{ref} and the current consumption I_{dd} while sweeping the supply voltage V_{dd}, the temperature T, and the output current I_{ref} generates sets of variates to determine the model coefficients $Y_{\mathrm{bg}_1}, \ldots, Y_{\mathrm{bg}_{10}}$ in (5.30) and (5.31).

Probabilistic Model Calibration

Based on (5.30) and (5.31), a probabilistic analog behavioral bandgap model can be established by treating the model coefficients as an $n_y = 10$-dimensional RV $\boldsymbol{Y}_{\mathbf{bg}}$ with its components $Y_{\mathrm{bg}_1}, \ldots, Y_{\mathrm{bg}_{10}}$. Without considering variability, a circuit simulation determines the reference output voltage $V_{\mathrm{ref},0}$ and the reference current consumption $I_{\mathrm{dd},0}$ at the reference supply voltage $V_{\mathrm{dd},0}$, temperature T_0, and output current $I_{\mathrm{ref},0}$. These quantities are kept constant in the probabilistic model.

In a second step, the characterization procedure described above is repeatedly performed for two instances of the bandgap voltage reference based on MC circuit simulations that apply the technology-specific variability information from the PDK[1]. Consequently, it generates characterization sample data of the form $\tilde{\boldsymbol{Y}}_{\mathbf{char}} = \left(\tilde{\boldsymbol{Y}}_{\mathbf{bg}}^{[1]}, \tilde{\boldsymbol{Y}}_{\mathbf{bg}}^{[2]} \right)$ as the input for model calibration. As for the voltage divider in Sec. 5.4.2, the characterization sample size is set to $N_{\mathrm{char}} = 1000$.

According to SW tests with a $(1-\alpha_c) = 0.95$ confidence level, only the coefficients Y_{bg_1}, Y_{bg_2}, and Y_{bg_4} can be considered Gaussian while the others cannot. The Q-Q plots of selected coefficients on the main diagonal of the scatterplot matrix in Fig. 5.27 and the Q-Q plots of all coefficients in App. C.4.2 demonstrate that while the component Y_{bg_2} is slightly non-Gaussian, the remaining non-Gaussian components have significantly less pronounced tails than their Gaussian approximations. Therefore, their Gaussian approximations over-estimate the distribution tails. Contrastingly, the GLD-FKML approximations accurately represent the characterization data. This is confirmed by KS tests: by comparing the characterization data with $N_s = 10^5$ samples from their

[1] This approach extends the characterization in [LHE+15], which is based on a single instance of the bandgap voltage reference circuit and neglects inter-instance correlations.

Tab. 5.5: Statistical test results for analog behavioral bandgap model coefficient distributions; SW tests with results **+**: *Gaussian* and **–**: *non-Gaussian*; KS tests comparing characterization data and GLD-FKML approximations of marginal distributions with results **o**: *accurate approximation* and x: *inaccurate approximation*; confidence level $(1-\alpha_c)=0.95$

Coefficient	SW test	KS test
Y_{bg_1}	+	o
Y_{bg_2}	+	o
Y_{bg_3}	–	o
Y_{bg_4}	+	o
Y_{bg_5}	–	o

Coefficient	SW test	KS test
Y_{bg_6}	–	o
Y_{bg_7}	–	o
Y_{bg_8}	–	o
Y_{bg_9}	–	o
$Y_{\mathrm{bg}_{10}}$	–	o

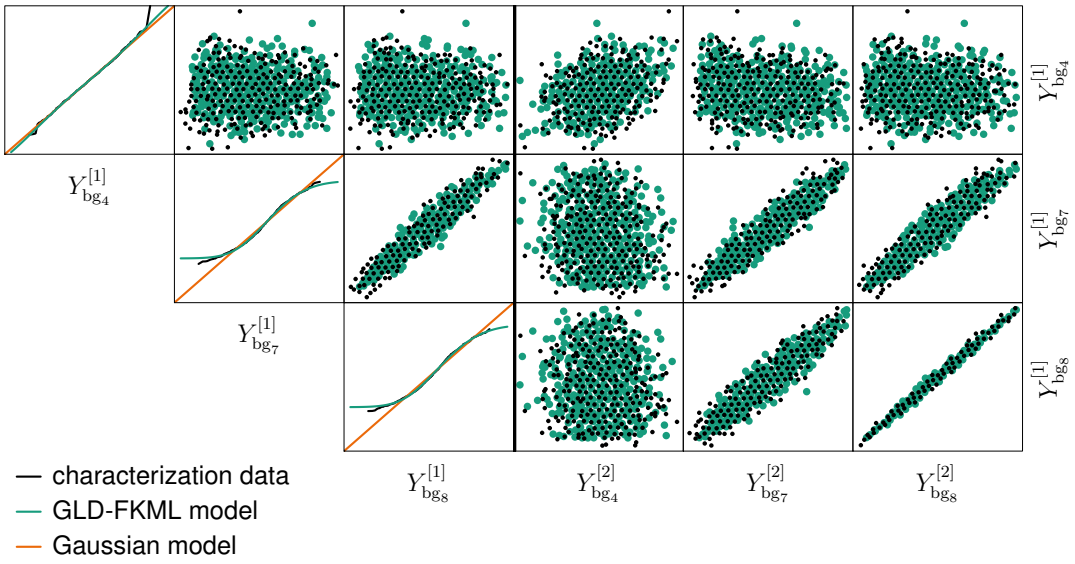

Fig. 5.27: Selected coefficients of probabilistic analog behavioral bandgap model; Q-Q plots of marginal distributions; scatter plots visualizing intra-instance and inter-instance correlations for characterization data and probabilistic GLD-FKML model

GLD-FKML approximations, these tests do not reveal significant differences at a $(1-\alpha_c)=0.95$ confidence level.

In addition, as depicted in the scatter plots in Fig. 5.27, which compare $N_s=1000$ samples from the model with the $N_{\mathrm{char}}=1000$-sample characterization data $\tilde{\boldsymbol{Y}}_{\mathbf{char}}$, the probabilistic GLD-FKML model captures the intra-instance correlations and the inter-instance correlations in the characterization data. For the sake of completeness, the scatter plots in App. C.4.2 illustrate all intra-instance correlations that are captured in the behavioral model.

Probabilistic Model Implementation and Application

To apply the probabilistic GLD-FKML model in simulations, the analog behavioral bandgap model has to be extended in a similar manner as the voltage divider model in Sec. 5.4.2. As a reference, a multivariate Gaussian analog behavioral bandgap model is additionally derived from the characterization data $\tilde{\boldsymbol{Y}}_{\mathbf{char}}$ and implemented.

For model validation, the variation behavior of the bandgap voltage reference circuit is analyzed in $N = 1000$-sample MC simulations for multiple combinations of supply voltages V_{dd}, temperatures T, and output currents I_{ref}: their boundaries as well as 40 random combinations. While evaluating two instances of the original circuit as well as of the *Verilog-A* implementations of the multivariate Gaussian model and the probabilistic GLD-FKML model, the simulations observe the reference voltages V_{ref} and the current consumptions I_{dd}.

To evaluate the model accuracy, KS tests compare the obtained empirical distributions with a $(1-\alpha_c) = 0.95$ confidence level. Their results are summarized in Tab. 5.6, and they reveal that multivariate Gaussian models and probabilistic GLD-FKML models perform similarly with respect to the bandgap output voltage V_{ref}. For both models, significant deviations from the simulations of the original circuit can be observed in 3 of the 48 test scenarios, corresponding to $6.25\,\%$. Representative for these results, the scatterplot matrix in Fig. 5.28 depicts the simulation results for one of these scenarios: supply voltage $V_{\mathrm{dd}} = 3.6\ V$, temperature $T = -40\,^{\circ}C$, and output current $I_{\mathrm{ref}} = 1\,\mu A$. Although KS tests report significant deviations, both behavioral model implementations are very close to the reference simulation results for the bandgap output voltage V_{ref}. Hence, they can be considered misclassified due to the KS test properties. The reason for the high accuracy of the multivariate Gaussian models is that $50\,\%$ of the related model coefficients, Y_{bg_1}, Y_{bg_2}, and Y_{bg_4} are Gaussian, and these coefficients dominate the bandgap output voltage V_{ref} in (5.30).

According to the KS test results, multivariate Gaussian models introduce significant deviations from the reference simulations, that is significant inaccuracies, in the variability of the current consumption I_{dd} of the bandgap voltage reference circuit. The over-estimation of the distribution tails of all model coefficients $Y_{\mathrm{bg}_7}, \ldots, Y_{\mathrm{bg}_{10}}$ in (5.31) by Gaussian approximations maps to an over-estimation of the distribution tails of the bandgap current consumption I_{dd} by generating too extreme values, which is illustrated by the marginal distributions in Fig. 5.28. In contrast, the probabilistic

Tab. 5.6: KS tests that compare bandgap circuit performance parameter distributions from MC circuit simulations of original circuit (with statistical device models from the PDK) with MC evaluations of probabilistic analog behavioral bandgap models in *Verilog-A* syntax (correlated Gaussian models and probabilistic GLD-FKML models); test results are **o**: *behavioral model accurately represents original circuit* and x: *significant differences between behavioral model and original circuit*; $(1-\alpha_c)=0.05$

V_{dd} $[V]$	T $[°C]$	I_{ref} $[nA]$	KS test results			
			Gaussian models		GLD-FKML models	
			V_{ref}	I_{dd}	V_{ref}	I_{dd}
3	−40	1	**o**	x	**o**	**o**
3	−40	1000	**o**	x	x	**o**
3	160	1	**o**	x	**o**	**o**
3	160	1000	**o**	x	**o**	**o**
3.6	−40	1	**o**	x	**o**	**o**
3.6	−40	1000	x	x	x	**o**
3.6	160	1	x	x	x	**o**
3.6	160	1000	**o**	x	**o**	**o**
3.16	124	20.1	**o**	x	**o**	**o**
3.22	89	137	**o**	x	**o**	**o**
3.34	117	15.8	**o**	x	**o**	**o**
3.54	71	9.46	**o**	x	**o**	**o**
3.12	66	187	**o**	x	**o**	**o**
3.54	118	4.06	**o**	x	**o**	**o**
3.57	−35	136	**o**	x	**o**	**o**
3.4	55	2.32	**o**	x	**o**	**o**
3.38	106	5.45	**o**	x	**o**	**o**
3.04	99	2.69	**o**	x	**o**	**o**
3.12	56	5.23	**o**	x	**o**	**o**
3.11	132	1.5	**o**	x	**o**	**o**
3.41	48	84.5	**o**	x	**o**	**o**
3.23	9	425	**o**	x	**o**	**o**
3.46	−26	217	**o**	x	**o**	**o**
3.3	−20	247	**o**	x	**o**	**o**

V_{dd} $[V]$	T $[°C]$	I_{ref} $[nA]$	KS test results			
			Gaussian models		GLD-FKML models	
			V_{ref}	I_{dd}	V_{ref}	I_{dd}
3.43	23	23.2	**o**	x	**o**	**o**
3.6	64	17	**o**	x	**o**	**o**
3.23	92	271	**o**	x	**o**	**o**
3.47	41	65.3	**o**	x	**o**	**o**
3.56	143	92.1	**o**	x	**o**	**o**
3.13	19	11.5	**o**	x	**o**	**o**
3.39	52	6.47	**o**	x	**o**	**o**
3.08	26	951	x	x	**o**	**o**
3.16	90	79.5	**o**	x	**o**	**o**
3.23	12	4.36	**o**	x	**o**	**o**
3.01	56	2.44	**o**	x	**o**	**o**
3.23	113	27.2	**o**	x	**o**	**o**
3.52	−23	592	**o**	x	**o**	**o**
3.2	135	62.6	**o**	x	**o**	**o**
3.29	28	848	**o**	x	**o**	**o**
3.36	128	157	**o**	x	**o**	**o**
3.3	29	11.8	**o**	x	**o**	**o**
3.11	27	19.7	**o**	x	**o**	**o**
3.5	55	2.78	**o**	x	**o**	**o**
3.4	138	1.09	**o**	x	**o**	**o**
3.48	133	140	**o**	x	**o**	**o**
3.06	38	2.04	**o**	x	**o**	**o**
3.43	115	21.8	**o**	x	**o**	**o**
3.25	152	83.2	**o**	x	**o**	**o**

GLD-FKML models well represent the original circuit behavior, which holds for the marginal distributions of the bandgap performance parameters, that is output voltage V_{ref} and current consumption I_{dd}, their intra-instance correlations, as well as their inter-instance correlations.

Accurately representing the original circuit behavior, the major benefit of the probabilistic GLD-FKML behavioral analog model of the bandgap voltage reference circuit is its efficiency in simulations. The $N=1000$-sample MC reference simulations of two instances take approximately $47\,min\ \ 15\,s$ for the 48 scenarios listed in Tab. 5.6, corresponding to $30\,ms$ for evaluating one sample point per bandgap instance at a particular combination of supply voltage V_{dd}, temperature T, and output current I_{ref}. In contrast, evaluating $N=1000$ samples of two instances of the probabilistic GLD-FKML model in *Verilog-A* syntax takes $6\,min\ \ 52\,s$ for these 48 scenarios, corresponding to $4.3\,ms$ per sample point and instance at a particular combination of supply voltage

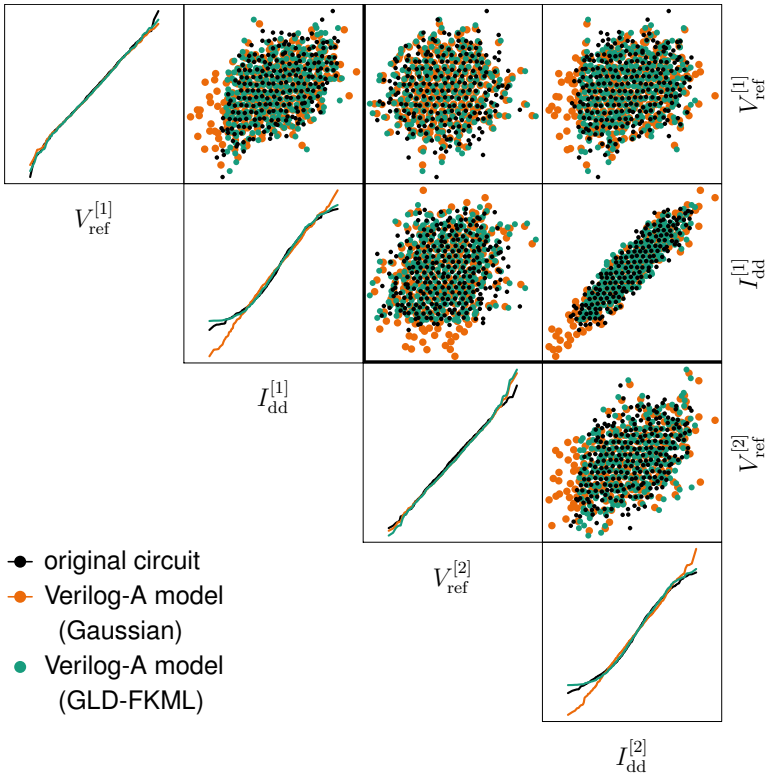

Fig. 5.28: Comparison of the bandgap performance parameter distributions, output voltage V_{ref} and current consumption I_{dd} of two instances $^{[1]}$ and $^{[2]}$ for the original circuit as well as the *Verilog-A* implementations of the probabilistic GLD-FKML model and the multivariate Gaussian model; sample size $N = 1000$; supply voltage $V_{\mathrm{dd}} = 3.6\ V$, temperature $T = -40\,^{\circ}C$, output current $I_{\mathrm{ref}} = 1\,\mu A$; Q-Q plots of marginal distributions and scatter plots visualizing intra-instance as well as inter-instance correlations

V_{dd}, temperature T, and output current I_{ref}. Overall, without losing accuracy, the probabilistic GLD-FKML model in *Verilog-A* syntax achieves an approximate $6.9\,X$ speed-up compared with the original circuit. At the cost of accuracy, multivariate Gaussian models can further increase the simulation performance slightly.

5.4.4 Results of Analog Behavioral Modeling Scenarios

Variability information from a PDK can be transferred into behavioral models of analog cells by considering selected behavioral model coefficients as multi-dimensional RVs and applying the probabilistic GLD-FKML modeling approach. For example, the variation-aware analog behavioral models can be implemented in *Verilog-A* modules that access random samples generated by a circuit simulator, such as *Spectre*.

The bandgap voltage reference scenario demonstrates that the majority of the behavioral model coefficients of an analog cell are non-Gaussian when variability is taken into account. However, the GLD-FKML approach well represents the empirical data obtained from characterization, including Gaussian and non-Gaussian marginal distributions. Furthermore, probabilistic GLD-FKML analog behavioral bandgap model captures intra-instance and inter-instance correlations. Its implementation allows an efficient evaluation in MC simulation studies: a $6.9\,X$ speed-up can be achieved with respect to simulating the original circuit without a loss in accuracy.

5.5 Conclusions from Application Scenarios

The main conclusions that can be drawn from the application scenarios in Secs. 5.1–5.4 are summarized in Tab. 5.7. Overall, these scenarios reveal the following results.

1. The generation of empirical data for calibrating probabilistic GLD-FKML models can be computationally expensive. However, this effort is required to derive fully statistical models.
2. While uncorrelated Gaussian models are not feasible and correlated Gaussian models often introduce inaccuracies, probabilistic GLD-FKML models accurately capture the empirical characterization data, both in terms of marginal distributions and correlations.
3. Probabilistic GLD-FKML models can be applied to modeling tasks in different design styles and at different levels of abstraction models. They can be applied efficiently and properly with some standard tools, for instance circuit simulators, or with adapted analysis methods.

However, some aspects remain to be addressed in future research. They include the fact that Gaussian models appear appropriate for slightly non-Gaussian but infeasible for considerably non-Gaussian data. The acceptable deviation from Gaussian data for Gaussian modeling approaches might have to be quantified. Furthermore, some GLD-FKML approximations of standard cell leakage power distributions are inaccurate. When these inaccuracies become critical, an alternative approach to model marginal distributions may be required. Nevertheless, the successful applications of probabilistic GLD-FKML models in different scenarios demonstrate their wide-spread usability, which has been a main goal for the research documented in this thesis.

Tab. 5.7: Major conclusions from application scenarios for probabilistic modeling

Section	Scenario	Main conclusions
Secs. 5.1–5.4	All	– Most empirical characterization data non-Gaussian – Correlated Gaussian models mostly inaccurate – Probabilistic GLD-FKML models accurate in terms of marginal distributions and correlations – Probabilistic GLD-FKML models suit abstraction of variability information for different design styles and at multiple levels of abstraction
Sec. 5.1	Device compact models	– Correlations have to be taken into account – Gaussian approximations of slightly non-Gaussian data feasible – GLD-FKML approximations equally fit Gaussian and non-Gaussian parameters – Probabilistic GLD-FKML models can be implemented in PDKs
Sec. 5.2	Standard cell models	– Assumption of Gaussian delay distributions in SSTA inaccurate – GLD-FKML approximations equally fit delay, dynamic energy, and leakage power distributions – Standard tools need adaptations to employ probabilistic GLD-FKML models in statistical gate level analyses of digital circuits
Sec. 5.3	Gate level RO analyses	– Probabilistic GLD-FKML models can be applied in gate level analyses of digital circuits with regular structures – Correlated Gaussian models infeasible for leakage power, i.e. for considerably non-Gaussian parameters – Gate level RO analyses based on probabilistic GLD-FKML models accurate and efficient
Sec. 5.4	Analog behavioral models	– Probabilistic GLD-FKML models can be implemented for variation-aware behavioral model evaluations, for example as a combination of *Spectre* and *Verilog-A*

6 Summary and Conclusions

Variability has always been a challenge to the semiconductor industry. Global variation effects from manufacturing process imperfections, which affect all devices in a circuit in the same manner, used to dominate *integrated circuit* (IC) variability. They have been taken into account in circuit design and analysis by corner-based approaches that assume worst-case parameter combinations to predict the worst-case circuit behavior. Local variations from process variability, which affect devices individually and lead to mismatch, have always been present as well. However, their impact has grown with shrinking feature sizes. Furthermore, since manufacturing process improvements and new materials have enabled technology nodes with feature sizes of $100\,nm$ and below, atomic-level fluctuations have rapidly gained importance and increased the impact of local variations. Overall, the devices in an IC vary in a correlated manner.

To meet the performance targets of ICs at reasonable costs and times to market, it is important to take variability into account already during design. For this purpose, a variety of approaches are available, and they cover different levels of abstraction, such as the transfer of measured device variability into device compact models, *Monte Carlo* (MC) circuit simulations, *statistical static timing analysis* (SSTA), or high-yield estimation methods for memory design. However, as reviewed in Chap. 3, these approaches are tailored to particular problems and often make simplifying assumptions, such as Gaussian distributions or linear approximations, which have been criticized for introducing inaccuracies.

The goal of this thesis was to consistently and efficiently transfer variability information between different levels of abstraction. For this purpose, a probabilistic modeling approach for IC analysis was introduced in Chap. 4. It captures global and local variations, statistical correlations, and marginal distributions of nearly arbitrary shapes. Arbitrary underlying models are extended by treating selected model parameters as multivariate *random variables* (RVs). This approach is universal in terms of being applicable to arbitrary standard or custom models on arbitrary levels of abstraction.

To describe the RVs, marginal distributions and correlations are handled separately. On the one hand, instead of assuming Gaussian distributions, marginal distributions are mapped to *generalized lambda distributions in FKML parametrization* (GLD-FKMLs). With its four distribution parameters, the GLD-FKML supports a wide range of distribution shapes so that it can be well adapted to most empirical data. On the other hand, correlations are captured by Spearman's rank correlation matrices. Neglecting spatial local correlations and based on the fact that, in IC design, instances of a limited number of circuit elements are connected, correlations are sub-divided into intra-instance correlations to model inter-dependencies of parameters within a particular instance; inter-instance correlations to model inter-dependencies of parameters between instances of a particular circuit element; and inter-element correlations to model inter-dependencies of parameters between instances of distinct circuit elements.

Probabilistic GLD-FKML models can be calibrated from sample data. To derive fully statistical models, sample data for two instances per circuit element under consideration have to be generated during characterization. The calibrated models are intended to be evaluated in sampling-based circuit analyses, which requires the generation of random samples for arbitrary numbers of circuit elements and instances. Based on the conversion of Spearman's rank correlation matrices into covariance matrices, an efficient sampling approach is derived for this purpose.

In application scenarios with practical orientations, the applicability of the probabilistic GLD-FKML modeling approach is demonstrated in Chap. 5. In device compact modeling, standard cell modeling, as well as variation-aware analog behavioral modeling, a significant number of parameters are non-Gaussian so that a more advanced modeling approach is required and justified. The GLD-FKML approximations accurately represent the majority of the characterization data, including Gaussian and non-Gaussian parameters. In addition, the calibrated probabilistic GLD-FKML models capture the correlations in the characterization data well.

The evaluations of probabilistic GLD-FKML models and Gaussian models as references in MC circuit simulations, statistical gate level analyses, and sampling-based behavioral model evaluations reveal the major results of this thesis.

- Statistical correlations have to be captured in a variability model to achieve reasonable accuracy.
- Correlated Gaussian models may perform well even if the underlying characterization data is non-Gaussian to a certain degree, but they fail when the deviations from Gaussian distributions are too large.
- Properly calibrated probabilistic GLD-FKML models allow accurate circuit examinations, both in terms of marginal distributions and correlations of circuit performance parameters.

Although probabilistic GLD-FKML models perform well, future improvements might become necessary. Potential directions for future research include methods to

- additionally consider spatial local correlations;
- capture correlations across different levels of abstraction and design styles;
- quantify deviations from Gaussian distributions, which are acceptable for the continued use of Gaussian models; and
- replace the GLD-FKML by an alternative distribution if required.

Some standard tools can evaluate probabilistic GLD-FKML models already. For example, the application scenarios demonstrate model implementations into different circuit simulators to use their capabilities for the generation of random samples. However, standard tools for digital circuit design and analysis cannot handle probabilistic GLD-FKML standard cell models yet so that industrial tools and environments for digital design need to be adapted. Nevertheless, the gate level RO analysis scenarios demonstrate the potentials of variation-aware digital circuit analyses based on probabilistic GLD-FKML standard cell models.

The further evolution of variability in semiconductors is hard to predict. Scaling was often expected to increase variability [Ase07, WACA13]. In contrast to this, a reduction of atomic-level fluctuations by approximately $20\,\%$ and at least constant process variations were reported for a transition from a $65\,nm$ to a $45\,nm$ technology [KKK+08]. Furthermore, fully depleted SOI or FinFET technologies are expected to decrease variability [WACA13]. Nevertheless, especially due to cost issues [Lap15], many future ICs will still use bulk processes at feature sizes $\geq 28\,nm$, which are considered susceptible to variability. Especially for these technology nodes, probabilistic GLD-FKML models to abstract variability at arbitrary levels of abstraction can support the design of performance-compliant ICs with reasonable times to market.

A Selected Principles of Statistics

A.1 Principal Component Analysis

Based on [HS12, Jol86], this section outlines the basic calculations for *principal component analysis* (PCA) to supplement Sec. 2.2.3.

It is assumed that $\boldsymbol{X}_{\mathbf{G}} \sim \mathbf{N}(\boldsymbol{\mu}_{\mathbf{X_G}}, \boldsymbol{\Sigma}_{\mathbf{X_G}})$ is a multivariate Gaussian RV with the mean vector $\boldsymbol{\mu}_{\mathbf{X_G}}$ and the positive definite covariance matrix $\boldsymbol{\Sigma}_{\mathbf{X_G}}$.

An eigenvalue decomposition of the covariance matrix [HS12, Jol86]

$$\boldsymbol{\Sigma}_{\mathbf{X_G}} = \boldsymbol{\Gamma}\boldsymbol{\Lambda}\boldsymbol{\Gamma}^{\mathrm{T}}, \tag{A.1}$$

with $\boldsymbol{\Gamma}^{\mathrm{T}}$ being the transposed of the matrix $\boldsymbol{\Gamma}$, yields the diagonal matrix $\boldsymbol{\Lambda}$ and the orthogonal matrix $\boldsymbol{\Gamma}$. The diagonal matrix $\boldsymbol{\Lambda}$ contains the eigenvalues of the covariance matrix $\boldsymbol{\Sigma}_{\mathbf{X_G}}$ in descending order. The k-th column of the orthogonal matrix $\boldsymbol{\Gamma}$ is the eigenvector of the covariance matrix $\boldsymbol{\Sigma}_{\mathbf{X_G}}$ that corresponds to the k-th eigenvalue.

With the linear transformation [HS12]

$$\boldsymbol{X}_{\mathbf{G}} \quad \longmapsto \quad \boldsymbol{X}_{\mathbf{Gu}} = \boldsymbol{\Gamma}^{\mathrm{T}} \left(\boldsymbol{X}_{\mathbf{G}} - \boldsymbol{\mu}_{\mathbf{X_G}} \right), \tag{A.2}$$

a multivariate RV $\boldsymbol{X}_{\mathbf{Gu}} \sim \mathbf{N}(\mathbf{0}, \boldsymbol{\Lambda})$ with zero means and uncorrelated components $X_{Gu,i}$ is obtained.

A.2 Sample Data Generation & Evaluation

While in this thesis, standard *Monte Carlo* (MC) sampling is applied, this appendix briefly introduces a selection of random sample generation techniques with their basics for data evaluation.

Standard Monte Carlo (MC) sampling [HLT83, LLP06]: Sets of input parameters $\boldsymbol{x}^{(\mathrm{k})}$ are randomly drawn according to the original input parameter distribution known from the multi-dimensional RV $\boldsymbol{X}$. This method optimally mimics overall process variability and provides the most general view on performance parameter distributions.

Stratified sampling [HLT83, Liu08, VCBS11]: Stratified sampling divides the input parameter space $\mathbb{R}_{\mathbf{X}}$ into disjoint sub-regions, so called strata. In each stratum, random samples $\boldsymbol{x}^{(\mathrm{k})}$ are generated and evaluated. Stratified sampling can be used for creating more evenly distributed sample points $\boldsymbol{x}^{(\mathrm{k})}$ in the input parameter space $\mathbb{R}_{\mathbf{X}}$. However, it is only efficient for a small number of input parameters.

Latin hypercube sampling [LLP06, VCBS11]: To generate N samples from an arbitrary univariate RV X, latin hypercube sampling divides the distribution into N intervals of equal probability of occurrence $1/N$. To extend latin hypercube sampling to multivariate input data $\boldsymbol{X}$, this procedure is repeated for each random component X_i of the RV $\boldsymbol{X}$. A subsequent random combination of the samples from the random components yields the multivariate sample $\tilde{\boldsymbol{X}}$ of size N.

Quasi-Monte Carlo (MC [LLP06, VCBS11]: Instead of using random numbers, the sample points $\boldsymbol{x}^{(\mathrm{k})}$ are selected from a deterministic sequence. Such a procedure ensures a more uniform sample point distribution in the input parameter space $\mathbb{R}_{\mathbf{X}}$. A rising number of input parameters drastically reduces the quasi-MC quality.

Importance sampling [HLT83, LLP06, Liu08]: Instead of the original input parameter distribution $\varphi_{\boldsymbol{X}}(\boldsymbol{x})$, a distorted distribution $\varphi^*_{\boldsymbol{X}}(\boldsymbol{x})$ is used to select random samples. To compensate for the distortion, sample points have to be weighted by $w(\mathbf{x}) = \varphi_{\mathbf{x}}(\mathbf{x}) \;/\; \varphi^*_{\boldsymbol{X}}(\boldsymbol{x})$. The distribution $\varphi^*_{\boldsymbol{X}}(\boldsymbol{x})$ can be tuned to emphasize important regions, e.g. distribution tails or regions of extreme performance $\mathbf{y}$, but may be hard to find, especially in case of high-dimensional input parameter spaces $\mathbb{R}_{\mathbf{X}}$.

Guided sample point selection [Eli94, MBDG13, SR07, SR09, SR10]: From an initial sample of input parameters $\boldsymbol{x}^{(\mathrm{k})}$ and corresponding performance parameters $\boldsymbol{y}^{(\mathrm{k})}$, models are derived. They allow an efficient classification of further sample points $\boldsymbol{x}^{(\mathrm{l})}$. Only important sample points $\boldsymbol{x}^{(\mathrm{l}^*)}$ are simulated to obtain sample data of important performance parameter values $\boldsymbol{y}^{(\mathrm{l}^*)}$, for instance extreme or close-to-specification performance values. The methods differ in the types of models and their applications. Sec. 3.5.2 discusses two application cases in more detail: *High-Sigma Monte Carlo* (HSMC) [MBDG13] and *statistical blockade* (SB) [SR07, SR09, SR10].

B A Probabilistic Model for Integrated Circuit Analysis

B.1 Probability Distributions with Various Shapes

This appendix defines probability distributions that cover a wide range of distribution shapes to supplement Sec. 4.1.2.1. The *Generalized Lambda Distribution* (GLD) is not mentioned here since it is discussed in Sec. 4.1.2.2 in detail. The equations below describe a univariate RV Y.

Fleishman Transformation [Fle78, Tad80]

The RV Y is modeled as a polynomial of a standard Gaussian RV $Z \sim \mathrm{N}(0,1)$, Usually, a third-order polynomial is applied:

$$Y = a + bZ + cZ^2 + dZ^3.$$

A closed-form PDF $\varphi_{\mathrm{Y}}(.)$, CDF $\phi_{\mathrm{Y}}(.)$, or quantile function $\phi_{\mathrm{Y}}^{-1}(.)$ does not exist.

Johnson System [Joh49, Tad80]

The Johnson system contains three transformations of a standard Gaussian RV $Z \sim \mathrm{N}(0,1)$,

$$\begin{aligned}
Y^{(1)} &= \xi + \lambda \cdot \exp\left(\frac{Z-\gamma}{\delta}\right) && \Rightarrow \quad Y^{(1)} > \xi \\
Y^{(2)} &= \xi + \frac{\lambda}{1+\exp\left(\frac{-(Z-\gamma)}{\delta}\right)} && \Rightarrow \quad \xi < Y^{(2)} < \xi + \lambda \\
Y^{(3)} &= \xi + \lambda \cdot \sinh\left(\frac{Z-\gamma}{\delta}\right) && \Rightarrow \quad Y^{(3)} > \xi
\end{aligned}$$

with the four parameters ξ, λ, γ, and δ.

Tadikamalla–Johnson system [TJ82, Tad80]

The Tadikamalla–Johnson system uses the transformations of the Johnson system, but it assumes the RV Z to follow a standard logistic distribution defined by the CDF

$$\phi_{\mathrm{Z}}(z) = \left(1 + \exp\left(-z\right)\right)^{-1}.$$

Schmeiser–Deutsch System [SD77, Tad80]

The Schmeiser–Deutsch system is defined by the quantile function of the RV Y,

$$\phi_{\mathrm{Y}}^{-1}(u) = \begin{cases} \lambda_1 + \lambda_2 \left(-(\lambda_4 - u)^{\lambda_3}\right) & : u \leq \lambda_4 \\ \lambda_1 + \lambda_2 \left(u - \lambda_4\right)^{\lambda_3} & : u > \lambda_4 \end{cases},$$

with $0 \leq u \leq 1$ and the four parameters λ_1, λ_2, λ_3, and λ_4.

Burr System [Bur42, Bur73, Tad80]

The Burr system of distributions consists of two CDFs with the parameters $c, k > 0$:

$$\phi_{\mathrm{Y}}(y) = \begin{cases} 1 - \left[1 + y^{c}\right]^{-k} & : \; y \geq 0 \\ 0 & : \; y < 0 \end{cases} \qquad \text{and}$$

$$\phi_{\mathrm{Y}}(y) = \begin{cases} \left[1 + y^{-c}\right]^{-k} & : \; y \geq 0 \\ 0 & : \; y < 0 \end{cases}.$$

They cover a broad range of distribution shapes and can be adapted to arbitrary mean values and standard deviations by linear transformations.

Pearson System [Pol79, Tad80]

The Pearson system of distributions is defined by PDFs $\varphi_{\mathrm{Y}}(y)$ that satisfy the differential equation

$$\frac{1}{\varphi_{\mathrm{Y}}(y)} \frac{\mathrm{d}\varphi}{\mathrm{d}y} = -\frac{a + y}{c_0 + c_1 \cdot y + c_2 \cdot y^2}.$$

Depending on the parameters a, c_0, c_1, and c_2, twelve different types can be defined [Pol79] and treated by distinctions of cases.

B.2 R Function FitGLD to Map Sample Data to GLD

```
## R function to fit data to GLD
## implemented because to improve performance of starship() from package 'gld'

## requires package 'gld' anyway to find starting point for GLD parameters
require('gld');

## function call:     L <- FitGLD(x,param);
## input arguments:   x: vector of sample data
##                    param: identifier for GLD parametrization,
##                    "FKML" (default) or "RS"
## returns:           L: vector of GLD parameters
##
FitGLD <- function( data, param="FKML" ) {
  ## determine sample size and empirical CDF
  sample_size <- length(x);
  x <- sort(x); ecdf <- seq(from=1, to=sample_size, by=1) / (sample_size+1);
  ## definition of optimization function: minimize squared error between
  ## empirical and theoretical quantiles
  if( param=="RS" ) {
    opt_fun <- function(L,x,ecdf) {
      sum((L[1]+(ecdf^L[3]-(1-ecdf)^L[4])/L[2]-x)^2);
    }
  } else {
    opt_fun <- function(L,x,ecdf) {
      sum((L[1]+((ecdf^L[3]-1)/L[3]-((1-ecdf)^L[4]-1)/L[4])/L[2]-x)^2);
    }
  }
  ## use starship() to determine starting point from small sample
  if( sample_size > 100 ) {
    x1  <- approx(ecdf,x,seq(0.01,0.99,0.01))$y;
    Lstart <- starship(data=x1, param=param)$lambda;
  } else {
    Lstart <- starship(data=x, param=param)$lambda;
  }
  ## make sure L[3]!=0 and L[4]!=0
```

```
  if( Lstart[3]==0 ) { Lstart[3]=1e-1; }
  if( Lstart[4]==0 ) { Lstart[4]=1e-1; }
  ## run the optimization
  L <- optim(par=Lstart, fn=opt_fun, x=x, ecdf=ecdf);
  ## return
  return(L$par);
}
```

B.3 Illustration Example for Model Calibration

This example illustrates the calibration of a probabilistic model from sample data $\tilde{\boldsymbol{Y}}_{\mathbf{char}}$ and the generation of random samples referring to the principles in Sec. 4.2 and Sec. 4.3. It is assumed that two circuit elements are available: element A with two components a_1 and a_2 as well as element B with one component b. The characterization resulted in a sample $\tilde{\boldsymbol{Y}}_{\mathbf{char}}$ of the size $N_{\mathrm{char}} = 100$ of the RV $\boldsymbol{Y}_{\mathbf{char}} = \left(\boldsymbol{Y}_{\mathbf{A}}^{[1]}, \boldsymbol{Y}_{\mathbf{A}}^{[2]}, \boldsymbol{Y}_{\mathbf{B}}^{[1]}, \boldsymbol{Y}_{\mathbf{B}}^{[2]}\right)$, which contains two instances per circuit element. The first 15 sample points are listed in Tab. B.1.

Tab. B.1: Sample data for probabilistic modeling; sample size $N_{\mathrm{char}} = 100$

Observation k	A				B	
	$\widetilde{\mathbf{Y}}_{\mathbf{A}}^{[1]}$		$\widetilde{\mathbf{Y}}_{\mathbf{A}}^{[2]}$		$\widetilde{\mathbf{Y}}_{\mathbf{B}}^{[1]}$	$\widetilde{\mathbf{Y}}_{\mathbf{B}}^{[2]}$
	a_1	a_2	a_1	a_2	b	b
1	1.14	0.12	1.12	0.00	0.73	0.76
2	1.41	-0.09	1.42	-0.26	0.71	0.67
3	1.18	-0.49	1.07	-0.07	0.99	1.18
4	1.25	-0.12	1.21	-0.05	0.69	1.09
5	0.94	0.22	1.04	-0.14	0.52	0.55
6	0.77	-0.18	0.70	0.22	1.02	0.97
7	0.92	0.02	1.02	-0.26	0.63	0.91
8	0.90	0.14	0.95	0.01	1.00	1.30
9	1.09	-0.15	1.01	0.09	0.76	0.84
10	1.29	0.01	1.25	0.22	0.95	0.50
11	1.24	-0.11	1.23	-0.08	0.90	0.59
12	0.95	0.08	1.07	-0.13	0.31	1.04
13	1.06	-0.16	1.05	0.12	0.72	0.55
14	1.16	0.01	1.13	0.05	0.88	1.26
15	1.20	-0.15	1.22	-0.10	0.91	0.70
...	...	...	...	...	...	...

Correlations

The rank correlation matrix $\mathbf{R}_{\mathbf{Ychar}}$ can be estimated from the sample $\tilde{\boldsymbol{Y}}_{\mathbf{char}}$ applying (2.51) in Sec. 2.2.4 to all its components, which is performed by the *R* function *cor*. The significance test in (2.52) sets rank correlation coefficients $|\widetilde{\rho}_{\mathrm{ij}}^{(\mathrm{sp})}| \leq 0.197$ to 0 due to the sample size $N_{\mathrm{char}} = 100$. The following correlation submatrices can be derived applying (4.11)–(4.13) in Sec. 4.2.

$$\mathbf{R}_{\mathbf{A}} = \begin{pmatrix} 1 & 0 \\ 0 & 1 \end{pmatrix} \qquad \mathbf{R}_{\mathbf{A,A}} = \begin{pmatrix} 0.882 & 0 \\ 0 & 0 \end{pmatrix} \qquad \mathbf{R}_{\mathbf{A,B}} = \begin{pmatrix} 0 \\ 0 \end{pmatrix}$$

$$\mathbf{R}_{\mathbf{B}} = \begin{pmatrix} 1 \end{pmatrix} \qquad \mathbf{R}_{\mathbf{B,B}} = \begin{pmatrix} 0.256 \end{pmatrix}$$

For the characterization data in Tab. B.1, the components a_1 and a_2 of element A are uncorrelated. However, there is a relatively strong inter-instance correlation between the components a_1 of different instances of element A. Furthermore, a weak inter-instance correlation can be observed for element B, but an inter-element correlation between the elements A and B cannot be found.

Marginal Distributions

The GLD-FKML parameters are determined by the *R* function *FitGLD* in App. B.2:

$$\begin{aligned} Y_{\mathrm{A},a_1} &\sim \mathrm{GLD}(1.11, 8.2, 0.0136, 0.135), \\ Y_{\mathrm{A},a_2} &\sim \mathrm{GLD}(-0.0352, 7.66, 0.101, 0.025), \text{ and} \\ Y_{\mathrm{B},b} &\sim \mathrm{GLD}(0.82, 5.78, 0.227, 0.108). \end{aligned}$$

Modeling Summary

After model calibration, analytical descriptions of the RVs $\boldsymbol{Y}_{\mathbf{A}}^{[\mathrm{k}]}$ and $\boldsymbol{Y}_{\mathbf{B}}^{[\mathrm{l}]}$ modeling the variability in arbitrary instances k and l of the circuit elements A and B are available in terms of their intra-instance rank correlation matrices $\mathbf{R}_{\mathbf{A}}$ and $\mathbf{R}_{\mathbf{B}}$ as well as the GLD-FKML approximations of their marginal distributions. Furthermore, different instances of element A follow the same probability distribution, and different instances of element B follow the same probability distribution. The correlations between

instances of element A are described by the inter-instance correlation matrix $\mathbf{R}_{\mathbf{A,A}}$; the correlations between instances of element B are described by the inter-instance correlation matrix $\mathbf{R}_{\mathbf{B,B}}$; and the correlations between an instance of A and an instance of element B are described by the inter-element correlation matrix $\mathbf{R}_{\mathbf{A,B}}$.

Covariance Matrices for Random Sampling

The covariance matrix for improved random sampling can be derived from the rank-correlation matrices by (2.54) in Sec. 2.3.2 and the principles discussed in Sec. 4.3.2. The (3×3) global covariance matrix

$$\mathbf{\Sigma}_{\mathbf{glob}} = \begin{pmatrix} 0.891 & 0 & 0 \\ 0 & 0 & 0 \\ 0 & 0 & 0.267 \end{pmatrix}$$

captures the element A in the first and the second columns and rows as well as the element B in the third column and row.

For the local covariance matrices,

$$\mathbf{\Sigma}_{\mathbf{A}} - \mathbf{\Sigma}_{\mathbf{A,A}} = \begin{pmatrix} 0.109 & 0 \\ 0 & 1 \end{pmatrix} \qquad \text{and} \qquad \mathbf{\Sigma}_{\mathbf{B}} - \mathbf{\Sigma}_{\mathbf{B,B}} = \begin{pmatrix} 0.733 \end{pmatrix}$$

can be obtained. In this particular example, all the required matrices are positive semi-definite and hence valid covariance matrices that do not have to be adapted further.

Validation

To validate the model, generated random samples $\tilde{\boldsymbol{Y}}$ of the RV $\boldsymbol{Y} = \left(\boldsymbol{Y}_{\mathbf{A}}^{[1]}, \boldsymbol{Y}_{\mathbf{A}}^{[2]}, \boldsymbol{Y}_{\mathbf{B}}^{[1]}, \boldsymbol{Y}_{\mathbf{B}}^{[2]}\right)$ are compared with the empirical characterization data $\tilde{\boldsymbol{Y}}_{\mathbf{char}}$ in Tab. B.1.

In the conventional approach in Sec. 4.3.1, the rank correlation matrix is constructed from the submatrices as

$$\mathbf{R}_{\mathbf{Y}} = \begin{pmatrix} \mathbf{R}_{\mathbf{A}} & \mathbf{R}_{\mathbf{A,A}} & \mathbf{R}_{\mathbf{A,B}} & \mathbf{R}_{\mathbf{A,B}} \\ \mathbf{R}_{\mathbf{A,A}} & \mathbf{R}_{\mathbf{A,A}} & \mathbf{R}_{\mathbf{A,B}} & \mathbf{R}_{\mathbf{A,B}} \\ \mathbf{R}_{\mathbf{A,B}}^{\mathrm{T}} & \mathbf{R}_{\mathbf{A,B}}^{\mathrm{T}} & \mathbf{R}_{\mathbf{B}} & \mathbf{R}_{\mathbf{B,B}} \\ \mathbf{R}_{\mathbf{A,B}}^{\mathrm{T}} & \mathbf{R}_{\mathbf{A,B}}^{\mathrm{T}} & \mathbf{R}_{\mathbf{B,B}} & \mathbf{R}_{\mathbf{B}} \end{pmatrix}.$$

This rank correlation matrix is fed into the sampling algorithm in Sec. 2.3.2, and a sample $\tilde{\boldsymbol{Y}}$ of the size $N_s = 200$ is generated from the RV $\boldsymbol{Y}$. In Fig. B.1, this sample $\tilde{\boldsymbol{Y}}$ is compared with the characterization data $\tilde{\boldsymbol{Y}}_{\mathbf{char}}$ in Tab. B.1.

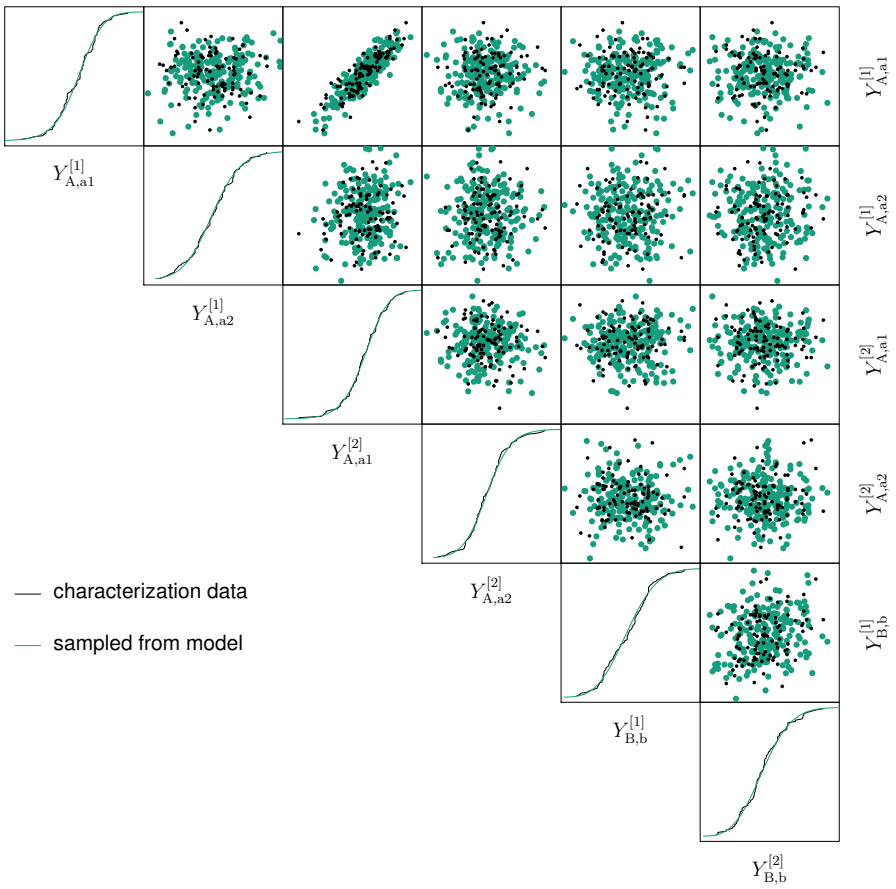

Fig. B.1: Visualization of GLD-FKML model example with conventional sampling approach; scatterplot matrix comparing empirical characterization data $\tilde{\boldsymbol{Y}}_{\mathbf{char}}$ with $N_s = 200$ random samples $\tilde{\boldsymbol{Y}}$ from probabilistic model

The improved approach applies the covariance matrices from the previous section to more efficiently generate a random sample $\tilde{\boldsymbol{Y}}^*$ of the size $N_s = 200$ from the RV $\boldsymbol{Y}$. It is compared with the characterization data $\tilde{\boldsymbol{Y}}_{\mathbf{char}}$ in Fig. B.2.

The data in Fig. B.1 and Fig. B.2 are in good agreement so that significant deviations cannot be observed between the samples $\tilde{\boldsymbol{Y}}$ and $\tilde{\boldsymbol{Y}}^*$ and the characterization data $\tilde{\boldsymbol{Y}}_{\mathbf{char}}$. Consequently, the model well represents the characterization data and the model calibration can be considered successful.

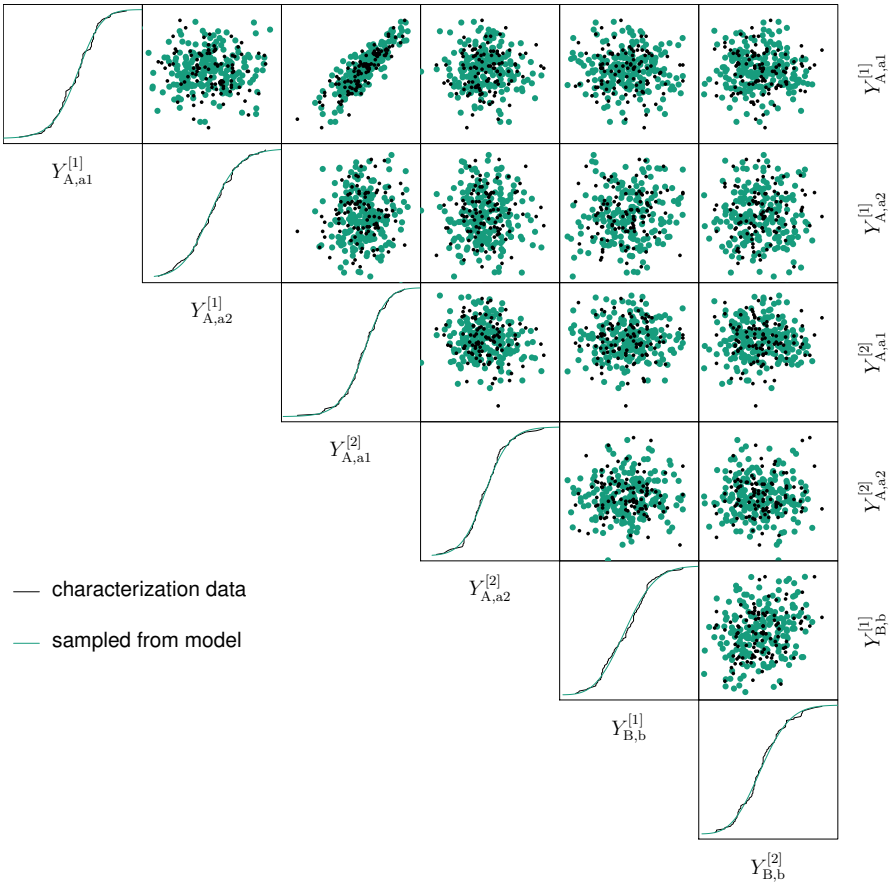

Fig. B.2: Visualization of GLD-FKML model example with improved sampling approach; scatterplot matrix comparing empirical characterization data $\tilde{\boldsymbol{Y}}_{\mathbf{char}}$ with $N_s = 200$ random samples $\tilde{\boldsymbol{Y}}^*$ from probabilistic model

B.4 Correctness of Improved Sampling Approach

This appendix proves the validity of the improved sampling algorithm derived in Sec. 4.3.2.

Let

- $\boldsymbol{G}_{\mathbf{E}}^{[\mathrm{k}_1]} = \boldsymbol{G}_{\mathbf{E}}^{[\mathrm{glob}]} + \boldsymbol{G}_{\mathbf{E}}^{[\mathrm{loc:k}_1]}$ and $\boldsymbol{G}_{\mathbf{E}}^{[\mathrm{k}_2]} = \boldsymbol{G}_{\mathbf{A}}^{[\mathrm{glob}]} + \boldsymbol{G}_{\mathbf{E}}^{[\mathrm{loc:k}_2]}$ be n_E-dimensional Gaussian RVs with zero means and $\boldsymbol{G}_{\mathbf{F}}^{[\mathrm{l}]} = \boldsymbol{G}_{\mathbf{F}}^{[\mathrm{glob}]} + \boldsymbol{G}_{\mathbf{F}}^{[\mathrm{loc:l}]}$ be an n_F-dimensional Gaussian RV with zero means;
- $\boldsymbol{G}_{\mathbf{E}}^{[\mathrm{loc:k}_1]}, \boldsymbol{G}_{\mathbf{E}}^{[\mathrm{loc:k}_2]} \sim \mathbf{N}(\mathbf{0}, \boldsymbol{\Sigma}_{\mathbf{E}} - \boldsymbol{\Sigma}_{\mathbf{E},\mathbf{E}})$ be independent n_E-dimensional Gaussian RVs with $\mathrm{Cov}\left[\boldsymbol{G}_{\mathbf{E}}^{[\mathrm{loc:k}_1]}, \boldsymbol{G}_{\mathbf{E}}^{[\mathrm{loc:k}_2]}\right] = \mathbf{0}$ and $\boldsymbol{G}_{\mathbf{F}}^{[\mathrm{loc:l}]} \sim \mathbf{N}(\mathbf{0}, \boldsymbol{\Sigma}_{\mathbf{F}} - \boldsymbol{\Sigma}_{\mathbf{F},\mathbf{F}})$ be an n_F-dimensional Gaussian RV;
- $\mathrm{Cov}\left[\boldsymbol{G}_{\mathbf{E}}^{[\mathrm{glob}]}\right] = \boldsymbol{\Sigma}_{\mathbf{E},\mathbf{E}}$, $\mathrm{Cov}\left[\boldsymbol{G}_{\mathbf{F}}^{[\mathrm{glob}]}\right] = \boldsymbol{\Sigma}_{\mathbf{F},\mathbf{F}}$, and $\mathrm{Cov}\left[\boldsymbol{G}_{\mathbf{E}}^{[\mathrm{glob}]}, \boldsymbol{G}_{\mathbf{F}}^{[\mathrm{glob}]}\right] = \boldsymbol{\Sigma}_{\mathbf{E},\mathbf{F}}$ such that $\boldsymbol{G}_{\mathbf{glob}} = \left(\boldsymbol{G}_{\mathbf{E}}^{[\mathrm{glob}]}, \boldsymbol{G}_{\mathbf{F}}^{[\mathrm{glob}]}\right)^{\mathrm{T}} \sim \mathbf{N}(\mathbf{0}, \boldsymbol{\Sigma}_{\mathbf{glob}})$ with $\boldsymbol{\Sigma}_{\mathbf{glob}} = \begin{pmatrix} \boldsymbol{\Sigma}_{\mathbf{E},\mathbf{E}} & \boldsymbol{\Sigma}_{\mathbf{E},\mathbf{F}} \\ \left(\boldsymbol{\Sigma}_{\mathbf{E},\mathbf{F}}\right)^{\mathrm{T}} & \boldsymbol{\Sigma}_{\mathbf{F},\mathbf{F}} \end{pmatrix}$; and
- $\boldsymbol{G}_{\mathbf{E}}^{[\mathrm{loc:k}_1]}$, $\boldsymbol{G}_{\mathbf{E}}^{[\mathrm{loc:k}_2]}$, $\boldsymbol{G}_{\mathbf{F}}^{[\mathrm{loc:l}]}$, as well as $\boldsymbol{G}_{\mathbf{glob}}$ be independent RVs.

Theorem

Under the aforementioned assumptions, the following statements are true.

- $\mathrm{Cov}\left[\boldsymbol{G}_{\mathbf{E}}^{[\mathrm{k}_1]}\right] = \boldsymbol{\Sigma}_{\mathbf{E}}$, $\mathrm{Cov}\left[\boldsymbol{G}_{\mathbf{E}}^{[\mathrm{k}_2]}\right] = \boldsymbol{\Sigma}_{\mathbf{E}}$, and $\mathrm{Cov}\left[\boldsymbol{G}_{\mathbf{F}}^{[\mathrm{l}]}\right] = \boldsymbol{\Sigma}_{\mathbf{F}}$ describe the intra-instance covariances
- $\mathrm{Cov}\left[\boldsymbol{G}_{\mathbf{E}}^{[\mathrm{k}_1]}, \boldsymbol{G}_{\mathbf{E}}^{[\mathrm{k}_2]}\right] = \boldsymbol{\Sigma}_{\mathbf{E},\mathbf{E}}$; and
- $\mathrm{Cov}\left[\boldsymbol{G}_{\mathbf{E}}^{[\mathrm{loc:k}_1]}, \boldsymbol{G}_{\mathbf{F}}^{[\mathrm{l}]}\right] = \boldsymbol{\Sigma}_{\mathbf{E},\mathbf{F}}$

Proof

Applying (2.46) and (2.49) in Sec. 2.2.3, the required calculations can be performed:

$$\begin{aligned}
\mathrm{Cov}\left[\boldsymbol{G}_{\mathbf{E}}^{[\mathrm{k}_1]}\right] &= \mathrm{Cov}\left[\boldsymbol{G}_{\mathbf{E}}^{[\mathrm{glob}]}\right] + \mathrm{Cov}\left[\boldsymbol{G}_{\mathbf{E}}^{[\mathrm{loc:k}_1]}\right] = \boldsymbol{\Sigma}_{\mathbf{E},\mathbf{E}} + \boldsymbol{\Sigma}_{\mathbf{E}} - \boldsymbol{\Sigma}_{\mathbf{E},\mathbf{E}} = \boldsymbol{\Sigma}_{\mathbf{E}} \\
\mathrm{Cov}\left[\boldsymbol{G}_{\mathbf{E}}^{[\mathrm{k}_2]}\right] &= \mathrm{Cov}\left[\boldsymbol{G}_{\mathbf{E}}^{[\mathrm{glob}]}\right] + \mathrm{Cov}\left[\boldsymbol{G}_{\mathbf{E}}^{[\mathrm{loc:k}_2]}\right] = \boldsymbol{\Sigma}_{\mathbf{E},\mathbf{E}} + \boldsymbol{\Sigma}_{\mathbf{E}} - \boldsymbol{\Sigma}_{\mathbf{E},\mathbf{E}} = \boldsymbol{\Sigma}_{\mathbf{E}} \\
\mathrm{Cov}\left[\boldsymbol{G}_{\mathbf{F}}^{[\mathrm{l}]}\right] &= \mathrm{Cov}\left[\boldsymbol{G}_{\mathbf{F}}^{[\mathrm{glob}]}\right] + \mathrm{Cov}\left[\boldsymbol{G}_{\mathbf{F}}^{[\mathrm{loc:l}]}\right] = \boldsymbol{\Sigma}_{\mathbf{F},\mathbf{F}} + \boldsymbol{\Sigma}_{\mathbf{F}} - \boldsymbol{\Sigma}_{\mathbf{F},\mathbf{F}} = \boldsymbol{\Sigma}_{\mathbf{F}}
\end{aligned}$$

$$\mathrm{Cov}\left[\boldsymbol{G}_{\mathbf{E}}^{[\mathrm{k}_1]}, \boldsymbol{G}_{\mathbf{E}}^{[\mathrm{k}_2]}\right] = \mathrm{Cov}\left[\boldsymbol{G}_{\mathbf{E}}^{[\mathrm{glob}]}\right] = \boldsymbol{\Sigma}_{\mathbf{E},\mathbf{E}}$$

$$\mathrm{Cov}\left[\boldsymbol{G}_{\mathbf{E}}^{[\mathrm{k}_1]}, \boldsymbol{G}_{\mathbf{F}}^{[\mathrm{l}]}\right] = \mathrm{Cov}\left[\boldsymbol{G}_{\mathbf{E}}^{[\mathrm{glob}]}, \boldsymbol{G}_{\mathbf{F}}^{[\mathrm{glob}]}\right] = \boldsymbol{\Sigma}_{\mathbf{E},\mathbf{F}}$$

These calculations prove the theorem above and, therefore, verify that the improved sampling approach in Sec. 4.3.2 is valid.

C Application Scenarios

C.1 Statistical Device Compact Modeling Results

This appendix completes data evaluation, probabilistic device model calibration, as well as model application in Sec. 5.1.

C.1.1 Q-Q Plots of Marginal Distributions

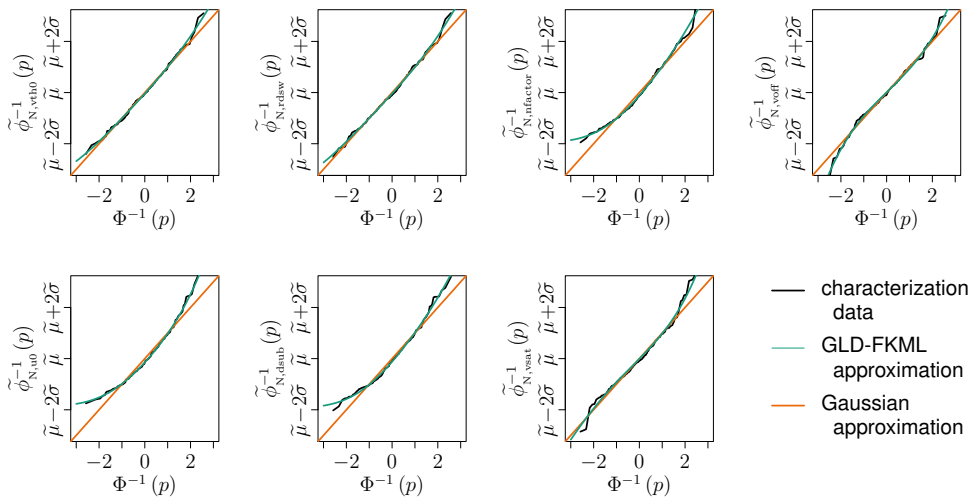

Fig. C.1: Marginal distributions of the NFET parameters

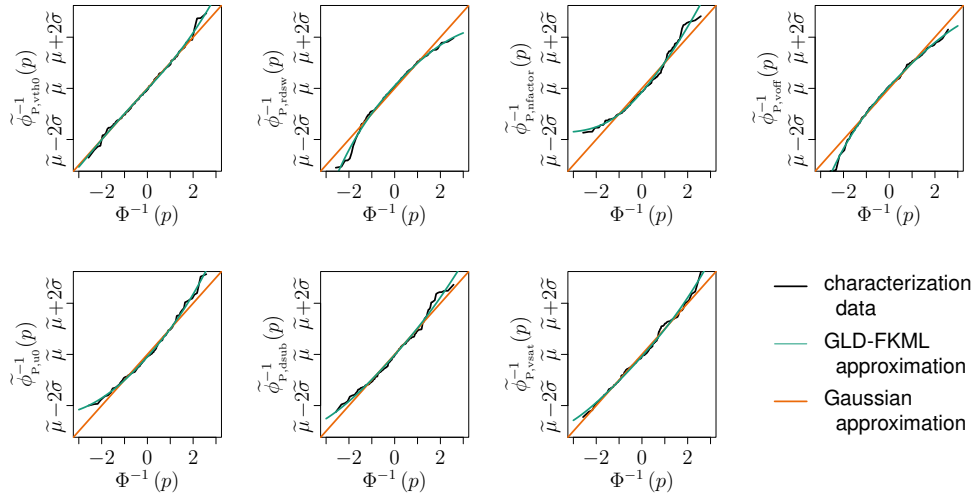

Fig. C.2: Marginal distributions of the PFET parameters

C.1.2 Scatterplot Matrices

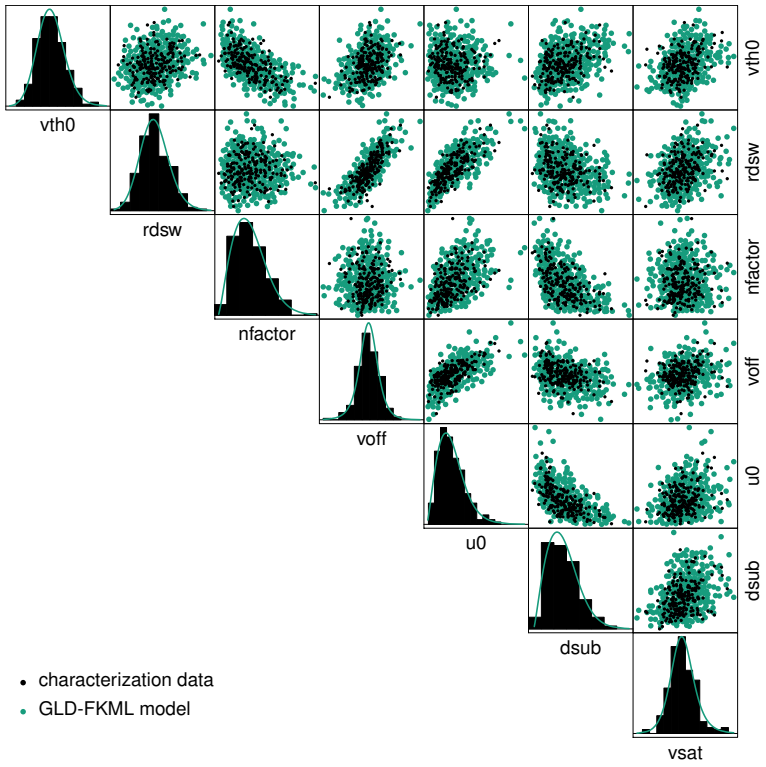

Fig. C.3: Scatterplot matrix for NFET model

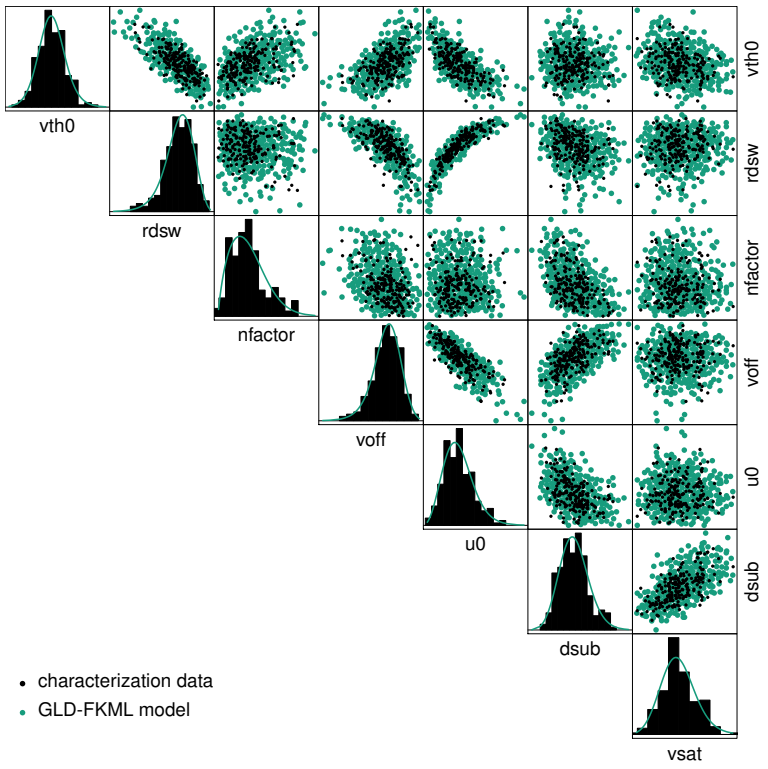

Fig. C.4: Scatterplot matrix for PFET model

C.1.3 HSPICE Netlists for Simulation Scenarios

NFET & PFET

```
*** NFET current measurements
*** NFET (L=35nm, W=70nm)
*** load device models
.include "models.inc"
*** instantiate nfet
* variation parameters sampled
* inside device subcircuit
xn d g s b NFET L=35n W=70n
*** voltage sources
.param vdd=1
.param vgate=0
vd d 0 dc=vdd
vs s 0 dc=0
vb b 0 dc=0
vg g 0 dc=vgate
*** analysis statement
.dc vgate 0 vdd 'vdd/100'
+ sweep monte=5e3
.option ingold=2
.option measform=1
*** measurements
.measure dc ioff_
+ find i(vd) at=0 print=0
.measure dc ioff param='-ioff_'
.measure dc ion_
+ find i(vd) at=vdd print=0
.measure dc ion  param='-ion_'
.end
```

```
*** PFET current measurements
*** PFET (L=35nm, W=140nm)
*** load device models
.include "models.inc"
*** instantiate pfet
* variation parameters sampled
* inside device subcircuit
xn d g s b PFET L=35n W=140n
*** voltage sources
.param vdd=1
.param vgate=0
vd d 0 dc=0
vs s 0 dc='-vdd'
vb b 0 dc=0
vg g 0 dc=vgate
*** analysis statement
.dc vgate '-vdd' 0 'vdd/100'
+ sweep monte=5e3
.option ingold=2
.option measform=1
*** measurements
.measure dc ioff_
+ find i(vd) at=0 print=0
.measure dc ioff param='-ioff_'
.measure dc ion_
+ find i(vd) at='-vdd' print=0
.measure dc ion  param='-ion_'
.end
```

Inverter

```
*** Inverter circuit to test statistical models
***
*** load device models
.include "models.inc"
*** inverter as a subcircuit
.subckt inverter a z vdd vss
    * note: variation parameters sampled inside device subcircuits
    xmn z a vss vss NFET L=35n W=70n
    xmp z a vdd vdd PFET L=35n W=140n
.ends
*** instantiate inverter
x1 a z vdd vss inverter
*** voltage sources
.param vdd=1
vvdd vdd 0 dc='vdd'
vvss vss 0 dc=0
* voltage at pin a rises linearly from 0 to 1
va a 0 pwl 0 0 10p 0 11p 'vdd' 100p 'vdd'
*** analysis statement
.tran .1p 100p sweep monte=5e3
.option autostop
*** measure fall delay
.meas tran fall_delay
+ trig v(a) val='vdd/2' rise=1
+ targ v(z) val='vdd/2' fall=1
.end
```

Ring Oscillator Netlist

```
*** Ring oscillator circuit to test statistical models
***
*** load device models
.include "models.inc"
*** inverter subcircuit with variations sampled inside device subcircuits
.subckt inverter a z vdd vss
    xmn z a vss vss NFET L=35n W=70n
    xmp z a vdd vdd PFET L=35n W=140n
.ends
*** NAND2 subcircuit with variations sampled inside device subcircuits
.subckt nand2 a b z vdd vss
    xmn1 ni a  vss vss NFET L=35n W=70n
    xmn2 z  b  ni  vss NFET L=35n W=70n
    xmp1 z  a  vdd vdd PFET L=35n W=140n
    xmp2 z  b  vdd vdd PFET L=35n W=140n
.ends
*** options
.option autostop runlvl=6 ingold=2 list=1 measform=1
*** instantiate cells
x1 n1 en n2 vdd vss nand2
x2 n2 n3 vdd vss inverter
x3 n3 n1 vdd vss inverter
*** voltage sources
.param vdd=1
vvdd vdd 0 dc='vdd'
vvss vss 0 dc=0
ven  en  0 dc=0 pwl 0 0 10p 0 11p 'vdd'
*** measure leakage + period / frequency
.meas tran leakage avg par('-v(vdd)*i(vvdd)') from=2p to=8p
.meas tran period
+ trig v(n1) val='vdd/2' rise=2
+ targ v(n1) val='vdd/2' rise=3 print=0
.meas tran freq param='1/period'
*** analysis statement
.tran .1p 1000p sweep monte=5e3
.end
```

C.1.4 Monte Carlo Circuit Simulation Results

The following figures depict the simulated distributions of the figures of merit per simulation scenario from Sec. 5.1.4.

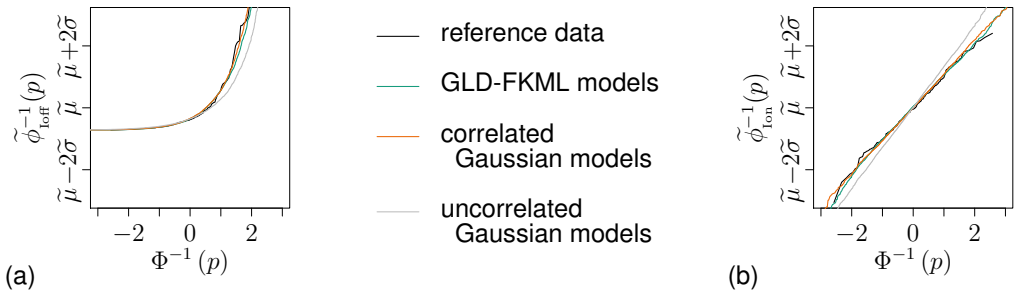

Fig. C.5: Q-Q plots of static NFET performance parameters; (a) off-current; (b) on-current

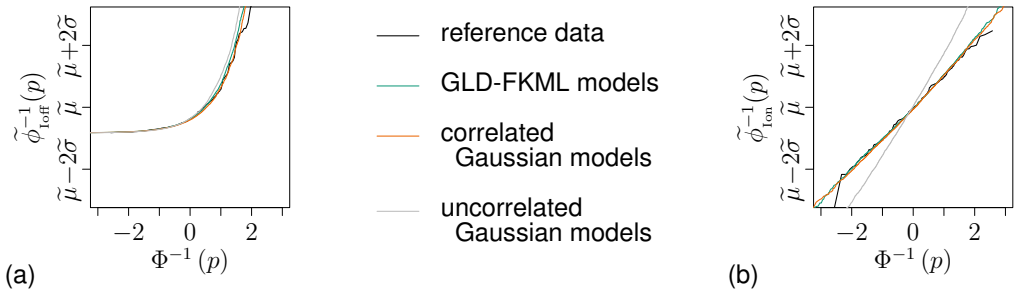

Fig. C.6: Q-Q plots of static PFET performance parameters; (a) off-current; (b) on-current

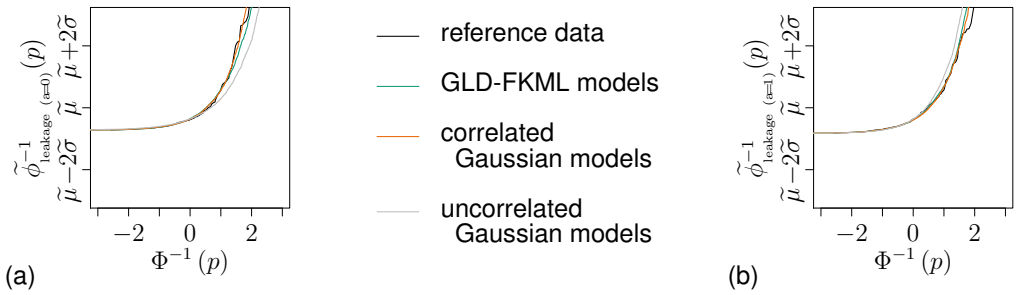

Fig. C.7: Q-Q plots of state-dependent inverter leakage power distributions; (a) input $a=0$; (b) input $a=1$

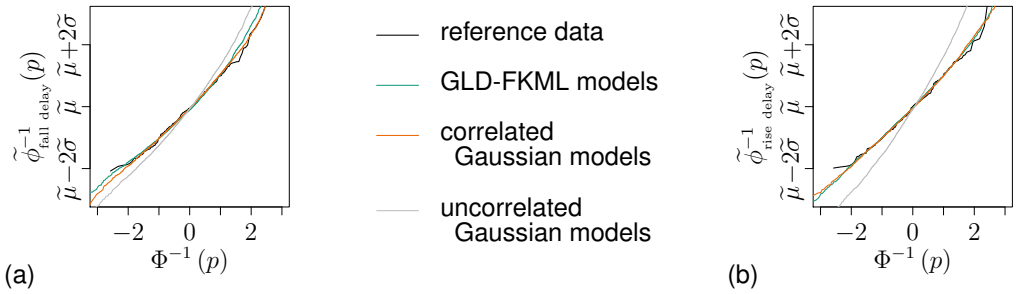

Fig. C.8: Q-Q plots of inverter propagation delay distributions; (a) fall delay; (b) rise delay

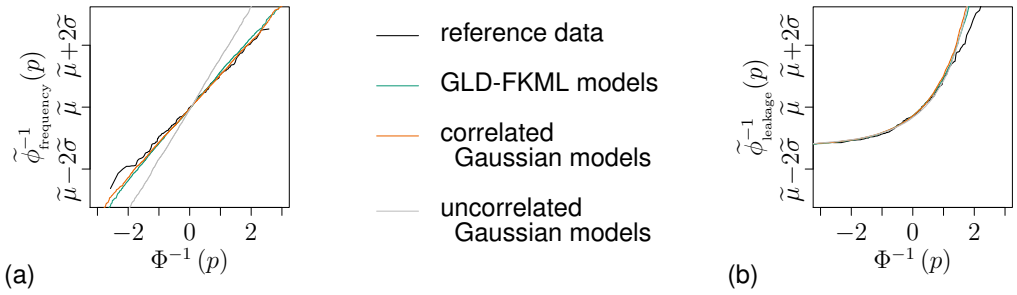

Fig. C.9: Q-Q plots of RO performance parameter distributions; (a) frequency; (b) leakage; compare Fig. 7 in [LSJ+16]

C.2 Statistical Test Results for Standard Cell Models

Tab. C.1: AND2 gate, $N_{\mathrm{char}} = 1000$, $(1-\alpha_c) = 0.95$

Parameter	Boundary conditions	SW test for Gaussianity		KS test for GLD-FKML approximations	
		p-value	Result	p-value	Result
fall delay a–z	2.5ps; 5fF	0	–	0.976	**o**
fall delay a–z	2.5ps; 10fF	0	–	0.972	**o**
fall delay a–z	5ps; 5fF	0	–	0.973	**o**
fall delay a–z	5ps; 10fF	0	–	0.98	**o**
fall delay b–z	2.5ps; 5fF	0	–	0.973	**o**
fall delay b–z	2.5ps; 10fF	0	–	0.999	**o**
fall delay b–z	5ps; 5fF	0	–	0.996	**o**
fall delay b–z	5ps; 10fF	0	–	0.995	**o**
fall energy a–z	2.5ps; 5fF	0	–	0.868	**o**
fall energy a–z	2.5ps; 10fF	0	–	0.785	**o**
fall energy a–z	5ps; 5fF	0	–	0.716	**o**
fall energy a–z	5ps; 10fF	0.008	–	0.821	**o**
fall energy b–z	2.5ps; 5fF	0.029	–	0.852	**o**
fall energy b–z	2.5ps; 10fF	0.031	–	0.73	**o**
fall energy b–z	5ps; 5fF	0.204	**+**	0.844	**o**
fall energy b–z	5ps; 10fF	0.322	**+**	0.845	**o**
leakage power	a=0; b=0	0	–	0.144	**o**
leakage power	a=0; b=1	0	–	0.645	**o**
leakage power	a=1; b=0	0	–	0.158	**o**
leakage power	a=1; b=1	0	–	0.385	**o**
rise delay a–z	2.5ps; 5fF	0	–	0.76	**o**
rise delay a–z	2.5ps; 10fF	0	–	0.48	**o**
rise delay a–z	5ps; 5fF	0	–	0.746	**o**
rise delay a–z	5ps; 10fF	0	–	0.62	**o**
rise delay b–z	2.5ps; 5fF	0	–	0.719	**o**
rise delay b–z	2.5ps; 10fF	0	–	0.554	**o**
rise delay b–z	5ps; 5fF	0	–	0.799	**o**
rise delay b–z	5ps; 10fF	0	–	0.686	**o**
rise energy a–z	2.5ps; 5fF	0.007	–	0.93	**o**
rise energy a–z	2.5ps; 10fF	0.008	–	0.93	**o**
rise energy a–z	5ps; 5fF	0	–	0.424	**o**
rise energy a–z	5ps; 10fF	0	–	0.371	**o**
rise energy b–z	2.5ps; 5fF	0.167	**+**	0.977	**o**
rise energy b–z	2.5ps; 10fF	0.166	**+**	0.986	**o**
rise energy b–z	5ps; 5fF	0	–	0.998	**o**
rise energy b–z	5ps; 10fF	0	–	0.999	**o**

SW tests with results **+**: *Gaussian* and –: *non-Gaussian*

KS tests with results **o**: *accurate GLD-FKML approximation* and x: *inaccurate GLD-FKML approximation*

Tab. C.2: Buffer, $N_{\mathrm{char}} = 1000$, $(1-\alpha_c) = 0.95$

Parameter	Boundary conditions	SW test for Gaussianity		KS test for GLD-FKML approximations	
		p-value	Result	p-value	Result
fall delay a–z	2.5ps; 5fF	0	–	0.649	**o**
fall delay a–z	2.5ps; 10fF	0	–	0.825	**o**
fall delay a–z	5ps; 5fF	0	–	0.718	**o**
fall delay a–z	5ps; 10fF	0	–	0.812	**o**
fall energy a–z	2.5ps; 5fF	0	–	0.857	**o**
fall energy a–z	2.5ps; 10fF	0	–	0.836	**o**
fall energy a–z	5ps; 5fF	0	–	0.72	**o**
fall energy a–z	5ps; 10fF	0.009	–	0.801	**o**
leakage power	a=0	0	–	0.796	**o**
leakage power	a=1	0	–	0	x
rise delay a–z	2.5ps; 5fF	0	–	0.872	**o**
rise delay a–z	2.5ps; 10fF	0	–	0.492	**o**
rise delay a–z	5ps; 5fF	0	–	0.908	**o**
rise delay a–z	5ps; 10fF	0	–	0.803	**o**
rise energy a–z	2.5ps; 5fF	0	–	0.412	**o**
rise energy a–z	2.5ps; 10fF	0	–	0.492	**o**
rise energy a–z	5ps; 5fF	0	–	0.814	**o**
rise energy a–z	5ps; 10fF	0	–	0.665	**o**

SW tests with results **+**: *Gaussian* and –: *non-Gaussian*

KS tests with results **o**: *accurate GLD-FKML approximation* and x: *inaccurate GLD-FKML approximation*

Tab. C.3: Inverter, $N_{\mathrm{char}} = 1000$, $(1-\alpha_c) = 0.95$

Parameter	Boundary conditions	SW test for Gaussianity		KS test for GLD-FKML approximations	
		p-value	Result	p-value	Result
fall delay a–z	2.5ps; 5fF	0	–	0.981	**o**
fall delay a–z	2.5ps; 10fF	0	–	0.999	**o**
fall delay a–z	5ps; 5fF	0	–	0.96	**o**
fall delay a–z	5ps; 10fF	0	–	0.989	**o**
fall energy a–z	2.5ps; 5fF	0.328	**+**	0.969	**o**
fall energy a–z	2.5ps; 10fF	0.257	**+**	0.697	**o**
fall energy a–z	5ps; 5fF	0.474	**+**	0.967	**o**
fall energy a–z	5ps; 10fF	0.37	**+**	0.995	**o**
leakage power	a=0	0	–	0.126	**o**
leakage power	a=1	0	–	0.095	**o**
rise delay a–z	2.5ps; 5fF	0.007	–	0.997	**o**
rise delay a–z	2.5ps; 10fF	0.004	–	0.995	**o**
rise delay a–z	5ps; 5fF	0.031	–	0.992	**o**
rise delay a–z	5ps; 10fF	0.008	–	0.994	**o**
rise energy a–z	2.5ps; 5fF	0	–	0.908	**o**
rise energy a–z	2.5ps; 10fF	0	–	0.901	**o**
rise energy a–z	5ps; 5fF	0	–	0.957	**o**
rise energy a–z	5ps; 10fF	0	–	0.977	**o**

SW tests with results **+**: *Gaussian* and –: *non-Gaussian*

KS tests with results **o**: *accurate GLD-FKML approximation* and x: *inaccurate GLD-FKML approximation*

Tab. C.4: NAND2 gate, $N_{\mathrm{char}} = 1000$, $(1-\alpha_c) = 0.95$

Parameter	Boundary conditions	SW test for Gaussianity		KS test for GLD-FKML approximations	
		p-value	Result	p-value	Result
fall delay a–z	2.5ps; 5fF	0	–	0.546	**o**
fall delay a–z	2.5ps; 10fF	0	–	0.352	**o**
fall delay a–z	5ps; 5fF	0	–	0.658	**o**
fall delay a–z	5ps; 10fF	0	–	0.521	**o**
fall delay b–z	2.5ps; 5fF	0	–	0.408	**o**
fall delay b–z	2.5ps; 10fF	0	–	0.537	**o**
fall delay b–z	5ps; 5fF	0	–	0.584	**o**
fall delay b–z	5ps; 10fF	0	–	0.473	**o**
fall energy a–z	2.5ps; 5fF	0.459	**+**	0.532	**o**
fall energy a–z	2.5ps; 10fF	0.817	**+**	0.976	**o**
fall energy a–z	5ps; 5fF	0.066	**+**	0.824	**o**
fall energy a–z	5ps; 10fF	0.24	**+**	0.265	**o**
fall energy b–z	2.5ps; 5fF	0.885	**+**	0.992	**o**
fall energy b–z	2.5ps; 10fF	0.435	**+**	0.968	**o**
fall energy b–z	5ps; 5fF	0.902	**+**	0.993	**o**
fall energy b–z	5ps; 10fF	0.955	**+**	0.985	**o**
leakage power	a=0; b=0	0	–	0.784	**o**
leakage power	a=0; b=1	0	–	0.008	x
leakage power	a=1; b=0	0	–	0.007	x
leakage power	a=1; b=1	0	–	0.586	**o**
rise delay a–z	2.5ps; 5fF	0	–	0.997	**o**
rise delay a–z	2.5ps; 10fF	0	–	0.999	**o**
rise delay a–z	5ps; 5fF	0	–	0.993	**o**
rise delay a–z	5ps; 10fF	0	–	0.995	**o**
rise delay b–z	2.5ps; 5fF	0	–	0.929	**o**
rise delay b–z	2.5ps; 10fF	0	–	0.937	**o**
rise delay b–z	5ps; 5fF	0	–	0.995	**o**
rise delay b–z	5ps; 10fF	0	–	0.96	**o**
rise energy a–z	2.5ps; 5fF	0.145	**+**	0.999	**o**
rise energy a–z	2.5ps; 10fF	0.113	**+**	0.999	**o**
rise energy a–z	5ps; 5fF	0.396	**+**	1	**o**
rise energy a–z	5ps; 10fF	0.168	**+**	1	**o**
rise energy b–z	2.5ps; 5fF	0.01	–	0.99	**o**
rise energy b–z	2.5ps; 10fF	0.007	–	0.985	**o**
rise energy b–z	5ps; 5fF	0.033	–	0.992	**o**
rise energy b–z	5ps; 10fF	0.012	–	0.988	**o**

SW tests with results **+**: *Gaussian* and –: *non-Gaussian*

KS tests with results **o**: *accurate GLD-FKML approximation* and x: *inaccurate GLD-FKML approximation*

Tab. C.5: NOR2 gate, $N_{\mathrm{char}} = 1000$, $(1-\alpha_c) = 0.95$

Parameter	Boundary conditions	SW test for Gaussianity		KS test for GLD-FKML approximations	
		p-value	Result	p-value	Result
fall delay a–z	2.5ps; 5fF	0	–	0.819	**o**
fall delay a–z	2.5ps; 10fF	0	–	0.857	**o**
fall delay a–z	5ps; 5fF	0	–	0.69	**o**
fall delay a–z	5ps; 10fF	0	–	0.832	**o**
fall delay b–z	2.5ps; 5fF	0	–	0.924	**o**
fall delay b–z	2.5ps; 10fF	0	–	0.912	**o**
fall delay b–z	5ps; 5fF	0	–	0.792	**o**
fall delay b–z	5ps; 10fF	0	–	0.787	**o**
fall energy a–z	2.5ps; 5fF	0.395	**+**	0.988	**o**
fall energy a–z	2.5ps; 10fF	0.416	**+**	0.959	**o**
fall energy a–z	5ps; 5fF	0.699	**+**	0.831	**o**
fall energy a–z	5ps; 10fF	0.592	**+**	0.97	**o**
fall energy b–z	2.5ps; 5fF	0.138	**+**	0.871	**o**
fall energy b–z	2.5ps; 10fF	0.269	**+**	0.963	**o**
fall energy b–z	5ps; 5fF	0.134	**+**	0.971	**o**
fall energy b–z	5ps; 10fF	0.09	**+**	0.971	**o**
leakage power	a=0; b=0	0	–	0.005	x
leakage power	a=0; b=1	0	–	0.154	**o**
leakage power	a=1; b=0	0	–	0.197	**o**
leakage power	a=1; b=1	0	–	0.94	**o**
rise delay a–z	2.5ps; 5fF	0	–	0.903	**o**
rise delay a–z	2.5ps; 10fF	0	–	0.872	**o**
rise delay a–z	5ps; 5fF	0	–	0.868	**o**
rise delay a–z	5ps; 10fF	0	–	0.876	**o**
rise delay b–z	2.5ps; 5fF	0	–	0.876	**o**
rise delay b–z	2.5ps; 10fF	0	–	0.943	**o**
rise delay b–z	5ps; 5fF	0	–	0.689	**o**
rise delay b–z	5ps; 10fF	0	–	0.882	**o**
rise energy a–z	2.5ps; 5fF	0.002	–	0.872	**o**
rise energy a–z	2.5ps; 10fF	0.002	–	0.92	**o**
rise energy a–z	5ps; 5fF	0.003	–	0.903	**o**
rise energy a–z	5ps; 10fF	0.002	–	0.915	**o**
rise energy b–z	2.5ps; 5fF	0.003	–	0.801	**o**
rise energy b–z	2.5ps; 10fF	0.003	–	0.83	**o**
rise energy b–z	5ps; 5fF	0.005	–	0.73	**o**
rise energy b–z	5ps; 10fF	0.003	–	0.75	**o**

SW tests with results **+**: *Gaussian* and –: *non-Gaussian*

KS tests with results **o**: *accurate GLD-FKML approximation* and x: *inaccurate GLD-FKML approximation*

C.3 Statistical Ring Oscillator Analysis

C.3.1 Statistical Test Results for Standard Cell Performance Parameters

The RO-internal standard cell characterization in Sec. 5.3.2 is performed for different sample sizes N_{char}. The following tables list the statistical test results for RO-internal standard cell performance parameter distributions at $(1-\alpha_c)=0.95$ confidence level for $N_{\mathrm{char}}=500$ and $N_{\mathrm{char}}=1000$: SW tests of components of characterization data with results **+**: *Gaussian* and –: *non-Gaussian*; KS tests comparing characterization data and GLD-FKML approximations of marginal distributions with results **o**: *accurate approximation* and x: *inaccurate approximation*; compare TABLE II in [LSJ+16]

Tab. C.6: Results of statistical tests for $N_{\mathrm{char}}=500$-sample characterization data

Performance parameter	Inverter		NAND2		NOR2	
	SW test	KS test	SW test	KS test	SW test	KS test
t_{r}	–	o	+	o	+	o
t_{f}	–	o	+	o	+	o
W_{r}	+	o	–	o	+	o
W_{f}	+	o	+	o	+	o
$P_{\mathrm{leak}}^{(\mathrm{a=0,b=0})}$			–	o	–	o
$P_{\mathrm{leak}}^{(\mathrm{a=0,b=1})}$			–	o	–	o
$P_{\mathrm{leak}}^{(\mathrm{a=1,b=0})}$			–	x	–	o
$P_{\mathrm{leak}}^{(\mathrm{a=1,b=1})}$			–	o	–	o

Tab. C.7: Results of statistical tests for $N_{\mathrm{char}}=1000$-sample characterization data

Performance parameter	Inverter		NAND2		NOR2	
	SW test	KS test	SW test	KS test	SW test	KS test
t_{r}	–	o	–	o	–	o
t_{f}	–	o	–	o	+	o
W_{r}	+	o	–	o	+	o
W_{f}	+	o	+	o	+	o
$P_{\mathrm{leak}}^{(\mathrm{a=0,b=0})}$			–	o	–	o
$P_{\mathrm{leak}}^{(\mathrm{a=0,b=1})}$			–	o	–	o
$P_{\mathrm{leak}}^{(\mathrm{a=1,b=0})}$			–	o	–	o
$P_{\mathrm{leak}}^{(\mathrm{a=1,b=1})}$			–	o	–	o

C.3.2 Scatterplot Matrices for RO-Internal Probabilistic Models

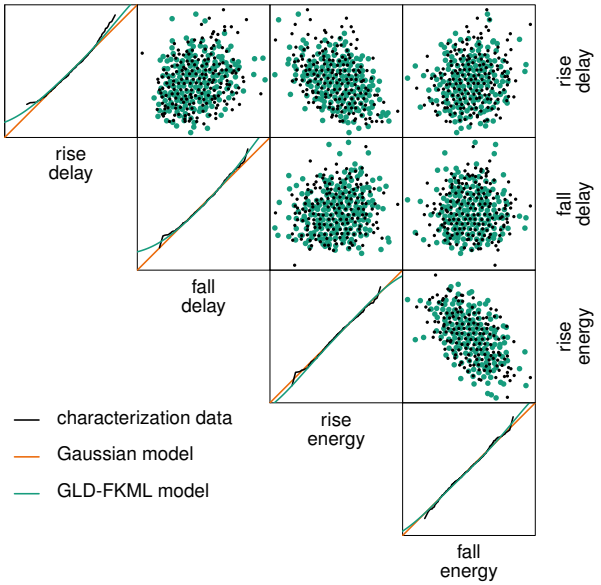

Fig. C.10: RO-internal probabilistic inverter model calibrated in Sec. 5.3.2; $N_{\mathrm{char}} = 500$; Gaussian approximations and GLD-FKML approximations of marginal distributions; scatter plots from $N_s = 500$ samples from inverter model; correlations in Gaussian model not shown

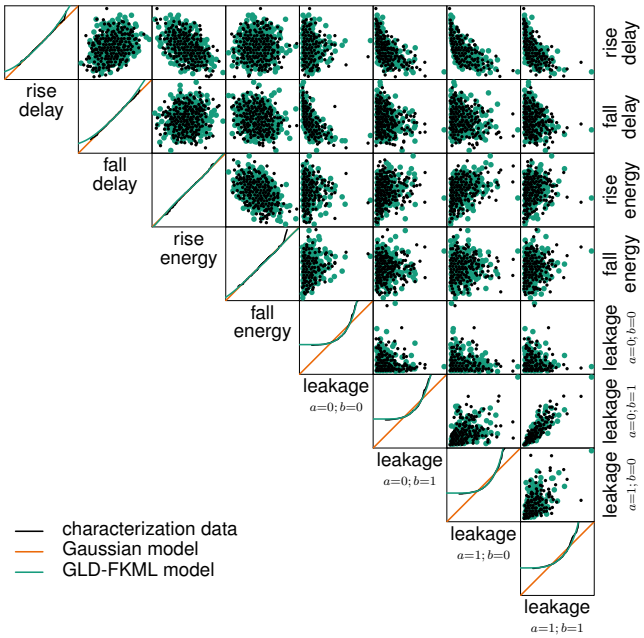

Fig. C.11: RO-internal probabilistic NOR2 model calibrated in Sec. 5.3.2; $N_{\mathrm{char}} = 500$; Gaussian approximations and GLD-FKML approximations of marginal distributions; scatter plots from $N_s = 500$ samples from NOR2 model; correlations in Gaussian model not shown

C.3.3 Statistical Test Results for RO Performance Parameters

Fig. C.12 illustrates the results of statistical tests conducted to evaluate the probabilistic model accuracy in statistical gate level RO analyses in Sec. 5.3.3.

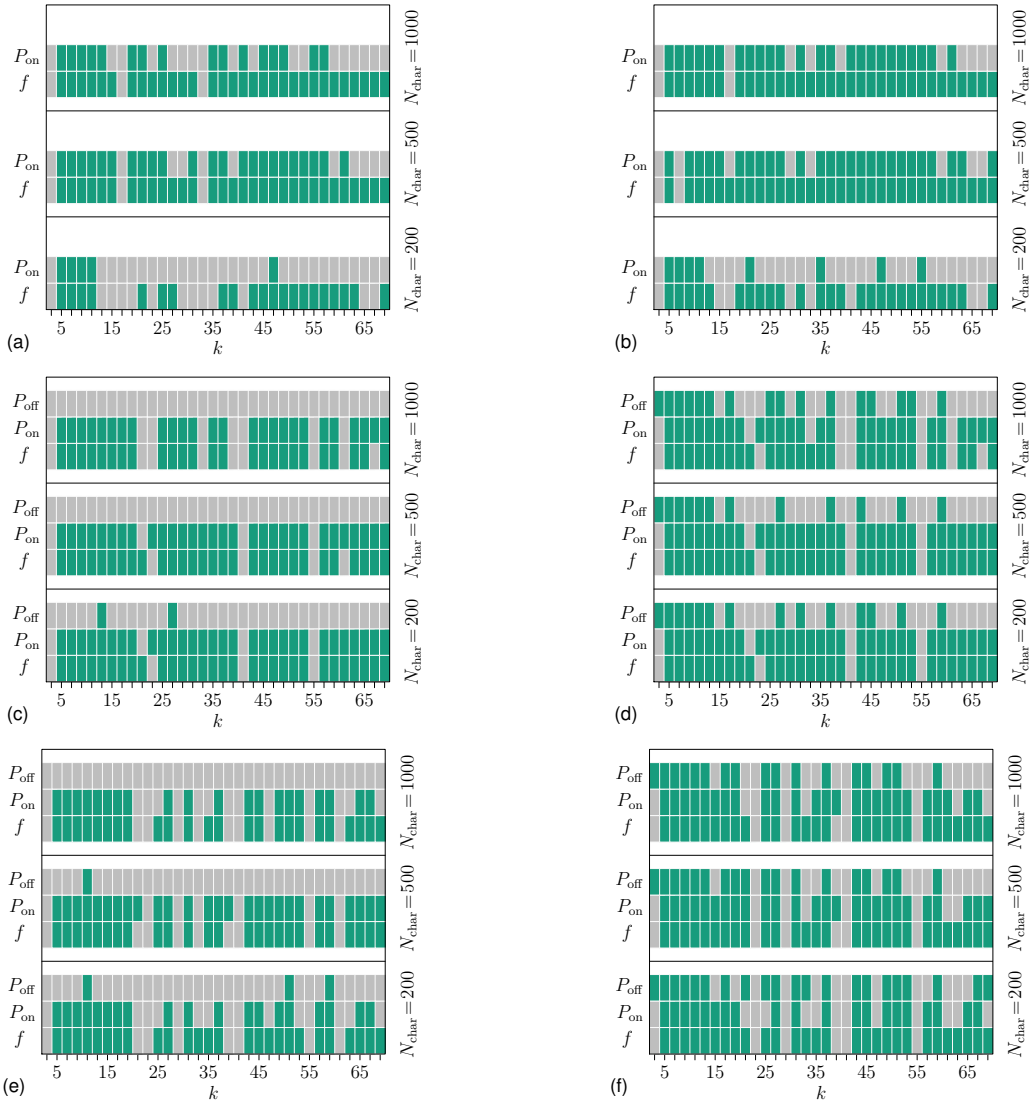

Fig. C.12: Results of KS tests for RO performance parameter distributions; comparison of $N_{\text{ref}} = 200$-sample reference MC circuit simulation results and gate level analyses at $(1-\alpha_c) = 0.95$ confidence level; null-hypothesis "reference data and gate level analysis represent same underlying distribution" accepted (green) or rejected (grey); (a) inverter-based ROs with correlated Gaussian models; (b) inverter-based ROs with probabilistic GLD-FKML models; (c) NAND2-based ROs with correlated Gaussian models; (d) NAND2-based ROs with probabilistic GLD-FKML models; (e) NOR2-based ROs with correlated Gaussian models; (f) NOR2-based ROs with probabilistic GLD-FKML models

C.4 Probabilistic Analog Behavioral Models

C.4.1 Analog Behavioral Voltage Divider Model

Statistics Section

```
simulator lang=spectre
//// nominal values
parameters vd_z1_g=0 vd_z1_l=0
parameters vd_z2_g=0 vd_z2_l=0
parameters vd_z3_g=0 vd_z3_l=0
//// statistics section
statistics {
  // global variations
  process {
    vary vd_z1_g dist=gauss std=0.748 percent=no
    vary vd_z2_g dist=gauss std=0.849 percent=no
    vary vd_z3_g dist=gauss std=0.853 percent=no
  }
  correlate param=[vd_z1_g vd_z2_g] cc=0.184
  correlate param=[vd_z1_g vd_z3_g] cc=-0.253
  correlate param=[vd_z2_g vd_z3_g] cc=0.904
  // local votage divider variations
  mismatch {
    vary vd_z1_l dist=gauss std=1 percent=no
    vary vd_z2_l dist=gauss std=1 percent=no
    vary vd_z3_l dist=gauss std=1 percent=no
  }
}
```

Verilog-A Module

```
‘include "constants.vams"
‘include "disciplines.vams"
////// probabilistic Voltage divider Verilog-A module
module voltage_divider_va (VDD, VSS, OUT);
  //// pins
  inout VDD, VSS, OUT;
  electrical VDD, VSS, OUT;
  //// declarations
  real z1_l, z2_l, z3_l, Yvd1, Yvd2, Yvd3;
  //// catch global variation parameters from Spectre
  (* cds_inherited_parameter *) parameter real vd_z1_g = 0;
  (* cds_inherited_parameter *) parameter real vd_z2_g = 0;
  (* cds_inherited_parameter *) parameter real vd_z3_g = 0;
  //// catch local variation parameters from Spectre
  (* cds_inherited_parameter *) parameter real vd_z1_l = 0;
  (* cds_inherited_parameter *) parameter real vd_z2_l = 0;
  (* cds_inherited_parameter *) parameter real vd_z3_l = 0;
  //// internal functions
  // pnorm to approximate standard Gaussian CDF [AA08]
  analog function real pnorm;
    input z;
    real z;
    if (z>=0)
      pnorm = 0.5 + 0.5*sqrt(1.0-exp(-sqrt(0.3926991)*z*z));
    else
      pnorm = 0.5 - 0.5*sqrt(1.0-exp(-sqrt(0.3926991)*z*z));
  endfunction
  // qgl to implement GLd-FKML quantile function
  analog function real qgl;
    input u,l1,l2,l3,l4;
    real u,l1,l2,l3,l4;
    qgl =  l1 + ( (pow(u,l3)-1)/l3 - (pow(1-u,l4)-1)/l4 ) / l2;
  endfunction
```

```
  //// analog voltage divider behavior
  analog begin
   @(initial_step) begin
    // assignment of model parameters at initial step
    if (vd_z1_g == 0) begin
     // use nominal values in non-MC run
     Y1 = 6.67e-01;
     Y2 = -6.67e+02;
     Y3 = 3.33e-04;
    end else begin
     // MC simulation: conversion of local params to correlated Gaussians
     z1_l = +0.664*vd_z1_l;
     z2_l = +0.148*vd_z1_l +0.509*vd_z2_l;
     z3_l = -0.167*vd_z1_l +0.487*vd_z2_l +0.086*vd_z3_l;
     // assignment of model parameters - GLD approximations
     Yvd1=qgl(pnorm(vd_z1_g+z1_l),6.69e-01, 5.85e+01, 4.47e-02, 1.13e-01);
     Yvd2=qgl(pnorm(vd_z2_g+z2_l),-6.66e+02,  2.61e-02,  1.39e-01,  1.51e-01);
     Yvd3=qgl(pnorm(vd_z3_g+z3_l),3.31e-04, 5.08e+04, 2.55e-01, 6.78e-02);
    end
   end // initial step
   // analog circuit behavior - output voltage and supply current
   V(OUT,VSS) <+ Yvd1*V(VDD,VSS) + Yvd2*I(VSS,OUT);
   I(VDD,VSS) <+ Yvd3*V(VDD,VSS) + Yvd1*I(VSS,OUT);
  end
endmodule
```

C.4.2 Analog Behavioral Model of Bandgap Voltage Reference Circuit

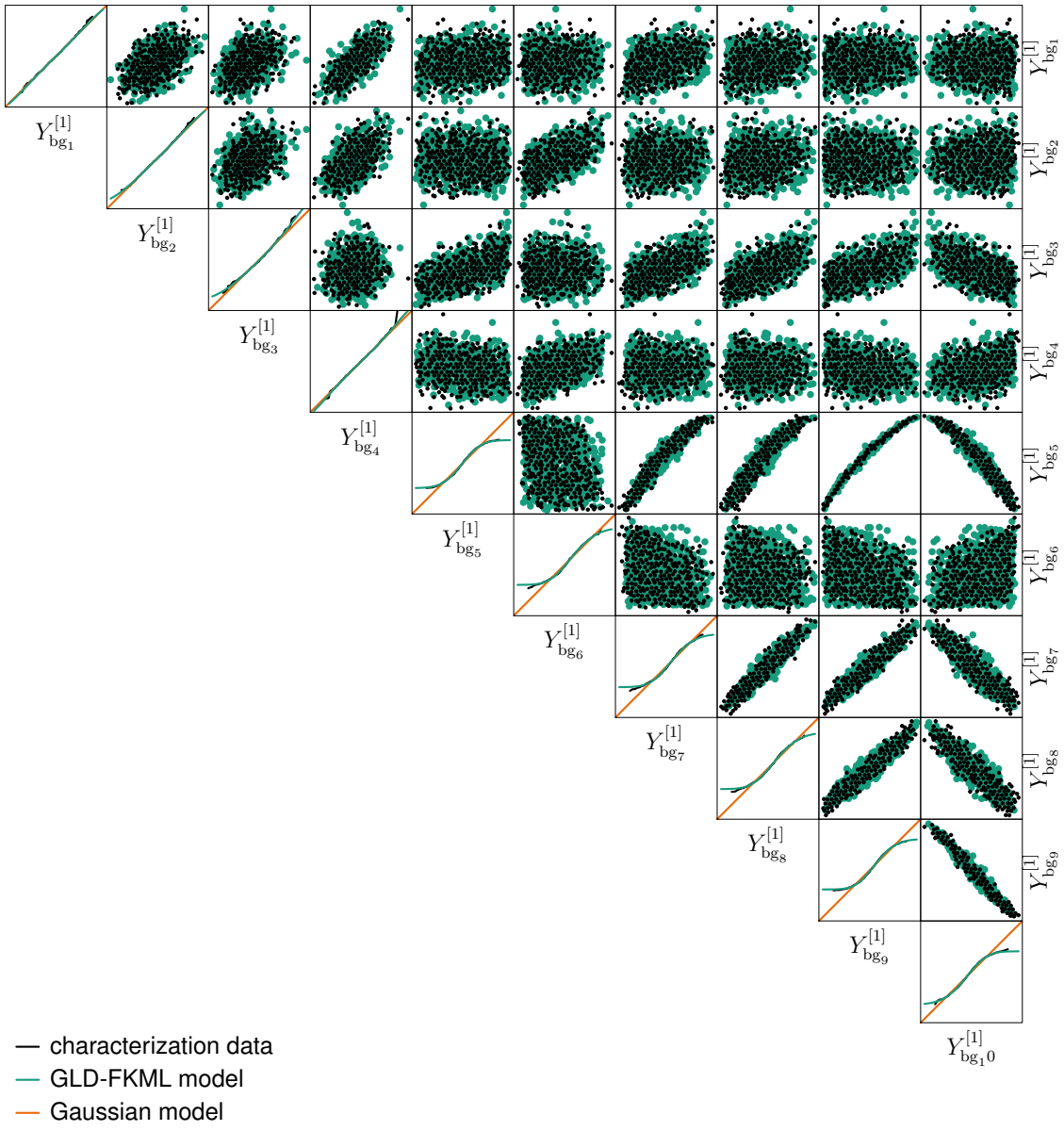

Fig. C.13: Scatterplot matrix to illustrate marginal distributions and intra-instance correlations of probabilistic GLD-FKML model of bandgap voltage reference circuit in Sec. 5.4.3; Gaussian approximations of marginal distributions as references; $N_{\mathrm{char}} = N_s = 1000$

Bibliography

[AA08] K.M. Aludaat and M.T. Alodat. A Note on Approximating the Normal Distribution Function. *Applied Mathematical Sciences*, 2(9):425–429, 2008.

[aA16] ams AG. hitkit v4.10 for 0.35m CMOS Processes (C35/S35/H35). http://asic.ams.com/hitkit/hk410/index.html, 2016.

[AAB+12] C. Auth et al. A 22nm high performance and low-power CMOS technology featuring fully-depleted tri-gate transistors, self-aligned contacts and high density MIM capacitors. In *IEEE Symposium on VLSI Technology (VLSIT)*, pages 131–132, Jun. 2012.

[Acc14] Accellera Organization, Inc., Napa, CA, USA. *Verilog-AMS Language Reference Manual*, May 2014. Version 2.4.

[AD52] T. W. Anderson and D.A. Darling. Asymptotic Theory of Certain "Goodness of Fit" Criteria Based on Stochastic Processes. *The Annals of Mathematical Statistics*, 23(2):193–212, June 1952.

[Adv00] Advanced Micro Devices, Inc. AMD Announces First Revenue Shipments From Dresden "MEGAFAB". Press Release, May 2000.

[AGW94] K.J. Antreich, H.E. Graeb, and C.U. Wieser. Circuit analysis and optimization driven by worst-case distances. *IEEE Transactions on Computer-Aided Design of Integrated Circuits and Systems*, 13(1):57–71, 1994.

[AKWW09] S. Ali et al. Improved performance and variation modelling for hierarchical-based optimisation of analogue integrated circuits. In *Design, Automation and Test in Europe (DATE)*, pages 712–717, Apr. 2009.

[Ali09] S.H.M. Ali. *System Level Performance and Yield Optimisation for Analogue Integrated Circuits*. PhD thesis, University of Southampton, Nov. 2009. Faculty of Engineering, Science and Mathematics; School of Electronics and Computer Science.

[AMG12] O. Assare, M. Momtazpour, and M. Goudarzi. Accurate Estimation of Leakage Power Variability in Sub-micrometer CMOS Circuits. In *Euromicro Conference on Digital System Design (DSD)*, pages 18–25, Sep. 2012.

[ARA13] M.H. Abu-Rahma and M. Anis. *Nanometer Variation-Tolerant SRAM*. Springer, New York, NY, USA, 2013.

[Ase07] A. Asenov. Simulation of Statistical Variability in Nano MOSFETs. In *IEEE Symposium on VLSI Technology (VLSIT)*, pages 86–87, Jun. 2007.

[BC09] J. Bhasker and R. Chadha. *Static Timing Analysis for Nanometer Designs: A Practical Approach*. Springer, New York, NY, USA, 2009.

[BCSS08] D. Blaauw et al. Statistical Timing Analysis: From Basic Principles to State of the Art. *IEEE Transactions on Computer-Aided Design of Integrated Circuits and Systems*, 27(4):589–607, 2008.

[BFG+06] K. Bernstein et al. High-performance CMOS variability in the 65-nm regime and beyond. *IBM Journal of Research and Development*, 50(4.5):433–449, Jul./Sep. 2006.

[Bha02] H. Bhatnagar. *Advanced ASIC Chip Synthesis*. Kluwer, Boston, MA, USA, 2nd edition, 2002.

[Boh07] M. Bohr. A 30 Year Retrospective on Dennard's MOSFET Scaling Paper. *IEEE Solid-State Circuits Newsletter*, 12(1):11–13, 2007.

[BRA07] A.R. Brown, G. Roy, and A. Asenov. Poly-Si-Gate-Related Variability in Decananometer MOSFETs With Conventional Architecture. *IEEE Transactions on Electron Devices*, 54(11):3056–3063, Nov. 2007.

[Bur42] I.W. Burr. Cumulative Frequency Functions. *Annals of Mathematical Statistics*, 13(2):215–232, 1942.

[Bur73] I.W. Burr. Pameters for a general system of distributions to match a grid of $\alpha 3$ and $\alpha 4$. *Communications in Statistics - Theory and Methods*, 2(1):1–21, 1973.

[Bur74] I.W. Burr. *Applied Statistical Methods*. Cambridge University Press, New York, NY, USA, 1974.

[BV08] S. Bhardwaj and S. Vrudhula. Leakage Minimization of Digital Circuits Using Gate Sizing in the Presence of Process Variations. *IEEE Transactions on Computer-Aided Design of Integrated Circuits and Systems*, 27(3):445–455, Mar. 2008.

[BVG08] S. Bhardwaj, S. Vrudhula, and A. Goel. A Unified Approach for Full Chip Statistical Timing and Leakage Analysis of Nanoscale Circuits Considering Intradie Process Variations. *IEEE Transactions on Computer-Aided Design of Integrated Circuits and Systems*, 27(10):1812–1825, Oct. 2008.

[Cada] Cadence Design Systems, Inc. *Custom IC Design*. Retrieved: Feb. 09, 2016.

[Cadb] Cadence Design Systems, Inc. Spectre Circuit Simulator – Fast, accurate SPICE-level simulation. [Online] Available from: http://www.cadence.com/products/cic/spectre_circuit/pages/default.aspx. Retrieved: May 07, 2015.

[Cad14] Cadence Design Systems, Inc. *Virtuoso Analog Design Environment Family – Advanced design simulation for fast and accurate verification*, 2014. Retrieved: Jan. 08, 2015.

[Cat00] A. Cataldo. AMD samples Athlon with copper interconnects. [Online] Available from: http://www.eetimes.com/electronics-news/4040123/AMD-samples-Athlon-with-copper-interconnects, Apr. 2000. Retrieved: May 07, 2015.

[CDM+10] Binjie Cheng et al. Statistical-Variability Compact-Modeling Strategies for BSIM4 and PSP. *IEEE Design and Test of Computers*, 27(2):26–35, 2010.

[CFGR06] R. Castro-Lopez et al. *Reuse-Based Methodologies and Tools in the Design of Analog and Mixed-Signal Integrated Circuits*. Springer, Dordrecht, the Netherlands, 2006.

[CGO+07] F. Centurelli et al. A Statistical Model of Logic Gates for Monte Carlo Simulation Including On-chip Variations. In *International Conference on Integrated Circuit and System Design: Power and Timing Modeling, Optimization and Simulation (PATMOS)*, pages 516–525, Berlin, Heidelberg, 2007. Springer-Verlag.

[CGX+12] Lerong Cheng et al. Fourier Series Approximation for Max Operation in Non-Gaussian and Quadratic Statistical Static Timing Analysis. *IEEE Transactions on Very Large Scale Integration (VLSI) Systems*, 20(8):1383–1391, Aug. 2012.

[Cha12] L. Chamness. A Look Back at the Semiconductor Equipment and Materials Market and Outlook – Semiconductor Market Trends. [Online] Available from: http://www.semi.org/en/node/41166, Apr. 2012. Retrieved: Oct. 05, 2015.

[Che12] J. Chen. A Practical Methodology for Verifying RF Designs. In J. Chen et al., editors, *Mixed-Signal Methodology Guide – Advanced Methodology for AMS IP and SOC Design, Verification and Implementation*, chapter 5, pages 145–190. Cadence Design Systems, Inc., San Jose, CA, USA, August 2012.

[Cla61] C.E. Clark. The Greatest of a Finite Set of Random Variables. *Operations Research*, 9(2):145–162, 1961.

[CMC] http://www.si2.org/?page=1684.

[Cou12] Compact Model Council. CMC Standard Netlist Language and Model File Format. [Online] Available from: http://www.si2.org/?page=1683, 2012. Retrieved: Jun. 18, 2014.

[CS05] Hongliang Chang and S.S. Sapatnekar. Full-chip analysis of leakage power under process variations, including spatial correlations. In *Proceedings of the 42nd Design Automation Conference (DAC)*, pages 523–528, June 2005.

[CVB04] K. Chopra, S.B.K. Vrudhula, and S. Bhardwaj. Efficient algorithms for identifying the minimum leakage states in CMOS combinational logic. In *International Conference on VLSI Design*, pages 240–245, 2004.

[CXH07] Lerong Cheng, Jinjun Xiong, and Lei He. Non-Linear Statistical Static Timing Analysis for Non-Gaussian Variation Sources. In *Proceedings of the 44th Design Automation Conference (DAC)*, pages 250–255, June 2007.

[Dec05] G. Declerck. A look into the future of nanoelectronics. In *Symposium on VLSI Technology (VLSIT)*, pages 6–10, June 2005.

[DEH10] M. Dietrich, U. Eichler, and J. Haase. Digital statistical analysis using VHDL: Impact of variations on timing and power using gate-level Monte Carlo simulation. In *Design, Automation and Test in Europe (DATE)*, pages 1007–1010, Mar. 2010.

[DGR+74] R.H. Dennard et al. Design of Ion-Implanted MOSFET's with Very Small Physical Dimensions. *IEEE Journal of Solid-State Circuits*, 9(5):256–268, 1974.

[DGS03] W. Daems, G. Gielen, and W. Sansen. Simulation-based generation of posynomial performance models for the sizing of analog integrated circuits. *IEEE Transactions on Computer-Aided Design of Integrated Circuits and Systems*, 22(5):517–534, May 2003.

[DH12] M. Dietrich and J. Haase, editors. *Process Variations and Probabilistic Integrated Circuit Design*. Springer, New York, NY, USA, 2012.

[DM03] P.G. Drennan and C.C. McAndrew. Understanding MOSFET mismatch for analog design. *IEEE Journal of Solid-State Circuits*, 38(3):450–456, 2003.

[DMD+07] B. Dierickx et al. Propagating variability from technology to system level. In *International Workshop on Physics of Semiconductor Devices (IWPSD)*, pages 74–79, Dec. 2007.

[Dur98] P.A. Duran. *A Practical Guide to Analog Behavioral Modeling for IC System Design*. Kluwer, Norwell, MA, USA, 1998.

[Dwa70] M. Dwass. *Probability and Statistics*. W.A. Benjamin, New York, NY, USA, 1970.

[Eli94] N.J. Elias. Acceptance Sampling: An Efficient, Accurate Method for Estimating and Optimizing Parametric Yield. *IEEE Journal of Solid-State Circuits*, 29(3):323–327, Mar. 1994.

[Eve06] B.S. Everitt. *The Cambridge Dictionary of Statistics*. Number 3. Cambridge University Press, Cambridge, UK, 2006.

[Fac] P.L. Fackler. Generating Correlated Multidimensional Variates. [Online] http://www4.ncsu.edu/∼pfackler/randcorr.ps. Retrieved: May 07, 2015.

[FEHP11] C. Forbes et al. *Statistical Distributions*. Number 4. Wiley, Hoboken, NJ, USA, 2011.

[FF02] A. Ferré and J. Figueras. Leakage power bounds in CMOS digital technologies. *IEEE Transactions on Computer-Aided Design of Integrated Circuits and Systems*, 21(6):731–738, June 2002.

[FKML88] M. Freimer et al. A study of the generalized tukey lambda family. *Communications in Statistics – Theory and Methods*, 17(10):3547–3567, 1988.

[Fle78] A.I. Fleishman. A method for simulating non-normal distributions. *Psychometrika*, 43(4):521–532, 1978.

[Fra] Fraunhofer Institute for Industrial Mathematics ITWM. Analog Insydes - The Intelligent Symbolic Design System for Analog Circuits. [Online] Available from: www.analog-insydes.de. Retrieved: Feb. 09, 2016.

[GMP11] G. Giustolisi, R. Mita, and G. Palumbo. Verilog-A modeling of SPAD statistical phenomena. In *International Symposium on Circuits and Systems (ISCAS)*, pages 773–776, May 2011.

[Gol] Gold Standard Simulations Ltd. Mystic statistical compact model extractor. [Online] Available from: http://www.goldstandardsimulations.com/products/mystic/. Retrieved: May 07, 2015.

[GP06] G.G.E. Gielen and J.R. Phillips. Simulation and Modeling for Analog and Mixed-Signal Integrated Circuits. In L. Scheffer, L. Lavagno, and G. Martin, editors, *Electronic Design Automation for Integrated Circuits Handbook – EDA for IC Implementation, Circuit Design, and Process Technology*, chapter 15. Taylor & Francis, Boca Raton, FL, USA, 2006.

[GR00] G.G.E. Gielen and R.A. Rutenbar. Computer-aided design of analog and mixed-signal integrated circuits. *Proceedings of the IEEE*, 88(12):1825–1854, Dec 2000.

[Gut13] A. Gut. *Probability: A Graduate Course*. Springer Texts in Statistics. Springer, New York, NY, USA, 2nd edition, 2013.

[Haz95] M. Hazewinkel, editor. *Encyclopaedia of Mathematics*. Kluwer, Dordrecht, the Netherlands, 1995. Volume 5: Risk of a Statistical Procedure – Zygmund Class of Functions.

[HE07] E. Hartung and B. Elpelt. *Multivariate Statistik – Lehr- und Handbuch der angewandten Statistik*. Number 14. R. Oldenbourg Verlag, München, Germany, 2007.

[HEK09] J. Hartung, B. Elpelt, and K.-H. Klösener. *Statistik – Lehr- und Handbuch der angewandten Statistik*. Number 15. R. Oldenbourg Verlag, München, Germany, 2009.

[HF96] R.J. Hyndman and Yanan Fan. Sample Quantiles in Statistical Packages. *The American Statistician*, 50(4):361–365, 1996.

[HHPP15] N. Heidmann et al. Variability-aware aging modeling for reliability analysis of an analog neural measurement system. In *IEEE European Test Symposium (ETS)*, pages 1–6, May 2015.

[Hig02] N.J. Higham. Computing the nearest correlation matrix – a problem from finance. *IMA Journal of Numerical Analysis*, 22(3):329–343, 2002.

[Hil04] U. Hilleringmann. *Silizium-Halbleitertechnologie*. Teubner, Stuttgart, Germany, 4th edition, 2004.

[Hir10] T. Hiramoto. Variability research: accomplishments and further directions – a Japanese perspective. Presented at DATE 10 Friday Workshop "The Fruits of Variability Research in Europe", Dresden, Germany, Mar. 2010.

[HKK13] Eun Ju Hwang, Wook Kim, and Young Hwan Kim. Timing Yield Slack for Timing Yield-Constrained Optimization and Its Application to Statistical Leakage Minimization. *IEEE Transactions on Very Large Scale Integration (VLSI) Systems*, 21(10):1783–1796, Oct 2013.

[HLT83] D.E. Hocevar, M.R. Lightner, and T.N. Trick. A Study of Variance Reduction Techniques for Estimating Circuit Yields. *IEEE Transactions on Computer-Aided Design of Integrated Circuits and Systems*, 2(3):180–192, Jul. 1983.

[HP36] H. Hotelling and M.R. Pabst. Rank Correlation and Tests of Significance Involving No Assumption of Normality. *The Annals of Mathematical Statistics*, 7(1):29–43, Mar. 1936.

[HS99] T.C. Headrick and S.S. Sawilowsky. Simulating correlated multivariate nonnormal distributions: Extending the Fleishman power method. *Psychometrika*, 64(1):25–35, 1999.

[HS12] W.K. Härdle and L. Simar. *Applied Multivariate Statistical Analysis*. Springer, Heidelberg, Germany, 3rd edition, 2012.

[ITR11a] International Technology Roadmap for Semiconductors: Design, 2011. http://www.itrs.net/Links/2011ITRS/Home2011.htm.

[ITR11b] International Technology Roadmap for Semiconductors: Executive summary, 2011. http://www.itrs.net/Links/2011ITRS/Home2011.htm.

[ITR11c] International Technology Roadmap for Semiconductors: System drivers, 2011. http://www.itrs.net/Links/2011ITRS/Home2011.htm.

[Joh49] N.L. Johnson. Systems of frequency curves generated by methods of translation. *Biometrika*, 36(1-2):149–176, 1949.

[Jol86] I.T. Jolliffe. *Principal Component Analysis*. Springer Series in Statistics. Springer, New York, NY, USA, 1986.

[JS06] R. Jancke and P. Schwarz. Supporting analog synthesis by abstracting circuit behavior using a modeling methodology. In *IEEE International Symposium on Circuits and Systems (ISCAS)*, pages 1471–1474, May 2006.

[Jun06] W.G. Jung. *Op Amp Applications Handbook*. Analog Devices series. Newnes, Amsterdam, the Netherlands, 2006.

[Kah07] A.B. Kahng. Variability Mitigation in Highly Scaled CMOS: Challenges for EDA. In *IEEE International Electron Devices Meeting (IEDM)*, pages 644–644, 2007.

[KC96] T. Koskinen and P.Y.K. Cheung. Hierarchical tolerance analysis using statistical behavioral models. *IEEE Transactions on Computer-Aided Design of Integrated Circuits and Systems*, 15(5):506–516, May 1996.

[KD00] Z.A. Karian and E.J. Dudewicz. *Fitting Statistical Distributions – The Generalized Lambda Distribution and Generalized Bootstrap Methods*. CRC Press, Boca Raton, FL, USA, 2000.

[KDC+10] U. Kovac et al. A novel approach to the statistical generation of non-normal distributed PSP compact model parameters using a nonlinear power method. In *International Conference on Simulation of Semiconductor Processes and Devices (SISPAD)*, pages 125–128, 2010.

[KDK14] R. King, B. Dean, and S. Klinke. *gld: Estimation and use of the generalised (Tukey) lambda distribution*, 2014. R package version 2.2.1.

[KGB+11] K.J. Kuhn et al. Process Technology Variation. *IEEE Transactions on Electron Devices*, 58(8):2197–2208, 2011.

[KJS12] C. Knoth, H. Jedda, and U. Schlichtmann. Current source modeling for power and timing analysis at different supply voltages. In *Design, Automation and Test in Europe (DATE)*, pages 923–928, Mar. 2012.

[KKK+08] K. Kuhn et al. Managing Process Variation in Intel's 45nm CMOS Technology. *Intel Technology Journal*, 12(2):93–109, June 2008. http://www.intel.com/content/dam/www/public/us/en/documents/research/2008-vol12-iss-2-intel-technology-journal.pdf.

[KLLH09] Chin-Cheng Kuo et al. Fast Statistical Analysis of Process Variation Effects Using Accurate PLL Behavioral Models. *IEEE Transactions on Circuits and Systems I: Regular Papers*, 56(6):1160–1172, June 2009.

[KM99] R.A.R. King and H.L. MacGillivray. Theory & Methods: A Starship Estimation Method for the Generalized λ Distributions. *Australian & New Zealand Journal of Statistics*, 41(3):353–374, 1999.

[Kno12] C. Knoth. *Accurate Waveform-based Timing Analysis with Systematic Current Source Models*. PhD thesis, Technische Universität München, Sep. 2012. Chair of Electronic Design Automation.

[KOB14] A. Krause, M. Olbrich, and E. Barke. Variation-aware behavioral models of analog circuits using support vector machines with interval parameters. In *Computer Science and Electronic Engineering Conference (CEEC)*, pages 121–126, Sept 2014.

[KSP+13] V. Kuruvilla et al. Speeding up Computation of the max/min of a set of Gaussians for Statistical Timing Analysis and Optimization. In *Proceedings of the 50th Design Automation Conference (DAC)*, pages 1–7, May 2013.

[Lap15] M. Lapedus. FinFET Rollout Slower Than Expected. [Online] Available from: http://semiengineering.com/finfet-rollout-slower-than-expected/, Apr. 2015. Retrieved: Mar. 30, 2016.

[LBC+11a] J.K. Lorenz et al. Hierarchical Simulation of Process Variations and Their Impact on Circuits and Systems: Results. *IEEE Transactions on Electron Devices*, 58(8):2227–2234, Aug 2011.

[LBC+11b] J.K. Lorenz et al. Hierarchical Simulation of Process Variations and Their Impact on Circuits and Systems: Methodology. *IEEE Transactions on Electron Devices*, 58(8):2218–2226, Aug 2011.

[LCXS13] Bing Li et al. On Timing Model Extraction and Hierarchical Statistical Timing Analysis. *IEEE Transactions on Computer-Aided Design of Integrated Circuits and Systems*, 32(3):367–380, March 2013.

[Leh51] D.H. Lehmer. Mathematical methods in large-scale computing units. In *Annals of the Computation Laboratory of Harvard University*, volume 26, pages 141–146. Harvard University Press, Cambridge, MA, USA, 1951.

[LH12] A. Lange and J. Haase. Moving variability from devices to higher levels of abstraction. Presentation at MOS Modeling and Parameter Extraction Working Group MOS-AK/GSA Workshop, Dresden, Germany, Apr. 2012. http://www.mos-ak.org/dresden/publications/T10_Lange_MOS-AK_12.pdf.

[LHDK14] A. Lange et al. Ein universeller Ansatz zur Beschreibung von Prozessvariationen mit beliebig verteilten Modellparametern. In *Tagungsband: edaWorkshop 14*, pages 7–12, Berlin, May 2014. VDE Verlag.

[LHE+15] A. Lange et al. Towards Probabilistic Analog Behavioral Modeling. In *IEEE International Symposium on Circuits and Systems (ISCAS)*, pages 2728–2731, May 2015.

[Liu08] J.S. Liu. *Monte Carlo Strategies in Scientific Computing*. Springer Series in Statistics. Springer, New York, NY, USA, 2008.

[Liu14] Hongzhou Liu. High Yield Analysis and Optimization – How to Design the Circuit to Six Sigma. [Online] Available from: http://community.cadence.com/cadence_blogs_8/b/cic/archive/2014/05/12/how-to-optimize-the-design-to-6-sigma_3f00_, May 2014. Retrieved: Mar. 30, 2016.

[LJH+13] A. Lange et al. Probabilistic Standard Cell Modeling Considering Non-Gaussian Parameters and Correlations. In *TAU Workshop*, Mar. 2013.

[LKBF09] J. Lorenz et al. Impact of lithography variations on advanced CMOS devices. In *International Symposium on VLSI Technology, Systems, and Applications (VLSI-TSA)*, pages 17–18, April 2009.

[LLP06] X. Li, J. Le, and L. T. Pileggi. Statistical Performance Modeling and Optimization. In *Foundations and Trends in Electronic Design Automation*, volume 1, pages 331–480. now Publishers, Delft, the Netherlands, 2006.

[LSJ+11] A. Lange et al. A General Approach for Multivariate Statistical MOSFET Compact Modeling Preserving Correlations. In *Proceedings of the European Solid-State Device Research Conference (ESSDERC), 2011*, pages 163–166, Sep. 2011.

[LSJ+14] A. Lange et al. Probabilistic Standard Cell Modeling Considering Non-Gaussian Parameters and Correlations. In *Design, Automation and Test in Europe (DATE)*, Mar. 2014.

[LSJ+16] A. Lange et al. Multivariate Modeling of Variability Supporting Non-Gaussian and Correlated Parameters. *IEEE Transactions on Computer-Aided Design of Integrated Circuits and Systems*, 35(2):197–210, Feb. 2016.

[M+09] T.H. Morshed et al. *BSIM4.6.4 MOSFET Model – User's Manual*. Department of Electrical Engineering and Computer Sciences, University of California, Berkeley, 2009.

[M+11] T.H. Morshed et al. *BSIM4v4.7 MOSFET Model – User's Manual*. Department of Electrical Engineering and Computer Sciences, University of California, Berkeley, 2011.

[MAA+07] K. Mistry et al. A 45nm Logic Technology with High-k+Metal Gate Transistors, Strained Silicon, 9 Cu Interconnect Layers, 193nm Dry Patterning, and 100% Pb-free Packaging. In *IEEE International Electron Devices Meeting (IEDM)*, pages 247–250. IEEE, 2007.

[MAW+11] M. Merrett et al. Modelling Circuit Performance Variations due to Statistical Variability: Monte Carlo Static Timing Analysis. In *Design, Automation and Test in Europe (DATE)*, pages 1–4, Mar. 2011.

[MBDG13] T. McConaghy et al. *Variation-Aware Design of Custom Integrated Circuits: A Hands-on Field Guide*. Springer, New York, NY, USA, 2013.

[MDO05] M. Mani, A. Devgan, and M. Orshansky. An efficient algorithm for statistical minimization of total power under timing yield constraints. In *Proceedings of the 42nd Design Automation Conference (DAC)*, pages 309–314, 2005.

[MDOZ07] M. Mani et al. A Statistical Algorithm for Power- and Timing-Limited Parametric Yield Optimization of Large Integrated Circuits. *IEEE Transactions on Computer-Aided Design of Integrated Circuits and Systems*, 26(10):1790–1802, 2007.

[MG05] T. McConaghy and G. Gielen. IBMG: Interpretable Behavioral Model Generator for Nonlinear Analog Circuits via Canonical Form Functions and Genetic Programming. In *IEEE International Symposium on Circuits and Systems (ISCAS)*, pages 5170–5173 Vol. 5, May 2005.

[MI93] C. Michael and M. Ismail. *Statistical modeling for computer-aided design of MOS VLSI circuits*. The Kluwer international series in engineering and computer science - Analog circuits and signal processing. Kluwer, Boston, MA, USA, 1993.

[Mir12] M. Miranda. When Every Atom Counts. *IEEE Spectrum*, 49(7):32–37, 2012.

[MK86] R.S. Muller and T.I. Kamins. *Device Electronics for Integrated Circuits*. Kluwer, 2nd edition, 1986.

[MLMC09] A. Mutlu et al. A Parametric Approach for Handling Local Variation Effects in Timing Analysis. In *Proceedings of the 46th Design Automation Conference (DAC)*, pages 126–129, New York, NY, USA, 2009. ACM.

[MLSG10] C.C. McAndrew et al. Extensions to Backward Propagation of Variance for Statistical Modeling. *IEEE Design Test of Computers*, 27(2):36–43, 2010.

[Moo65] G. Moore. Cramming more components onto integrated circuits. *Electronics*, 38(8), Apr. 1965.

[Mun] MunEDA GmbH. Solutions Overview. [Online] Available from: http://muneda.com/pdf/MunEDA-Solutions-Overview.pdf. Retrieved: Feb. 10, 2016.

[Niz12] M. Nizic. Mixed-Signal Design Trends and Challenges. In J. Chen et al., editors, *Mixed-Signal Methodology Guide – Advanced Methodology for AMS IP and SOC Design, Verification and Implementation*, chapter 1,

pages 1–10. Cadence Design Systems, Inc., San Jose, CA, USA, August 2012.

[ONB08] M. Orshansky, S.R. Nassif, and D. Boning. *Design for Manufacturability and Statistical Design: A Constructive Approach*. Series on Integrated Circuits and Systems. Springer, New York, NY, USA, 2008.

[Owe88] D.B. Owen. The starship. *Communications in Statistics – Simulation and Computation*, 17(2):315–323, 1988.

[PDW89] M.J.M. Pelgrom, A.C.J. Duinmaijer, and A.P.G. Welbers. Matching properties of MOS transistors. *IEEE Journal of Solid-State Circuits*, 24(5):1433–1439, 1989.

[PG11] K.-W. Pieper and E. Gondro. An effective method for solving the covariance equation for statistical modeling. In *Semiconductor Conference Dresden (SCD), 2011*, pages 1–4, 2011.

[PMM+07] A. Papanikolaou et al. At Tape-out: Can System Yield in Terms of Timing/Energy Specifications Be Predicted? In *IEEE Custom Integrated Circuits Conference (CICC)*, pages 773–778, Sep. 2007.

[Po11] A.V. Prokhorov (originator). Spearman coefficient of rank correlation. Encyclopedia of Mathematics. [Online] Available from: http://www.encyclopediaofmath.org/index.php?title=Spearman_coefficient_of_rank_correlation&oldid=15078, Feb. 2011. Retrieved: Feb 19, 2016.

[Pol79] J.H. Pollard. *A Handbook of Numerical and Statistical Techniques – with examples mainly from the life sciences*. Cambridge University Press, Cambridge, UK, 1979.

[PQH04] Kok-Kwang Phoon, Ser-Tong Quek, and Hongwei Huang. Simulation of non-Gaussian processes using fractile correlation. *Probabilistic Engineering Mechanics*, 19(4):287–292, 2004.

[R C14] R Core Team. *R: A Language and Environment for Statistical Computing*. R Foundation for Statistical Computing, Vienna, Austria, 2014.

[RDL+09] T. Reich et al. A post-layout optimization method with automatic device type selection for BiCMOS analog circuits. In *IEEE International Conference on Electronics, Circuits, and Systems (ICECS)*, pages 803–806, December 2009.

[REO+06] G. Rappitsch et al. Experimental Verification of Simulation Based Yield Optimization for Power-On Reset Cells. In *IEEE Custom Integrated Circuits Conference (CICC)*, pages 857–860, 2006.

[RERB13] T. Reich et al. Design of a 12-bit cyclic RSD ADC sensor interface IC using the intelligent analog IP library. In *ANALOG 2013 – Entwicklung von Analogschaltungen mit CAE-Methoden*, 2013.

[Ros13] D. Rosso. Semiconductor Industry Posts Near-Record Sales Total in 2012. [Online] Available from: http://www.semiconductors.org/news/2013/02/04/global_sales_report_2012/semiconductor_industry_posts_near_record_sales_total_in_2012/, Feb. 2013. Retrieved: Oct. 05, 2015.

[Ros15] D. Rosso. Global Semiconductor Industry Posts Record Sales in 2014. [Online] Available from: http://www.semiconductors.org/news/2015/02/02/global_sales_report_2014/global_semiconductor_industry_posts_record_sales_in_2014/, Feb. 2015. Retrieved: Oct. 05, 2015.

[RS74] J.S. Ramberg and B.W. Schmeiser. An Approximate Method for Generating Asymmetric Random Variables. *Communications of the ACM*, 17(2):78–82, Feb. 1974.

[Sab16] M. Sabra. Entwicklung eines Verfahrens zur automatischen Generierung parametrierbarer Verhaltensmodelle analoger Schaltungskomponenten für verschiedene CMOS-Technologien. Master's thesis, Technische Universität Dresden, 2016.

[Sah10] S.K Saha. Modeling Process Variation in Scaled CMOS Technology. *IEEE Design & Test of Computers*, 27(2):8–16, 2010.

[Sap04] S. Sapatnekar. *Timing*. Kluwer, Norwell, MA, USA, 2004.

[SD77] B.W. Schmeiser and S.J. Deutsch. A versatile four parameter family of probability distributions suitable for simulation. *AIIE Transactions*, 9(2):176–182, 1977.

[SEGS11] M. Strasser et al. Deterministic Analog Placement by Enhanced Shape Functions. In H.E. Graeb, editor, *Analog Layout Synthesis – A Survey of Topological Approaches*, chapter I.3, pages 95–145. Springer, New York,

NY, USA, 2011.

[SH10] C. Salzig and M. Hauser. Design of robust electronic circuits for yield optimization. In *International Workshop on Symbolic and Numerical Methods, Modeling and Applications to Circuit Design (SM2ACD)*, pages 1–5, Oct 2010.

[SKS08a] M. Schmidt, H. Kinzelbach, and U. Schlichtmann. Genauere Laufzeitanalyse digitaler Schaltungen durch Berücksichtigung statistischer Schwankungen der Signalformen. In *edaWorkshop 08*. VDE Verlag, May 2008.

[SKS08b] M. Schmidt, H. Kinzelbach, and U. Schlichtmann. Variational Waveform Propagation for Accurate Statistical Timing Analysis. In *TAU Workshop*, Feb. 2008.

[SLM+10] I. Stevanović et al. Statistical modeling of inter-device correlations with BPV. *Solid-State Electronics*, 54(8):796–800, 2010.

[SM09] I. Stevanović and C.C. McAndrew. Quadratic Backward Propagation of Variance for Nonlinear Statistical Circuit Modeling. *IEEE Transactions on Computer-Aided Design of Integrated Circuits and Systems*, 28(9):1428–1432, 2009.

[Spe12] E. Sperling. What Happened To Statistical Static Timing Analysis? [Online] Available from: http://semiengineering.com/what-happened-to-statistical-static-timing-analysis/, Dec. 2012. Retrieved: Feb. 26, 2016.

[SR07] A. Singhee and R.A. Rutenbar. Statistical Blockade: A Novel Method for Very Fast Monte Carlo Simulation of Rare Circuit Events, and its Application. In *Design, Automation and Test in Europe (DATE)*, Apr. 2007.

[SR09] A. Singhee and R.A. Rutenbar. Statistical Blockade: Very Fast Statistical Simulation and Modeling of Rare Circuit Events and Its Application to Memory Design. *IEEE Transactions on Computer-Aided Design of Integrated Circuits and Systems*, 28(8):1176–1189, 2009.

[SR10] A. Singhee and R.A. Rutenbar, editors. *Extreme Statistics in Nanoscale Memory Design*. Springer, New York, NY, USA, 2010.

[SS97] R. Spence and R.S. Soin. *Tolerance Design of Electronic Circuits*. Imperial College Press, London, UK, 1997.

[SSA+05] A. Srivastava et al. Accurate and efficient gate-level parametric yield estimation considering correlated variations in leakage power and performance. In *Proceedings of the 42nd Design Automation Conference (DAC)*, pages 535–540, June 2005.

[SSK+09] U. Schlichtmann et al. Digital Design at a Crossroads – How to Make Statistical Design Methodologies Industrially Relevant. In *Design, Automation and Test in Europe (DATE)*, pages 1542–1547, Apr. 2009.

[SVV+12] D. Sinha et al. Reversible statistical max/min operation: Concept and applications to timing. In *Proceedings of the 49th Design Automation Conference (DAC)*, pages 1067–1073, June 2012.

[SW65] S.S. Shapiro and M.B. Wilk. An analysis of variance test for normality (complete samples). *Biometrika*, 52(3-4):591–611, 1965.

[SWCR08] A. Singhee et al. Recursive Statistical Blockade: An Enhanced Technique for Rare Event Simulation with Application to SRAM Circuit Design. In *International Conference on VLSI Design (VLSID)*, pages 131–136, 2008.

[Syn15] Synopsys, Inc. HSPICE® – The Gold Standard for Accurate Circuit Simulation. [Online] Available from: http://www.synopsys.com/Tools/Verification/AMSVerification/CircuitSimulation/HSPICE/Pages/default.aspx, 2015. Retrieved: May 07, 2015.

[TAA+04] S.E. Thompson et al. A 90-nm Logic Technology Featuring Strained-Silicon. *IEEE Transactions on Electron Devices*, 51(11):1790–1797, Nov. 2004.

[Tad80] P.R. Tadikamalla. On simulating non-normal distributions. *Psychometrika*, 45(2):273–279, 1980.

[TAU13] TAU Workshop 2013. EDA Court: Hierarchical Construction and Timing Sign-Off of SoCs, Mar. 2013. panel discussion.

[TCR+09] F.J. Twaddle et al. RC Variability of Short-Range Interconnects. In *International Workshop on Computational Electronics (IWCE)*, pages 1–3, May 2009.

[Tec12] Tech Design Forum. On-chip variation (OCV). [Online] Available from: http://www.techdesignforums.com/practice/guides/on-chip-variation-ocv/, 2012. Retrieved: May 07, 2015.

[Tho13] N.T. Thomopoulos. *Essentials of Monte Carlo Simulation*. Springer, New York, NY, USA, 2013.

[TJ82] P.R. Tadikamalla and N.L. Johnson. Systems of frequency curves generated by transformations of logistic variables. *Biometrika*, 69(2):461–465, 1982.

[TS02] U. Tietze and C. Schenk. *Halbleiter-Schaltungstechnik*. Springer, Berlin, Germany, 12th edition, 2002.

[Uo11] V.G. Ushakov (originator). Conditional probability. Encyclopedia of Mathematics. [Online] Available from: http://www.encyclopediaofmath.org/index.php?title=Conditional_probability&oldid=15106, Feb. 2011. Retrieved: Feb 19, 2016.

[VCBS11] V. Veetil et al. Fast Statistical Static Timing Analysis Using Smart Monte Carlo Techniques. *IEEE Transactions on Computer-Aided Design of Integrated Circuits and Systems*, 30(6):852–865, June 2011.

[Ver06] IEEE Standard for Verilog Hardware Description Language. *IEEE Std 1364-2005 (Revision of IEEE Std 1364-2001)*, 2006.

[VHD09a] Behavioural languages - Part 6: VHDL Analog and Mixed-Signal Extensions. *IEEE Standard 61691-6*, Dec. 2009.

[VHD09b] IEEE Standard VHDL Language Reference Manual. *IEEE Standard 1076-2008 (Revision of IEEE Standard 1076-2002)*, Jan. 2009.

[VM83] C.D. Vale and V.A. Maurelli. Simulating multivariate nonnormal distributions. *Psychometrika*, 48(3):465–471, 1983.

[Vog12] R.S. Vogelsong. AMS Behavioral Modeling. In J. Chen et al., editors, *Mixed-Signal Methodology Guide – Advanced Methodology for AMS IP and SOC Design, Verification and Implementation*, chapter 3, pages 25–70. Cadence Design Systems, Inc., San Jose, CA, USA, August 2012.

[VRK+04] C. Visweswariah et al. First-order incremental block-based statistical timing analysis. In *Proceedings ot the 41st Design Automation Conference*, pages 331–336, Jul. 2004.

[VRK+06] C. Visweswariah et al. First-Order Incremental Block-Based Statistical Timing Analysis. *IEEE Transactions on Computer-Aided Design of Inte-*

grated Circuits and Systems, 25(10):2170–2180, 2006.

[WACA13] Xingsheng Wang et al. Geometry, Temperature and Body Bias Dependence of Statistical Variability in 20nm Bulk CMOS Technology: A Comprehensive Simulation Analysis. *IEEE Transactions on Electron Devices*, 60(5):1547–1554, May 2013.

[Wal09] S. Walia. *PrimeTime Advanced OCV Technology – Easy-to-Adopt, Variation-Aware Timing Analysis for 65-nm and below*. Synopsys Inc., Apr. 2009. White Paper.

[Wol90] S. Wolf. *Silicon Processing for the VLSI Era, Volume 2 – Process Integration*. Lattice Press, Sunset Beach, CA, USA, 1990.

[WT86] S. Wolf and R.N. Tauber. *Silicon Processing for the VLSI Era, Volume 1 – Process Technology*. Lattice Press, Sunset Beach, CA, USA, 1986.

[XLL04] Yongjun Xu, Zuying Luo, and Xiaowei Li. A maximum total leakage current estimation method. In *International Symposium on Circuits and Systems (ISCAS)*, volume 2, pages II–757–II–760, May 2004.

[YTG10] M. Yakupov, D. Tomaszewski, and W. Grabinski. Process control monitor based extraction procedure for statistical compact MOSFET modeling. In *Proceedings of the 17th International Conference Mixed Design of Integrated Circuits and Systems (MIXDES)*, pages 85–90, 2010.

[ZSH+12] V. Zolotov et al. Timing analysis with nonseparable statistical and deterministic variations. In *Proceedings of the 49th Design Automation Conference (DAC)*, pages 1061–1066, June 2012.